ktu
kaunas university of technology
1922

MEDICAL PHYSICS in the BALTIC STATES 2025

PROCEEDINGS OF THE 17th INTERNATIONAL CONFERENCE ON *MEDICAL PHYSICS*

6-8 November, 2025
Kaunas, Lithuania

ISSN 1822-5721

KAUNAS UNIVERSITY OF TECHNOLOGY

MEDICAL PHYSICS IN THE BALTIC STATES

Proceedings of the 17th International Conference on Medical Physics

Kaunas, Lithuania
6 – 8 November, 2025

Executive editor **Diana Adlienė**

CONFERENCE IS ORGANIZED BY:

Kaunas University of Technology
Lund University
Medical Physicists Society
University Hospital of Lithuanian University of Health Sciences „Kauno klinikos“

SCIENTIFIC COMMITTEE

Diana ADLIENĖ - Kaunas University of Technology (Lithuania)
Sören MATTSSON - Lund University, Skåne University Hospital (Sweden)
Jurgita LAURIKAITIENĖ - Kaunas University of Technology (Lithuania)
Eeva BOMAN - EFOMP, Tampere University Hospital (Finland)
Todorka DIMITROVA - Plovdiv University "Paisii Hilendarski" (Bulgaria)
Birutė GRICIENĖ - Vilnius University (Lithuania)
Martins PIKSIS - Liepaja Regional Hospital (Latvia)
Kirill SKOVORODKO - Society of Medical Physicists (Lithuania), Vilnius Unviersity Hospital Santaros klinikos (Lithuania)
Agnieszka KUCHCINSKA - 4th Military Clinical Hospital with Polyclinic (Poland)
Reda ČERAPAITĖ–TRUŠINSKIENĖ - Lithuanian University of Health Sciences (Lithuania)
Christian BERNHARDSSON - Lund University (Sweden)
Joosep KEPLER - Foundation Pärnu Hospital (Estonia); Chairman of the Estonian Society for Biomedical Engineering and Medical Physics (Estonia)
Romualdas GRIŠKEVIČIUS - National Cancer Center (Lithuania)

ORGANISING COMMITTEE

Benas Gabrielis URBONAVIČIUS - Kaunas University of Technology
Lena CIBULSKYTĖ - Kaunas University of Technology
Judita PUIŠO - Kaunas University of Technology
Dalia BAREIŠIENĖ - Kaunas University of Technology
Evelina JASELSKĖ - Kaunas University of Technology
Greta KARPAVIČIENĖ - Lithuanian University of Health Sciences
Gustė LAURIKAITYTĖ - Kaunas University of Technology

CONFERENCE IS SUPPORTED BY:

Kaunas University of Technology
Lund University
Medical Physicists Society
European Federation of Organisations for Medical Physics (EFOMP)

Papers included in the Proceedings were reviewed by independent peer reviewers

MEDICAL PHYSICS IN THE BALTIC STATES 17 (2025)

Proceedings of International Conference "Medical Physics 2025"
06-08 November 2025, Kaunas, Lithuania

COMPARATIVE STUDY OF OCCUPATIONAL RADIATION EXPOSURE DURING COMMON FLUOROSCOPY AND ANGIOGRAPHY PROCEDURES

Inga ANDRIULEVIČIŪTĖ[1,2], Kirill SKOVORODKO[2], Tomas ŠINKŪNAS[2], Birutė GRICIENĖ[1,2]
[1]Department of Radiology, Nuclear medicine and Medical physics, Faculty of Medicine, Vilnius University, Vilnius; [2]Vilnius University Hospital Santaros Klinikos, Vilnius, Lithuania
[1]inga.andriuleviciute@mf.stud.vu.lt; [2]kirill.skov@gmail.com; [3]tomas.sinkunas@santa.lt; [4]birute.griciene@mf.vu.lt

***Abstract*:** Medical personnel performing fluoroscopy and angiography procedures are routinely exposed to ionizing radiation. To ensure effective radiation protection in the workplace, it is essential to identify procedures associated with the highest occupational exposure doses and perform optimization. This study aimed to compare occupational exposure doses received by workers performing different fluoroscopy and angiography procedures and to identify dose optimization means.

Keywords: Occupational Exposure; Radiation Protection; Fluoroscopy; Angiography

1. Introduction

The use of medical imaging has significantly increased due to changes in demographics, and improvements in healthcare delivery. Consequently, medical personnel may experience higher occupational radiation doses as a result of increased workload, which could raise their long-term risk of developing cataracts and radiation-induced malignancies [1].

The usage of fluoroscopy and angiography techniques has become an important part of modern medicine, that includes different medical specialties such as gastroenterology, interventional radiology/oncology, and orthopaedics. Even though these procedures demonstrate great therapeutic and diagnostic benefits, healthcare workers still experience a health risk from the use of ionizing radiation [2].

Ionizing radiation doses to workers depends on multiple factors, including procedure type, duration, anatomical region, C-arm angulation, staff positioning and behavior in operating room, and the use of personal protective equipment [3].

To evaluate $H_p(10)$ doses, passive dosimetry, such as optically stimulated luminescence (OSL) or thermoluminescent (TL) dosimeters is routinely implemented in clinical practice. While this method reliably provides cumulative dose, it does not inform workers about real-time exposure or procedure-specific risks, and these methods are further limited by high uncertainty and a relatively high minimum detectable dose [4]. Therefore, it is important to gain a deeper understanding of dose variations across different procedure types and anatomical regions.

The aim of this study was to compare exposure doses received by workers performing orthopaedical trauma, endoscopic retrograde cholangiopancreatography and radioembolization with Ho-166 procedures.

2. Methods and materials

The study was conducted at Vilnius University Hospital Santaros Klinikos during the period from 2024 to 2025.

Occupational radiation doses $H_p(10)$ to physicians and radiology technologists were collected during fluoroscopic and angiographic procedures: orthopaedical trauma surgery, endoscopic retrograde cholangiopancreatography (ERCP), and radioembolization with Ho-166. Additionally, to further evaluate ionizing radiation exposure doses in orthopaedical procedures, they were subdivided into 5 anatomical regions: shoulder/humerus, forearm/wrist/hand, hip/pelvis, knee/tibia, and ankle/foot (Fig. 1).

During orthopaedical trauma procedures, fluoroscopy is used to guide fracture reduction and implant positioning [5], with the C-arm operated by the radiology technologist. During an ERCP procedure, the guidewire is inserted onto the common bile duct using a C-arm. Afterwards a catheter is placed for contrast injection so as the physician could obtain visualization of the biliary and pancreatic ducts in real time. During this procedure, C-arm is operated by a radiology technologist [6]. Radioembolization with Ho-166 is performed with an angiography system under catheter guidance by the interventional radiologist, while the radiology technologist assists in the preparation and injection of Ho-166 microspheres. This type of procedure is performed to treat hepatic cancer [7].

To evaluate personal dose equivalent Hp(10) doses, DMC 3000 active personal dosimeters (APD) by Mirion Technologies were used, worn at chest level over personal radiation protective equipment. The dimensions of the dosimeter were 87 x 60 x 21 mm, and the dose equivalent range was 0.1 µSv to 10 Sv. All dosimeters have been metrologically verified by the Vilnius Metrology Centre.

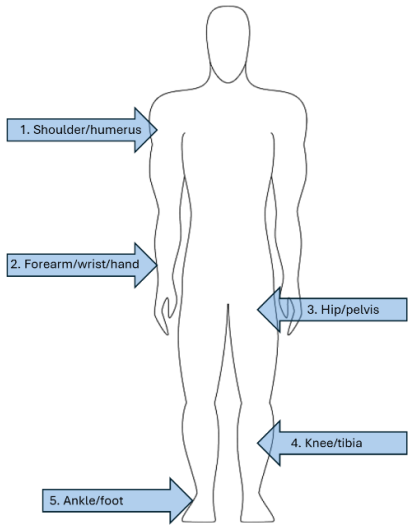

Fig. 1. Anatomical regions of orthopaedical procedures.

Additionally, to assess the correlation between personnel dose and examination parameters, data such as dose area product (DAP), air kerma, and fluoroscopy time were collected.

During orthopaedical and ERCP procedures, fluoroscopy was performed using Philips Healthcare BV Endura (manufactured in 2015) and OEC Elite C-arm (manufactured in 2020) units, whereas radioembolization procedures were carried out with a Philips Healthcare Azurion 7 Cath lab system (manufactured in 2020).

Statistical analysis was calculated using R environment (RStudio version 2025.05.1+513) with Rcmdr package. The Shapiro-Wilk test was used to assess the normality of continuous variables. Since occupational radiation dose values were not normally distributed, results are presented as median with interquartile range (IQR). Comparisons between physician and radiology technologist doses within each procedure group were performed using the Wilcoxon signed-rank test. To compare the radiation doses obtained during different types of procedures, the Kruskal–Wallis test was performed. A p-value <0.05 was considered statistically significant.

3. Results and discussion

The results of physician and radiology technologist doses, as well as DAP, fluoroscopy time, and air kerma, are summarized in Table 1. The highest radiation physician doses were received during radioembolization with Ho-166 (median 27.1 µSv, IQR 11.9-29.2 µSv), meanwhile the doses during ERCP and orthopaedical procedures were substantially lower, resulting in 4.2 (IQR 3.5-4.6 µSv) and 0.9 (IQR 0.4-2.6) µSv, respectively. Also, a Kruskal–Wallis test showed a statistically significant difference in physician radiation doses across procedure types ($p < 0.001$). The highest exposure doses in interventional radiologists during radioembolization can be explained by the combined use of X-rays and additional irradiation from Ho-166 radionuclides, resulting in two distinct sources of exposure. During this type of procedure, interventional radiologists are mainly exposed to scattered radiation from fluoroscopy, meanwhile radiology technologists receive a relatively higher doses from Ho-166 due to their involvement in preparing, handling radioactive microspheres and related materials.

Comparing the occupational exposure distribution of radiology technologists, the same pattern as for physicians was observed: the highest doses were recorded during radioembolization with Ho-166 (median 11.9 µSv, IQR 5.3-13.3 µSv), followed by ERCP (median 0.4 µSv, IQR 0.2-0.5 µSv), and orthopaedical procedures (median 0.1 µSv, IQR 0.0-0.2 µSv).

Analyzing examination parameters also showed that radioembolization with Ho-166 had the highest values, requiring significantly longer fluoroscopy times (median 276 seconds), higher DAP values (median 17.59 Gy·cm², Fig. 2) and more air kerma (median 167.00 mGy) than ERCP (median 62 s, 0.65 Gy·cm², 3.19 mGy), and orthopaedical procedures (median 16 s, 0.09 Gy·cm², 0.21 mGy).

Across all procedure types, the median occupational radiation doses for physicians were significantly higher than those for radiology technologists ($p < 0.001$; see Fig. 3).

The median dose for orthopaedical procedures was 0.9 µSv for physicians compared to for technologists (0.1 µSv), for ERCP - 4.2 versus 0.4 µSv, and for radioembolization with Ho-166 - 27.1 versus 11.9 µSv. Depending on the procedure type, physicians generally received doses that were up to 10 times higher than those given to radiology technologists. This consistent difference can be explained by the fact that during procedures, physicians are closer to the patient and X-ray source, whereas technologists are generally positioned at a greater distance, resulting in substantially lower exposure.

Figure 4 presents the comparison of physician doses across different anatomical regions. To maintain readability, two extreme outliers found in the orthopaedical hip/pelvis procedures (39.3 and 37.5 µSv) were not included in the boxplot visualization, however, the statistical analysis included their values.

In comparison between different orthopaedical procedures, the highest median doses for physicians were found to be during hip/pelvis operations (median 2.5 µSv). Lower median doses were recorded for knee/tibia, forearm/wrist/hand, ankle/foot, and shoulder/humerus procedures (1.2, 0.6, 0.6, and 0.6 µSv, respectively).

According to the results shown in Figure 4, the hip/pelvis anatomical region group showed the broadest distribution of physician doses, suggesting a wide range of exposures. The differences in case complexity, body anatomy, surgical time, and other factors that have a profound effect on fluoroscopy consumption can each account for this variability.

Table 1. Occupational radiation doses and examination parameters during different fluoroscopic/angiographic procedures

Procedure / Region (number of procedures)	Physician dose (µSv)		Radiology technologist dose (µSv)		DAP (Gy·cm²)	Fluoroscopy time (s)	Air kerma (mGy)
	Median (IQR)	Min-max	Median (IQR)	Min-max	Median (IQR)		
Orthopaedical, total (71)	0.9 (0.4-2.6)	0.1-39.3	0.1 (0.0-0.2)	0.0-0.9	0.09 (0.05-0.28)	16 (9-42)	0.21 (0.11-1.03)
– Shoulder/Humerus (8)	0.6 (0.3-1.2)	0.0-9.0	0.1 (0.0-0.2)	0.0-0.3	0.09 (0.04-0.10)	7 (2-13)	0.20 (0.20-0.33)
– Forearm/Wrist/ Hand (13)	0.6 (0.3-0.9)	0.2-3.1	0.1 (0.0-0.1)	0.0-0.3	0.05 (0.04-0.07)	14 (10-23)	0.12 (0.09-0.16)
– Hip/Pelvis (25)	2.5 (1.4-7.1)	0.1-39.3	0.1 (0.1-0.3)	0.0-0.8	0.34 (0.16-0.71)	33 (21-56)	1.70 (0.88-2.30)
– Knee/Tibia (7)	1.2 (0.5-2.5)	0.1-2.8	0.1 (0.1-0.4)	0.0-0.9	0.11 (0.06-0.41)	70 (35-76)	0.72 (0.33-0.93)
– Ankle/Foot (18)	0.6 (0.2-0.9)	0.1-4.2	0.1 (0.0-0.1)	0.0-0.3	0.06 (0.04-0.08	10 (6-17)	0.13 (0.10-0.17)
ERCP (7)	4.2 (3.5-4.6)	2.1-5.5	0.4 (0.2-0.5)	0.0-0.5	0.65 (0.55-0.97)	62 (57-69)	3.19 (2.44-3.76)
Radioembolization (Ho-166, 13)	27.1 (11.9-29.2)	5.1-105.6	11.9 (5.3-13.3)	2.0-27.9	17.59 (9.47-19.1)	276 (204-372)	167.00 (85.60-233.00)

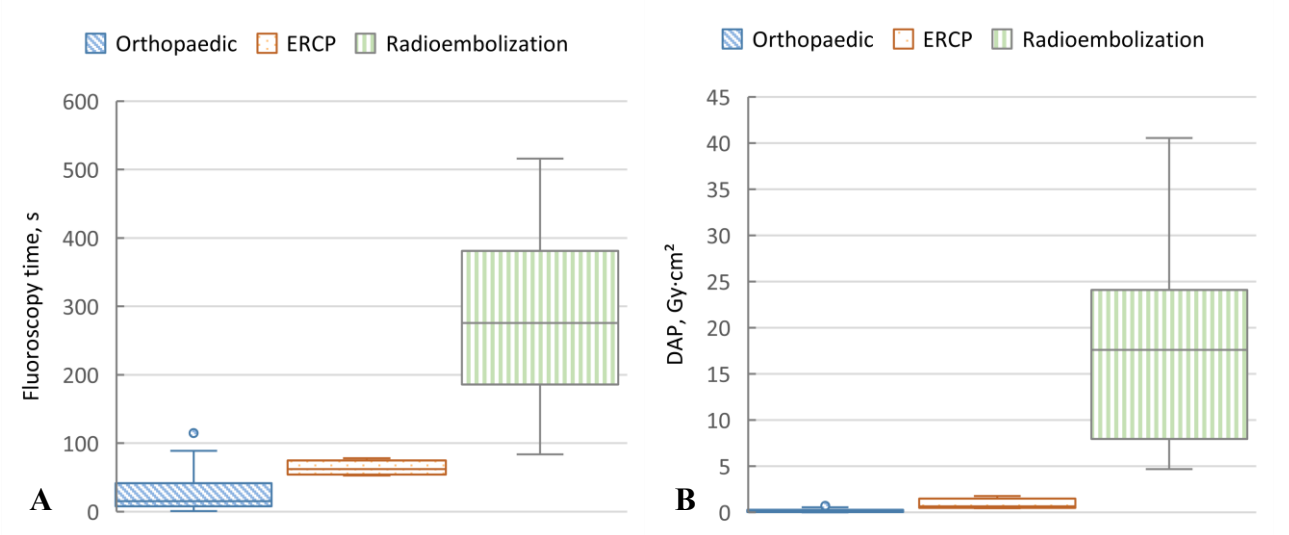

Fig. 2. Comparison of fluoroscopy time (A) and DAP values (B) across orthopaedical, ERCP and radioembolization procedures

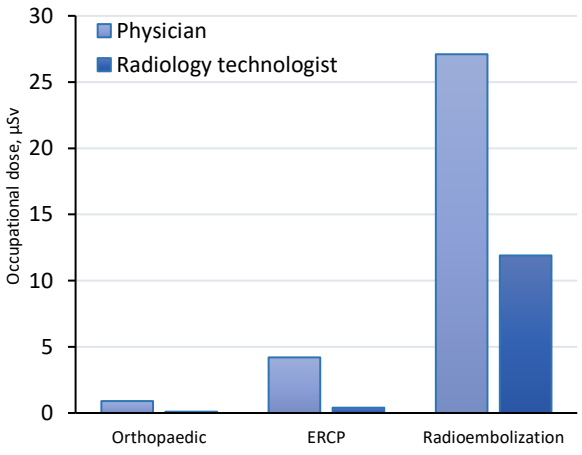

Fig. 3. Comparison of median doses between physicians and radiology technologists across different procedures

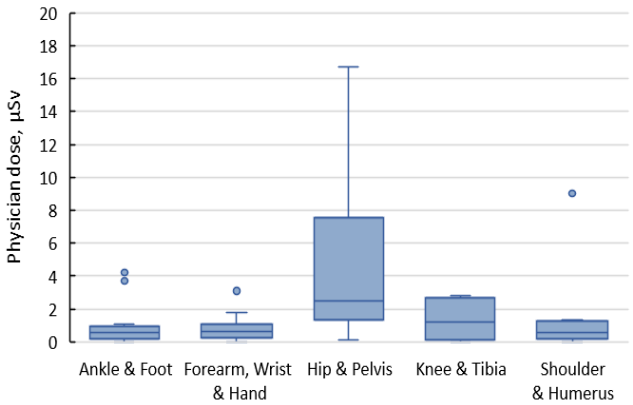

Fig. 4. Comparison of physician doses across different orthopaedical procedures

Evaluation of the doses of radiology technologists during different orthopaedical procedures were found to be low, with a median of 0.1 μSv across all anatomical regions. The highest doses were found during knee/tibia and hip/pelvis operations (maximum values 0.9 and 0.8, respectively), however during majority of procedures no measurable dose was detected, with the dosimeters frequently recording values of zero.

4. Conclusions

Occupational ionizing radiation exposure doses were found to differ between procedure types and anatomical regions. The highest doses were received during radioembolization with Ho-166, while ERCP and orthopaedical procedures resulted in much lower exposure to physicians and radiology technologists. Such procedural parameters, as fluoroscopy time, DAP, and air kerma, closely mirrored this distribution, demonstrating that more complex and prolonged interventions result in higher doses to personnel.

Based on these results, it is indicated that monitoring and protective measures should be adapted to the specificity and characteristics of radiological procedure. A better understanding of these factors can lead to the application of more effective strategies aimed at reducing occupational exposure in clinical practice and this data can also be used for dose prediction and to further improvement of radiation safety.

5. References

1. Tamam N., Salah H., Almogren K. S., Mahgoub O., Saeed M. K., Abdullah Y., Bradley D. A. Evaluation of patients' and occupational radiation risk dose during conventional and interventional radiology procedures. Radiation Physics and Chemistry, 2023, 207, 110818.
2. Jenkins N. W., Parrish J. M., Sheha E. D., Singh K. Intraoperative risks of radiation exposure for the surgeon and patient. Annals of Translational Medicine, 2021, 9(1), p. 84.
3. Hurley R. J., McCabe F. J., Turley L., Maguire D., Lucey J., Hurson C. J. Whole-body radiation exposure in Trauma and Orthopaedic surgery. Bone & Joint Open, 2022, 3(11), p. 907–912.
4. Vano E., Fernandez-Soto J. M., Ten J. I., Sanchez Casanueva R. M. Occupational and patient doses for interventional radiology integrated into a dose management system. The British Journal of Radiology, 2023, 96(1143), 20220607.
5. Thibault J., Naciri W., Rouleau D. M., Chapleau J. Intraoperative radiation exposure in a level 1 trauma centre orthopedic operating room. Canadian Journal of Surgery, 2025, 68(3), p. E235.
6. Sippey M., Maskal S., Anderson M., Marks J. Use of fluoroscopy in endoscopy: Indications, uses, and safety considerations. Annals of Laparoscopic and Endoscopic Surgery, 2019, 4.
7. Kühnel C., Köhler A., Brachwitz T., Seifert P., Gühne F., Aschenbach R., Drescher R. Clinical Results of Holmium-166 Radioembolization with Personalized Dosimetry for the Treatment of Hepatocellular Carcinoma. Journal of Personalized Medicine, 2024, 14(7), 747.

MEDICAL PHYSICS IN THE BALTIC STATES 17 (2025)

Proceedings of International Conference "Medical Physics 2025"
06-08 November 2025, Kaunas, Lithuania

PRIMARY RESULTS OF RADIOGRAPHIC IMAGE QUALITY ASSESSMENT ACROSS MULTIPLE X-RAY SYSTEMS: PH-1 LUNGMAN PHANTOM STUDY

Vilius MILASIUS[1], Feliksas SAKALAUSKAS[2], Kristina REPSE[3], Marius GEDVILAS[4], Vytenis PUNYS[5], Nikolajus MEDVEDEVAS[6]
[1]Klaipeda University Hospital; [2]Klaipeda University Hospital; [3]Klaipeda University Hospital; [4]Klaipeda University Hospital; [5]Klaipeda University; [6]LSMU Kaunas Hospital
[1]mvmilasius@gmail.com; [2]felsaka@gmail.com; [3]kristinarepse@gmail.com; [4]mariusged@gmail.com; [5]vytenis.punys@ku.lt; [6]medvedevk@yahoo.com

***Abstract*:** In conventional radiology, digital radiography has become a standard tool in routine clinical practice because of its high-quality image performance and post-processing options, which have led to enhanced visualisation of anatomical structures. However, this advancement has also been associated with the phenomenon of 'dose creep' related to progressively higher patient radiation exposures, as it can tolerate a wide range of DAP values without noticeable image degradation. This risk is exacerbated when X-ray systems lack effective communication or when automatic exposure control fails to detect the required number of photons.Moreover, X-ray systems rely on image processing techniques that affect the displayed image's grey levels. Therefore, this study presents a comprehensive evaluation of image quality indices (IQI) (signal-to-noise ratio (SNR), contrast-to-noise ratio (CNR)) and total amount of radiation delivered to patients (dose area product (DAP)). The findings highlight variations in image display performance across different tissues and IQIs with respect to changing acquisition parameters (kV, mAs, DAP). These results offer meaningful implications for radiography lung protocol optimisation.

Keywords: Image quality, X-ray systems, PH-1 "Lungman" phantom, ImageJ, SNR, CNR

1. Introduction

Digital chest radiography (DCR) is the gold standard for the initial assessment of thoracic abnormalities [1]. Nevertheless, radiographic image interpretation can be challenging due to the overlapping anatomical structures and the rendering of X-ray systems. The improvement of conventional radiology systems demonstrated high detective quantum efficiency, resolution, broad dynamic range, as well as acceptable image quality even in under- or over-exposure scenarios [2,3]. These scenarios can be affected not only by X-ray systems' malfunctions but also by the performance of the radiology technologist [3]. Prior research indicates that stricter dose management is necessary. Studies have demonstrated that radiology technologists tend to increase exposure levels to prevent re-imaging. It was reported that the entrance surface dose in digital radiography increased by 55%, highlighting the importance of careful dose optimization [4]. While DR detectors exhibit relatively low dependence on exposure parameters during image acquisition, significant variability arises from the way different X-ray systems process raw detector signals and render images for display. Therefore, even under identical exposure parameters, the diagnostic appearance of images may vary considerably across systems [2,5]. However, even minor variations in grey level representation can increase misdiagnosis on chest radiographs, a challenge that is particularly noticeable among less experienced radiologists [6]. For these reasons, this study aimed to compare and analyse how commonly used X-ray systems display different tissue IQI, using an anthropomorphic phantom.

2. Materials and methods

2.1. Diagnostic procedure planning

The anthropomorphic chest region phantom (multipurpose chest phantom N1 "LUNGMAN" PH-1 model) (Fig. 1) was used for the radiographic image acquisition [7]. The phantom was irradiated using different X-ray systems (RADspeed, RADspeed MC, RADspeed Pro, RADspeed Pro EDGE, Aceso), each equipped with a distinct digital radiography (DR) detector (DRTECH EVS 4343, VIVIX-S 3643VW, DR-ID 900, FLAATZ-750, CXDI-410C) at the Klaipeda University Hospital Clinic of Radiology.

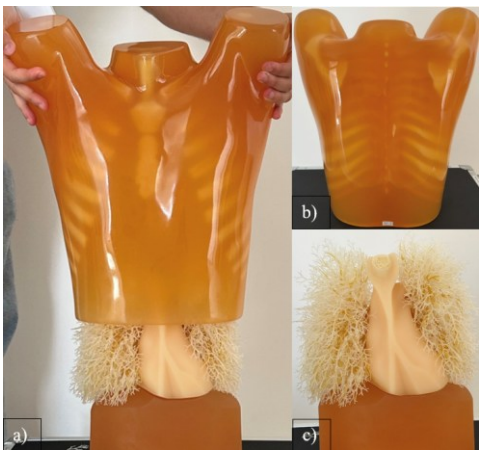

Fig. 1. Anthropomorphic phantom PH-1 model a) phantom structure, b) chest wall, c) heart, trachea, pulmonary vessels and diaphragm

The basic acquisition protocol was employed for multiple successive acquisitions, as outlined in Fig. 2. The chest phantom was positioned in the posterior-anterior projection, with a source-to-image distance (SID) of180 cm andcollimation set to 37x30 cm. Chest radiographs were acquired by changing tube voltage from 60 kV to 130 kV in 10 kV increments, using tube currents of 160, 250, 320 mA, and exposure times determined by the automatic exposure control system. For each X-ray system, a total of 24 radiographic images were acquired, corresponding to 24 distinct combinations of scanning parameters (tube voltage, tube current, time).
A total of 240 radiographic images (attenuation and inverse) were systematically acquired for analysis.

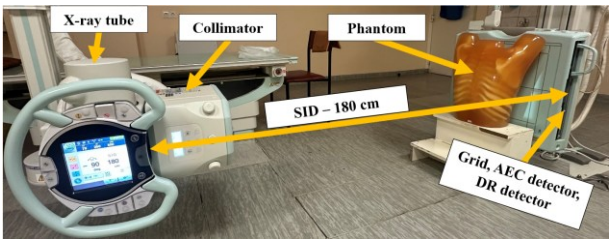

Fig. 2. Schematic representation of the experimental geometry employed in this study

2.2. Radiographic image analysis

All image review and quantitative analyses were performed using a 24.1-inch, 2.3-megapixel EIZO RadiForce MX241W diagnostic monitor. Each image was acquired with a 16-bit grayscale depth and retained in this bit depth throughout preprocessing and analysis to ensure high-fidelity representation of intensity variations. ImageJ, a widely used open-source software platform specifically developed for multidimensional scientific image analysis [8], was utilised for the quantitative evaluation of these images (Fig. 3).
For this analysis, seven regions of interest (ROIs) were set, and DCR images, including both attenuation and inverse radiographs, were analysed to evaluate these regions. Each ROI corresponded to a distinct tissue type: transverse process (bone), left lung, right bronchus, oesophagus, soft tissue, background, and the right lung (Fig. 4).

To evaluate the IQI of every scanning combination, signal-to-noise ratio (SNR) and contrast-to-noise ratio (CNR) were calculated. The SNR within a region of interest (ROI) inside the object can be quantified as the ratio of the mean grey value μ_1 of the ROI to the noise present in that region, represented by the standard deviation σ_1 of the ROI's grey values. Accordingly, the SNR can be expressed as follows [9]:

$$SNR = \frac{\mu_1}{\sigma_1} \quad (1)$$

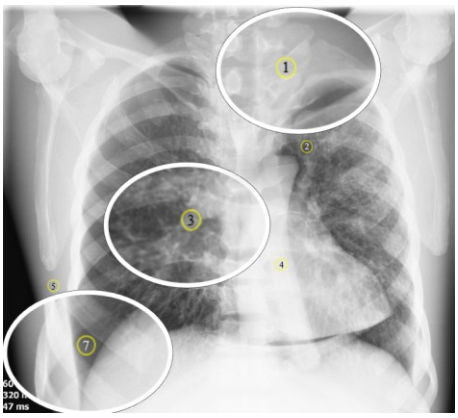

Fig. 3. The resulting phantom radiograph with selected ROIs circles

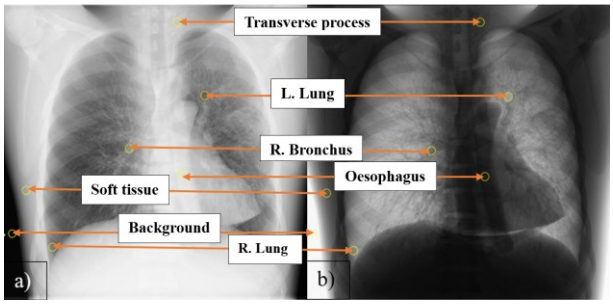

Fig. 4. Evaluation of a) attenuation and b) inverse radiographic images

The CNR is a key parameter, as it directly affects the detectability of defects within a volume. It can be calculated from the mean grey values of the object (μ_1) and the background (μ_b), with the noise quantified by the SD of the background pixel values (σ_b), as follows [10]:

$$CNR = \frac{|\mu_1 - \mu_b|}{\sigma_b} \quad (2)$$

2.3. Statistical data analysis

Statistical analysis was performed using SPSS software version 31.0 (IBM Inc, Armonk, New York, US). Normality of continuous variables, including kilovoltage (kV), milliampere-seconds (mAs), dose-area product (DAP), signal-to-noise ratio (SNR), and contrast-to-noise ratio (CNR), was evaluated with the *Kolmogorov–Smirnov test*. As the data significantly deviated from normality, parametric tests were considered inappropriate. Non-parametric analyses were therefore applied: *the Mann-Whitney U test* was used to compare variables between two independent groups; *the Kruskal–Wallis H test* was applied for comparisons among more than two independent groups. Relationships between exposition parameters (kV, mAs, DAP), technical setup (filtration, grid ratio, lines) and

SNR or CNR were explored using *Spearman's rank correlation*. To normalise the results and reduce the effect of large numerical variations, the base-10 logarithm (log10) was applied to all measured values. This transformation compressed the range of the data, facilitating statistical analysis and visualisation. All values were positive before transformation. Data are presented; p-values < 0.05 were considered statistically significant.

3. Results and discussion

Previous studies have extensively examined how basic X-ray parameters influence image quality in different settings [11,12]. This study demonstrates that detector performance should be evaluated using both attenuation and inverse image metrics, even when derived from the same dataset, as shown in Table 1. As observed, detector 4 consistently outperformed the others across both standard and inverse metrics, achieving high SNR, CNR, INSNR, and INCNR values across all tissues. Conversely, detectors 1 and 2 exhibited lower image quality metrics, especially in lung and soft tissue regions. These findings suggest that pixel size alone does not determine detector performance. Instead, intrinsic properties of the detector and signal processing play a crucial role in shaping both standard and inverse image quality.

Table 1. X-ray systems differences compared between exposure parameters and IQI.

Detector type	*1*	*2*	*3*	*4*	*5*
Pixel (mm²)	.016	.019		.023	.028
Grid ratio	10:1	12:1		12:1	10:1
Grid density	52 l/cm	40 l/cm		40 l/cm	36 l/cm
Filtration	1.5/0.2 Al/Cu	2.1 Al	2.5 Al	2.1 Al	2.5 Al
mAs	0.83	0.77	0.64	0.52	0.74
DAP	0.66	1.12	0.83	0.87	1.08
$SNR_{Bronch.}$	1.19	1.34	1.34	1.09	1.19
SNR_{Soft}	1.29	1.39	1.47	0.94	1.00
SNR_{T2}	1.66	1.83	1.75	1.43	1.45
$SNR_{Eosophag.}$	1.81	1.99	2.05	1.58	1.69
$SNR_{R.Lung}$	1.13	1.41	1.60	1.17	1.14
$SNR_{L.Lung}$	1.06	1.31	1.26	1.29	1.38
$CNR_{Bronch.}$	2.33	1.92	2.67	2.92	2.82
CNR_{Soft}	2.53	1.98	2.78	3.00	2.87
CNR_{T2}	2.51	2.06	2.84	3.07	2.97
$CNR_{Eosophag}$	2.62	2.11	2.92	3.13	2.99
$CNR_{R.Lung}$	2.23	1.82	2.47	2.82	2.76
$CNR_{L.Lung}$	2.23	1.79	2.47	2.74	2.69
$INSNR_{Bronch.}$	1.28	1.32	1.44	1.08	1.32
$INSNR_{Soft}$	1.12	1.38	1.39	1.20	1.13
$INSNR_{T2}$	1.21	1.39	1.36	1.81	1.83
$INSNR_{Eosoph.}$	1.23	1.37	1.67	1.90	2.00
$INSNR_{R.Lung}$	1.28	1.66	1.82	1.08	1.23
$INSNR_{L.Lung}$	1.29	1.49	1.54	1.07	1.27
$INCNR_{Bronch.}$	2.13	1.30	2.16	2.98	2.82
$INCNR_{Soft}$	2.30	1.42	2.35	3.04	2.82
$INCNR_{T2}$	2.35	1.52	2.45	3.14	2.97
$INCNR_{Eosoph.}$	2.43	1.56	2.51	3.20	3.00
$INCNR_{R.Lung}$	2.24	1.61	2.60	2.90	2.76
$INCNR_{L.Lung}$	2.07	1.31	2.20	2.80	2.70

In the present study, SNR values generally aligned with those reported in a previous investigation. However, CNR values showed significant discrepancies despite using the same ImageJ analysis. A likely reason for this difference is the size of the region of interest (ROI), which was not specified in the earlier study [12]. Visual assessment indicates that their ROIs were significantly larger than the 70 px² ROIs used in the current analysis, which may have contributed to the variation observed in CNR. This highlights the importance of clearly reporting ROI selection criteria, as differences in ROI size can greatly influence quantitative image metrics.

While acquisition parameters (kV, mA, ms, mAs) and technical settings (grid ratio, lines, filtration) were maintained, the stability ($p > 0.05$), dose-area product (DAP), and image quality indices (SNR, CNR, INSNR, INCNR) differed significantly ($p < 0.001$) across X-ray systems.

Nonparametric analyses using Mann–Whitney U and Wilcoxon Signed Ranks tests showed that grid lines significantly affected radiographic image quality and radiation exposure. The grid density of 52 lines/cm consistently provided superior SNR as well as CNR compared to the 36 and 40 lines/cm grids. The most pronounced improvements in SNR were most notable in the bronchus, soft tissue, transverse process, lungs, and oesophagus ($p < 0.001$). CNR enhancements were notable in the bronchus, bone, and lung regions ($p < 0.05$), while soft tissue and oesophagus showed trends towards improvement without reaching statistical significance.

In contrast, an alternative pattern was observed in the application of new pixel-aligned (PA) grids. The PA grid density of 66.93 lines/cm does not provide improved SNR relative to the conventional grid (40 lines/cm). However, up to 50 kV PA and conventional grids provided comparable image quality [13]. Therefore, these findings indicate that the improved radiographic image quality cannot be attributed solely to grid density. However, these findings suggest tissue-specific grey value differences in response to grid lines. Increasing the number of grid lines is especially beneficial in areas demanding detailed structural resolution.

Nevertheless, the total quantity of X-ray photons (mAs) was significantly higher for the 52 lines/cm grid ($p < 0.001$), reflecting the importance of 1.5 Al and 0.2 Cu X-ray beam filtration, as additional exposure levels necessary for improved image quality were not observed. When normalised to dose, the 52 lines/cm grid demonstrated enhanced SNR and CNR per unit exposure, indicating efficient exposure utilisation despite the higher tube current. Lower-density grids (36–40 lines/cm) maintained adequate image quality while minimising dose, supporting their use in routine imaging.

Variations in grid ratio significantly enhance image quality by reducing scattered radiation, although higher ratios may require adjustments in exposure to control patient dose. The 12:1 grid ratio showed higher SNR and CNR in bronchus, soft tissue, transverse process, oesophagus, and lungs ($p < 0.003$). Importantly, kV, mAs, and DAP were comparable between grid ratio groups ($p > 0.05$), indicating that image quality was independent of radiation dose. However, increasing the grid ratio considerably improves image quality by reducing scatter, though higher ratios may require careful exposure adjustments to avoid increasing patient dose [13,14].

The comparative analysis of three radiographic filtrations demonstrated significant differences in image quality across multiple anatomical regions. Signal-to-noise ratio (SNR) was highest in Group 1 (2.5 mm Al) for bronchus, soft tissue, transverse process, oesophagus, and right lung ($p < 0.004$), while left lung SNR showed a non-significant trend ($p = 0.109$). Group 2 (2.1 mm Al) demonstrated moderate SNR values, while Group 3 (1.5 mm Al + 0.2 mm Cu) provided slightly lower SNR than Group 1 but achieved more consistent contrast across tissues, particularly in soft tissue regions. Contrast-to-noise ratio (CNR) followed a similar pattern. Group 1 consistently demonstrated the highest CNR for bronchus, soft tissue, transverse process, and oesophagus, although not all differences reached statistical significance ($p > 0.05$). Lung CNR was generally higher in Groups 1 and 2 compared to Group 3, with left lung CNR reaching significance for Group 1 ($p = 0.002$). Group 3 showed modest improvements over Group 2 in certain regions, suggesting that the addition of Cu filtration can enhance tissue contrast while reducing patient exposure. Similar results were reported, indicating that using additional filtration, the effective dose can be reduced by up to 50% without compromising image quality [15]. Additionally, depending on the thickness of the Cu filter, the entrance skin dose can be reduced up to 20% without affecting image quality [16].

Patient exposure analysis revealed a direct relationship between filtration thickness and patient exposure. A phantom group with 2.5 mm Al filtration revealed the highest milliampere-seconds (mAs) and dose-area product (DAP) (both $p < 0.001$), reflecting increased photon attenuation associated with thicker filtration. In comparison, the last group using 1.5 mm Al + 0.2 mm Cu achieved the lowest DAP while maintaining clinically acceptable SNR and CNR.

Tube voltage (kV), pixel size, and grid ratio were similar across all groups ($p > 0.05$), confirming that observed differences in image quality were primarily attributable to filtration rather than other acquisition parameters. Collectively, these results highlight that careful optimisation of grid density, grid ratio, and beam filtration can enhance radiographic image quality, particularly in anatomically complex regions such as the bronchus and lungs. Importantly, many of these improvements can be achieved without proportionally increasing radiation dose, emphasising the potential for protocol optimisation to balance diagnostic performance and patient safety.

The X-ray beam's energy (kV) groups demonstrated statistically significant variation, reflecting region-dependent sensitivity to imaging parameters. In particular, the comparison between 60 kV and 100 kV revealed pronounced differences. $INSNR_{bronchus}$ values were significantly higher at 60 kV ($p < 0.05$), while other SNR and CNR measures remained largely unchanged. Similarly, comparisons between other groups revealed significant differences in $INSNR_{bronchus}$ ($p < 0.05$), suggesting that airway structures are particularly affected by kilovoltage adjustments, even when overall image quality appears stable (Fig. 5).

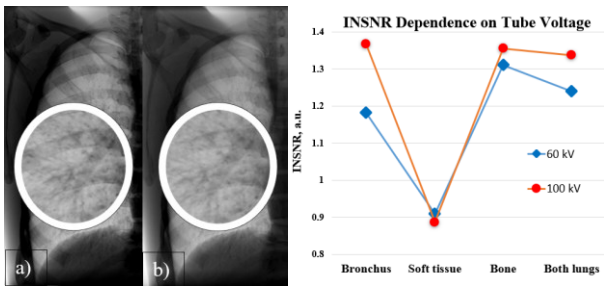

Fig. 5. Comparison of inverse image SNR values at different tube voltages: (a) 60 kV and (b) 100 kV

Pixel size was a major determinant of image quality. Larger pixel sizes were associated with increased SNR in lung regions (right lung $\rho = 0.627$, left lung $\rho = 0.626$, $p < 0.001$), reflecting improved signal homogeneity due to higher photon sampling per pixel. However, SNR in bronchial ($\rho = -0.299$, $p < 0.001$) and soft tissue ($\rho = -0.584$, $p < 0.001$) regions decreased with larger pixels, indicating a trade-off between spatial resolution and signal detectability in finer structures.

The comparisons between pixel size groups confirmed significant differences in SNR and CNR metrics across bronchial, lung, soft tissue, bone, and oesophagus regions ($p < 0.05$), although bronchial SNR was not statistically significant. These results highlight the need to tailor pixel size based on the clinical target, balancing noise reduction in low-density lung tissue with the resolution required for small structures.

As expected, X-ray beam intensity and exposure parameters (mAs, DAP) demonstrated a strong association with image quality, a relationship that has likewise been documented by other investigators [12,17]. X-ray beam quantity parameter (mAs) correlated positively with DAP ($\rho = 0.721$, $p < 0.001$), reflecting expected dose scaling. Higher mAs values were associated with improved SNR and CNR across lung, soft tissue, oesophagus and bone regions, and pairwise comparisons showed statistically significant differences in $SNR_{R.Lung}$ ($p = 0.046$), $SNR_{L.Lung}$ ($p = 0.037$), $CNR_{Bronchus}$ ($p = 0.034$), CNR_{T2} ($p = 0.038$), $CNR_{Eosophagus}$ ($p = 0.041$), and CNR_{Soft} ($p = 0.041$). Similarly, DAP-based grouping revealed significant differences in most SNR and CNR indices ($p < 0.05$), emphasising that higher patient exposure is linked to enhanced signal and contrast in pulmonary imaging (Fig. 6).

As it could be seen more signal relative to noise for each unit of exposure. The highest dose efficiency can be observed in the DR-ID 900 detector. However, almost all X-ray systems represented better image quality with less radiation exposure.

However, SNR in bronchial regions, bone, and oesophagus tissue in some cases did not differ significantly, suggesting these areas are less sensitive to dose changes. Correlation analyses revealed interdependencies between acquisition parameters and image quality metrics. Tube voltage correlated negatively with mAs ($\rho = -0.941$, $p < 0.001$) and exposure time (ms; $\rho = -0.904$, $p < 0.001$), reflecting automatic exposure control in higher-kV acquisitions. Increased tube voltage tended to reduce SNR in

bronchial and soft tissue regions, consistent with reduced subject contrast at higher photon energies.

Across tissue types, SNR measures were highly intercorrelated (e.g., SNR_{Bronch}–SNR_{soft} $\rho = 0.777$, $p < 0.001$; SNR_{Bronch}–SNR_{T2} $\rho = 0.773$, $p < 0.001$), and CNR values showed strong correlations ($\rho \geq 0.95$, $p < 0.001$), suggesting that enhancements in a specific region typically correspond to improvements in overall image quality.

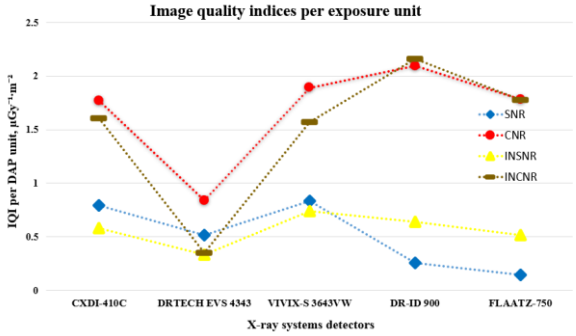

Fig. 6. Comparison of X-ray systems' performance through image quality indices per exposure unit

4. Conclusions

The quality of digital chest radiography images depends on detector properties, grid setup, beam filtration, and acquisition parameters.

Tailoring these factors to specific anatomical targets maximises diagnostic performance while minimising radiation exposure, supporting protocol standardisation and adherence to ALARA principles.

The detector properties and signal processing critically influence both standard and inverse image quality metrics, as evidenced by the consistently superior performance of Detector 4 across SNR, CNR, INSNR, and INCNR measures.

High-density grids (52 lines/cm) and higher grid ratios (12:1) delivered notable improvements in SNR and CNR, particularly in anatomically complex regions such as the bronchus, lungs, and soft tissues. These gains were achieved efficiently, with normalised SNR and CNR, demonstrating effective use of exposure despite higher mAs requirements, highlighting the importance of parameter calibration to balance image quality and radiation dose.

Beam filtration similarly affects image quality and patient exposure. Thicker aluminium filtration increased SNR and CNR but required higher exposure, whereas combination aluminium-copper filtration maintained clinically acceptable contrast with lower dose, illustrating the trade-offs between contrast enhancement and radiation safety.

Acquisition parameters—including tube voltage, mAs, DAP, and pixel size—exert tissue-specific influences. Larger pixel sizes improved SNR in lung parenchyma but reduced detectability in finer structures such as bronchi and soft tissue. Higher mAs and DAP were associated with improved SNR and CNR across multiple regions, whereas higher tube voltage reduced contrast in bronchial and soft tissue structures. Strong intercorrelations among SNR and CNR metrics suggest that optimisation in one region generally enhances overall image quality, although fine structures remain sensitive to parameter adjustments.

5. References

1. Fyles F., FitzMaurice T. S., Robinson R. E., Bedi R., Burhan H., Walshaw M. J. Dynamic chest radiography: a state-of-the-art review. Insights into Imaging, Vol. 14(1), 2023, article number: 107. doi: 10.1186/s13244-023-01451-4. PMID: 37332064; PMCID: PMC10277270.
2. Tsalafoutas I. A., AlKhazzam S., Tsapaki V., AlNaemi H., Kharita M. H. Digital radiography image quality evaluation using various phantoms and software. J Appl Clin Med Phys., Vol. 23:e13823, 2022. doi: https://doi.org/10.1002/acm2. 13823
3. Yoon Y., Park H., Kim J., Kim J., Roh Y., Tanaka N., Morishita J. Proper Management of the Clinical Exposure Index Based on Body Thickness Using Dose Optimization Tools in Digital Chest Radiography: A Phantom Study. Int. J. Environ. Res. Public Health, Vol. 18, 2021, 5203. doi: https:// doi.org/10.3390/ijerph18105203
4. Seo D., Jang S., Kim J., Kim J., Sung D., Kim H., Yoon Y. A comparative assessment of entrance surface doses in analogue and digital radiography during common radiographic examinations. Radiat. Prot. Dosim., Vol. 158, 2014, p. 22–27.
5. Rama K., Esser M., Spogis J., Wanninger F., Hoberg B., and Schäfer, J. Dose-optimised image acquisition parameters for neonatal chest radiography: a phantom study comparing computed radiography and wireless digital radiography needle detectors. RöFo - Fortschritte Auf Dem Gebiet Der Röntgenstrahlen Und Der Bildgebenden Verfahren. 2025. doi: https://doi.org/10.1055/a-2525-9430
6. Wu J., Chen W., Zeng F., Ma L., Xu W., Yang W., Qin G. Improved detection of solitary pulmonary nodules on radiographs compared with deep bone suppression imaging. Quant Imaging Med Surg., Vol.11(10), 2021, p. 4342-4353. doi: 10.21037/qims -20-1346
7. Kyoto Kagaku. N.d. Multipurpose Chest Phantom N1 "LUNGMAN". [online]. [viewed 15 August, 2025]. https://www.kyotokagaku.com/en/products_i ntroduction/ph-1/
8. Rasband W. S., ImageJ, U. S. National Institutes of Health, Bethesda, Maryland, USA. [online]. [viewed 15 August, 2025]. https://imagej.net/ij/, 1997-2018
9. Jeon P.-H., Jeon S.-H., Ko, D., An G., Shim H., Otgonbaatar C., Son K., Kim D., Ko S.M., Chung M.-A. Assessment of Image Quality of Coronary CT Angiography Using Deep Learning-Based CT Reconstruction: Phantom and Patient Studies. Diagnostics, Vol. 13, 2023, 1862. doi: https://doi.org /10. 3390/diagnostics13111862
10. Meng D., Wang Z., Bai C. et al. Assessing the effect of scanning parameter on the size and density of pulmonary nodules: a phantom study. BMC Med Imaging, Vol. 24, 2024, 12. doi: https://doi.org/10. 1186/s12880-023-01190-4
11. Abdallah N. A., Gar-Elnabim M. E. M., Esmeal M. Y. Design of Prototype Phantom to Measure Quality Control for Conventional X-ray Machine Using Quantitative Image Parameters. Journal of Clinical Engineering, Vol. 49(4), 2024, p. 143-148. doi: 10.1097/JCE.0000000000000662
12. Al-Murshedi S., Hogg P., England A. The impact of being overweight on image quality when undertaking adult chest X-ray examinations using routine protocols. Conference: European Congress of Radiology (ECR), 2019. doi: 10.26044/ecr2019/C -0722.
13. Kawashima H., Ichikawa K., and Iida Y. A new stationary grid, with grid lines aligned to pixel lines with submicron-order precision, to suppress grid artifacts. Medical Physics, Vol., 48(9), 2021, p. 4935-4943. doi: https://doi.org/10.1002/mp.15099
14. Massera R., Bosmans H., Perez S., and Marshall N. A combined analytical and monte carlo method for detailed simulations of antiscatter grids in x-ray medical imaging: implementing scatter within the grid. Physics in Medicine and Biology, Vol. 69(7), 2024, 075021. doi: https://doi.org/10.1088/1361-656 0/ad2b93
15. Grewal R. K., Young N., Colins L., Karunnaratne N., Sabharwal N. Digital chest radiography imagequality assessment with dose reduction. Australasian physical & engineering sciences in medicine, Vol. 35(1), 2012, p. 71–80.
16. Lee W., Lee S., Chong S., Lee K., Lee J., Choi J. C., et al. Radiation dose reduction and improvement of image quality in digital chest radiography by new spatial noise reduction algorithm. PLoS ONE, Vol. 15(2): e0228609, 2020. doi: https://doi. org/10.1371/ journal.pone.0228609
17. Al-Murshedi S., Hogg P. and England A. Evaluation of image quality and entrance surface dose for routine adult chest radiography examinations in 8 hospitals. 2018, doi: 10.1594/ecr2018/C-1353

MEDICAL PHYSICS IN THE BALTIC STATES 17 (2025)

Proceedings of International Conference "Medical Physics 2025"
06 - 08 November 2025, Kaunas, Lithuania

REFINING LOW - DOSE CT PROTOCOLS USING SIMULATED IMAGE QUALITY EVALUATION

Marius BURKANAS[1], Mindaugas DŽIUGELIS[1], Jurgita UŠINSKIENĖ[2], Jonas VENIUS[1], Romualdas GRIŠKEVIČIUS[1]
[1]National Cancer Centre, Medical Physics Department, Vilnius, Lithuania, [2]National Cancer Centre, Department of Diagnostics and Interventional Radiology, Vilnius, Lithuania
marius.burkanas@nvc.santa.lt, mindaugas.dziugelis@nvc.santa.lt, jurgita.usinskiene@nvc.santa.lt, jonas.venius@nvc.santa.lt, romualdas.griskevicius@nvc.santa.lt

***Abstract*:** According to 2022 WHO data, in Lithuania, lung cancer is the leading cause of cancer - related deaths among men and ranks second in case rate. Among women, it is the third most common cause of cancer mortality and ranks fourth in new incidence rate. Early diagnosis of lung cancer significantly improves disease control and overall quality of life. However, symptoms often emerge only at advanced stages and are frequently mistaken for other conditions such as bronchitis or asthma. As a result, lung cancer screening in the population should become a standardized practice.
Dose reduction is crucial because individuals undergoing CT screening are exposed to significant levels of radiation, which can increase the risk of stochastic effects. Low - dose CT (LDCT) aims to minimize radiation exposure while maintaining sufficient image quality for accurate diagnosis.
The goal of this study is to create simulated low-dose images from high - quality scans in a way that mirrors real-world dose reduction scenarios. CT images will be generated in such a way that would mimic real CT image data, which was acquired by changing mAs.
Most of CT images are the simulated using sinogram domain, which does not include real-world CT image quality nuances such as electronic noise, processing noise and etc. Therefore, in this study, simulation will be performed using image domain which means that reconstructed image quality after optimization will be more accurate.

Keywords: CT image reconstruction, noise index evaluation, CTDI optimization

1. Introduction

Lung cancer remains one of the most lethal malignancies worldwide [1]. This is because the disease is usually diagnosed at an advanced stage, when curative treatment is no longer possible or it is very complicated to perform. Early detection is very important, as identifying small pulmonary nodules, infiltrations or any suspicious malignancies before symptoms develop further can drastically improve survival outcomes [2]. Conventional diagnostics, such as X-ray, however, are usually insufficient for screening large populations at risk, therefore a more extensive diagnostic procedures should become a new standard [3].
Low-dose computed tomography (LDCT) provides a great improvement for the detection of early lung cancer [3]. Several large clinical trials have demonstrated that LDCT screening reduces lung cancer mortality in high - risk populations by early detection of lung cancer, resulting in better treatment outcomes later - on, thus it became a preferred strategy for population - based programs [2]. Despite these benefits, the cumulative radiation exposure from repeated scans raises legitimate concerns [4].
Although individual LDCT examinations deliver relatively small radiation doses, the stochastic risk associated with radiation exposure cannot be ignored when millions of people undergo annual screening. Therefore, optimization of CT protocols is essential to balance diagnostic performance and radiation safety.
Traditionally, protocol optimization has been carried out by acquiring phantom and patient images with different parameters. However, this approach is time-consuming and not entirely accurate, as it is not possible to simulate different dose levels on real patient images due to exposure limitations. Moreover, phantom images typically do not contain malignancies, and when they do, these are often clearly visible and well known to radiologists. This makes the development of LDCT protocols more complex. [5].
One of the attempts was more systematic approach for CT image quality assessment was developed using a Catphan 700 phantom. This method evaluated parameters such as CT number accuracy, modulation transfer function (MTF), contrast - to - noise ratio (CNR), and the effects of iterative reconstruction (Clearview IR) under varying acquisition settings [6]. To further

overcome these challenges, researchers have developed noise - insertion and dose - simulation techniques that allow high - quality CT images to be converted into realistic low - dose equivalents. These methods provide a powerful platform for evaluating dose–image quality trade - offs without subjecting patients to unnecessary scans [7]. Most simulation strategies have operated in the sinogram domain, where projection data are artificially degraded before reconstruction. While effective for modeling quantum noise, such approaches often fail to reproduce scanner - specific post - processing characteristics, including electronic and reconstruction - related noise correlations.

More recently, image - domain simulation models have gained attention because they preserve the full texture of reconstructed images while still allowing precise control over noise characteristics. By calibrating against phantom measurements, these models can generate synthetic low - dose images that closely resemble real acquisitions, capturing both noise power spectrum features and intensity - dependent variance. For example, machine learning has introduced a new dimension to CT simulation. Generative adversarial networks (GANs), particularly CycleGAN architectures, have shown promise in mapping standard - dose images to their low - dose counterparts while learning complex texture patterns directly from data [8, 9]. Unlike traditional physics - based noise insertion, GANs can capture subtle scanner characteristics and generate visually convincing low - dose images that may improve the realism of simulation pipelines. Despite this potential, it was unable to fully implement a GAN - based framework within the timeframe and resources available for this study. Nevertheless, CycleGAN - based approaches represent a promising future direction for CT dose simulation, especially as datasets and computational resources expand.

Within this framework, CT simulation emerges not only as a research tool but also as a practical solution for clinical protocol development. By validating simulation against both phantom and patient data, it becomes possible to define the lowest acceptable tube current settings that maintain diagnostic confidence, thereby supporting safe and effective lung cancer screening practices.

2. Methods

2.1. CT data acquisition

A CIRS Inc., Norfolk, VA, USA IMRT Thorax Phantom, Model 002LFC anthropomorphic chest phantom (see fig. 1) was scanned repeatedly on a CT scanner (GE Revolution HD 750) at ten different tube current levels: 10, 20, 50, 75, 100, 200, 300, 500, 600, and 700 mAs. All acquisitions were performed at 120 kVp, pitch 1.0, collimation 40 mm, and reconstructed into 2.5 - mm slices using filtered back projection (FBP) with the vendor's standard lung kernel. Repeated acquisitions at each exposure level were performed to capture noise variability.

In addition to phantom imaging, retrospectively selected, fully anonymized patient chest CT datasets were included for retrospective studies. These datasets served as the testing domain for the simulation framework, enabling generation of synthetic low - dose reconstructions at dose levels not physically acquired. Patient selection was limited to routine chest CT scans without severe motion artifacts to ensure robust simulation creations.

Fig. 1. CIRS 002LFC anthropomorphic chest phantom.

2.2. Noise extraction

For stochastic noise calibration, two identical water phantom (Fig. 2.) scans at each mAs setting were acquired. Raw DICOM images were resampled and converted to sinograms using a discrete Radon transform implemented in Pycharm. Noise components were isolated as the half - difference between paired sinograms.

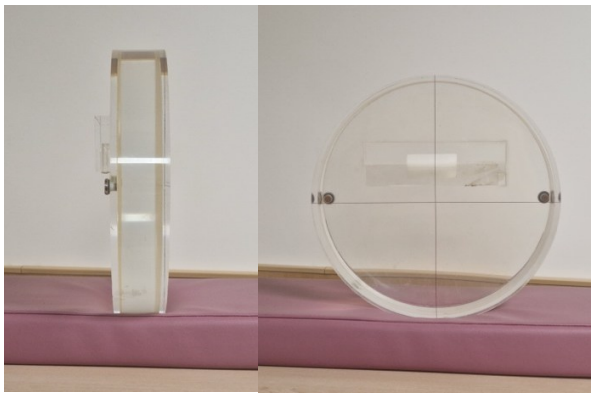

Fig. 2. Water uniformity phantom.

Row - wise mean subtraction (removal of the zero - frequency/DC component) was applied within the ROI to eliminate baseline shifts and slow system drift, ensuring zero - mean noise and avoiding low - frequency inflation in the noise power spectrum (NPS).

The spatial frequency distribution of noise was characterized by calculating the 2D Fourier transform of Δ. The magnitude spectrum A(f) was preserved, while random phases $\phi \sim U(-\pi,\pi)$ were substituted to simulate spatially uncorrelated noise distributions. Synthetic noise fields were reconstructed via inverse Fourier transform (see equation 1) and normalized to zero mean and unit

variance. Radial averaging of the NPS was performed to compare frequency content across dose levels, allowing validation of the model against measured phantom data.

$$Z = F^{-1}\{A(f)e^{i\phi}\} \quad (1)$$

where Z is the synthesized noise field in the image domain, F^{-1} the inverse Fourier transform operator, A(f) the amplitude spectrum of the noise derived from the measured noise power spectrum (NPS), and ϕ - a random phase uniformly distributed between −π and π.

2.3. Noise modulation and image reconstruction

For each phantom or patient sinogram, synthetic noise projections were generated by modulating the calibrated noise field:

$$sino_{noisy}(i,j) = sino(i,j) + Z(i,j)\,\sigma(I_{ij})g(i) \quad (2)$$

where $I_{i,j}$ is the original intensity, $\sigma(I_{i,j})$ the calibrated noise standard deviation, and g(i) detector - specific correction factor according to detector position.

Noisy sinograms were reconstructed using FBP with the same reconstruction kernel as the original acquisitions to ensure comparability. Both phantom and patient reconstructions were visually and quantitatively compared against real low - dose CT images. Validation metrics included lesion visibility and standard deviation of the measured ROIs with different attenuation coefficients.

For benchmarking, results from the sinogram - based simulation were compared with direct phantom acquisitions at equivalent mAs levels, and image - domain noise insertion methods, which added Gaussian - distributed noise post - reconstruction. This comparative evaluation allowed assessment of the advantages of sinogram - domain simulation in preserving realistic noise correlations.

3. Results

3.1. Phantom evaluation

For benchmarking, we compared against direct phantom acquisitions and a sinogram - injection baseline. In our data, an image - domain model calibrated to the measured 2D NPS and ROI SD reproduced the mid–high - frequency noise texture of real images within ±10%, whereas the sinogram - only approach under - represented low - frequency power and over - attenuated the high - frequency tail.

3.2. Standard deviation of CT noise by tissue

Across eight repeats per tissue, the simulation reproduces the ranking of noise magnitude (lung > bone ≈ soft tissue) and shows variability comparable to the real acquisitions (Fig. 3.). Median/mean ROI SDs (HU) were:

- Lungs: real 15.54 ± 1.45 vs simulated 16.40 ± 1.70 (mean Δ = +0.86 HU; 95% CI −0.92 to +2.64; p = 0.29, n.s.).
- Soft tissue: real 11.10 ± 0.60 vs simulated 12.51 ± 1.30 (mean Δ = +1.41 HU; 95% CI +0.32 to +2.50; p = 0.018).
- Bone: real 15.42 ± 1.39 vs simulated 18.16 ± 1.33 (mean Δ = +2.75 HU; 95% CI +1.51 to +3.98; p = 0.0012).

Visually, the lung distributions overlap strongly, for soft tissue and bone the simulated boxes are shifted upward by ~1 –3 HU with similar IQRs, indicating a small, consistent SD overestimation while preserving variability. These results show the simulation captures both noise level and texture well enough for dose - protocol comparisons, with a modest positive bias in denser materials.

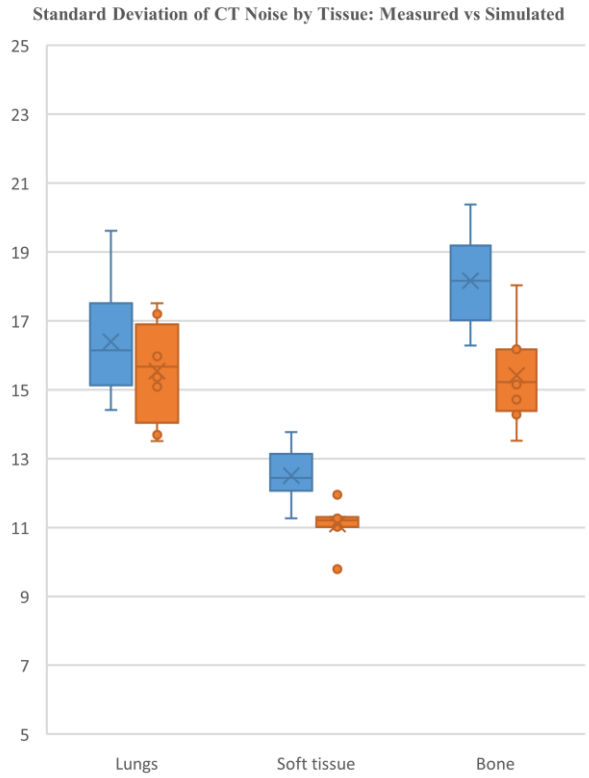

Fig. 3. Standard deviation comparison of regular and simulated CT scan acquisitions over different tissues.

3.3. Patient image evaluation

Noise simulation applied to patient chest CT datasets successfully generated realistic low - dose equivalents across all tested mAs values. At ≥ 100 mAs, both simulated and real reconstructions were visually indistinguishable. At 75 mAs, simulated reconstructions preserved parenchymal structures and remained diagnostically acceptable. Below 50 mAs, however, both simulated and real acquisitions exhibited excessive noise, compromising lung malignancy visibility.

3.4. Radiologist Evaluation of Malignancy Detection

Two board - certified thoracic radiologists independently assessed the visibility of Stage I - II lung cancer nodules in simulated low - dose images. Each image was scored as either “detectable” (+) or “not detectable” (−). Table 1 summarizes their assessments across dose levels.

Table 1. Radiologist detection of Stage I lung cancer across simulated mAs levels.

mAs level	Radiologist 1	Radiologist 2
10	−	−
20	−	+
30	−	−
40	+	+
50	−	+
75	+	+
100	+	+
200	+	+
300	+	+
500	+	+
600	+	+
700	+	+

Inter - observer agreement reflecting differences in reader sensitivity at borderline dose levels (20–50 mAs). Despite this variability, both radiologists agreed that exposures of ≥ 75 mAs consistently provided diagnostic quality sufficient for malignancy detection.

Using the ROI standard deviation (SD in HU) as the primary quantitative noise metric, the simulation tracked the measured noise levels across lung, soft - tissue, and bone equivalent attenuation materials, reproducing the dose–noise trend seen in real data. At 75 mAs, simulated SDs stayed within our acceptance band relative to the measured SDs (small positive bias but preserved ranking across tissues), and blinded reads remained concordant. Below 75 mAs, SD rose beyond tolerance - especially in denser materials - corresponding to degraded lesion visibility and reduced inter - reader agreement. Taken together, SD behavior and reader performance indicate that 75 mAs is the lowest dose that consistently maintains diagnostic acceptability for lung cancer screening.

4. Conclusions

The acquired image - domain simulation, calibrated on phantom data reproduced the noise intensity of real low - dose CT closely enough for protocol simulations to be accurate, even without access to raw sinogram projections. At 75 mAs, simulated ROI SDs remained within our acceptance limits and preserved the expected tissue ranking (lung as the most important, following up with bone and soft tissue), with small biases - lungs +0.86 HU, soft tissue +1.41 HU, bone +2.75 HU - relative to measurements. Reader performance reproduced these findings: images at ≥ 75 mAs were consistently diagnostic, whereas < 75 mAs produced higher SD, loss of fine structure, and this resulted in reader disagreement. Although 75 mAs met our technical acceptance in SD terms, the combined evidence from reader behavior, small SD bias in denser materials, and the need for a safety margin in real - world variability leads us to set 100 mAs as the minimum allowable tube current for routine screening - the practical floor to reliably preserve lesion detectability. This workflow reduces the need for confirmatory scans,, while future work will refine intensity-dependent and non - stationary noise modeling, as well as expand patient datasets to further improve CT image simulation accuracy.

5. References

1. Pinsky P.F.. Lung cancer screening with low-dose CT: a world-wide view. Translational Lung Cancer Research, 2018, 7(3): 234–242.
2. Gierada D.S., Black W.C., Chiles C., Pinsky P.F., and Yankelevitz D.F.. Low-Dose CT Screening for Lung Cancer: Evidence from 2 Decades of Study. Radiology: Imaging Cancer, 2020, 2(2). Published online: 27 March 2020.
3. van Beek E.J.R., Mirsadraee S., and Murchison J.T.. Lung cancer screening: Computed tomography or chest radiographs? World Journal of Radiology, 2015, 7(8): 189–193.
4. Cao C.-F., Ma K.-L., Shan H., Liu T.-F., Zhao S.-Q., Wan Y., Wang H.-Q., and colleagues. CT Scans and Cancer Risks: A Systematic Review and Dose-response Meta-analysis. BMC Cancer, 2022, 22: 1238.
5. Trattner S., Pearson G.D.N., Chin C., Cody D.D., Gupta R., Hess C.P., Kalra M.K., Kofler J. Jr, Krishnam M.S., and Einstein A.J.. Standardization and Optimization of Computed Tomography Protocols to Achieve Low-Dose. Journal of the American College of Radiology, 2014, 11(3): 271–278.
6. Prabsattroo T., Wachirasirikul K., Tansangworn P., Punikhom P., and Sudchai W.. The Dose Optimization and Evaluation of Image Quality in the Adult Brain Protocols of Multi-Slice Computed Tomography: A Phantom Study. J. Imaging, 2023, 9(12): 264.
7. Lepcha D.C., Goyal B., Dogra A., Vaghela K., Singh A., Ravi Kumar K.S., and Bavirisetti D.P.. Low-dose computed tomography image denoising using pixel-level non-local self-similarity prior with non-local means for healthcare informatics. Scientific Reports, 2025, 15: 25095.
8. Mansour M., Djenouri D., Said L.A., Latif S., Maalel A., and Abdelhadi A.M.S.. ARUC-GAN: A CycleGAN-Based Attention Residual U-Net for Low-Dose CT Denoising in Smart Healthcare. IEEE Access, 2025, 13.
9. Tan C., Yang M., You Z., Chen H., and Zhang Y.. A selective kernel-based cycle-consistent generative adversarial network for unpaired low-dose CT denoising. Precision Clinical Medicine, 2022, 5(2): pbac011.3

MEDICAL PHYSICS IN THE BALTIC STATES 17 (2025)

Proceedings of International Conference "Medical Physics 2025"
06-08 November 2025, Kaunas, Lithuania

ASSESSMENT OF PATIENT DOSES IN A PILOT LOW-DOSE CT LUNG CANCER SCREENING PROGRAM CONDUCTED AT VILNIUS UNIVERSITY HOSPITAL SANTAROS KLINIKOS

Leonid KRYNKE[1], Dileta VALANCIENE[2,3], Antonio JREIJE[1]
[1]Clinical Radiation Surveillance Division, Vilnius University Hospital Santaros Klinikos, Vilnius, Lithuania; [2]Department of Radiology, Nuclear Medicine and Medical Physics, Institute of Biomedical Sciences, Faculty of Medicine, Vilnius University, Vilnius, Lithuania; [3]Centre of Radiology and Nuclear Medicine, Vilnius University Hospital Santaros Klinikos, Vilnius, Lithuania
[1]leonid.krynke@santa.lt; [2]dileta.valanciene@santa.lt; [3]antonio.jreije@santa.lt

***Abstract*:** This retrospective study aimed to assess radiation dose metrics in a pilot LDCT lung cancer screening program and explore demographic predictors of dose variability. A total of 1,014 asymptomatic individuals aged 50–70 years (mean age 60.5; 52.1% male) underwent LDCT using a dedicated low-dose protocol. Participants were stratified by both BMI and weight groups to assess dose trends. The median effective dose remained below 1 mSv for BMI groups except for the obese group (with median dose of about 1.3 mSv). Multivariate analysis identified BMI (and similarly patient weight) as dominant predictors of both DLP and effective dose. These findings support the implementation of nationwide screening and provide dose benchmarks to guide the development of future Lithuanian DRLs, which could be established as BMI-stratified values to better reflect achievable performance across diverse population groups.

Keywords: LDCT, Lung cancer, screening, DRLs, Diagnostic reference level

1. Introduction

Lung cancer ranks third among the most common cancers in Europe and is second in the USA, accounting for nearly 2.2 million new cases per year. Moreover, lung cancer remains the leading cause of cancer-related mortality worldwide, with an estimated 1.8 million deaths in 2020 [1]. Despite not being the most frequently diagnosed malignancy, lung cancer carries one of the poorest prognoses: over half of patients die within the first year after diagnosis, and the overall 5-year survival rate is approximately 17.8% [2]. Therefore, early detection is essential to improving survival outcomes. Low-dose computed tomography (LDCT) screening in high-risk populations enables detection of lung cancer at potentially curable stages. Large randomized controlled trials have demonstrated its mortality benefit: the U.S. National Lung Screening Trial (NLST) reported approximately 20% relative reduction in lung cancer mortality (and a 6.7% reduction in all-cause mortality) with LDCT compared to chest radiography [3], while the European NELSON trial found a 24% reduction in high-risk men and 33% in women after 10 years of follow-up [4]. These findings have driven the adoption of LDCT screening protocols and the initiation of national and pilot screening programs in several countries.

Because LDCT screening targets asymptomatic individuals, minimizing radiation exposure is a critical consideration. All participants are exposed to ionizing radiation, yet only a small fraction will benefit from early cancer detection; thus, the modest mortality reduction must be weighed against the potential risk of radiation-induced malignancy in the screened population [5]. This concern is emphasized by regulatory guidance that requires specific justification for radiological examinations in asymptomatic people [6]. LDCT screening protocols typically involve repeated annual or biennial examinations for those who remain at risk, resulting in the possibility of more than 25 scans over a lifetime. This cumulative exposure underscores the need for each screening examination to comply with the ALARA (as low as reasonably achievable) principle, delivering the lowest possible radiation dose without compromising diagnostic accuracy in nodule detection [6]. Advances in CT technology—such as automated exposure control, iterative reconstruction algorithms, and AI-enhanced image reconstruction—provide a practical solution to this challenge, enabling sub-millisievert LDCT protocols that substantially reduce cumulative radiation burden while preserving effective lung cancer detection.

In this context, the present study aimed to evaluate patient radiation dose metrics in a pilot LDCT lung cancer screening program. Specifically, the study sought to benchmark dose metrics against international guidelines and assess their variability in relation to demographic factors, including BMI, weight, gender, and age.

2. Methods

This retrospective study analyzed data from 1,014 asymptomatic adults enrolled in a pilot low-dose computed tomography (LDCT) lung cancer screening program at Vilnius University Hospital Santaros Klinikos between 26 September 2024 and 14 February 2025, all of whom met the program's eligibility criteria. At the time of LDCT examination, demographic (age, gender) and anthropometric (weight, height) data were collected, and body mass index (BMI) was calculated as weight in kilograms divided by height in meters squared (kg/m^2).

All LDCT examinations were performed on a GE Revolution HD 64-slice CT scanner (2020) using a low-dose protocol developed in accordance with the recommendations, protocol guidelines, and technical standards of international societies, including the American Association of Physicists in Medicine (AAPM) [7], the European Society of Thoracic Imaging (ESTI) [8], and the American College of Radiology/Society of Thoracic Radiology [9]. The protocol was optimized to ensure participant radiation exposure remained within international recommendations while maintaining sufficient image quality for diagnostic purposes. The dose parameters were kept below the following targets in a standard-sized participant: an effective doses below 1 mSv, CT dose index (CTDIvol) below 3 mGy, and dose–length product (DLP) below 75 mGy·cm.

Low-dose chest CT scans were acquired without intravenous or oral contrast. Participants were positioned supine with arms raised above the head when feasible, and each scan was acquired in a single breath-hold at full inspiration to minimize motion artifacts. A standardized low-dose spiral protocol was applied, covering the entire lung field from apices to bases, with acquisition parameters including a tube voltage of 100 kVp, automatic tube current modulation (GE Smart mA), tube rotation time of 0.4 s, pitch factor of 1.38, slice thickness of 0.625 mm, and collimation width of 40 mm. Standard (body) and lung-specific reconstruction filters were used.

Radiation dose metrics, including CTDIvol (mGy), DLP (mGy·cm), and effective dose (mSv; calculated as DLP × 0.014 $mSv \cdot mGy^{-1} \cdot cm^{-1}$), were extracted from the CT dose report. Participants were stratified by BMI (<18.5, 18.5–24.9, 25.0–29.9, ≥30.0 kg/m^2) and weight (<65, 65–84.9, 85–104.9, ≥105 kg), with dose metrics summarized as median and interquartile range (IQR) within each category. Gender- and age-based subgroups were also compared.

Statistical analyses were conducted using R version 4.5.1 (R Foundation for Statistical Computing, Vienna, Austria). Continuous variables were reported as median, and categorical variables as counts and percentages. Spearman's rank correlation coefficient (ρ) was used to assess the association between BMI and weight, with $\rho \geq 0.70$ indicating potential collinearity. To avoid multicollinearity, BMI and weight were modeled separately, and variance inflation factors (VIF) were calculated for all predictors. Multiple linear regression models were developed for each dose metric (CTDIvol, DLP, effective dose), adjusting for age and gender. Continuous variables were standardized (z-scores) to enable direct comparison of effect sizes, reported as standardized regression coefficients (β) with 95% confidence intervals (CIs) and p-values. For each outcome, two models—one including BMI and one including weight—were compared using adjusted R^2, Akaike Information Criterion (AIC), and Bayesian Information Criterion (BIC). Statistical significance was defined as a two-tailed $p < 0.05$.

3. Results

In total, 1,014 participants underwent low-dose computed tomography (LDCT) examinations as part of the pilot lung cancer screening program. The cohort consisted of 528 males (52.1%) and 486 females (47.9%), with a mean age of 60.5 ± 5.2 years (Table 1). Among them, 21.4% were active smokers, 78.4% were non-smokers, and 0.2% had an unknown smoking status. For current smokers, the mean cumulative smoking exposure for traditional tobacco users was 23.63 ± 16.50 pack-years and for e-cigarette users, the mean duration was 4.5 ± 4.2 years.

Table 1. Baseline demographic characteristics of the study population

Metric/Parameter	Value
Number of participants	1014
Sex—male/female (%)	528 (52.1%)/486 (47.9%)
Age, years (mean ± SD)	60.5 ± 5.2
Smoking status—yes/no/unknown (%)	217 (21.4%)/795 (78.4%)/ 2 (0.2%)
Smoking history (current smokers)	
Traditional tobacco (pack-years, mean ± SD)	23.63 ± 16.50
E-cigarettes (years, mean ± SD)	4.5 ± 4.2

Median CTDIvol, DLP, and effective dose increased with higher BMI and weight categories (Figure 1). For BMI, median CTDIvol ranged from 0.56 mGy in underweight to 2.32 mGy in obese participants, with corresponding increases in DLP (from 24.02 to 86.11 mGy·cm) and effective dose (from 0.34 to 1.21 mSv). In weight-based stratification, the same trend was observed, ranging from 0.59 mGy (< 65 kg) to 3.23 mGy (> 105 kg) for CTDIvol (Table 2). The highest recorded effective dose (2.7 mSv) was observed in the heaviest weight group. Males had higher median doses than females (CTDIvol: 1.66 vs 0.91 mGy; DLP: 66.10 vs 35.91 mGy·cm), reflecting their greater median body mass (90 kg vs. 75 kg). Across age groups, dose metrics were relatively stable, with medians ranging between 1.12 and 1.39 mGy for CTDIvol (Table 2).

Table 2. Radiation dose metrics across both BMI and weight categories

	Median Weight (kg)	Median Height (cm)	CTDIvol (mGy)		DLP (mGy·cm)		effective dose (mSv)	
			Median	Max	Median	Max	Median	Max
BMI Categories								
Underweight	52	170	0.56	1.2	24.02	53.3	0.34	0.7
normal weight	67	170	0.72	1.8	30.22	69.3	0.42	1.0
Overweight	82	173	1.25	3.0	49.79	130.0	0.70	1.8
Obese	100	172	2.32	5.0	86.11	191.7	1.21	2.7
Weight Categories								
<65	60	164	0.59	1.3	24.82	51.2	0.35	0.7
65-75	70	168	0.81	1.6	33.55	63.7	0.47	0.9
75-85	80	170	1.15	2.6	46.28	92.9	0.65	1.3
85-95	90	176	1.64	3.8	63.38	122.6	0.89	1.7
95-105	100	180	2.28	4.0	86.14	145.4	1.21	2.0
>105	115	182	3.23	5.0	121.06	191.7	1.69	2.7

A Spearman's correlation analysis revealed a strong positive correlation between BMI and body weight (ρ = 0.836, p < 0.0001), exceeding the pre-defined collinearity threshold of 0.70. Consequently, BMI and weight were not included in the same regression models. Variance inflation factors (VIFs) for the remaining predictors (BMI, age, gender) were all below 1.05, indicating no further collinearity concerns.

Multiple linear regression analyses with standardized coefficients were performed to identify the relative contributions of BMI, gender, and age to each dose metric (CTDIvol, DLP, and effective dose). In BMI-based models (adjusted for age and gender), BMI emerged as the dominant predictor of CTDIvol (β = 0.792), DLP (β = 0.759), and effective dose (β = 0.759), followed by gender ($\beta \approx 0.65–0.75$). Age showed a minimal negative effect ($\beta \approx -0.04$). Model fit was high across outcomes (adjusted R^2 of 0.767 and 0.779 for Effective dose and CTDIvol respectively).

When weight replaced BMI, its influence on dose metrics increased further (β = 0.882–0.900), and the gender effect diminished substantially ($\beta \approx -0.03$ to +0.08), suggesting that weight captures much of the gender-related variation in dose. Weight-based models consistently achieved higher adjusted R^2 values (0.812 and 0.798 for Effective dose and CTDIvol) and lower AIC/BIC scores than BMI-based models, indicating slightly better predictive performance. Across all models, variance inflation factors were close to 1.0, confirming minimal residual multicollinearity.

4. Discussion

The success of a lung screening program relies on selecting an appropriate target population, ensuring test accuracy, determining optimal screening intervals, and balancing benefits against costs and potential harms [10]. In lung cancer screening, radiation exposure is a key concern due to its potential risk of radiation-induced cancer. Evidence from several studies indicates that both healthcare providers and the general public often have limited awareness of the radiation risks associated with medical imaging, which can lead to a biased perception of the benefit–risk balance of radiological examinations [11]. Over the past five years, low-dose CT (LDCT) has gained wider use for lung cancer screening, highlighting the need to assess the radiation doses incurred by this asymptomatic population.

The American College of Radiology (ACR), Society of Thoracic Radiology (STR), and the European Society of Thoracic Imaging (ESTI) have published practice guidelines and technical standards to assist radiologists and medical physicists in developing local CT lung cancer screening protocols [8-9]. Guidelines from these bodies provide target dose levels for LDCT screening to ensure patient safety. In the United States, the American College of Radiology (ACR) specify that lung cancer screening CT protocols should use a volumetric CT dose index (CTDIvol) of ≤3.0 mGy for a standard-sized adult (~170 cm, 70 kg), corresponding to an effective dose on the order of 1 mSv or less [9]. Our program's median CTDIvol for average-weight participants (~1 mGy) and median effective dose (~0.6–0.7 mSv) are well below the recommended low-dose limits [9]. Even the upper end of our dose range for standard-sized individuals was below 3 mGy, reflecting appropriate adherence to low-dose techniques.

In a European context, similar dose standards have been advocated. The European Society of Thoracic Imaging (ESTI), under the ESR, has issued technical guidance for lung screening CT aiming for extremely low doses [8]. Their recommendations call for using modern multi-detector CT scanners (64-row or more) with patient-size–adjusted CTDIvol targets of roughly 0.4 mGy for small patients (<50 kg), 0.8 mGy for medium (50–80 kg), and 1.6 mGy for large patients (>80 kg) – with appropriate tube current modulation and iterative reconstruction – such that the resulting effective dose for an average patient is ~0.7 mSv. Our observed doses are in line with this approach: for instance, medium-weight participants in our study (≈70 kg) had median CTDIvol around 1.15 mGy and effective dose around 0.65 mSv, matching the ESTI target range. Our heaviest patients (BMI ≥30 or weight >80 kg) had median CTDIvol in the ~2–3 mGy range,

which is higher than the ESTI's 1.6 mGy guidance scaled for larger body size. However, the overall dose distribution in our pilot compares favorably with international reference levels.

When benchmarked against published dose registries and trials, our program's doses also perform favorably. For example, the UK's Yorkshire Lung Screening Trial reported a median CTDIvol of 1.1 mGy and median effective dose of 1.15 mSv across 3,521 LDCT scans [12]. For standard-weight participants in that trial (60–80 kg), the median dose was ~1.0 mGy (≈0.97 mSv), virtually identical to what we achieved in that weight group. This suggests that our protocol delivers low-dose levels comparable to other international screening efforts. Likewise, the National Lung Screening Trial (NLST) in the U.S., which used earlier-generation scanners, reported an average effective dose of ~1.5–2 mSv per LDCT [3]. The fact that our median effective dose is around half of that (~0.7 mSv) reflects advancements in CT technology and aggressive dose optimization since the time of NLST. In essence, our pilot program's doses are well within the range deemed acceptable by international standards (ACR/ESTI) and are lower than or comparable to those in major lung screening trials. This benchmarking confirms that participants in our program are receiving minimal radiation exposure by current international norms. It also provides an objective reference for quality assurance to be used by the ongoing Lithuanian national screening programs.

Furthermore, the analysis revealed that patient demographic factors, particularly weight and BMI, have a strong influence on radiation dose in LDCT screening. In direct model comparisons, weight consistently outperformed BMI for predicting CTDIvol, DLP, and effective dose, explaining 2–4.5% more variance and yielding better model fit statistics (Figure 2). While BMI adjusts for height and may be advantageous in research settings, weight alone provided a stronger and more parsimonious predictor in this screening population. Given its ease of measurement and superior predictive performance, weight may be preferable for rapid, practical dose stratification in clinical settings.

This influence of body size on doses is biologically and technically expected: larger patients attenuate more X-rays and thus require higher tube currents and other protocol adjustments to achieve sufficient image quality, resulting in higher dose indices. In our cohort, dose metrics increased markedly with rising BMI categories. For example, the median CTDIvol for underweight participants (<18.5 kg/m²) was only ~0.6 mGy, whereas for obese participants (BMI ≥30) it was about 2.3 mGy (nearly four times higher). A similar trend was seen with effective dose, which rose from ~0.3–0.4 mSv in underweight individuals to ~1.2 mSv or more in the obese group. Body weight showed a near-linear correlation with CTDIvol (and DLP) in our data. This finding is consistent with reports from larger studies: Iball et al. note a very strong correlation between patient weight and CTDIvol (Spearman r ≈0.91) in a UK lung screening cohort, with dose escalating steadily as weight increases [12]. Our results mirror this pattern, confirming that patient size is the dominant driver of dose variation in LDCT exams.

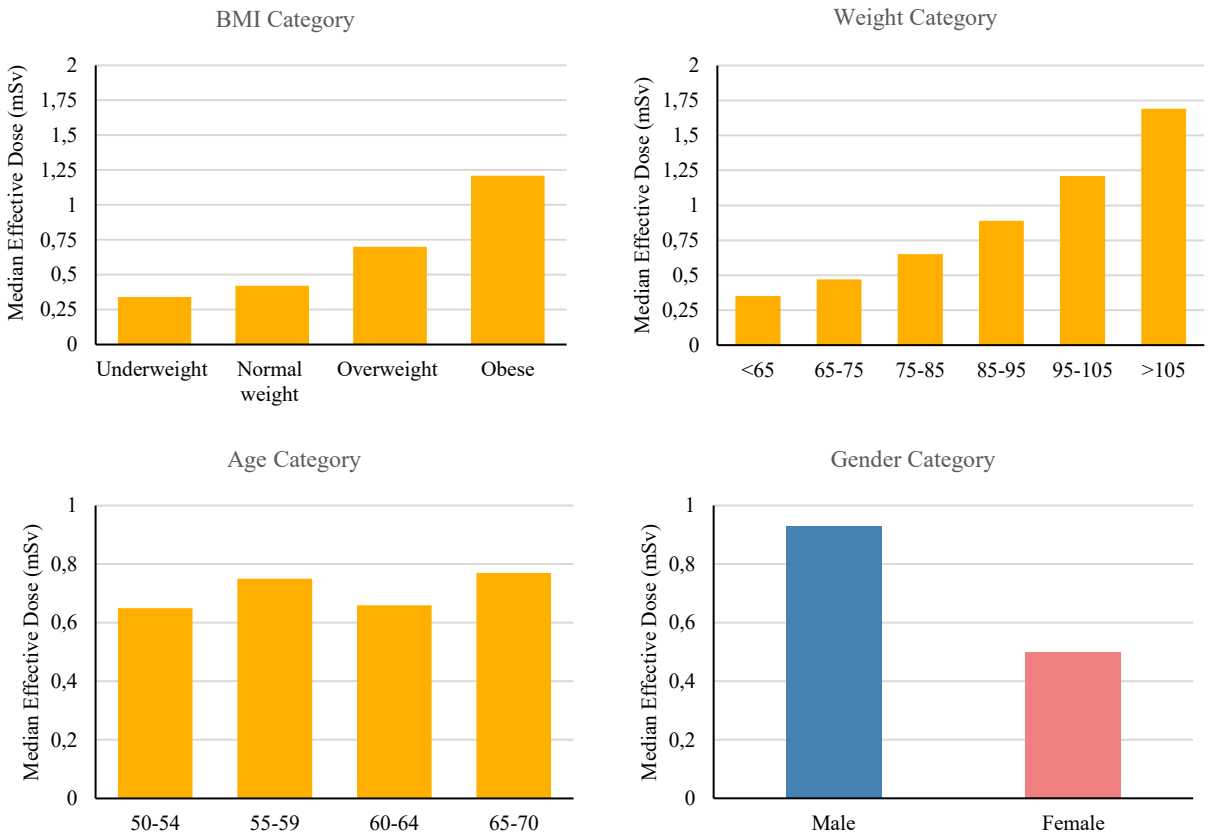

Fig. 1. Effective dose distribution across BMI, weight, age, and gender groups.

Interestingly, some differences were observed in dose by sex and age, but these appear to be largely secondary to body habitus. Male participants in our study had a higher median dose (CTDIvol and DLP) than females (e.g. median effective dose ~0.9 mSv in men vs ~0.5 mSv in women) which correlates with men's higher average weight (median ~90 kg for males vs 75 kg for females in our sample). After accounting for weight, sex itself was not a significant independent predictor of dose in our data. Thus, gender differences in dose are primarily a reflection of size differences (men typically being larger) rather than intrinsic sex-related factors. As for age, no strong direct correlation between age and dose was found after controlling for BMI. Older participants (e.g. age >65) in our cohort had slightly higher median doses than younger participants, but this was confounded by the tendency for older individuals to have different body composition or for technologists to use slightly more conservative settings in frail older patients.

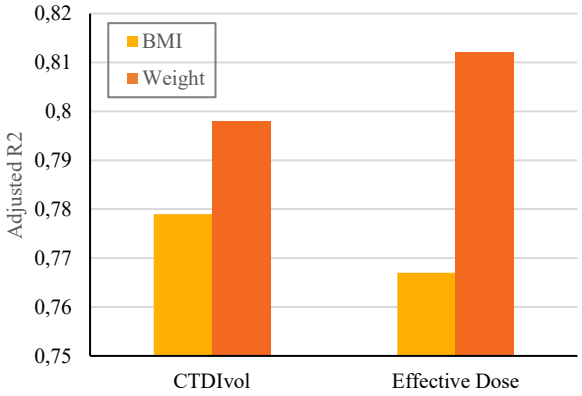

Fig. 2. Adjusted R^2 Comparison of weight vs BMI models across dose metrics.

Radiation protection principles are foundational in the context of a screening program that may expose a large number of healthy individuals to X-rays. Three key principles – justification, optimization, and dose limitation – guide the use of ionizing radiation in medicine. In lung cancer screening, multiple randomized trials (such as NLST, NELSON, etc.) have demonstrated a mortality benefit, thereby justifying LDCT screening in appropriately selected high-risk populations. However, this justification critically depends on using low-dose techniques. If the dose per scan were as high as a standard diagnostic chest CT (~7 mSv), the risk of radiation-induced cancers would increase to an unacceptable level. Model-based analyses have pointed out that high doses could negate the life-saving benefit of screening by inducing cancers in a fraction of participants [13]. Fortunately, our program adheres to strict low-dose methods (median ~0.7 mSv per scan), keeping the risk per exam extremely low. Using the International Commission on Radiological Protection (ICRP) risk coefficients, a single 1 mSv LDCT scan confers an estimated lifetime attributable cancer incidence of approximately 0.01% (1 in 10,000), and fatal cancer mortality risk of around 0.005% (1 in 20,000), highlighting that the radiation risk is negligible in the context of benefits from screening [14]. This tiny risk is far outweighed by the potential to prevent an early lung cancer death in roughly 1 in a few hundred high-risk individuals screened. Thus, the benefit-risk analysis for our screening remains highly favorable – a point underscored by recent analyses showing benefit-to-radiation-risk ratios on the order of 10:1 to 20:1 in modern screening cohorts [15].

5. Conclusions

The findings of this pilot low-dose CT lung cancer screening program confirm that protocol optimization can achieve sub-millisievert doses across a broad BMI range without compromising image quality. Median effective doses were <1 mSv for underweight, normal-weight, and overweight participants (averaging 0.65 mSv for participants weighing 70 ± 5 kg), and <1.3 mSv for obese individuals, with standard-size patient values well below ACR/AAPM thresholds and closely aligned with ESTI targets. Multivariate analysis identified both BMI and weight as dominant predictors of dose metrics, with a strong correlation between them ($\rho = 0.836$). While both measures showed comparable predictive value, BMI provides a standardized, height-adjusted metric that facilitates comparison across individuals. Nevertheless, weight remains a practical alternative when rapid assessment is required and height data are unavailable. The dose benchmarks established in this work provide a robust foundation for the safe nationwide rollout of LDCT screening and support the establishment of BMI-stratified Lithuanian DRLs, setting a new standard for radiation protection and protocol optimization in population-based screening.

6. References

1. Sung, H., Ferlay, J., Siegel, R. L., Laversanne, M., Soerjomataram, I., Jemal, A., & Bray, F. (2021). Global cancer statistics 2020: GLOBOCAN estimates of incidence and mortality worldwide for 36 cancers in 185 countries. *CA: a cancer journal for clinicians*, *71*(3), 209-249.
2. Zappa, C., & Mousa, S. A. (2016). Non-small cell lung cancer: current treatment and future advances. *Translational lung cancer research*, *5*(3), 288.
3. National Lung Screening Trial Research Team. (2011). Reduced lung-cancer mortality with low-dose computed tomographic screening. *New England Journal of Medicine*, *365*(5), 395-409.
4. de Koning, H. J., van Der Aalst, C. M., de Jong, P. A., Scholten, E. T., Nackaerts, K., Heuvelmans, M. A., & Oudkerk, M. (2020). Reduced lung-cancer mortality with volume CT screening in a randomized trial. *New England journal of medicine*, *382*(6), 503-513.
5. Pozzessere, C., von Garnier, C., & Beigelman-Aubry, C. (2023). Radiation exposure to low-dose computed tomography for lung cancer screening: should we be concerned?. *Tomography*, *9*(1), 166-177.
6. Nekolla, E. A., Brix, G., & Griebel, J. (2022). Lung cancer screening with low-dose CT: radiation risk and benefit–risk assessment for different screening scenarios. *Diagnostics*, *12*(2), 364.
7. AAPM CT Scan Protocols—The Alliance for Quality Computed Tomography. Lung Cancer Screening CT Protocols Version 6.0. Available online: https://www.aapm.org/pubs/CTProtocols/documents/LungCancerScreeningCT.pdf (accessed on 14 August 2025 2025).
8. LCS Project | ESTI—European Society of Thoracic Imaging. Technical Standards. Available online: https://www.myesti.org/content-esti/uploads/ESTI-LCS-technical-standards_2019-06-14.pdf (accessed on 14 August 2025).
9. American College of Radiology. ACR-STR Practice Parameters for the Performance and Reporting of Lung Cancer Screening Thoracic Computed Tomography (CT). Available online: https://gravitas.acr.org/PPTS/DownloadPreviewDocument?ReleaseId=2& DocId=38 (accessed on 14 August 2025).

10. Lee, E., & Kazerooni, E. A. (2022, December). Lung cancer screening. In *Seminars in respiratory and critical care medicine* (Vol. 43, No. 06, pp. 839-850). Thieme Medical Publishers, Inc.
11. Bastiani, L., Paolicchi, F., Faggioni, L., Martinelli, M., Gerasia, R., Martini, C., & Caramella, D. (2021). Patient perceptions and knowledge of ionizing radiation from medical imaging. *JAMA Network Open*, *4*(10), e2128561-e2128561.
12. Iball, G. R., Beeching, C. E., Gabe, R., Tam, H. Z., Darby, M., Crosbie, P. A., & Callister, M. E. (2024). An evaluation of CT radiation doses within the Yorkshire Lung Screening Trial. *British Journal of Radiology*, *97*(1154), 469-476.
13. Demb, J., Chu, P., Yu, S., Whitebird, R., Solberg, L., Miglioretti, D. L., & Smith-Bindman, R. (2019). Analysis of computed tomography radiation doses used for lung cancer screening scans. *JAMA internal medicine*, *179*(12), 1650-1657.
14. Balter, S., Zanzonico, P., Reiss, G. R., & Moses, J. W. (2011). Radiation is not the only risk. *American journal of roentgenology*, *196*(4), 762-767.
15. Hendrick, R. E., & Smith, R. A. (2024). Benefit-to-radiation-risk of low-dose computed tomography lung cancer screening. *Cancer*, *130*(2), 216-223.

MEDICAL PHYSICS IN THE BALTIC STATES 17 (2025)

Proceedings of International Conference "Medical Physics 2025"
06-08 November 2025, Kaunas, Lithuania

USE OF ELECTRON IRRADIATION OF SOME WATER-SOLUBLE ANTI-TUMOR DRUGS IS A WAY TO CHANGE THEIR PROPERTIES

Liudmyla ASLAMOVA[1], Mykhaylo ZABOLOTNYY[2], Galina DOVBESHKO[3], Olena GNATYUK[4], Maksym BARABASH[5], Valerii OREL[6]
[1,2]Taras Shevchenko National University of Kyiv, Ukraine, [3,4]Institute of Physics of NASU, Kyiv, Ukraine, [5]Technical Center, N.A.S. of Ukraine, Ukraine, [6]National Cancer Institute, Kyiv, Ukraine
[1]liudmyla.aslamova@knu.ua; [2]mykhailo.zabolotnyi@knu.ua; [3]matinelli@gmail.com; [4]hrysantemka@gmail.com; [5]bashik_77@ukr.net; [6]valeriiorel@gmail.com

Abstract: This study investigated the effect of 1 MeV electron irradiation of sodium chloride on the properties of antitumor drugs dissolved in it: doxorubicin (anthracycline class) or conium (alkaloid class). The absorbed radiation dose ranged from 2 to 90 kGy. Irradiation induced notable changes in the optical absorption spectra of the drug solutions acress IR, visible and UV ranges, as well as an increase in cytostatic activity. The cytostaticity of the drug solution is determined by the energetic interaction of the drug itself and the irradiated solvent.

Keywords: doxorubicin, conium, sodium chloride, irradiation

1. Introduction

The use of antitumor drugs is associated with a number of significant problems. These include nonspecific action and high toxicity of antitumor drugs toward healthy organs and tissues. In addition, a serious obstacle to the therapeutic effect of drug therapy is the resistance of malignant neoplasms to cytostatics [1,2]. Addressing these limitations requires the design of new materials, the investigation of relationships between physicochemical and cytostatic properties, and ultimately the development of more effective and less toxic antitumor drugs. One of the promising methods for modifying water-soluble antitumor drugs was introduced by researchers at Taras Shevchenko National University of Kyiv [3, 4], which is based on the use of irradiation with high-energy (1 or 2 MeV) electrons of sodium chloride for infusions before dissolving antitumor drugs in it. The aim of the work is to study the mechanisms by which high-energy electron irradiation of sodium chloride influences the optical spectra and cytostatic activity of doxorubicin or conium, in order to determine the possibility of modifying existing antitumor drugs without the use of foreign nanoimpurities.

2. Materials and experimental methods

The absorption spectra of doxorubicin (Pharmacia Italia SpA, Italy) and conium (Weleda, Germany) dissolved in sodium chloride solution for infusions (Yuria Pharm, Ukraine) were studied. Conium contains alkaloids - coniine, N-methylconiine, γ-coniine, conhydrin and pseudoconhydrin.
The solvent was irradiated with electrons with an energy of 1 MeV using a resonant linear electron accelerator (Argus). Infrared (IR) absorption spectra were recorded on a Bruker IFS-66 spectrometer, absorption spectra in the visible and ultraviolet (UV) ranges were recorded on a Shimadzu UV-260 spectrophotometer. The absorbed dose (I) by the solvent ranged from 2 to 90 kGy. Luminescence was recorded on a CaryEclipse spectrofluorometer (Varian). The cytostatic activity of doxorubicin was determined using Lewis lung carcinoma cells (LLC). The number of living cells in the wells after 24 hours of incubation was determined using the MTT test using a plate reader at a wavelength of 545 nm. [3]. All samples for recording IR spectra of conium were prepared in KBr tablets. IR spectra were recorded using a Bruker IFS 66 IR Fourier spectrometer in transmission geometry. Numerical analysis of the obtained results andmodeling of optical spectra as linear combinations of distribution functions was carried out using Origin 2021 program.

3. Experimental results and their analysis

3.1. Dependences of optical spectra on the radiation dose

The effect of preliminary electron irradiation of sodium chloride for infusions on the optical and cytostatic properties of doxorubicin and conium dissolved in it was investigated. The results of the Fourier transform infrared (FTIR) absorption spectra of doxorubicin after its dissolution in sodium chloride for infusions, previously irradiated with high-energy electrons in the UV range, are shown in Fig. 1.

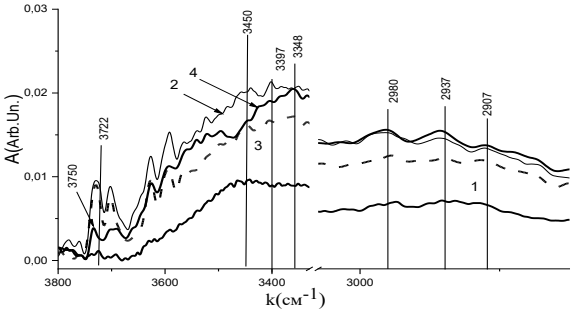

Fig. 1. FTIR absorption spectra of doxorubicin in the 3800–3030 cm^{-1} range: curve 1 at (I = 0 kGy), curve 2 at (I = 10 kGy), curve 3 at (I = 40 kGy), curve 4 at (I = 80 kGy)

Analysis of the spectra Fig. 1 revealed correspondence between the location of the absorption maxima and the values of the corresponding normal vibration of a certain molecular group. When comparing the positions of the peaks responsible for the vibrations of the same groups of atoms of samples of solutions with irradiation at different doses and unirradiated sodium chloride, a shift, splitting and sometimes attenuation of some absorption maxima were found. Such effects can be due to specific interactions between molecular groups with radiation-induced bubstones and free radicals . Complete attenuation of the maxima in comparison with the control sample occurs due to a change in the conformational characteristics of molecules localized in those molecular groups whose vibrations correspond to the frequencies that disappear. Since IR-active vibrations are detected only when accompanied by changes in the molecular dipole moment, disappearance of a spectral maximum indicates that the corresponding vibration no longer contributes to the net dipole moment.

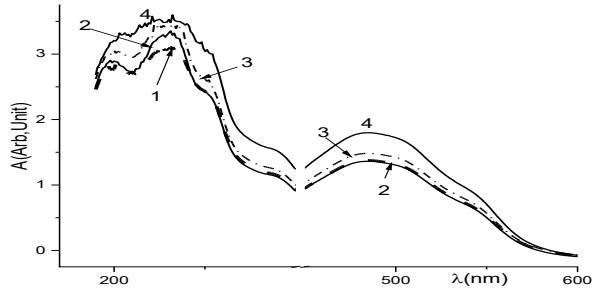

Fig. 2. Optical absorption spectra of doxorubicin solution in the UV and visible range, curve 1 at (I = 0 kGy), curve 2 at (I = 10 kGy), curve 3 at (I = 40 kGy), curve 4 at (I = 80 kGy)

The dependence of the optical absorption spectra of a doxorubicin solution in the UV and visible ranges on the absorbed dose was investigated. Analysis of the obtained spectra (Fig. 2) indicates a shift of the maxima and sharp changes in their intensities, depending on the dose of solvent irradiation. These spectral modifications may be attributed to conformational rearrangements of drug molecules induced by interactions with bubstones and their clusters in the irradiated solvent. While the behavior of individual bubstones has been studied [4,5], cluster formation remains less understood.The complications of such a problem are, on the one hand, caused by the nonlinear nature of the equations describing the electric field of the double electric layer of a bubston. Also, there is not enough information about the polarization and deformation-force characteristics of individual bubstons and their clusters - during the coagulation of bubstons, their spherical symmetry is broken, the fractal dimension of coagulants depends on the mechanisms of cluster growth [4, 5, 6]. For comparison with the drug of the anthracycline class (doxorubicin), a study of the effect of the irradiated solvent on the drug of the alkaloid class (conium) was conducted. The results of the studies are illustrated in the dependencies Fig. 3.

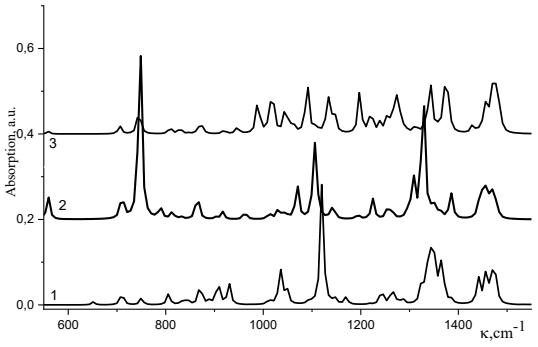

Fig. 3. Dependence of IR spectra of conium on dose I: curve 1 was obtained at I = 0 kGy, 2 at I = 5 kGy, 3 at I = 10 kGy

Defined that the addition of irradiated solvent (Fig. 3) at different doses of absorbed electron irradiation affects the position of the maxima of the conium absorption bands, namely, a shift of the 1120 cm^{-1} line (curve 1) to the position of 1106 cm^{-1} (curve 2), and then to 1089 cm^{-1} (curve 3). This effect of shifting the conium absorption lines in the vibrational region of the IR spectrum is evidence of a change in its conformational state caused by the interaction with bubstones (their clusters) present in the irradiated solvent.

3.2 Effect of electron irradiation on cytostaticity

The cytostatic part of the studies was carried out according to the standardized methodology [3, 4]. Special studies were conducted to determine the effect of pre-irradiation of sodium chloride on the antitumor properties of doxorubicin or conium dissolved in it. Experiments were conducted in vitro using the LLC cell line. During the studies, tumor cells were plated in the wells of a 96-well plate in 0.1 ml of nutrient medium (2×10^5 cells/ml) and incubated overnight. After that, drugs were added to the cells in 0.1 ml of fresh medium in a wide range of concentrations, which were progressively reduced. Fresh medium was added to the control wells in the same volume without the test agent. The number of living cells in the wells after 24 hours of incubation was determined using the MTT test [3, 4]. The results of studies of the effect of RF irradiation on the cytotoxic/cytostatic effect of doxorubicin are illustrated in Fig. 4, which shows the dependences of the percentage of the number (N) of living LLC cells after 24-hour incubation of a doxorubicin solution at its various concentrations (X).

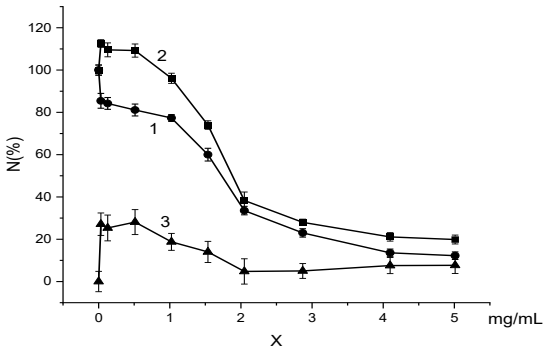

Fig. 4. Cytostatic activity of doxorubicin against LLC cells when dissolved in sodium chloride: curve 1 — irradiated solvent (40 kGy), curve 2 — non-irradiated solvent, curve 3 — difference between irradiated and non-irradiated samples.

In Fig. 4, curve (1) illustrates the percentage of live LLC cells after incubation with doxorubicin dissolved in irradiated (I = 40 kGy) sodium chloride at different concentrations of doxorubicin, (2) is the percentage of live cells for the non-irradiated solvent, (3) is the difference between graphs (2) and (1). The dependences in Fig. 4 indicate that the effect of the irradiated solvent at a fixed I essentially depends on the concentration of doxorubicin. Thus, it can be concluded that the cytostatic activity of doxorubicin dissolved in the irradiated solvent is not the sum of the cytostatic activity of doxorubicin dissolved in non-irradiated sodium chloride and the cytostatic activity of the irradiated solvent.

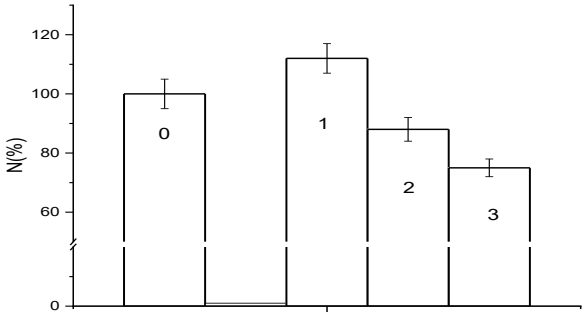

Fig. 5. Effect of sodium chloride irradiation on LLC cell survival. (0) baseline before solvent addition; (1) non-irradiated solvent; (2) irradiated solvent I = 40 kGy; (3) irradiated solvent I = 80 kGy.

Figure 5 shows the survival of LLC tumor cells in medium supplemented with solvent irradiated no more than 14 days prior to the experiments. The results showed clear dose-dependent effects: sample 1 (0 kGy), sample 2 (40 kGy), and sample 3 (80 kGy). Thus, when using pre-irradiated sodium chloride as a solvent for doxorubicin and conium, the resulting solutions acquire new optical and cytostatic properties. The spectra of the extinction range of sodium chloride in the range of 190 - 1000 nm were studied during the third week after its irradiation with high-energy electrons as measurements during one week were reported elsewhere [3, 7]. To obtain a description of the exact numerical results, the correlation coefficients between the extinction spectra were determined at the dose values 1_1 = 0 kGy, I_2 = 10 kGy, I_3 = 40 kGy, I_4 = 80 kGy. It should be noted that these coefficients reflect the degree of similarity between the optical absorption spectra at different doses, but do not imply the existence of a direct functional relationship.

3.3. Effect of electron irradiation on fluorescence

To obtain additional information about the properties of the force centers of sodium chloride, the fluorescence of sodium chloride and the effect of electron irradiation on it were investigated. In the study of fluorescence, the irradiation dose was 0, 10, 40 and 80 kGy; the wavelength of the exciting light was 260 nm. The fluorescence spectra are presented in Fig. 6.

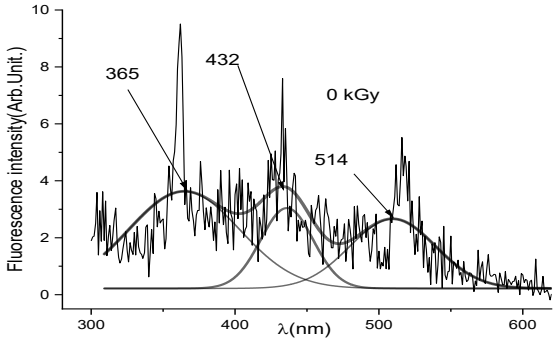

Fig. 6. Fluorescence spectrum of the solvent, I = 0 kGy

An approximation of the fluorescence spectra of sodium chloride at different irradiation doses was carried out, the results of which are illustrated in Fig. 7. The dependences of the fluorescence spectra were approximated by linear combinations of sums of Gaussian distributions using Origin 2021 program.

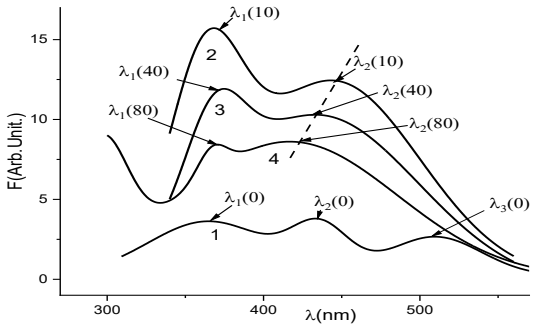

Fig. 7. Dependences of the approximation of the fluorescence spectra of sodium chloride on the value of the absorbed dose of electron irradiation

Figure 7 presents the approximated fluorescence spectra of sodium chloride at different irradiation doses: curve 1 (0 kGy), curve 2 (10 kGy), curve 3 (40 kGy), and curve 4 (80 kGy). The values of λ_j (I) significantly depend on I. The spectrum at I = 0 kGy has three emission bands, and the spectra at I = 10, 40, 80 kGy contain four bands. The structures of the fluorescence spectra of nanoparticles in a liquid medium are determined by the characteristics of the power energy center [8]. Therefore, irradiation of sodium chloride with high-energy electrons generates long-lived power fluorescence centers, the parameters of which depend on the magnitude of the absorbed dose.

4. Conclusions

The influence of high-energy electron irradiation (1 MeV, 2–90 kGy) of sodium chloride infusion solutions on the optical spectra and cytostatic activity of two antitumor drugs—doxorubicin (anthracycline class) and conium (alkaloid class)—was investigated. The cytostatic activity of antitumor drugs was determined using Lewis lung carcinoma cells (LLC).

The absorption spectra of doxorubicin solution in the IR region of the spectrum were characterized by non-monotonicity of the dependence of the ratio of the amplitudes of high-frequency and low-frequency maxima on the absorbed dose. The effect was explained within the framework of the bubstone model by coagulation (clusterization) of bubstones, which is realized at high values of bubstone concentration.

The absorbed dose of sodium chloride irradiation significantly influenced the spectral characteristics of doxorubicin in the UV, visible, and IR ranges. Specifically, absorption decreased in the 175–250 nm region but increased in the 250–600 nm region compared with solutions prepared in non-irradiated solvent.

For conium solutions, irradiated sodium chloride induced shifts in the IR absorption bands, with the 1120 cm^{-1} line moving to 1106 cm^{-1} and then to 1089 cm^{-1}. These spectral modifications persisted for up to two weeks after irradiation at 2.5 kGy.A correlation was established between the optical properties and cytostatic activity of doxorubicin dissolved in irradiated sodium chloride, demonstrating that solvent pre-irradiation alters both the spectral behavior and biological effectiveness of the drug.

5. References

1. Sung H., Ferlay J., Siegel R.L., Laversanne M., Soerjomataram I., Jemal A., Bray F. Global Cancer Statistics 2020: Globocan Estimates of Incidence and Mortality Worldwide for 36 Cancers in 185 Countries. Cancer Journal for Clinicians, 71(3), 2021, 209–249.
2. Genevieve Housman, Shannon Byler, Sarah Heerboth, Karolina Lapinska, Mckenna Longacre, Nicole Snyder, Sibaji Sarkar. Drug Resistance in Cancer: An Overview, Cancers (Basel). (2014), Sep; 6(3): 1769–1792.
3. Aslamova L., Zabolotnyy M., Dovbeshko G., Solyanik G., Gnatyuk O., Tsapko M. Irradiation of physiological solutionwith high energy electrons – A way of increase cytotoxic/cytostatic effect. Proceedings of the 16th International Conference "Medical Physics Physics in the Baltic States", Kaunas, 2023, p. 149–152.
4. Zabolotnyy M.A., Kulish M.P., Dmytrenko O.P., Solyanyk G.I., Prylutskyi Yu.I., Drapikovskyi M.A., Kuzmenko M.O., Poluyan N.A., Kiyashko V.A., Method of modification of water-soluble anticancer drugs using radiation exposure, Patent for the invention of Ukraine, № 116 227 Registered on 26.02. 2018.
5. Xuelin Wang, Pan Li, Rongsheng Ning, Rehman Ratul, Xianren Zhang, Jun Ma. Mechanisms on stability of bulk nanobubble and relevant applications: A review. Journal of Cleaner Production Volume 426, 10 November 2023, 139153.
6. Rens Kamphorst, Maximilian F. Theisen, Ankur D. Bordoloi, Samir Salameh, Gabrie M. H. Meesters, J. Ruud van Ommen, On the structure of nanoparticle clusters: effects of long-range interactions. Phys. Chem. Chem. Phys., 2025, 27, 5476–5481. https://doi.org/10.1039/d4cp04235b
7. M.A. Zabolotnyy, L.I. Aslamova, G.I. Dovbeshko, O.P. Gnatyuk, V.B. Neimash, V.Yu. Povarchuk, V.E. Orel, D.L. Kolesnyk, L.M. Kirkilevska, G.I. Solyanyk. Effect of high energy electron exposure of the saline solution on physicochemical properties and cytotoxic activity of doxorubicin. Nuclear Physics and Atomic Energy, 23 (2022), 131–139.
8. Arindam Saha, SK Basiruddin, Rupa Sarkar, Narayan Pradhan, Nikhil R. Jana, Functionalized Plasmonic−Fluorescent Nanoparticles for Imaging and Detection. J. Phys. Chem. C (2009), 113, No 43, 18492–18498.

MEDICAL PHYSICS IN THE BALTIC STATES 17 (2025)

Proceedings of International Conference "Medical Physics 2025"
06-08 November 2025, Kaunas, Lithuania

THE RESPIRATORY MOTION MANAGEMENT IMPACTS IN LUNG STEREOTACTIC BODY RADIATION THERAPY (SBRT)

Akvilė KUNCYTĖ[1], Evelina JASELSKĖ[1,2]
[1] Physics department, Kaunas University of Technology, Kaunas, Lithuania, [2] HLUHS Kauno klinikos, Oncology and Hematology department, Kaunas, Lithuania
[1]akvkun4@ktu.lt; [2]evelina.jaselske@ktu.lt

***Abstract*:** This investigation covers a randomized study, which compares Planning Target Volume (PTV) differences between the three strategies of radiotherapy treatment for a lung tumour. All patients' treatment plans were grouped into three categories: SBRT with respiratory control and non-SBRT with and without breath monitoring. The research outcome shows a noticeable tendency that breath control minimizes PTV. Additionally, the SBRT technique stands out as a significant method, which could be applied for difficult malignancies.

Keywords: lung tumour, stereotactic radiotherapy, breath monitoring, planning target volume.

1. Introduction

SBRT of the lungs is implemented with Image-Guided Radiation Therapy (IGRT) real-time follow-up, which can achieve more precise dose delivery to the lung's target and reduce side effects on surrounding normal tissues compared with the conventional radiotherapy approach. Although variations in tumour position may occur due to patient respiration, in addition to potential geometric positioning errors, inter-fractional organ motion, and machine accuracy uncertainties, these factors must be rigorously accounted for in treatment planning and PTV delineation.

2. Characteristics of lung tumour treatment plans

Compared with other organs, the lungs exhibit continuous motion resulting from both respiratory and cardiac activity, thereby complicating precise tumour delineation and accurate radiation dose delivery.

Radiotherapy planning begins from diagnostic computed tomography (CT) images (generally with a thickness of 2.5 mm per slice). The Gross Tumour Volume (GTV) delineates the visible tumour and involved lymph nodes. The Clinical Target Volume (CTV), which accounts for microscopic disease spread, is generally considered equal to the GTV in lung SBRT because early-stage tumours rarely extend beyond the visible margins [1]. The Internal Target Volume (ITV) encompasses tumour motion during respiration, while the PTV is obtained by expanding the ITV or CTV with a 3–5 mm margin to account for setup inaccuracies, organ motion, and machine-related uncertainties.

However, SBRT demonstrates the highest efficacy in tumours measuring up to approximately 4–5 cm in diameter. Additionally, three-dimensional CT (3D-CT) alone may not adequately characterize moving targets in the lungs. Consequently, four-dimensional CT (4D-CT) is considered the most appropriate imaging modality for SBRT, as it acquires multiple phases of the respiratory cycle and enables assessment of tumour internal motion.

3. Uncertainties in Tumour Volume–Dose Fractionation during IGRT

Although stereotactic radiotherapy is regarded as a high-precision modality, radiation intended for the lung tumour may also be delivered to surrounding tissues. This may lead to underdosage in successive fractions or unintended dose escalation when tumour localization is compromised by respiratory motion.

To address these challenges, various motion management strategies are applied in SBRT. Active gating can be subdivided into phase-based and amplitude-based approaches. In phase gating, radiation is delivered during a predefined segment of the respiratory cycle, typically at end-exhalation [2]. This technique, however, is highly sensitive to irregular breathing patterns, which may interrupt dose delivery until regular respiration resumes. In amplitude gating, radiation is administered when the respiratory signal falls within a predefined amplitude range, thereby creating a 'window of delivery' [3].

When the target tumour is localized during the expiratory phase, the radiation delivery window can be selected from alternative intervals. Tumour position is stabilized,

and irradiation of healthy tissues is reduced, although treatment may still be compromised by irregular breathing. Even with gating, a margin of approximately 3 mm is recommended to compensate for residual uncertainties.

For patients unable to perform breath-hold, passive tumour tracking is recommended. Fiducial markers inserted or implanted close to the target during the bronchoscopy allow continuous motion tracking. According to Tanaka H., Ono T., Ueda K., and Karita M., et al., irradiation can be delivered by tracking these markers, which must be detected within a predefined region, referred to as the gating box (a three-dimensional sphere) [6]. In this approach, radiation is delivered at the end of exhalation, when the tumour position is relatively stable. However, due to irregular breathing patterns, a larger margin of 3–5 mm is typically required to ensure full target coverage.

The lowest-precision SBRT approach is free-breathing, in which radiation is delivered continuously throughout the entire respiratory cycle. Although technically simpler, this method requires larger PTV margins—often 5 mm or more—to compensate for full tumour motion [7], thereby increasing the dose to surrounding healthy tissues. Studies have reported that PTV may expand by up to 35–45% under free breathing compared with gated or tracking techniques [5].

4. Methods

For this quantitative study, radiotherapy plans, performed with a TrueBeam STx linear accelerator, were analysed. Three different groups of lung radiotherapy planning methods were evaluated. The first comprised SBTR with respiratory motion, accomplished with a 4D-CT and amplitude-based active respiratory gating. The other two groups consisted of conventional treatment plans based on 3D-CT. One employed respiratory management with surface imaging or infrared markers to monitor chest motion and deliver treatment during the exhalation phase, while the other was performed under free-breathing conditions.

Table 1. PTV data from different lung radiation therapy methods

Radiotherapy method	PTV, cm³
SBRT	73.8
	62.7
	60.4
	58.3
	81.6
	66.7
Non-SBRT with respiratory control	294.3
	138.2
	302.8
	252.2
	121.6
	147.7
Non-SBRT without respiratory control	177.8
	118.5
	1885.2
	209.6
	322.0
	760.6

Each group comprised six radiotherapy plans for the treatment of right lung tumour. Treatment planning was performed using Varian Eclipse 16.1, which enables target delineation and assessment of organs at risk (OAR), including the lungs, heart, oesophagus, spinal cord, and bones. This study compared PTV differences among the three groups (Table 1). Data visualization was conducted using RStudio software.

4.1 Research limitations

This study reviews random pulmonary radiotherapy plans for right lung tumour, therefore, direct case-by-case comparison across radiotherapy methods was not feasible. As the target volumes differed between plan approaches, an abstract comparison of PTV among the three methods was performed.

5. Results

5.1. PTV range in SBRT

Considering the PTV values of stereotactic radiotherapy (SR, Fig. 1) in the box plot, it can be observed that in random cases, PTV values range from 58 to 82 cm³. The mean PTV of approximately 67.25 cm³ shows minimal deviation from the median value of 64 cm³.

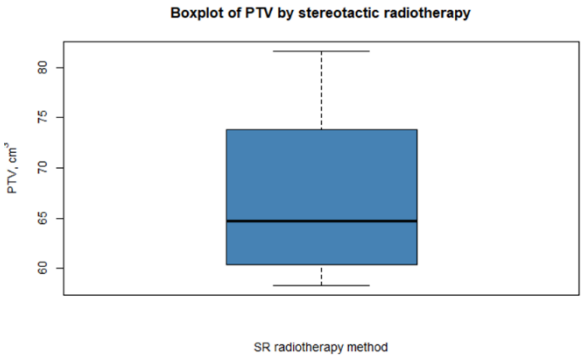

Fig. 1. PTV range variations in lung stereotactic RT

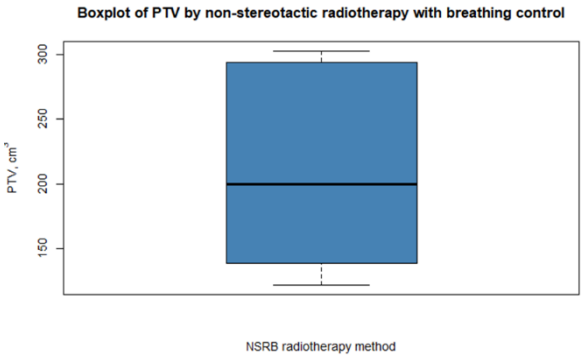

Fig. 2. PTV range in lung non-SBRT with respiratory monitoring

5.2. PTV range in non-SBRT method with respiratory control

Figure 2, representing the lung non-SBRT method with respiratory monitoring (NSRB), demonstrates a tall box plot, indicating a wide range of target volumes (121.6 - 302.8 cm³). The mean PTV was equal to 209.5 cm³, with an approximate 200 cm³ median. To sum up the collected

data, no exceptions with very low or high PTV were observed in the dataset.

This technique may be advantageous when tumour diameter exceeds the size typically suitable for SBRT (>4-5 cm), particularly when the lesion is located in the lower lung regions near critical organs. Respiratory control minimizes target motion and thereby limits the radiation dose to organs at risk and soft tissues.

5.3. PTV range in non-SBRT method without respiratory control

In most collected cases of lung radiotherapy without respiratory control (NSR in Fig. 3), the delineated PTV ranged from 120 to 760 cm³. However, the collected data has an extreme outlier 1885.2 cm³ PTV substantially inflated the mean PTV to 578.95 cm³. Excluding this outlier reduced the mean target volume to 317.7 cm³, a value more consistent with the median PTV of ~250 cm³ for non-stereotactic treatment without breathing control.

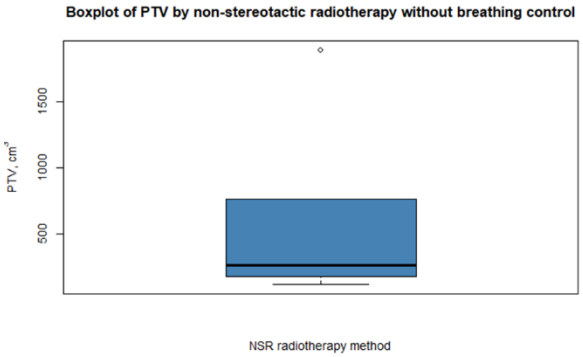

Fig. 3. PTV range in lung non-SBRT without breathing monitoring

This outlier case (Fig. 4) involved a tumour with a diameter exceeding 5 cm, rendering it unsuitable for stereotactic treatment. Moreover, respiratory control was not required, both due to the tumour's size and its localization in the superior lobe, where respiratory motion exerts minimal influence on tumour displacement.

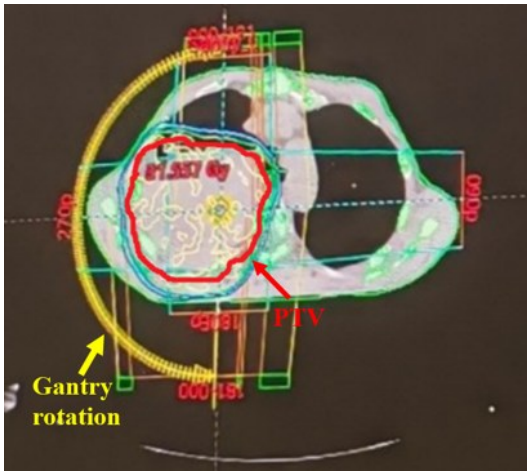

Fig. 4. Exceptional case of lung radiotherapy without breathing control (with 1885.2 cm³ PTV delineation)

6. Discussion

The boxplot of different lung radiotherapy methods (Fig. 5) demonstrates substantial contrasts in PTV values. The lung SBRT method PTV values do not overlap with other non-SBRT methods. SBRT achieved a threefold reduction in PTV (around 67.9%) compared with non-SBRT with respiratory control and an 8.6-fold reduction (−88.4%) relative to non-SBRT without respiratory monitoring (excluding the outlier). Although the PTV distributions for NSR and NSRB overlapped, the mean PTV of NSRB was 2.8 times smaller (−63.8%) than that of NSR.

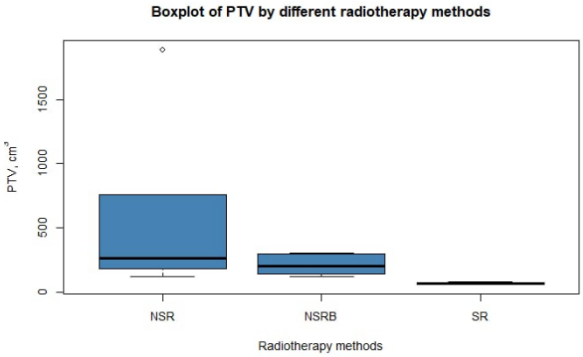

Fig. 5. Comparison of PTV between different lung radiotherapy methods

The PTV results obtained for SBRT and conventional methods with respiratory monitoring in this study are consistent with the findings reported by Nyman J., Hallqvist A., et al. In their randomized trial, the mean PTV in conventional radiotherapy was approximately 180 cm³ (using a 2 cm margin around the CTV in all directions), whereas in stereotactic radiotherapy the mean PTV was 74 cm³ (with a 0.5–1 cm margin). This corresponded to a 58.9% PTV reduction with SBRT, compared with a 67.9% reduction observed in the present study.

Although this comparison of PTV remains abstract due to heterogeneity in right lung treatment cases and target volumes, as no within-patient comparison across radiotherapy methods was performed, certain trends can be identified. SBRT generally yielded smaller PTVs, as high-dose delivery was achieved with greater precision through respiratory control and real-time target tracking using 4D-CT. The smaller PTVs in SBRT also reflect the treatment of smaller tumours compared with NSR or NSRB. Nevertheless, the results indicate that respiratory monitoring significantly reduces planning target volumes. Furthermore, 4D-CT demonstrates advantages over 3D-CT not only in reducing PTV but also in managing tumours in the lower lung lobes, which are more susceptible to positional shifts caused by breathing.

7. Conclusions

The results of this study indicate that respiratory monitoring significantly reduces planning target volume (PTV). Comparison between stereotactic and conventional radiotherapy with and without respiratory control demonstrated PTV reductions of 67.9% and 88.4%, respectively. Furthermore, within conventional

radiotherapy, respiratory monitoring was associated with a 63.8% reduction in PTV compared with free-breathing treatment.

8. References

1. Grosu A., Nieder C., Nicolay N. H.. Target volume Definition in radiation Oncology. Springer, Cham, 115–145 p., 2023.
2. Joe Y. Chang, L. Dong, H. Liu, G. Starkschall, P. Balter, R. Mohan et al. Image–Guided Radiation Therapy for Non–small Cell Lung Cancer. Journal of Thoracic Oncology, 3(2), 177-186 pages, 2008.
3. Meyers S. M., Kisling K., Atwood T. F., Ray X. A.. Standardized workflow for respiratory-gated motion management decision-making. Journal of Applied Clinical Medical Physics, 23(8), 2022.
4. Nyman J., Hallqvist A., Lund J., Brustugun O., Bergman B., Bergström P., Friesland S., Lewensohn R., Holmberg E., and Lax I. SPACE – A randomized study of SBRT vs conventional fractionated radiotherapy in medically inoperable stage I NSCLC. Radiotherapy and Oncology, 121(1), 1–8, 2016.
5. Prunaretty J., Boisselier P., Aillères N., Riou O., et al. Tracking, gating, free-breathing, which technique to use for lung stereotactic treatments? A dosimetric comparison. Reports of Practical Oncology & Radiotherapy, 24(1), 97-104 p., 2019.
6. Tanaka H., Ono T., Ueda K., Karita M., et al. Deep inspiration breath hold real-time tumor-tracking radiation therapy (DBRT) as a novel stereotactic body radiation therapy approach for lung tumors. Scientific Reports, 14(1), 2024.
7. Trémolières P., Gonzalez-Moya A., Paumier A., Mege M., Blanchecotte J., Theotime C., Autret D. & Dufreneix S. Lung stereotactic body radiation therapy: personalized PTV margins according to tumor location and number of four-dimensional CT scans. Radiation Oncology, 17(1), 2022.

Elekta

Elekta ONE® | Planning Pro

Powered by MIM

Combining comprehensive treatment management with highly-personalized patient care at lightning speed

Discover the new standard of excellence, converging the best of treatment planning components in one.

One for all in treatment planning

Elekta ONE | Planning Pro* is a software designed to manage a wide spectrum of treatment challenges, techniques, and delivery systems for both online and offline workflows—saving more time for planners to focus on what matters: personalizing treatment planning. Because a solution that's able to do everything, is everything.

Proven precision

- Simplify tumor motion management, automate registration, 4D - CT ITV creation, and motion analysis
- Your single source of planning for all treatment techniques, including 3D, IMRT, VMAT, stereotactic and particles
- Unique Multi-Criterial Optimization (MCO) for maximum target coverage, automatically sparing the normal tissue as much as possible
- Gold standard Monte Carlo dose calculation with >95% QA passing rate

Adaptive on demand

- Ensures you have the freedom to decide when and how to adapt, every step of the way
- Combine multiple treatment modalities with biological effective dose (BED) conversion and deformable dose summation

Online and offline

- Consistent experience across online and offline adaptive workflows with same plan quality

End-to-end speed

Featuring GPU-based dose calculation, image registration, and enhanced workflow automation. Elekta ONE | Planning Pro is accelerating every step of the process—from contouring to treatment planning, to decision-making, QA and treatment delivery—and eliminating repetitive tasks along the way. This is end-to-end speed in radiation therapy.

Accelerated dose calculation

- Experience the difference in speed with GPU-based Monte Carlo dose calculation in seconds
- 18x faster plan computation on average with GPU vs CPU**
- 180 seconds full Monte Carlo dose optimization and calculation***

Speed at every step

- True zero-click automated contouring** completed in less than 45 seconds
- Unlock higher treatment delivery efficiency with Elekta linacs, achieving the planned dose with one gantry rotation and less arcs used

Automated your way

- Swift planning process with less clicks through extended planning automation
- Best-in-class solution templates driving standardization and efficiency, reducing the inter-user variability in your clinical workflow, and helping your team achieve faster results

Designed for you

With easy adoption of MR in RT workflow, access on all available patient imaging data, and an unrivaled user experience that streamlines workflow with integration of advanced APIs, Elekta ONE | Planning Pro empowers clinicians with enhanced personalization in clinical decision making through streamlined workflows and analytics.

Superior physician space

- Seamless integration between AI contouring and planning workspaces, with unique built-in dashboards, for premium user experience
- Plan Analytics provides plan quality insights and upfront visibility into the maximum sparing achievable for each patient
- Full integration with Elekta ONE | OIS powered by MOSAIQ

MR in RT ready

- Real-time access to previous radiation treatments and imaging
- Multi-modality rigid and deformable image registration allows you to account for every detail

Scalable solution that evolves with you

- Optimize hardware deployment with distributed planning
- Remote access: review and approve daily adapted plans, in any location, at any time
- SaaS packages: different options to help you improve your productivity

Built for today. Designed for tomorrow. The first Elekta enterprise solution to deliver enhanced personalization, premium user experience, and superior dose planning—now accessible anywhere and ready to adapt to your needs, wherever you are.

Elekta ONE® | Planning Pro

Excellence, redefined

elekta.com

*Elekta ONE | Planning Pro includes Monaco and MIM software solutions. It may not be available for sale in all markets.
**Elekta data on file.
***Elekta data on file. Median of 180 seconds for full optimization calculated on a sample of >10 cases.

MEDICAL PHYSICS IN THE BALTIC STATES 17 (2025)

Proceedings of International Conference "Medical Physics 2025"
06-08 November 2025, Kaunas, Lithuania

EVALUATION AND ANALYSIS OF SECONDARY CANCER RISKS BASED ON IRRADIATION DOSES TO ORGANS AT RISK FOR HEAD AND NECK CANCER CASES

Sundus OSMAN[1], Shima IBNEDRESS[2], Esra YOSIEF[3], Kristina ŠUTIENĖ[1], Jurgita LAURIKAITIENĖ[1]
[1]Kaunas University of Technology; [2]AlneelainUniversity; [3]Khartoum Oncology Hospital
[1]sundousosman@gmail.com [2]shima.ibnedress@neelain.edu.sd [3]esrayahiayosif@gmail.com [1]kristina.sutiene@ktu.lt
[1]jurgita.laurikaitiene@ktu.lt

***Abstract*:** This study analysed demographic, anatomical, and clinical effects on irradiation doses of organs-at-risk (OARs) and secondary-cancer risk for head and neck cancer cases. It was found that the incidence was highest among men aged 60–69, while excess absolute risk (EAR) analysis revealed a higher long-term secondary-cancer risk in advanced disease. In addition, out-of-field doses were measured and analysed based on anthropomorphic phantom SHANE and compared to treatment planning system (TPS) calculations, using two different calculation algorithms AAA and Acuros XB. It was observed that both algorithms underestimated the peripheral dose by 4% to 57.1%, particularly at distances farther from the edge of the irradiation field.

Keywords: head and neck cancer, excess absolute risk (EAR), anthropomorphic phantom, out-of-field doses.

1. Introduction

Head and neck cancer (HNC) poses a significant public health challenge, with approximately 550,000 new cases and 300,000 deaths worldwide annually. These malignancies, originating from the oral cavity, pharynx, larynx, and salivary glands, are linked to high morbidity and mortality. The complexity of HNC treatment stems from the intricate anatomy of the head and neck region, where tumours are often near the vital organs affecting critical functions [1]. External beam radiation therapy is a cornerstone of HNC management, utilized in both curative and palliative settings. However, precision in dose calculation and delivery remains a critical concern [2], as treatment planning systems (TPSs) can show discrepancies from 30 % to 60 % in radiation doses calculations to organs at risk (OARs) (out-of-field doses), leading to potential overexposure of healthy tissues [3].

The unintended exposure of organs outside the treatment area raises concerns about long-term effects and secondary cancer risks. Evaluating patient-specific factors in secondary cancer risk, induced by irradiation of healthy tissues, becomes crucial for optimizing treatment plans and adapting dose constraints [4]. This study aims to evaluate the impact of patient-specific factors on secondary cancer risk for HNC, comparing 3D TPS Eclipse-calculated irradiation doses to organ-at -risk OARs with practical dosimetry measurements.

The specific objectives were as follows:

1. To analyse dosimetry data and evaluate the effects of gender, age, and disease stage on organ-at-risk (OAR) doses.
2. To estimate the excess absolute risk (EAR) of secondary cancer based on treatment planning system (TPS) data.
3. To measure out-of-field doses using a SHANE anthropomorphic phantom in conjunction with a 1D cylindrical ionization chamber.
4. To propose modifications to dose limitations to improve treatment safety.

2. Material and method

This study was conducted at the Hospital of Lithuanian University of Health Sciences Kaunas Clinics, Oncology Hospital.

2.1 Patient Cohort

The cohort included 118 head and neck cancer patients (21 females, 97 males), aged 40–80 years, treated between January 2022 and February 2025. Demographic, clinical, and treatment variables were recorded, including tumour location, stage, radiation doses, and organ-specific doses such as the oesophagus, spinal cord, and parotids. All treatments involved daily image guided radiotherapy (IGRT) using cone-beam computed tomography (CBCT).

2.2 Irradiation procedure

Irradiation was performed with a linear accelerator Halcyon (Varian) system (6 MeV FFF, 800 MU/min) with a dual-layer MLC for precise dose shaping with a daily image guidance via integrated kV-CBCT to ensure accurate patient's positioning.

2.3 Treatment Planning

Treatment plans were planned with TPS Eclipse using intensity-modulated radiation therapy (IMRT) and volumetric modulated arc therapy (VMAT) techniques. Target volumes and organs at risk (OARs) were delineated based on CT images. Dose constraints followed standard guidelines (RTOG and QUANTEC) (Table 1). Prescribed doses ranged from 50 Gy to 70 Gy, delivered over 25 or 35 fractions. Dose calculations employed two algorithms: AAA and Acuros XB, to evaluate differences in estimation of out-of-field dose.

Table 1. Dose constraints for organs at risk [5]

Organ at risk	Dose limitations, Gy
Oesophagus	*Dmean** < 30
Submandibular gland (left or right)	*Dmean* ≤ 35
Larynx	*Dmean* < 40
Oral cavity	*Dmean* ≤ 30
Parotid gland (left or right)	*Dmean* < 20
Both parotid glands (left and right)	*Dmean* ≤ 25
Spinal cord	*Dmax** ≤ 45
Brainstem	*Dmax* < 54
Thyroid	*Dmean* ≤ 40

**Dmean* – mean dose to the organ, *Dmax* – maximum dose to the organ.

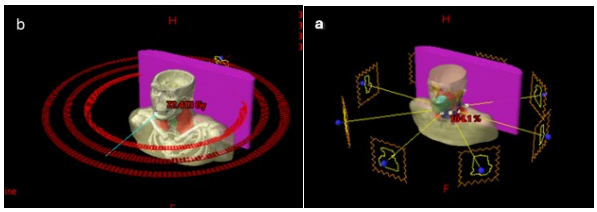

Fig. 1. Visualization of treatment planning techniques in Eclipse TPS: (a) IMRT plan, (b) VMAT plan

Treatment plans planned using the IMRT technique were based on specific angles (0°, 45°, 90°, 135°, 180°, 225°, 270°, 315°) and modulated intensity per irradiation field/beam, while VMAT plans were created using 2 or 3 full arcs (from 179° to 181° counter clockwise); in some specific cases, 2 or 3 partial arc strategies were used, depending on the patient's anatomy and tumour localization (Fig. 1).

2.4 Out-of-field Dose Measurement

Out-of-field doses were measured based on anthropomorphic phantom SHANE, which mimics head and neck anatomy (Fig.2).

2.5 Excess Absolute Risk (EAR) Estimation

The study employed the BEIR VII model (equation 1) to estimate EAR for secondary cancers, particularly focusing on the brainstem at 7 cm from the treatment field:

$$EAR = \beta_S D \exp(\gamma e^*)\left(\frac{a}{60}\right)^{\eta} \qquad (1)$$

D – dose [Sv], e – age at exposure [y], e^* – attained age [y], β_S – excess relative risk per sievert [EAR/Sv], γ and η being associated parameters for EAR/Sv.

Measurements were performed using cylindrical ionization chamber PTW 30013 and electrometer UNIDOS T10002, at 11 points along four channels, positioned at the distances from 0 cm to 22 cm per channels length (Fig.2). Calculated doses by TPS were compared with the measured doses.
Data from the four channels (measured and calculated via TPS) were scaled to a standard irradiation treatment plan (70 Gy total dose over 35 fractions). The EAR was adjusted using a linear dose-risk relationship, allowing the assessment of the impact of TPS underestimation on secondary cancer risk.

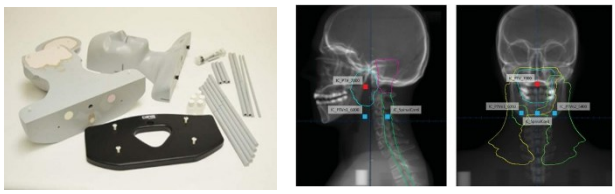

Fig. 2. Anthropomorphic phantom SHANE [7] and CT images of the phantom [8]

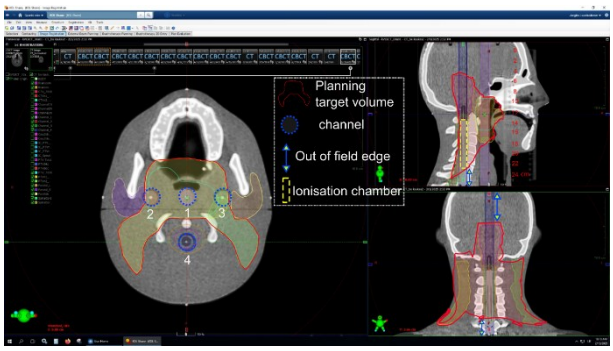

Fig. 3. Position of four channels and ionization chamber in a phantom

Table 2. Parameters in (BEIR VII model - Phase 2, table 12-2) [6]

Model parameter	Male	Female
β_S	0.85	1.35
η	0.18	0.18
γ	-0.14	-0.41

2.6. EAR estimation from measured out-of-field dose

To assess the impact of treatment planning system (TPS) dose underestimation on secondary cancer risk, the Excess Absolute Risk (EAR) model was employed. This analysis focused on the brainstem, a representative organ at risk (OAR), situated 7 cm from the edge of the treatment field. Dose measurements were obtained from channel 4 of the SHANE anthropomorphic phantom. Both TPS-calculated and physically measured doses were recorded using the Anisotropic Analytical

Algorithm (AAA) and Acuros XB (AXB) algorithms. To simulate a full course of treatment delivering 70 Gy to the primary field, doses per fraction were multiplied by 35 fractions. The EAR was adjusted using a linear dose-risk relationship, as follows:

$$Adjusted\ EAR = Baseline\ EAR \times \frac{Measured\ Dose}{TPS\ Dose} \quad (2)$$

This allowed quantification of EAR increase due to underestimation of out-of-field doses by TPS.

2.7 Statistical Analysis

Statistical analyses were performed using R statistical software (R Foundation for Statistical Computing, Vienna, Austria). A significance level of $p < 0.05$ was used for all statistical tests.

3. Results and discussion

3.1 Incidence of Head and Neck Cancer by Age, Gender, and Anatomical Site

This study identified a distinct age-related trend, with the highest incidence of HNC occurring in patients aged 60–69 years, representing 54.2 % of cases. This aligns with known epidemiological patterns linking increased age to prolonged carcinogenic exposure and declining immune function. The incidence was notably lower in the 40–49 age group (8.47 %), highlighting possibilities for early intervention through targeted screening and prevention (Fig. 4).

3.2 Influence of Age and Gender on Organ Radiation Doses

A pronounced gender disparity was observed, with males accounting for 82.2 % of cases compared to 17.8 % in females, likely reflecting differences in behavioural factors such as tobacco use and hormonal or genetic susceptibility. Anatomical site analysis revealed the oral cavity as the most affected region, with significant gender differences, followed by the oropharynx, larynx, and hypopharynx (Fig.5). These patterns are consistent with exposure to known risk factors such as tobacco and Human papillomavirus (HPV).

3.3 Effect of Tumour Stage and Location on EAR

The analysis revealed a progressive increase in the average EAR for second cancer development with advancing cancer stage. Stage IV patients, especially those with T4N1M0 classification, showed the highest average EAR (0.789) (Table 3). This indicates that more advanced and aggressive tumours are linked to a greater likelihood of secondary cancer development.

This variability indicated that while multiple patients may be at high risk due to similar treatment characteristics, some cases might have an elevated risk because of tumour-related factors or individual biological reactions to radiation. Thus, these findings emphasized the importance of individualized treatment approaches according to different stages of disease for enhancement of therapeutic effects and reduction of undesirable side effects. For example, patients with high-grade tumours may need closer surveillance and dose refinement for optimal outcome with the least toxicity (Fig. 6).

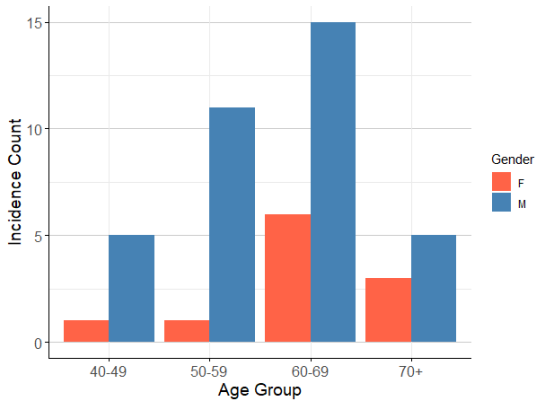

Fig.4. Head and neck cancer by age and gender

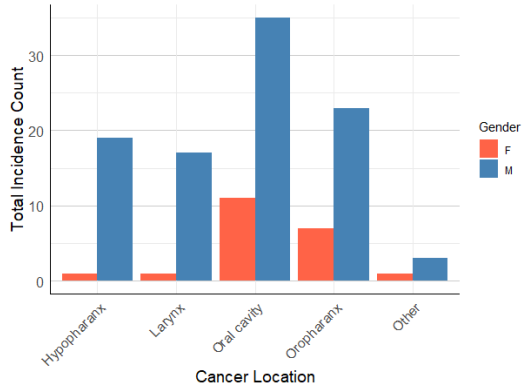

Fig. 5. Head and neck cancer incidence by anatomical sites and gender

Table 3. Mean Excess Absolute Risk (EAR) by disease stage

Stage	Mean_EAR	SD_EAR	Percentage of patients (%)
I	0.375	0.214	4.241
II	0.449	0.381	8.470
III	0.604	0.393	6.782
IV	0.789	0.512	55.931
X*	0.619	0.415	24.583

*X: Unknown primary tumours or classification when conventional staging is not applicable.

3.4 Out-of-field Dose Measurements

As outlined in the materials and methods section, dosimetry measurements with cylindrical ionization chamber were performed at 11 different points (in 2 cm step) along four defined channels (CH): CH1, CH2, CH3, and CH4 (Table 4 and Fig. 7).

Out-of-field doses were measured in a distance from the edge of the irradiation field (from 0 cm up to 7 cm), as imitating head and neck cancer irradiation procedure, longitudinal target with lymph nodes zone was equal to 12 cm. It is recommended to perform additional measurements imitating larger distances (>10 cm) from the edge of irradiation field. It was registered that for the maximum up to 7 cm distances from the irradiation field edge maximum percentage differences in a Channel 4 – blue was 51.1 % (AAA) and 57.1 % (Acuros XB – AC) (Fig. 8).

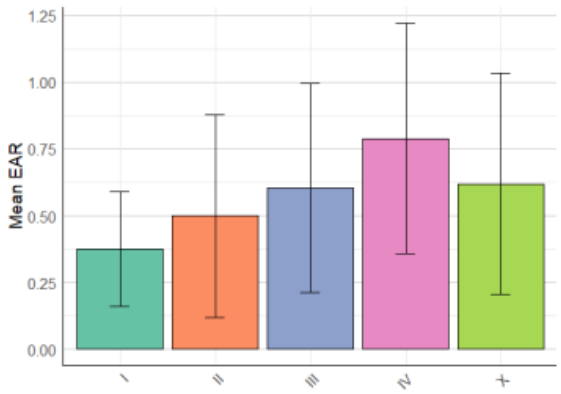

Fig. 6. Mean excess absolute risk by cancer stage

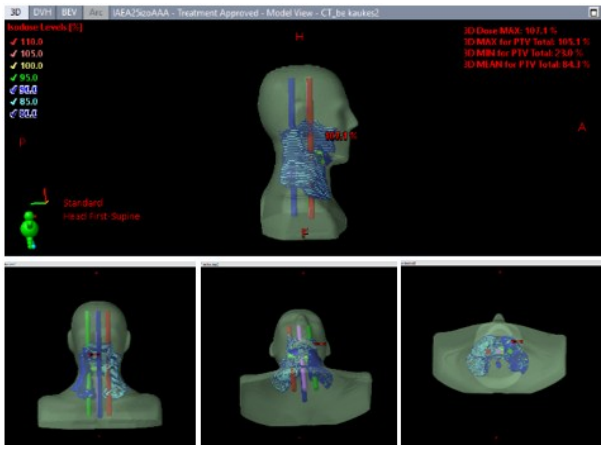

Fig. 7. Views of all the measurement channels (CH1 – purple; CH2 – red; CH3 – green; CH4 – blue) showed in different projections

Table 4. Absolute percentage error between measured and TPS calculated out-of-field doses using for the dose calculation AAA and Acuros XB algorithms throughout four anatomical channels

Position of ionization chamber in a CH, cm	CH1 - purple		CH2 - red		CH3 - green		CH4 - blue	
	Percentage difference (MD vs. TPS), %							
	AAA	AC	AAA	AC	AAA	AC	AAA	AC
0	42.3	41.4	46.4	44.0	44.9	41.1	51.1	57.1
2	19.0	24.0	17.6	20.0	22.2	20.9	28.9	26.8
4	16.3	17.4	16.5	17.2	14.7	10.6	25.9	18.9
6	13.4	15.3	7.6	15.6	16.4	11.4	10.0	19.4
8	4.3	13.7	3.4	6.1	5.5	2.7	7.9	5.3
10	0.6	2.5	1.5	3.6	0.2	1.2	3.3	1.5
12	1.5	2.1	2.0	9.0	5.7	2.6	4.3	7.3
14	2.1	11.2	3.9	8.4	0.5	3.6	16.6	21.3
16	6.4	11.9	0.8	3.0	3.1	3.8	13.4	21.6
18	2.5	8.2	2.3	7.2	0.1	1.6	14.6	12.2
20	2.9	9.5	5.8	5.4	0.7	0.4	8.5	12.9
22	2.6	10.0	4.8	4.1	0.3	1.4	13.3	23.4

Table 5. The EAR calculations for the brainstem (imitating the largest possible 7 cm distance from the irradiation field edge)

Parameter	AAA	AXB
TPS-calculated dose per 2 Gy fraction	0.13 Gy	0.15 Gy
Measured dose per 2 Gy fraction	0.16 Gy	0.18 Gy
TPS total dose over 35 fractions (70 Gy)	4.55 Gy	5.25 Gy
Measured total dose over 35 fractions (70 Gy	5.60 Gy	6.40 Gy
Baseline EAR	1.00	1.00
Adjusted EAR based on measured dose	1.28	1.23
Increase in EAR (%)	23 %	22 %

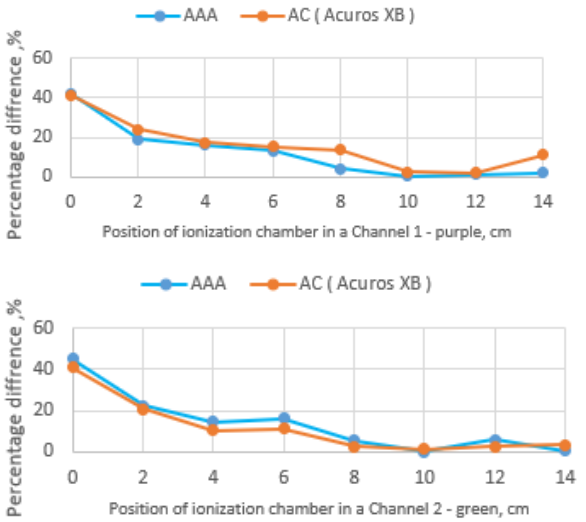

Fig. 8. Comparison of percentage differences for measured and treatment planning system (TPS) calculated out of-field doses using AAA and Acuros XB (AC) algorithms throughout Channel 1 and Channel 2.

These findings reveal a notable increase in Excess Absolute Risk (EAR) (23 % using the AAA algorithm and by 22 % using the Acuros XB (AXB) algorithm) due to the underestimation of out of field doses by the treatment planning system (TPS). This emphasizes the clinical significance of verifying out-of-field radiation doses through physical measurements, particularly for radiosensitive organs such as the brainstem.

Although the total accumulated dose to the brainstem in this scenario remains well below the widely accepted constraint of 54 Gy, such discrepancies could be more consequential for other organs at risk (OARs) or in different clinical contexts. Repeated underestimations across multiple treatment sessions or fields may result in cumulative doses that approach or exceed clinical tolerance limits, thereby elevating the risk of radiation-induced complications.

3.5 Clinical Implications and Recommendations

The experimental data demonstrate that treatment planning systems (TPS), particularly the Acuros XB algorithm, consistently underestimate out-of-field doses to organs located beyond 10 cm from the irradiation field edge. For example, underestimations reached up to 57.1 % in 4 (spinal cord region). These findings highlight the need to revise dose constraints for organs at risk (OARs) by including additional safety margins that reflect these systematic TPS limitations.

Out-of-field TPS-calculated doses should be complemented with direct measurements using ionization chambers or in vivo dosimeters particularly for radiosensitive, non-regenerative structures such as the spinal cord, parotid glands, thyroid, and gonads. This is especially important in paediatric, young adult (< 40 years), or long-term survivor populations, where the lifetime risk of secondary malignancy is a major clinical consideration. The use of anthropomorphic phantoms (e.g., SHANE) or in vivo tools ensures more accurate estimation of cumulative exposure, maintaining

compliance with evidence-based dose thresholds. TPS reliability for out-of-field dose estimation significantly decreases at distances beyond 10 cm from the field edge.

According to the measurements, percentage errors remain within 5–20 % up to 10 cm but increase dramatically (up to 23 %) beyond 18 cm, with trends indicating worsening accuracy with distance. Therefore, it is recommended to limit TPS-based dose calculations to within approximately 10 cm of the treatment field. For organs located further away, additional phantom-based dosimetry or Monte Carlo simulations should be employed to ensure accurate dose quantification and protect critical structures.

4. Conclusions

The estimated Excess Absolute Risk (EAR) increased progressively with advancing disease stage. Patients with Stage IV tumours and higher TNM classifications, particularly T4N1M0, exhibited the highest EAR values. Both the AAA and Acuros XB algorithms underestimated out-of-field doses, particularly at distances greater than 7 cm from the field edge, with discrepancies reaching up to 57.1%. These findings highlight the importance of incorporating phantom-based verification of out-of-field doses and further refining treatment planning system (TPS) algorithms. Moreover, clinical protocols should account for individual patient risk factors to minimize radiation-induced complications.

5. References

1. Marur S, Forastiere A.A.. Head and neck squamous cell carcinoma: update on epidemiology, diagnosis, and treatment. Elsevier Ltd; 2016.
2. Alterio D., Marvaso G., Ferrari A., Volpe S., Orecchia R., Jereczek-Fossa B.A.. Modern radiotherapy for head and neck cancer. W.B. Saunders; 2019.
3. Shine N.S., Paramu R., Gopinath M., Jaon Bos R.C., Jayadevan P.M.. Out-of-field dose calculation by a commercial treatment planning system and comparison by Monte Carlo simulation for Varian TrueBeam®. Journal of Medical Physics. 2019;44(3):156–175. DOI: 10.4103/jmp.JMP_82_18.
4. Pazzaglia S., Eidemüller M., Lumniczky K., Mancuso M., Ramadan R., Stolarczyk L., Moertl S.. Out-of-field effects: lessons learned from partial body exposure. Radiation and Environmental Biophysics. 2022;61(4):485–504. DOI: 10.1007/s00411-022-00988-0.
5. Bentzen S.M., Constine L.S., Deasy J.O., Eisbruch A., Jackson A., Marks L.B., Ten Haken R., Yorke E.D.. Quantitative analyses of normal tissue effects in the clinic (QUANTEC): an introduction to the scientific issues. International Journal of Radiation Oncology, Biology, Physics. 2010;76(3 Suppl): S1–S2. DOI: 10.1016/j.ijrobp.2009.09.040.
6. National Academies of Sciences, Engineering, and Medicine. Health risks from exposure to low levels of ionizing radiation: BEIR VII Phase 2. Washington, DC: The National Academies Press; 2006. ISBN 030909156X.
7. SHANE. Phantom Patient for VMAT-IMRT Verification.
8. Knapp P., Eva B., Reseigh G., Gibbs A., Sim L., Daly T., Cox J. and Bernard A.. The role of volumetric modulated arc therapy (VMAT) in gynaecological radiation therapy: A dosimetric comparison of intensity modulated radiation therapy versus VMAT. Journal of Medical Radiation Sciences, 66(1), 44–53, March 1, 2019. https://doi.org/10.1002/jmrs.311

MEDICAL PHYSICS IN THE BALTIC STATES 17 (2025)

Proceedings of International Conference "Medical Physics 2025"
06-08 November 2025, Kaunas, Lithuania

DOSIMETRIC IMPACT OF INTERFRACTIONAL ORGAN VARIATIONS IN CERVICAL CANCER IMRT: A CBCT-BASED REPLANNING STUDY

Hilolaknon ERKINOVA[1], Shirin ARSLONOVA[2], Diana ADLIENE[2]; Doniyor MUSAYEV[3], Satimboy POLVONOV[1]

[1] National University of Uzbekistan named after Mirzo Ulugbek; [2]Kaunas University of Technology; [3]Tashkent City Branch of Republican Specialized Scientific-Practical Medical Centre of Oncology and Radiology

[1]palvanov1960@gmail.com; [2]shirin.arslonova@ktu.lt; diana.adliene@ktu.lt; [3]doniyormuso199214@gmail.com

***Abstract*:** Interfractional variations of bladder and rectum volumes remain a major challenge in cervical cancer IMRT, as small margins make target coverage highly sensitive to anatomical changes. In this work, CBCT-based replanning was performed for ten patients (98 scans) to assess the dosimetric effects of such variations. It was found that CTV coverage decreased significantly (median $V_{98\%}$: 99.5% → 96.4%), while bladder and rectal doses increased with unstable filling patterns. Strong correlations were observed between bladder/rectal changes and dosimetric outcomes. Based on these findings, institutional protocols were developed for regional patient population, standardizing bladder volumes (120–150 cc) and rectal diameters (≤4.5–5.0 cm) to improve treatment consistency.

Keywords: IMRT; Cervical cancer, Interfractional organ motion; Cone-beam CT; Replanning.

1. Introduction

Radiotherapy (RT) remains one of the main treatment steps for cervical cancer, particularly in patients with locally advanced disease. In such a case, external beam radiotherapy (EBRT) combined with brachytherapy is delivered to treat patients [1, 2]. Modern techniques such as intensity-modulated radiotherapy (IMRT) and volumetric modulated arc therapy (VMAT) that enable highly conformal dose distributions and improved sparing of organs at risk (OARs) as compared with conventional three-dimensional conformal radiotherapy (3DCRT) can be used instead [2-5]. However, effectiveness of the modern techniques depends on the stability of pelvic anatomy, as smaller clinical target volume (CTV) compared to planning target volume (PTV) margins makes these approaches vulnerable to daily organ variations [6, 7]. Interfractional changes of bladder filling and rectal distension are recognized as the dominant sources of anatomical variability in pelvic radiotherapy. Several imaging studies using MRI and cone-beam CT (CBCT) have demonstrated that bladder filling can displace the uterus and cervix by more than a centimeter, while rectal distension is closely linked with cervix and vaginal motion [8, 9]. The uterus, in particular, is considerably more mobile than the cervix, with reported displacements up to several centimeters in extreme cases. These shifts may compromise target coverage or increase dose to the bladder and rectum [5,10,11]. To address this problem, adaptive strategies have been investigated. Offline replanning triggered by tumor regression has been shown to reduce hotspots and improve dose homogeneity while lowering rectal and bladder doses [12, 13]. Library-of-plans approaches allowed selection of the most appropriate plan for the anatomy of the day and have been validated as a robust alternative in clinical practice [14]. More recently, online adaptive radiotherapy (OART) guided by CBCT or MRI has demonstrated further improvements in CTV coverage and OAR sparing exploring artificial intelligence to automate plan selection and decision-making [15-19]. Although these strategies are promising their implementation is resource-intensive and not universally available.

In most clinical settings, bladder filling and rectal emptying protocols are routinely applied to reduce interfractional variability and ensure consistent CTV coverage [2, 9, 11, 20]. In the absence of preparation protocols, day-to-day variations in bladder and rectum volumes may lead to uncertainties in dose delivery. In 3DCRT, these are usually compensated by relatively large CTV-to-PTV margins of 1–1.5 cm, whereas in IMRT, where margins can be reduced to 5–7 mm, the impact of anatomical variability becomes more critical. To overcome these issues, CBCT-based dosimetric analysis with IMRT replanning was introduced, with the aim of evaluating the influence of bladder and rectum changes on target coverage and OAR doses and to support the development of protocols for routine clinical practice.

2. Methods and materials

2.1. Patient selection

This retrospective study included ten patients with cervical cancer treated with external beam radiotherapy at the Tashkent City Branch of the Republican Specialized Scientific and Practical Medical Center of Oncology and Radiology (RSSPMCOR). Patients were deliberately selected based on the largest interfractional anatomical variations observed during their original treatments, including marked differences in bladder filling, rectal diameter, and intrapelvic air content. At the time of treatment, no standardized bladder or rectum preparation protocols were in place. Consequently, three-dimensional conformal radiotherapy (3DCRT) was delivered with CTV-to-PTV margins of 1.0–1.5 cm, depending on the treatment machine, to compensate for these uncertainties.

2.2. Treatment planning

New IMRT plans were generated on the reference planning CT using the Monaco 5.11.03 treatment planning system (Elekta AB, Stockholm, Sweden). A uniform 7 mm margin was applied from CTV to PTV. Plans were created with a seven-field coplanar beam arrangement and optimized for adequate target coverage while respecting institutional clinical dose constraints protocol for organs at risk, including bladder, rectum, femoral heads and bowel (Table 2.1.). The prescription dose of 46 Gy was delivered in 23 fractions to the PTV.

Table 2.1. Planning objectives and organ-at-risk (OAR) dose constraints used for IMRT optimization.

Structure	Objective / Constraint
PTV	V95% ≥ 98%; V107% < 2%
CTV	V98% ≥ 98%; V100% ≥ 95%;
Bladder	V45Gy < 35%; Mean dose < 40 Gy
Rectum	V40Gy < 50%; Mean dose < 40 Gy
Bowel bag	V40Gy < 30%
Femoral heads	V40Gy < 40%; V45Gy < 25%

2.3. Imaging, contouring and dose recalculation

For each patient, cone-beam CT (CBCT) scans acquired during treatment were imported back into the Monaco 5.11.03 treatment planning system. Between 8 and 13 CBCTs were available per patient, giving a total of 98 scans, as offline IGRT protocol included daily CBCTs during the first four fractions and weekly imaging thereafter, provided no major positioning issues were observed. All scans were obtained on an Elekta Synergy XVI imaging system (Elekta AB, Stockholm, Sweden).
On each CBCT, the following structures were recontoured:

1) Bladder (whole organ)
2) Rectum (outer wall)
3) CTV (cervix and uterus)
4) Intrapelvic air (visible gas pockets in the intestines).

Contouring was performed by a single observer to maintain consistency and reduce inter-observer variation. The IMRT plan generated on the reference planning CT was then recalculated on each CBCT dataset without re-optimization or modification of beam parameters. This allowed assessment of dose distribution under the anatomical conditions of each treatment fraction.

2.4. Data analysis

Bladder volume (cc), rectal maximum anterior–posterior diameter (cm), and intrapelvic air volume (cc) from the reference CT, were recorded, and the same parameters were extracted from each CBCT to quantify anatomical changes.
CTV coverage was assessed using $V_{95\%}$, $V_{98\%}$, and $V_{100\%}$. For OARs, bladder (V_{30Gy}, V_{40Gy}, V_{46Gy}) and rectum (V_{30Gy}, V_{40Gy}, V_{46Gy}) dose–volume parameters were evaluated.
Comparisons between reference CT values (hypothesized mean, μ_0) and CBCT-based recalculated values were performed using a one-sample t-test:

$$t = \frac{\bar{x}-\mu_0}{s/\sqrt{n}} \quad (1)$$

where $\bar{x}$ is mean of CBCT values of the sample, s is the sample standard deviation, and n is the number of CBCTs. A p-value<0.05 was considered statistically significant.
To further explore the relationships between anatomical changes and dosimetric outcomes, patients were divided into three groups based on the parameters that showed the most significant deviations from the reference values:

I. Patients with marked variations in bladder volume.
II. Patients with pronounced changes in the maximum anterior–posterior rectal diameter.
III. Patients with notable increases in intrapelvic air volumes adjacent to the CTV.

Within each group, the relationship between the dominant anatomical parameter (bladder volume, rectal diameter, or air volume) and the corresponding dosimetric metrics (*CTV* $V_{95\%}$, $V_{98\%}$, $V_{100\%}$; *bladder* V_{30Gy}, V_{40Gy}, V_{46Gy}; *rectum* V_{30Gy}, V_{40Gy}, V_{46Gy}) was evaluated using Spearman's rank correlation coefficient *(ρ)*. Correlation strength was interpreted as:
- weak ($|\rho| \leq 0.39$);
- moderate ($0.4 \leq |\rho| \leq 0.59$);
- strong ($|\rho| \geq 0.6$);

A correlation was considered significant at $p < 0.05$.

3. Results and discussions

All IMRT plans fulfilled the predefined target coverage and OAR dose constraints. Median CTV $V_{98\%}$ and $V_{100\%}$ on the reference plans were *99.5%* and *96.0%*, respectively, with PTV $V_{95\%}$ exceeding *98%* in all patients. Mean bladder and rectum doses remained below *40 Gy*, with bladder $V_{45Gy} < 30\%$ and rectum $V_{40Gy} < 45\%$, while bowel and femoral head doses stayed within clinical tolerance. (Fig. 3.1).

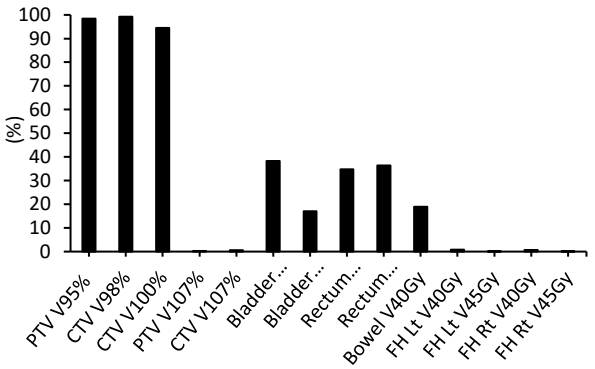

Fig. 3.1. Dose–volume parameters for IMRT reference plans. Mean values of the target coverage metrics (CTV and PTV), and mean values the organ-at-risk (OAR) dose metrics.

Bladder volumes demonstrated considerable variability across patients, with treatment values ranging from *29 cc* to *386 cc*. Moreover, a progressive reduction in the mean bladder volume was observed across the treatment course, decreasing from approximately *100–200 cc* at fractions 7–10 to around *50-100 cc* by fractions 15–23 (Fig.3.2).

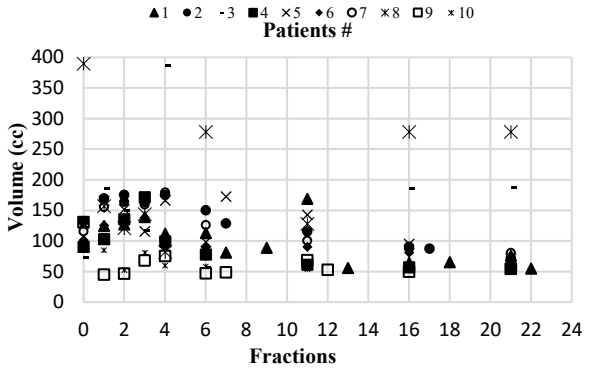

Fig. 3.2. Bladder volume variations across treatment fractions for all 10 patients.

The largest and most significant deviations from reference volumes ($p < 0.05$) were observed in patients 3, 8, 9, and 10, indicating unstable bladder filling and poor reproducibility that may compromise IMRT delivery (Table 3.1 and Fig.3.3).

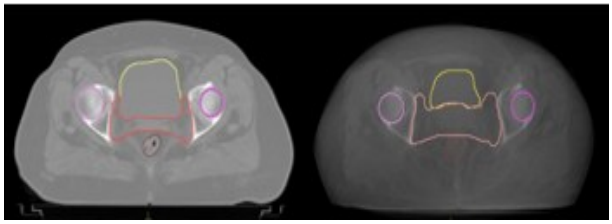

Fig. 3.3. Example from patient #8. The left image shows the original CT plan, and the right image shows CBCT the 11th treatment fraction. A marked reduction in bladder volume can be observed, which consequently affected the shape and position of the CTV.

The maximum rectal diameter in the anterior–posterior direction ranged from *2.0 cm* to *6.1 cm* across patients, but after the 11th fraction values were mostly stabilized around *3–4.5 cm* (Fig. 3.4.). Significant increases compared to the reference CT ($p < 0.05$) were observed in patients 1-7, and 9, reflecting pronounced distension. Stable diameters without significant deviations were found in patients 8 and 10 (Table 3.2).

Table 3.1. Bladder volume variations across patients based on CBCT imaging.

Bladder						
Patient	No of CBCT	Ref. volume (cc)	Median volume CBCT (cc)	Min. volume CBCT (cc)	Max. volume CBCT (cc)	t-test p value
1	13	89.99	88.37	35.59	168.86	0.33
2	10	131.50	139.60	71.01	175.10	0.49
3	8	73.26	173.20	56.13	386.34	<0.05
4	11	90.10	88.37	54.83	171.30	0.28
5	9	127.96	142.57	70.86	172.46	0.37
6	10	101.20	90.43	60.10	165.00	0.39
7	11	115.30	142.57	80.11	179.30	0.15
8	8	389.56	150.04	81.92	278.01	<0.05
9	10	130.16	50.41	29.59	74.82	<0.05
10	8	89.62	56.42	42.16	84.88	<0.05

Table 3.2. Rectum's maximum diameter variations in anterior-posterior direction across patients based on CBCT imaging.

Rectum						
Patient	No of CBCT	Ref. diameter (cm)	Median diameter CBCT (cm)	Min. diameter CBCT (cm)	Max. diameter CBCT (cm)	t-test p value
1	13	5.72	4.37	3.78	5.57	<0.05
2	10	3.45	4.08	3.37	5.83	<0.05
3	8	3.70	3.35	3.25	3.64	<0.05
4	11	6.22	4.87	4.28	6.07	<0.05
5	9	3.61	3.82	3.41	5.72	<0.05
6	10	5.49	4.74	4.10	6.10	<0.05
7	11	2.78	3.78	2.65	5.61	<0.05
8	8	3.79	3.88	2.66	3.94	0.25
9	10	2.18	2.44	2.00	2.76	<0.05
10	8	3.06	3.06	3.01	3.15	0.29

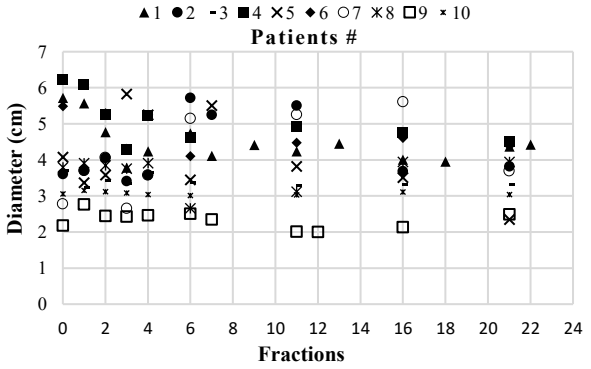

Fig. 3.4. The maximum rectal diameter in the anterior–posterior direction variations across treatment fractions for all 10 patients.

Intrapelvic air volumes varied widely, ranging from almost negligible levels to *178 cc* (Table 3.3). Apart from patients 4 and 6, all other patients showed significant deviations from reference CT values ($p < 0.05$).
CBCT-based recalculations showed systematically lower CTV coverage compared with the original CT plans as shown in Fig.3.5, with significant reductions in $V_{95\%}$, $V_{98\%}$, and $V_{100\%}$ across nearly all patients ($p < 0.05$).

Table 3.3. Intrapelvic air volumes variations across patients based on CBCT imaging.

Intrapelvic gas volume						
Patient	**No of CBCT images**	**Ref. volume (cc)**	**Median volume CBCT (cc)**	**Min. volume CBCT (cc)**	**Max. volume CBCT (cc)**	**t-test p value**
1	13	66.63	10.39	1.30	159.70	<0.05
2	10	0.80	8.15	1.10	42.30	<0.05
3	8	294.50	99.14	2.03	178.02	<0.05
4	11	25.31	10.39	1.30	85.30	0.21
5	9	0.20	14.84	1.92	51.57	<0.05
6	10	15.30	11.09	0.55	65.30	0.37
7	11	0.31	12.11	0.21	62.91	<0.05
8	8	103.44	10.03	0.21	48.77	<0.05
9	10	62.94	33.46	0.54	85.89	<0.05
10	8	122.80	48.64	0.32	135.95	<0.05

Median CTV $V_{98\%}$ dropped from *99.48%* to *96.41%*, and $V_{100\%}$ from *95.96%* to *92.12%*

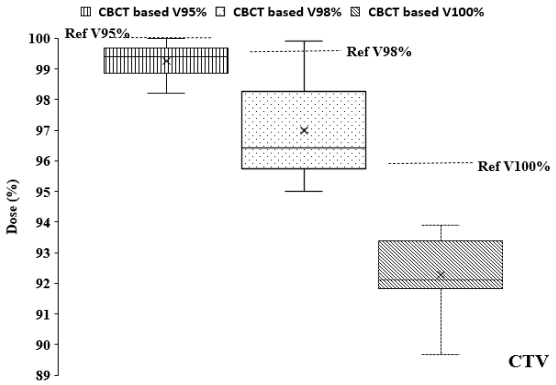

Fig. 3.5. Boxplots of CBCT-based dose coverage for the CTV ($V_{95\%}$, $V_{98\%}$, *and* $V_{100\%}$) across 10 patients. Median values from the original CT plans are shown as dashed reference lines.

In addition to target coverage, recalculations were made to assess interfractional dose variations in OARs.
For the bladder, CBCT-based recalculations showed pronounced inter-patient variability, with significant increases in the median value of V46Gy, while changes in median V40Gy and V30Gy were less pronounced (Fig.3.6.).

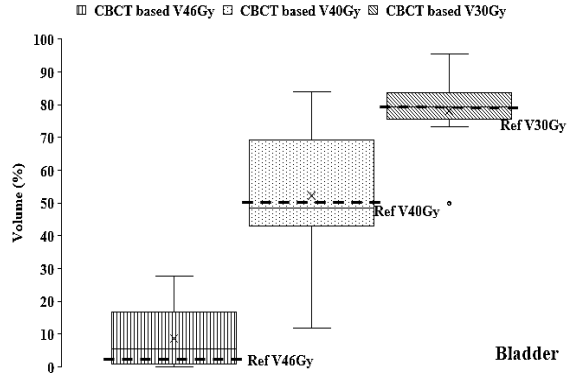

Fig. 3.6. Boxplots of CBCT-based bladder dose distributions for V_{46Gy}, V_{40Gy}, and V_{30Gy} across 10 patients. Boxes represent median values of CBCT-based recalculated doses. Median values from the original CT plans are shown as dashed reference lines.

However, individual patient assessments revealed inconsistent patterns. For example, in patient 3, V_{46Gy} increased from *0.2%* to *26.6%* and V_{40Gy} from *80%* to *83%*, whereas in patient 5, V_{46Gy} decreased from *20.8%* to *6.35%* and V_{40Gy} from *62.1%* to *43.9%.*

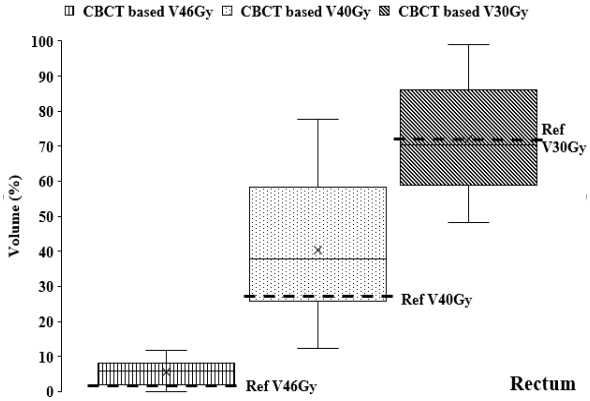

Fig. 3.7. Boxplots of CBCT-based rectal dose distributions for V_{46Gy}, V_{40Gy}, and V_{30Gy} across 10 patients. Boxes represent median values of CBCT-based recalculated doses. Median values from the original CT plans are shown as dashed reference lines.

For the rectum, median doses varied considerably, with median of V_{46Gy} rising up from *0.9%* to *~5.9%* and V_{40Gy} shifting between *28–37%*, reflecting the strong influence of interfractional rectal filling and motion. (Fig.3.7). Patient-specific values also varied considerably. For instance, in patient 1, V_{40Gy} decreased from *26.3%* to *12.4%* and V_{30Gy} from *60.6%* to *48.3%.* Examination of the CBCT structures showed that the rectum's anterior–posterior maximum diameter was reduced across fractions compared with the planning CT.
To investigate the interrelation of the results, Spearman correlation analysis (as mentioned in Methods) was used to explore the relationship between anatomical variations and dosimetric outcomes.

3.1. Patients with marked variations in bladder volume.

Bladder volume variations showed strong correlations with CTV coverage (ρ *= 0.74–0.98 for* $V_{98\%}$ *and* ρ *= 0.71–1.0 for* $V_{100\%}$) as well as bladder dose metrics in most patients, highlighting the impact of bladder filling on target coverage and OAR sparing (Table 3.4. and Fig.3. 8).

Table 3.4. Spearman correlation coefficients of Bladder volume (B-Vcc) vs. CTV and Bladder dose metrics.; *p < 0.05.

# **P-nt**	***Spearman correlation coefficient*** ***ρ*** ***weak (|ρ| ≤ 0.39);*** ***moderate (0.4 ≤ |ρ| ≤ 0.59);*** ***strong (|ρ| ≥ 0.6);***				
	B-V_{cc} vs CTV $V_{98\%}$	**B-V_{cc} vs CTV $V_{100\%}$**	**B-V_{cc} vs B-V_{45Gy}**	**B-V_{cc} vs B-V_{40Gy}**	**B-V_{cc} vs B-V_{30Gy}**
3	0.787*	0.711*	0.933*	0.361	0.008
7			0.709*	0.891*	0.903*
8	0.748*	0.244	-0.312	0.109	0.361
9	0.855*	0.791*	-0.526	0.236	0.436
10	0.983*	1*	0.683*	0.283	0.35

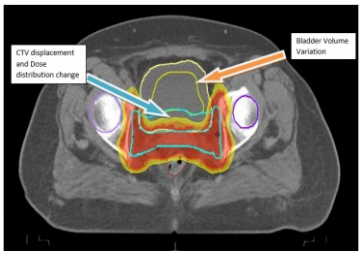

Fig. 3.8. Axial CT slice illustrating the effect of bladder volume variation on CTV displacement and dose distribution.

3.2. Patients with pronounced changes in the maximum anterior–posterior rectal diameter

Changes in the anterior–posterior rectal diameter showed significant positive correlations with both CTV coverage (ρ = *0.65–0.79*) and rectal dose metrics (ρ up to *0.92*), indicating that rectal distension directly influences target coverage and rectal dose distribution (Table 3.5.).

Table 3.5. Spearman correlation coefficients of Rectum's maximum diameter in A-P direction (B-Dcm) vs. CTV and Rectum dose metrics. *p < 0.05.

# P-nt	*Spearman correlation coefficient ρ weak (|ρ| ≤ 0.39); moderate (0.4 ≤ |ρ| ≤ 0.59); strong (|ρ| ≥ 0.6);*				
	R-D_{cm} vs CTV $V_{98\%}$	**R-D_{cm} vs CTV $V_{100\%}$**	**R-D_{cm} vs R-V_{46Gy}**	**R-D_{cm} vs R-V_{40Gy}**	**R-D_{cm} vs R-V_{30Gy}**
1	0.715*	0.689*	0.376	0.605*	0.719*
4	0.655*	0.213*	0.289	0.714*	0.567*
6	0.756*	0.791*	0.436*	0.283*	0.350*
7			0.697*	0.915*	0.661*
8			0.776*	0.777*	0.489*

3.3. Patients with notable increases in intrapelvic air volumes adjacent to the CTV

Intrapelvic air volumes demonstrated only moderate correlations with CTV $V_{95\%}$ but strong correlations with CTV $V_{98\%}$ (ρ = *0.82–0.92*) (Table 3.6), indicating that their dosimetric impact becomes significant mainly when gas pockets are located adjacent to the CTV in the rectum, where they alter its diameter and displace the target.

Table 3.6. Spearman correlation coefficients of in intrapelvic air volumes (A-Vcc) vs. CTV. *p < 0.05.

# P-nt	*Spearman correlation coefficient ρ weak (|ρ| ≤ 0.39); moderate (0.4 ≤ |ρ| ≤ 0.59); strong (|ρ| ≥ 0.6);*	
	A-V_{cc} vs CTV $V_{98\%}$	**A-V_{cc} vs CTV $V_{98\%}$**
2	0.413*	0.821*
5	0.394	0.915*
7	0.215	0.892*

CBCT-based analysis confirmed that interfractional bladder and rectal variations can significantly compromise CTV coverage and OAR sparing in IMRT for cervical cancer. Since the dose gradient in IMRT decreases rapidly outside the PTV, maintaining consistent organ volumes, as defined during CT simulation, is essential to ensure adequate target coverage and protection of surrounding organs.

Reductions in median CTV $V_{98\%}$ (*–3%*) and $V_{100\%}$ (*–4%*) across patients are consistent with previous MRI and CBCT studies, which showed that bladder filling variability can displace the uterus by up to *4–6 cm* and directly reduce dose coverage [6, 7]. Similarly, we observed strong correlations (ρ *>0.7*) between rectal distension and both CTV underdosage and increased rectal dose, in agreement with Heijkoop et al. [8] and Eminowicz et al. [9], who identified rectal diameter *>4 cm* as a predictor of cervix displacement.

Compared to planning CT, bladder V_{46Gy} rose by up to *27%* and rectal V_{40Gy} exceeded *70%* in some fractions, highlighting the limitations of uniform *7 mm* margins under variable anatomy. Similar dosimetric impacts of organ filling were recently reported by Koca et al. [11] and Liu et al. [12]. Adaptive approaches, including plan libraries and daily online ART [12-19], have demonstrated improved coverage and OAR sparing, suggesting that such strategies would benefit patients with unstable anatomy as in our cohort. This is especially critical in cervical cancer, where EBRT is routinely followed by brachytherapy, and excessive bladder or rectal doses during the external phase may limit the safe delivery of the brachytherapy boost [2]. Nevertheless, this study is limited by the relatively small cohort size and by the use of recalculated, non-reoptimized IMRT plans, which may underestimate the potential benefits of adaptive strategies.

4. Conclusions

Interfractional bladder and rectal variations were shown to compromise CTV coverage and increase OAR doses in cervical cancer IMRT. Based on these findings, developed institutional protocols were developed to maintain bladder volumes around *120–150 cc* and to limit rectal diameters to *≤4.5–5.0 cm*, aiming to reduce variability in future treatments. Daily IGRT was recommended to ensure treatment accuracy, particularly for high-dose IMRT, SIB, or EBRT–brachytherapy schedules. In cases where internal organs systematically change toward a consistent but altered size or shape, replanning should be considered to preserve target coverage and OAR sparing.

5. References

1. Pötter, R., Tanderup, K., Kirisits, C., de Leeuw, A., Kirchheiner, K., Nout, R., Tan, L. T., Haie-Meder, C., Mahantshetty, U., Segedin, B., Hoskin, P., Bruheim, K., Rai, B., Huang, F., van Limbergen, E., Schmid, M., Nesvacil, N., Sturdza, A., Fokdal, L., … Jürgenliemk-Schulz, I. (2018). The EMBRACE II study: The outcome and prospect of two decades of evolution within the GEC-ESTRO GYN working group and the EMBRACE studies. In Clinical and Translational Radiation Oncology (Vol. 9, pp. 48–60). Elsevier Ireland Ltd. https://doi.org/10.1016/j.ctro.2018.01.001

2. Gazsi, I., & Marcu, L. G. (2025). Comparative dosimetric assessment of combined treatment modalities in cervical cancer radiotherapy for optimal organ protection. Radiation and Environmental Biophysics, 64(2), 291–302. https://doi.org/10.1007/s00411-025-01113-7

3. Agrawal A, Hadi R, Rath S, et al. Dosimetric comparison of 3-dimensional conformal radiotherapy (3D-CRT) and volumetric-modulated arc therapy (VMAT) in locally advanced cancer cervix.

Journal of Radiotherapy in Practice. 2022;21(1):60-67. doi:10.1017/S1460396920000849
4. Patil, D. B., Zope, M. K., & Singh, D. (2025). Dosimetric Comparison of 3DCRT, IMRT, and Rapid Arc Treatment Techniques in Cervical Cancer: Evaluating Plan Quality and Organ at Risk Sparing. Mapan - Journal of Metrology Society of India, 40(2), 409–419. https://doi.org/10.1007/s12647-024-00797-4
5. Li, M., Wu, X., Liu, X., & Wen, M. (2025). Effects of intensity-modulated radiotherapy (IMRT) and volumetric modulated arc therapy (VMAT) on survival benefits and poor prognostic factors in patients with cervical cancer. BioMedical Engineering OnLine, 24(1). https://doi.org/10.1186/s12938-025-01433-1
6. Jadon, R., Pembroke, C. A., Hanna, C. L., Palaniappan, N., Evans, M., Cleves, A. E., & Staffurth, J. (2014). A Systematic Review of Organ Motion and Image-guided Strategies in External Beam Radiotherapy for Cervical Cancer. Clinical Oncology, 26(4), 185–196. https://doi.org/10.1016/j.clon.2013.11.031
7. Chan, P., Dinniwell, R., Haider, M. A., Cho, Y. bin, Jaffray, D., Lockwood, G., Levin, W., Manchul, L., Fyles, A., & Milosevic, M. (2008). Inter- and Intrafractional Tumor and Organ Movement in Patients with Cervical Cancer Undergoing Radiotherapy: A Cinematic-MRI Point-of-Interest Study. International Journal of Radiation Oncology Biology Physics, 70(5), 1507–1515. https://doi.org/10.1016/j.ijrobp.2007.08.055
8. Eminowicz, G., Motlib, J., Khan, S., Perna, C., & McCormack, M. (2016). Pelvic Organ Motion during Radiotherapy for Cervical Cancer: Understanding Patterns and Recommended Patient Preparation. Clinical Oncology, 28(9), e85–e91. https://doi.org/10.1016/j.clon.2016.04.044
9. Heijkoop, S. T., Langerak, T. R., Quint, S., Mens, J. W. M., Zolnay, A. G., Heijmen, B. J. M., & Hoogeman, M. S. (2015). Quantification of intra-fraction changes during radiotherapy of cervical cancer assessed with pre- and post-fraction Cone Beam CT scans. Radiotherapy and Oncology, 117(3), 536–541. https://doi.org/10.1016/j.radonc.2015.08.034
10. Collen, C., Engels, B., Duchateau, M., Tournel, K., de Ridder, M., Bral, S., Verellen, D., & Storme, G. (2010). Volumetric imaging by megavoltage computed tomography for assessment of internal organ motion during radiotherapy for cervical cancer. International Journal of Radiation Oncology Biology Physics, 77(5), 1590–1595. https://doi.org/10.1016/j.ijrobp.2009.10.021
11. Koca, T., Aksoy, R. A., Atak, E., Kizilkaya, M., Bilek, Y., Tunçel, N., Sarpün, İ. H., & Korcum, A. F. (2025). Evaluation of the Dosimetric Effects of Bladder and Rectum Filling in Patients with Gynecologic Cancer Receiving Adjuvant Radiotherapy. Turk Onkoloji Dergisi, 40(1), 11–19. https://doi.org/10.5505/tjo.2024.4429
12. Liu, X., Tian, W., Dai, A., Li, H., Zhu, M., Zeng, M., Feng, R., Zhang, Z., Jiang, X., Wen, Y., Wu, T., & Xiao, Z. (2025). A comparative analysis of toxicity and treatment outcomes of adaptive radiotherapy and intensity-modulated radiotherapy in cervical cancer. Scientific Reports, 15(1). https://doi.org/10.1038/s41598-024-85074-9
13. Tian, W., Du, Y., Zhou, P., Ren, H., Wen, Y., Li, S., Dong, W., Wang, H., Wu, Z., Wu, T., & Xiao, Z. (2025). Dosimetric evaluation of image-guided adaptive radiotherapy for locally advanced cervical cancer. Medicine (United States), 104(17). https://doi.org/10.1097/MD.0000000000042280
14. de Hond, Y. J. M., van Haaren, P. M. A., Verrijssen, A. S. E., Tijssen, R. H. N., & Hurkmans, C. W. (2025). Dosimetric evaluation of variation in Library of plans selection for cervical cancer radiotherapy. Radiotherapy and Oncology, 206. https://doi.org/10.1016/j.radonc.2025.110835
15. Manea, E., Anghel, B., Stanescu, A. D., Rata, A. M., Gafton, B., & Scripcariu, V. (2025). Adaptive Target Volume and Dosimetry in Image-Guided Radiotherapy for Cervical Cancer. Journal of Clinical Medicine, 14(10). https://doi.org/10.3390/jcm14103418
16. Yen, A., Zhong, X., Lin, M. H., Nwachukwu, C., Albuquerque, K., & Hrycushko, B. (2024). Improved Dosimetry with Daily Online Adaptive Radiotherapy for Cervical Cancer: Waltzing the Pear. Clinical Oncology, 36(3), 165–172. https://doi.org/10.1016/j.clon.2024.01.005
17. Shelley, C. E., Bolt, M. A., Hollingdale, R., Chadwick, S. J., Barnard, A. P., Rashid, M., Reinlo, S. C., Fazel, N., Thorpe, C. R., Stewart, A. J., South, C. P., & Adams, E. J. (2023). Implementing cone-beam computed tomography-guided online adaptive radiotherapy in cervical cancer. Clinical and Translational Radiation Oncology, 40. https://doi.org/10.1016/j.ctro.2023.100596
18. Jiang, D., Yang, C., Sun, S., Wang, D., Xiao, Z., Hu, J., Mei, Z., Xie, C., Liu, H., Qiu, H., & Wang, X. (2024). First implementation and results of online adaptive radiotherapy for cervical cancer based on CT-Linac combination. Frontiers in Oncology, 14. https://doi.org/10.3389/fonc.2024.1399468
19. Sun, S., Gong, X., Cheng, S., Cao, R., He, S., Liang, Y., Yang, B., Qiu, J., Zhang, F., & Hu, K. (2025). Fully Automated Online Adaptive Radiation Therapy Decision-Making for Cervical Cancer Using Artificial Intelligence. International Journal of Radiation Oncology Biology Physics, 122(4), 1012–1021. https://doi.org/10.1016/j.ijrobp.2025.04.012
20. Liu, H., Zhang, Z., Guo, X., Wang, T., Hu, J., Shao, J., Chi, F., & He, H. (2025). The Effect of Bladder and Rectum Volume Changes on Exposed Organ Volume During Intensity-Modulated Radiotherapy for Cervical Cancer. Clinical Medicine Insights: Oncology, 19. https://doi.org/10.1177/11795549251377910

MEDICAL PHYSICS IN THE BALTIC STATES 17 (2025)

Proceedings of International Conference "Medical Physics 2025"
06-08 November 2025, Kaunas, Lithuania

DEVELOPMENT OF RECOMMENDATIONS FOR THE QUALITY CONTROL OF MAGNETIC RESONANCE IMAGING IN LITHUANIAN HEALTH CARE INSTITUTIONS

Guste LAURIKAITYTE[1], Romualdas GRIŠKEVIČIUS[2], Marius BURKANAS[2], Marius LAURIKAITIS[3]
[1]Kaunas University of Technology [2]National Cancer Institute, Medical Physics Department, Vilnius, Lithuania
[3]Hospital of Lithuanian University of Health Sciences Kaunas Clinics, Oncology Hospital
[1]guste@medicinosfizika.lt [2]romualdas.griskevicius@nvc.santa.lt [2]marius.burkanas@nvc.santa.lt
[3]marius@medicinosfizika.lt

***Abstract*:** This research is aimed at creating and validating a magnetic resonance imaging (MRI) quality control (QC) protocol which can be used in Lithuanian clinical environments. The investigation relies on the phantom based QC measurements performed evaluating three MRI scanners: Siemens Magnetom Skyra (3T), Siemens Magnetom Altea (1.5T), and Philips Ingenia Prodiva (1.5T). Following phantom based QC tests have been performed: measurements of signal-to-noise ratio (SNR), image uniformity (PIU), geometric distortion, low-contrast detectability and high-contrast spatial resolution. The obtained results matched with American QC standards showing just minor variations among devices and sequences. This allowed prepare the unified recommendations for the creation of national MRI QC protocol. The implementation of such protocol would lead to the uniform requirements for image quality, diagnostic dependability and better patient protection throughout the country.

Keywords: magnetic resonance imaging, quality control.

1. Introduction

The diagnostic field of modern medicine relies heavily on Magnetic Resonance Imaging (MRI) because it creates comprehensive three-dimensional images of soft tissues using non-ionizing radiation technologies [1]. Due to the complexity and sensitivity of new technologies, MRI quality and consistency is very important step. Quality control (QC) in MRI involves periodic performance assessments through standardized test phantoms together with image quality metrics including signal-to-noise ratio (SNR), percent image uniformity (PIU), ghosting and geometric accuracy. The quality measures serve to detect system deterioration while enabling hardware component calibration and image quality optimization throughout time. The American College of Radiology (ACR) together with the American Association of Physicists in Medicine (AAPM) and the International Electrotechnical Commission (IEC) have established worldwide standards for QC practices through their guidelines [2, 3]. In Lithuania, currently there is no official national standards for MRI quality control except for annual service engineer inspections. The absence of structured QC programs in many facilities usually lead to suboptimal imaging and undetected system malfunctions and inconsistent diagnostic performance [4].

2. Material and method

2.1 MRI systems

Parameters of 3 MRI scanners used in Lithuania and their imaging data were analysed while developing recommendations for MRI quality assurance and quality control: Siemens Magnetom Skyra (Siemens Healthcare, Germany) a 3T MRI, Siemens Magnetom Altea (Siemens Healthcare, Germany) a 1.5T MRI and Philips MR Ingenia Prodiva (Philips, Netherlands) a 1.5T MRI.

2.2 Phantoms

All scanners employ plastic bottle phantoms. Siemens 3 and 1.5T use several bottle shapes filled with $NiSO_4 \cdot 6H_2O$ + NaCl to adjust relaxation and conductivity. Philips 1.5T uses a single bottle with "Phantom liquid 13" (Fig. 1A). These are appropriate for weekly QC (SNR, PIU, ghosting), but not for complete monthly/annual QC (geometric accuracy, high-contrast SR, low-contrast detectability), which necessitates an ACR-type phantom. In this work home-made spherical ACR style phantom with a 20 cm diameter was used to enable more detailed MRI quality

control assessments (Fig. 1B). 3D printed polylactic acid (PLA) phantom was filled with aqueous nickel chloride and sodium chloride water solution, to adjust the relaxation time of water hydrogen and to mimic tissue-like signal properties. This home-made phantom consists of several dedicated test structures designed to evaluate key aspects of image quality:

- Uniformity/SNR/ghosting – phantom middle part with no internal structures.
- Geometric grid – 160 squares, 10×10 mm, 2 mm border (Fig. 1D).
- Low-contrast detectability - 6 groups × 5 cylinders (Ø 2–10 mm), depths 0.25–2 mm (Fig. 1E).
- High-contrast spatial resolution plate – 1–6 lp/cm, parallel sets for phase/frequency directions (Fig. 1F).

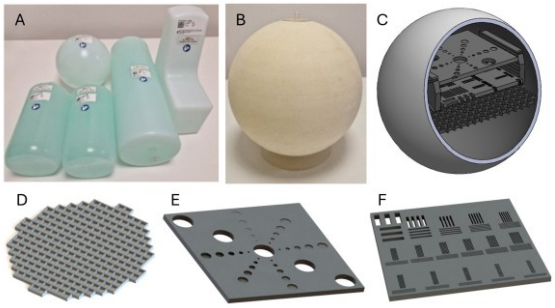

Fig. 1. Bottle (A) and home-made ACR phantom (B). 3D Computer-aided design (CAD) (C) with its structure: geometric distortions measurements grid (D), structure for low-contrast detection (E) and spatial resolution measurement structure (F)

2.3 Scanning protocol parameters

Bottle and ACR phantoms were scanned using head coil. Weekly bottle scans were done, for all MRI machines, using T_1, T_2 sequences and echo planar imaging (EPI). SNR and PIU were retrieved from T_1 and T_2 measurements. Parameters used for weekly bottle scans were:

- Siemens Magnetom Skyra (3T).
  Axial T_1 SE - TR/TE 600/20 ms, flip angle (FA) 90°, field of view (FOV) 250 mm, matrix 256 (phase), 27 slices, slice 5 mm with 6.5 mm spacing, bandwidth (BW) 250 Hz/px, phase encoding direction R→L.
  Axial T_2 SE - TR/TE 6000/100 ms, FA 150°; geometry/BW/phase as above; 27 slices.
- Siemens Magnetom Altea (1.5T).
  Axial T_1 SE - TR/TE 600/20 ms, FA 90°, FOV 250 mm, matrix 256 (phase), 25 slices, slice 5 mm with 6.5 mm spacing, BW 250 Hz/px, phase R→L.
  Axial T_2 SE - TR/TE 4000/80 ms, FA 150°; geometry/BW/phase as above; 25 slices.
- Philips Prodiva (1.5T).
  Axial T_1 SE - TR/TE 600/15 ms, FA 90°, FOV 250 mm, matrix 560 (phase), 30 slices, slice 5 mm, NEX 2, BW 250 Hz/px, phase R→L.
  Axial T_2 SE - TR/TE 1000/100 ms, FA 90°; geometry/NEX/BW/phase as above; 30 slices.

ACR phantom scans followed official ACR accreditation standards (Table 1), except for number of slices and slice gap. Instead of the 11 slices needed by accreditation (to guarantee specified structures show), 32 slices with a 2 mm gap were used to cover the whole length of the phantom and consistently capture all features.

Table 1. American College of Radiology parameters used for ACR phantom scanning [5, 6]

Series/ Pulse sequence	**Axial T_1 / Spin echo**	**Axial T_2 / Spin echo**
Coil used/ protocol	Head/ brain	Head/ brain
TR (ms)	500	2000
TE (ms)	20	80
FOV (mm)	250	250
Number of slices	32	32
Slice thickness (mm)	5	5
Slice Gap	2	2
Matrix (phase)	256	256

2.4 Calculations

To maximise SNR, the air region of interest (ROI) was set as big as possible while eliminating truncation and edge bleed. The signal ROI covered ≥75 % of the phantom, while the background ROI matched Fig. 2 (left). Mean values were collected using ImageJ, and SNR was calculated with Eq. (1).

$$SNR = \frac{\bar{S}}{\sigma_{bkg}} \quad (1)$$

The PIU window/level was changed to highlight the brightest and darkest locations inside the big ROI (≥75 %) (Fig. 2 (right)). The maximum and minimum intensities were obtained by ImageJ, and PIU was calculated using Eq. (2).

$$PIU = 100 \cdot \left(1 - \frac{S_{max} - S_{min}}{S_{max} + S_{min}}\right) \quad (2)$$

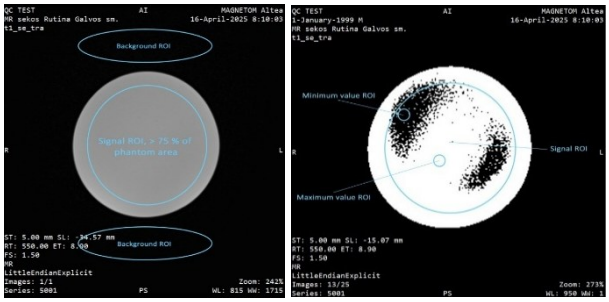

Fig. 2. Selection of signal and background ROIs for measurements (left); and selected ROIs for determining maximum and minimum signal areas (right)

Geometric distortion is expressed as percent geometric distortion (PGD) it quantifies geometric distortion between any two FOV points (Fig. 3). PGD is calculated with Eq. (3), $L_{true\ dimension}$ is the grid's actual dimension and $L_{observed\ dimension}$ the image-measured dimension. For this home-made ACR phantom the grid length was 15 cm.

$$PGD = \left(\frac{L_{true\ dimention} - L_{observed\ dimension}}{L_{true\ dimention}}\right) \cdot 100 \quad (3)$$

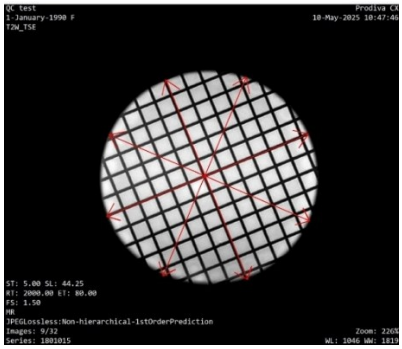

Fig. 3. Example of any two points that can be selected for PGD measurement

For Low-Contrast Detectability measurements the number of full spokes visible in the slice was counted. The ideal result for this measurement is 30 visible cavities since there are 30 cavities in total (exclude the 5 large and 4 small printing-only holes) (Fig. 4).

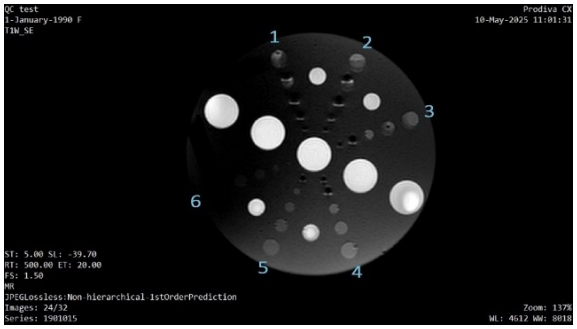

Fig. 4. Low-Contrast Detectability scan showing which group of cavities to count, 6 groups with each group having 5 cavities

High contrast resolution corresponds to a number of linear groups whose line pairs are visually distinguished. Labels indicate lp/cm; after group 6, subgroups 6.1/6.2 are still 6 lp/cm but with smaller spacing (Fig. 5).

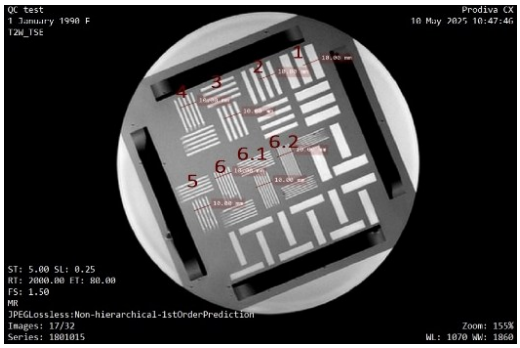

Fig. 5. High contrast resolution scan showing the number of line pairs per centimetre

3. Results and discussion

Image quality control in MRI is used for weekly and periodic routine evaluations, to optimise equipment performance and longevity, ensure patient safety and increase diagnostic quality. The recommendations for MRI quality assurance stem from the lack of formal regulations and national standards in Lithuania, so the recommendations include evaluation of key image quality parameters and establishment of baseline image quality parameter values. To achieve this, multiple scans must be performed under identical conditions across different sites. The evaluated MRI image quality parameters underwent measurement, recording and analysis with manufacturer provided and ACR style phantoms, acquisition protocols and comparison of results with ACR and AAPM guidelines.

3.1 Bottle Phantom QC – SNR, uniformity and signal ghosting

3.1.1 Signal-to-Noise Ratio

Signal-to-noise ratio (SNR) alone cannot identify imaging chain defects, and according to the AAPM acceptable levels vary by system. Baselines should be determined by installation measurements or manufacturer standards. In this study, the signal ROI covered 80 cm² (at least 75 % of the phantom), while the background ROI comprised 25 cm² (Fig. 6). In T_1-weighted scans, the Skyra 3T had the highest SNR (623.2), followed by the Altea 1.5T (499.5) and the Prodiva 1.5T (420.5) (Fig. 7). In T_2-weighted scans, all systems showed reduced SNR, as expected with longer echo times; the Skyra 3T had the lowest SNR (165.5) and the Prodiva 1.5T had the greatest SNR (192.7).

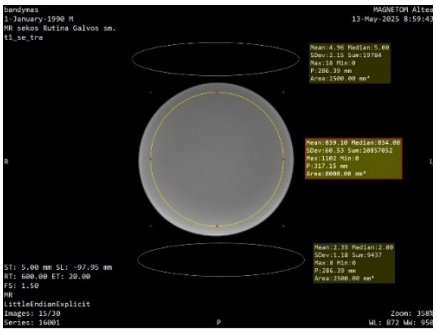

Fig. 6. Regions of interests used for signal and background measurement for SNR calculation

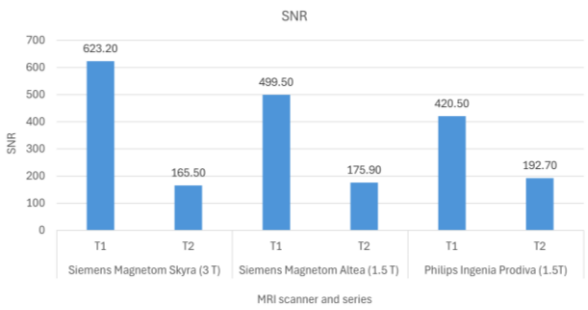

Fig. 7. Graphical representation of Signal-to-Noise Ratio results for T_1 and T_2 sequences across several MRI scanners

3.1.2 Uniformity

The phantom ROI's signal homogeneity was assessed using Percent Image Uniformity (PIU). According to AAPM, ≥90 % is predicted for ≤2 T systems, but values may be lower for >2 T with water phantoms [3]. An 80 cm² signal ROI and a 1 cm² max/min ROI (Fig. 8) was set. All the scanners scored above 90 % in T_1 and T_2 (Fig. 9). In T_1, the Philips Ingenia 1.5T scored the

best at 97.5 %, followed by 95.2 % in T_2. The Siemens Altea 1.5T measured 95.6 % and 96.3 %. Siemens Skyra 3T recorded 90.7 % and 90.4 %, which is consistent with estimates for increased field strength. Overall homogeneity was acceptable, suggesting stable coils and calibration.

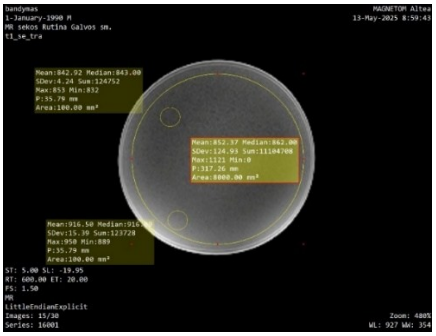

Fig. 8. Regions of interests used for maximum and minimum signal pixel intensity measurement for PIU calculation

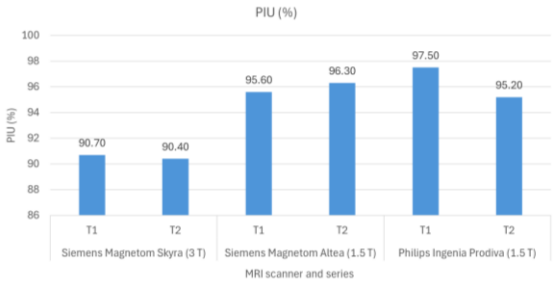

Fig. 9. Graphical representation of Percent Image Uniformity results for T_1 and T_2 sequences across several MRI scanners

3.2 ACR type phantom QC – geometric distortion, low-contrast object detectability and high-contrast spatial resolution

3.2.1 Geometric distortion

Geometric accuracy was evaluated by measuring phantom diameters in MicroDicom and comparing them with the known 15 cm diameter. The AAPM recommends absolute distortion of less than 2 %, however the ACR program allows for ±2 mm for the ACR phantom [3]. All systems met these limits (Fig. 10), with the highest variances being +1.18 mm (1.12 %) and -1.79 mm (-0.79 %). The Siemens Skyra 3 T demonstrated the biggest deviation (still acceptable), demonstrating a larger distortion risk at higher field strengths unless advanced corrections are applied [7]. Both 1.5T systems stayed under 1 mm and 0.8 %. Additional measurements should be made to determine whether the reported variations are consistent as normal expected variation or fall as a systematic issue.

Accurate image geometry is essential for diagnosis and planning. Even minor distortions can affect anatomy, skew lesion measurements, and cause registration issues across images. In the brain example (Fig. 12), axial slices reveal peripheral warping, which reduces diagnostic confidence and the precision of image-guided treatments. Geometric distortion should be routinely assessed as part of MRI quality control.

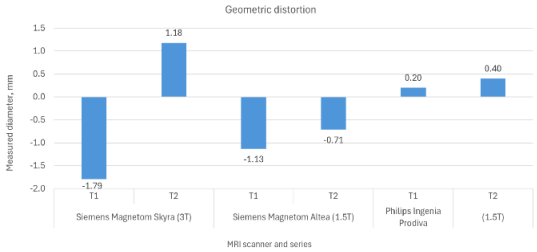

Fig. 10. Graphical representation of Geometric distortion results for T_1 and T_2 sequences across several MRI scanners

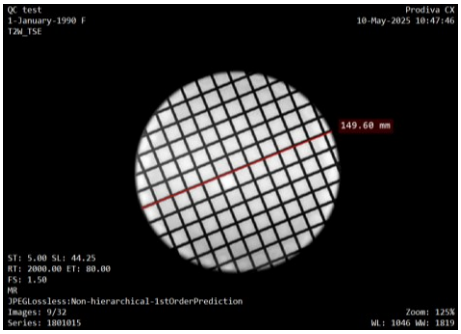

Fig. 11. Geometric accuracy evaluation on Philips Ingenia Prodiva (1.5 T) system, with T_2-weighted imaging

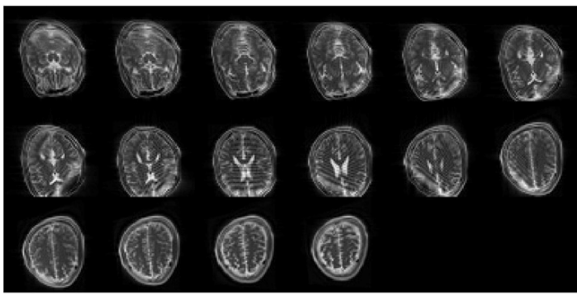

Fig. 12. An example of geometric distortion in brain MRI scans [8]

3.2.2 Low-contrast object detectability

Low-contrast detectability was assessed by counting visible spokes (ideal 30). Overall, the results (Fig. 13) were strong, with Siemens Skyra 3T and Altea 1.5T (Fig. 14) reaching 30 spokes in both T_1 and T_2. The Philips Ingenia 1.5T displayed 30 in T_1 and 28 in T_2, most likely due to setup issues such as phantom positioning. Because a non-standard ACR-type phantom was employed, no formal ACR acceptance thresholds were implemented. All systems performed well at low contrast.

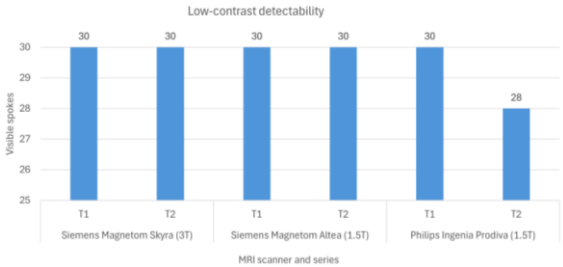

Fig. 13. Graphical representation of Low-contrast object detectability results for T_1 and T_2 sequences across several MRI scanners

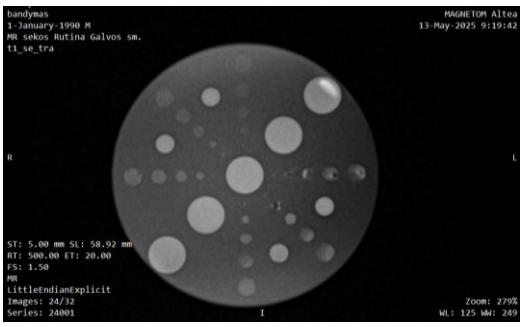

Fig. 14. Low-contrast object detectability evaluation on Siemens Magnetom Altea (1.5T) system with *T_1-weighted* images

The results of poor low-contrast detectability, in which differentiation between soft tissues with identical signal intensities becomes unreliable is shown in Fig. 15. Images from c-f exhibit blurring at structure boundaries, whilst a lover set of images with a green arrow shows how delicate anatomical characteristics can be lost or seem blurred when contrast detectability is insufficient. Such distortions make it difficult to distinguish small lesions and clinical abnormalities.

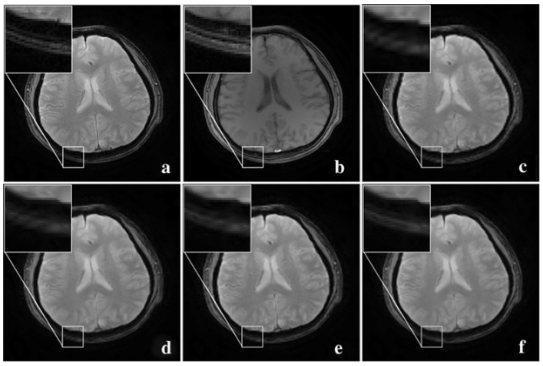

Fig. 15. MRI images showing degradation in low-contrast detectability – blurring of fine anatomical details, particularly at the edges of structures [9]

3.2.3 High-contrast spatial resolution

High-contrast resolution was assessed using line-pair patterns, with the highest group still distinguishable (Fig. 16). The AAPM standards employ dot phantoms, but the basic principle remains: in this phantom bars must be recognisable at ~1-pixel separations. The highest possible level was group 6.2. The 1.5T systems, Siemens Magnetom Altea (Fig. 17) and Philips Ingenia Prodiva, achieved 6.0-6.2 in T_1 and T_2, demonstrating constant high resolution. The 3T Siemens Magnetom Skyra measured group 5 in T_1 and improved to group 6 in T_2. The lower T_1 result might be due to setup or protocol issues rather than a hardware defect; repeated tests would reveal whether this is systematic.

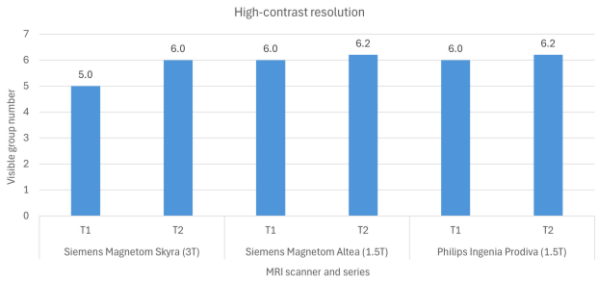

Fig. 16. Graphical representation of High-contrast spatial resolution results for T_1 and T_2 sequences across several MRI scanners

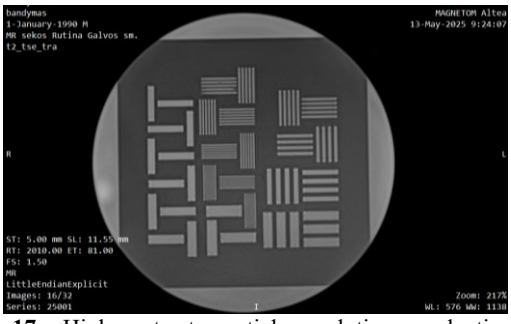

Fig. 17. High-contrast spatial resolution evaluation on Siemens Magnetom Altea (1.5T) system, with T_2 -weighted images

High-contrast spatial resolution determines edge sharpness and the visibility of fine anatomy. When it decreases, finding tiny lesions, vascular anomalies, or cortical thinning becomes more difficult, compromising diagnosis and surgical planning. Fig. 18 demonstrate the effect – blurring boundaries and unclear edges where sharp resolution is expected (red arrows).

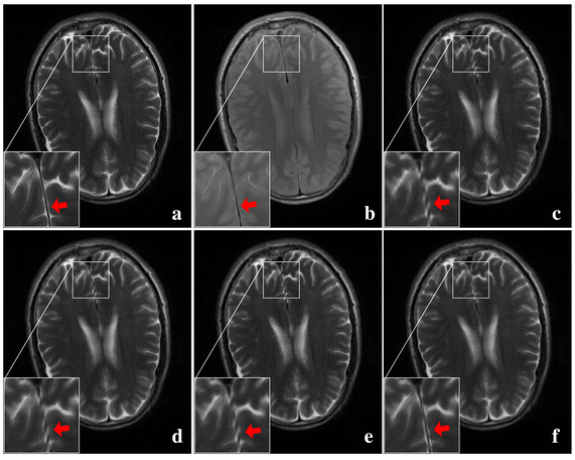

Fig. 18. Assessment of high-contrast spatial resolution using brain MRI. The reference images a (*T_1-weighted*) and b (*T_2-weighted*) shows high-resolution, while images c-f produce in lower high-resolution images [9]

3.3 Recommendations

According to ACR and AAPM evaluation of image data requires weekly measurements which should be performed using ACR phantom testing to assess geometric accuracy, high contrast spatial resolution, low contrast detectability, signal-to-noise ratio, image uniformity and artifact evaluation. Recommendations for MRI QC according to ACR and AAPM [3, 10]:

- **Staff.** To reduce variability and track changes, the same technologist should perform QC. A qualified medical physicist should review QC logs at least quarterly and reset action limits after hardware changes or service. Close collaboration among radiologists, technologists, physicists, and service teams ensures consistent QC, rapid issue detection, and ongoing quality improvement.
- **Measurements – baseline.** Establish a baseline from ~10 days of consistent QC using standard forms; use this data to set scanner-specific control limits.
- **Measurements – QC logs.** Record all tests in a standardized log with baseline values and any corrective actions. To log technical issues the same way. Keep logs at the scanner.
- **Measurements – sequences.** Evaluate both T_1 and T_2-weighted protocols for every QC metric to reflect clinical use and to reveal protocol-specific weaknesses.
- **Performance criteria and action limits**. A qualified medical physicist should set and periodically review limits based on ACR/AAPM guidance. SNR is system specific and should meet or exceed the manufacturer's baseline. Geometric accuracy must be within ±2 mm (or 2 % for FOV > 25 cm). Uniformity should be ≥90 % at 1.5T and ≥87.5 % at 3T. Percent signal ghosting should be ≤2.5 %. Low-contrast detectability with the ACR phantom should be at least 9 spokes at 1.5T and 37 spokes at 3T. High-contrast resolution is the highest line-pair level visibly resolved using the manufacturer or ACR thresholds.
- **Corrective actions.** If a result exceeds limits, repeat the phantom scan and review with the medical physicist and service engineer. If the failure persists, proceed with a structured investigation of software, hardware, and environmental factors.

4. Conclusions

This study developed and tested a standardized phantom-based MRI QC approach across three systems used in Lithuania – Siemens Skyra 3T, Siemens Altea 1.5T, and Philips Ingenia Prodiva 1.5T. All scanners performed within acceptable limits, with differences by field strength and sequence. Skyra 3T led in T_1 SNR but trailed in T_2, while Prodiva showed the best uniformity, underscoring the need for consistent acquisition when comparing systems.

Based on ACR/AAPM guidance, a practical QC protocol for Lithuanian clinics were proposed – weekly phantom checks of SNR, PIU, geometry, and resolution, with baseline values established at installation and stable acquisition settings for trend analysis. This protocol supports routine QC integration and demonstrates strong alignment with existing ACR and AAPM procedures. Its adoption as a standardized framework could enhance consistency and improve reproducibility across institutions.

5. References

1. Ozbay B. Magnetic resonance imaging (MRI). In: The brain, the nervous system, and their diseases: Volumes 1–3. 2014. p. 614–619.
2. Pedrosa I., Altman D.A., Dillman J.R., Hoff M.N., McKinney A.M., Reeder S.B., Rogg J.M., ... and Watson R.E. American College of Radiology manual on MR safety: 2024 update and revisions. Radiological Society of North America, 2025.
3. Jackson E., Bronskill M., Drost D., Och J., Pooley R., Sobol W., and Clarke G. AAPM n100 – Acceptance testing and quality assurance procedures for magnetic resonance imaging facilities. 2010.
4. Koller C.J., Eatough J.P., Mountford P.J. and Frain G. A survey of MRI quality assurance programmes. British Journal of Radiology, 79(943), 2006. p. 592–596.
5. American College of Radiology. Large/medium phantom testing: MRI: accreditation support.
6. Etman H.M., Mokhtar A., Abd-Elhamid M.I., Ahmed M.T. and El-Diasty T. The effect of quality control on the function of magnetic resonance imaging (MRI) using American College of Radiology (ACR) phantom. Egyptian Journal of Radiology and Nuclear Medicine, 48(1), 2017. p. 153–160.
7. Jezzard P. and Balaban R.S. Correction for geometric distortion in echo planar images from B0 field variations. Magnetic Resonance in Medicine, 34(1), 1995. p. 65–73.
8. Yeo D.T.B., Fessler J.A. & Kim B. Motion correction in fMRI by mapping slice-to-volume with concurrent field-inhomogeneity correction in echo-planar imaging (EPI) data. Conference Paper, Sep 2004.
9. Zheng H., Qu X., Bai Z., Liu Y., Guo D., Dong J., Peng X. and Chen Z. Multi-contrast brain magnetic resonance image super-resolution using the local weight similarity. BMC Medical Imaging, 17(1), 2017. p. 1–13.
10. Price R., Allison J., Clarke G., Dennis M., Hendrick R.E., Keener C., Masten J., and Reeve D. ACR – Magnetic Resonance Imaging Quality Control Manual. 2015

MEDICAL PHYSICS IN THE BALTIC STATES 17 (2025)

Proceedings of International Conference "Medical Physics 2025"
06-08 November 2025, Kaunas, Lithuania

THE NEUTRON FLUX AND DOSE RATE EVALUATION INSIDE AND OUTSIDE OF THE PU-BE NEUTRON SOURCES STORAGE DEVICE AT EXPERIMENTAL NUCLEAR PHYSICS LABORATORY OF FTMC

Džiugas VYŠNIAUSKAS[1], Marina KONSTANTINOVA[1], Rita PLUKIENĖ[1], Artūras PLUKIS[1]
Emilis SADREJEVAS[2], Paulius KAZLAUSKAS[2]
[1] Center for Physical Sciences and Technology, Savanorių pr. 231, LT-02300 Vilnius, Lithuania
[2]Radiation Protection Centre, Kalvarijų g. 153, LT-08352 Vilnius, Lithuania

***Abstract*:** PuBe neutrons sources at Experimental Nuclear Physics Laboratory of the FTMC (Center for Physical Sciences and Technology) are used in several activities including neutron activation and different material irradiation experiments. In this work we address the neutron flux and dose estimation at different points outside PuBe neutron sources storage device and in the new design irradiation chamber at the central channel dedicated for neutron irradiation experiments. The characterization of irradiation parameters is needed every time after reconstruction/ improvement of irradiation chanell, neutron source or speciments holders. PuBe neutron sources all together have $4.5 \cdot 10^7$ n/s of total activity. Calibration of PuBe neutron flux characteristics and dose estimation at the irradiation positions was performed using MCNP6 modelling, which was validated by neutron activation analysis (NAA) of irradiated well-known Fe, Al samples inside the central irradiation channel. The conclusions on the actual neutron flux energy distribution and model corrections were drawn. BF_3-NP neutron detector was used for dose rate estimation on the top and side wall of PuBe neutron sources storage device. The absolute neutron intensity and dose rates at dedicated irradiation points were evaluated. Experimentally measured reaction rates inside neutron sources storage device were in satisfactory agreement with modelling (MCNP6) reaction rates. The dose rate for the samples in the dedicated irradiation position of the central channel was of order of 42 mSv/h. Neutron dose rate above neutron sources device without plug measured with BF3-NP neutron detector was 140.6 μSv/h.

Keywords: PuBe neutron source, neutron activation analysis, MCNP6 modeling, BF_3-NP neutron detector

1. Introduction

Alpha-neutron sources produce neutrons through the (α, n) reaction: $^{9}Be + \alpha \rightarrow {}^{13*}C \rightarrow n + {}^{12}C$; $\rightarrow {}^{8}Be + n + \alpha$; $\rightarrow n + 3\alpha$. The Q-value of this reaction is 5.7 MeV and is shared among the reaction products. The intermediate state of this reaction is the formation of the compound nucleus ^{13}C, and neutrons are produced through different channels.

In the Experimental Nuclear Physics Laboratory at the Center for Physical Sciences and Technology (FTMC) the neutrons are emitted by 4 PuBe neutron sources (2 ^{239}PuBe and 2 ^{238}PuBe) all together having $4.5 \cdot 10^7$ n/s of total activity according to existing documents. They are used mainly for educational purposes. They are situated in the neutron storage device (container filled by polyethylene) on the first floor of the building which construction initially was designed to work with various kinds of radiation. In the neutron laboratory the student practical works of material irradiation, neutron activation, life time measurements, coincidence and other laboratory experiments are performed.

The characterization of irradiation parameters is needed every time after reconstruction/ improvement of irradiation chanells, neutron source or speciments holders change. Resently some reconstruction works with the central experimental channel pipe replacment and instalation of the newly designed organic glass container for 4 individual neutron sources have been performed in order to improve and enable better control of the neutron flux. For the acomodation of different sized specimens the new specimen holder was also designed. These changes demanded additional characterization of the updated neutron source instalation. For this reason, the neutron flux intensity and energy distribution evaluation in the particular positions dedicated for neutron activation/irradiation experiments washas been performed. Moreover, external neutron dose rates using BF_3-NP neutron detector were measured at

different positions (on the top and side walls) of PuBe neutron sources storage device. The physical features of the neutron source are important for planning of the experiments and for estimation safety and radiation protection level in the laboratory.
Neutron activation analysis (NAA) and MCNP6 modeling was used for identification of neutron flux parameters such as neutron flux intensity and energy distribution similarly as it was provided in [1]. The samples were irradiated at different positions and by measuring γ spectra the neutron flux intensity was identified. Peculiar elements with established neutron capture cross sections – Al roll and Fe powder (in the petri dish) have been used for neutron activation analysis to validate neutron activation energy in thermal to fast neutron range.

2. Numerical simulation

For neutron flux and energy distribution assessment MCNP6 code [2] and ENDF-VII [3] cross-section libraries have been used. The simultaneous coupled neutron-gamma transport calculations have been performed. MCNP6 has been used for neutron transport calculation, energy deposition and assessment of the reaction rates in the samples. The nuclear interaction (n,γ), (n,p) or (n,α) reaction rates (*RR*) were defined with the classic Fredholm equation of the first order [2]:

$$RR_i = N\int_0^\infty \sigma(E)\phi(r,E)dE \tag{1}$$

where RR_i - rate at which reactions are occurring in the nuclide *i* (reactions/s); *N* - number of target atoms in the sample; $\sigma(E)$- energy-dependent microscopic cross-section; $\phi(E)$ - energy-dependent neutron flux in the sample (n/cm^{2}s).

After solving the integral equation (1) by performing energy group discretization procedure for neutron flux and microscopic cross-section calculation in MCNP6 the average macroscopic values of σ and ϕ in the sample and nuclide *i* production rate were obtained*:*

$$RR_i = N\sigma\phi \tag{2}$$

Nuclide production reaction rate was further used to obtain number of daughter nuclide atoms (N_d) after target nuclide atoms (*N*) irradiation in the neutron flux:

$$N \xrightarrow{RR_i} N_d \xrightarrow{\lambda N_d} N_s \tag{3}$$

N_d is a function of the production and loss rates (λN_d):

$$\frac{dN_d}{dt} = N\sigma\phi - \lambda N_d \tag{4}$$

where λ - decay constant for the daughter nuclide; λ=0,693/$T_{1/2}$, $T_{1/2}$ is the half-life of the reaction.

If the initial concentration of the daughter nuclide N_d is 0 at t=0, then the solution of the Eq4. for the number of daughter nuclides present during the irradiation is:

$$N_d(t) = \frac{N\sigma\phi}{\lambda}(1-e^{-\lambda t}) \tag{5}$$

The activity *A* of the sample is given by λN. Hence, the activity (*A*) at the time of irradiation (t_i) will be:

$$A = N\sigma\phi(1-e^{-\lambda t_i}) \tag{6}$$

$1-e^{-\lambda t_i} = S$ is called the saturation factor, it means that the induced activity approaches a horizontal asymptote or saturated activity (A_∞) for an infinitely long irradiation time. The (A_∞) activity is derived from Eq.4: $A_\infty = N\sigma\phi = \lambda N_d$. If the irradiation of samples took time t_i at which the sample of initial activity A was removed, A_∞ can be calculated as follows;

$$A_\infty = \frac{A}{(1-e^{-\lambda t_i})} \tag{7}$$

The reaction rates and the corresponding saturation activity were calculated for the neutron activation samples at different locations (different channels and different heights).
The simplified scheme of the neutron sources storage container at the Experimental Nuclear Physics Laboratory is presented in Fig. 1. The neutron source storage container is the cylindrical well having 0.6 m, located at 1.8 m depth under the ground, which is filled by paraffin matrix as moderator. The neutron sources are placed in central channel of the well and two vertical experimental channels are situated 15 cm and 20 cm from the source to obtain different neutron flux characteristics during irradiation experiments.

Calculated neutron flux in the experimental channels of the well is presented in Fig. 2. The thermal flux dominates in all channels. In the Central channel thermal neutron share is ~68%, in V2 ~62% and in V1 55% with different neutron flux intensity as it can be seen in Fig. 2a). The neutron flux in the upper and lowest samples differs by a factor of 2 and the thermal neutrons part increses in the upper sample by 11% if compared with lower sample. This is shown in Fig.2 b). It should be taken into account that the dose rate in irradiation experiments varies corespondingly.

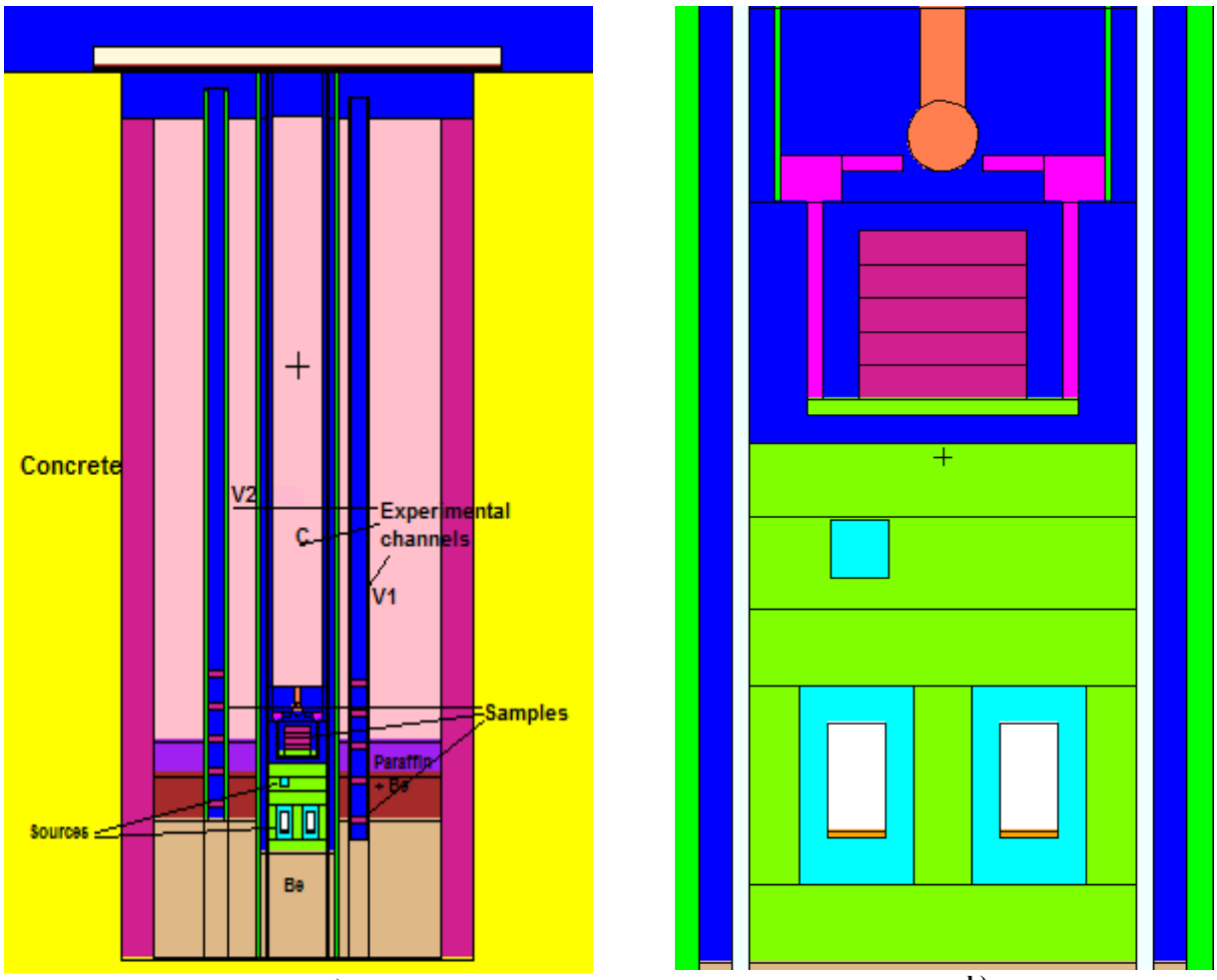

Fig. 1. The simplified scheme of the neutron sources container under the ground; b) magnified view of the sample holder with array of 5x5x1cm ABS samples on the top of box with neutron sources.

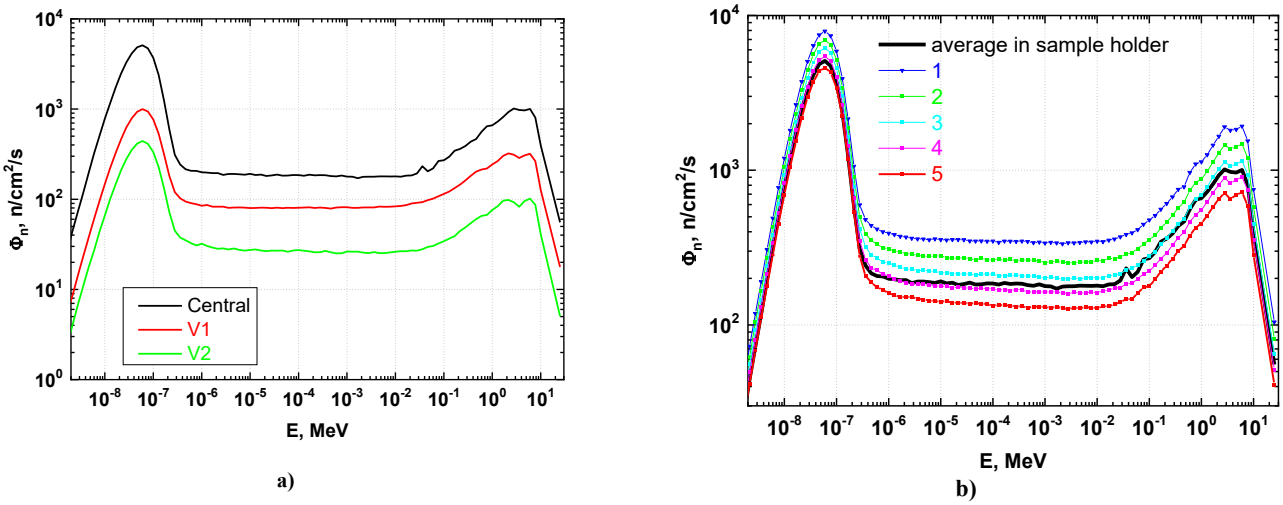

Fig. 2. a) Neutron flux spectra in the experimental channels of neutron well; **b)** neutron flux spectra in the array of 5x5x1cm ABS samples.

3. Neutron activation analysis

If the quantitative and nuclear properties of the activated element in the sample are known the neutron flux ϕ (n/cm^2/s), can be obtained from (6) equation [5]:

$$\phi = \frac{A \cdot w}{\sigma \cdot m \cdot N_A \cdot \alpha \cdot S} \quad (8)$$

where A is activity of the element in the sample at the end of irradiation (Bq), σ - reaction cross section (cm^2) , m - mass of the target element (g), N_A – Avogadro's number (6.023×10^{23} molecules/mole), α – fraction of the target isotope in the sample; $S = 1 - e^{-\lambda t_i}$ – saturation factor, w – atomic weight of the element.

The activity of the isotope can be obtained from the counts in the total absorption peak in the gamma spectrum of the sample registered using the high purity germanium (HPGe) detector [6]. The spectrum of the gamma radiation is accumulated for a time Δt, long enough to get reasonable statistics under the total absorption peak. The time is usually at least one half-life. The measured activity (A_m) can be determined from the following equation:

$$A_m = \frac{\Sigma_p / \Delta t - \Sigma_b / \Delta t}{\eta \cdot \varepsilon_t} \quad (8)$$

where Σ is sum of the counts under the total absorption peak, Σ_b is background for the same counting period Δt, η is the gamma transition yield; ε_t – absolute efficiency of registration in the detector (this value is obtained from the detector calibration curve at the energy of γ emitted by the sample see equation (12)), which was adjusted taking into account the MCNP modeling of detector registration for each sample geometry including the self absorption, distance, gamma ray coincidence effects, etc.).

The sample activity also decreases due to radioactive decay during the measurement time Δt and it should be taken into account:

$$A_0 = \frac{A_m \Delta t}{(1 - e^{-\lambda \Delta t})} \quad (9)$$

The sample activity at the beginning of the measurement (A_0):

$$A_0 = A \cdot e^{-\lambda t_d}, \quad (10)$$

where t_d is delay time between stop of irradiation and beginning of the measurement.

From these two equations we can obtain the activity of the sample A after irradiation:

$$A = \frac{A_m \Delta t \cdot e^{\cdot \lambda t_d}}{(1 - e^{-\lambda \Delta t})} \quad (11)$$

This calculated activity was used for calculation of the neutron flux (see 8) in the irradiation channels at certain irradiation positions. The value of the corresponding saturation activity is calculated using MCNP6. According to the experimental neutron activation results the certain adjustment of parameters of neutron source intensity are performed for exact neutron source representation.

4. Experimental equipment

Gamma-ray spectrometric measurements of the neutron-activated samples were carried out using HPGe detector coupled to the MCA Canberra DSA1000 with Genie-2000 gamma ray spectroscopy analysis software (Canberra Industries, USA). The HPGe detector was of GC2520 series by Canberra, USA, with relative efficiency of 25%, and energy resolution of 1,1 keV at 121.78 keV (^{152}Eu) and at 2 keV at 1332.5 keV (^{60}Co). Absolute detector efficiency has been calibrated for the each neutron activation sample (Al, Fe) geometry using MCNP6 modeling technique. The HPGe detector registration efficiency factors for the neutron activation products are presented in Fig. 3.

Table 1. Radioactive decay energies, transition probabilities and half-lives of gamma nuclides used in the neutron activation experiments.

Gamma ray transition	E (keV)	$T_{1/2}$, d	Probability (%)
^{58}Fe(n,g) → ^{59}Fe	1099.245	44.49.	56.5
^{58}Fe(n,g) → ^{59}Fe	1291.59	44.49	43.2
^{27}Al(n,g) → ^{28}Al	1779	2.245	99.98
^{27}Al(n,p) → ^{27}Mg	843	9.435	71.00
^{27}Al(n,p) → ^{27}Mg	1014	9.435	29.00
^{27}Al(n,a) → ^{24}Na	1368	14.956	99.99
^{27}Al(n,a) → ^{24}Na	2754	14.956	99.87

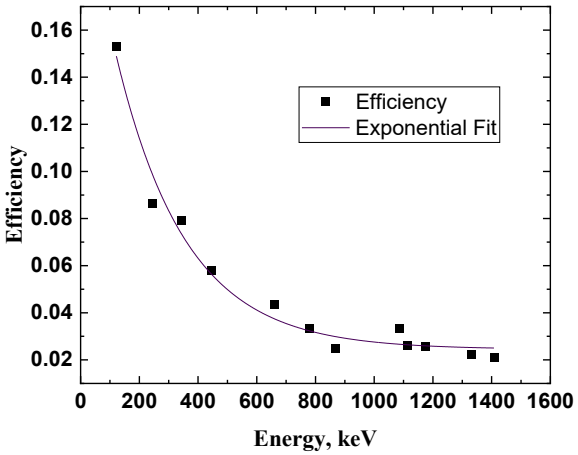

Fig. 3. HPGe detector registration efficiency.

5. Experimental measurements and dose rate determination

Neutron flux was experimentally validatd by NAA. Flux calculated using (8) from activated in this flux nuclide have been determined from its measured gamma activity.

The NAA experimental results were compared with the numerical simulation using MCNP code.
Two chemical samples were selected for NAA : 2.3g pure Al roll sample was irradiated for both thermal and fast neutron flux characterization, 12g Fe powder in plastic Petri dish – for thermal neutron characterization. Representative spectrum of activated Al sample in the central channel is presented in Fig. 4.
A comparison of experimentally and by simulation obtained neutron fluxes in the central channel is presented Table 2. Experimentally obtained thermal neutron flux is in satisfactory agreement with modeling (MCNP6) flux for thermal neurons in case of Al sample, but higher values are obtained for Fe sample. For fast neutron flux obtained by the numerical simulations gives higher values (coefficient of 1.4-1.7). This could be caused by inaccuracies in the model - mismatches between geometry and real parameters described in the model, inaccuracies in material composition, and more different samples for neutron activation analysis should be performed to find out the correct neutron flux values. As the higher part of the flux is thermal, we can assume, that approximately correct neutron flux value $4.5 \cdot 10^7$ n/s is used.

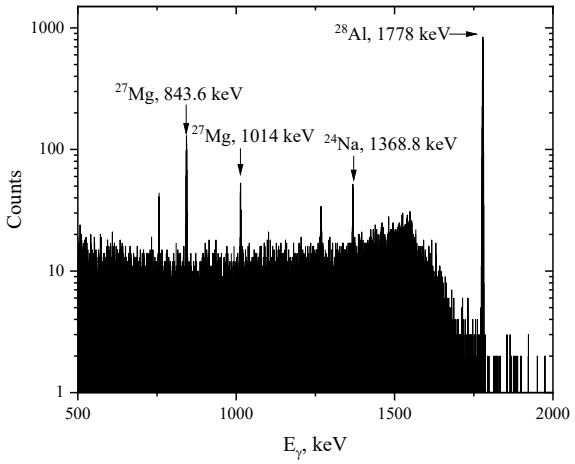

Fig. 4. Energy dependent gamma ray spectrum of Al sample activated in the Central channel of the Pu-Be neutron sources. Al sample measurement time is 993s.

Table 2. The comparison of modeled and experimentally estimated reaction rates (R) of the neutron activation in the samples in the Central channel of the neutron storage device.

Sample /reaction	φ(exp)/φ(MCNP)
Al / ^{27}Al(n,α)^{24}Na	1.4
Al / ^{27}Al(n,p)^{27}Mg	1.7
Al / ^{27}Al(n,g)^{28}Al	1.1
Fe / ^{58}Fe(n,g)^{59}Fe	5.4

Table 3. Calculated neutron flux and dose rate estimation for sample at the irradiation positions (h=0) at Central, Vertical I and Vertical II channels of the neutron storage device.

Channel	ϕ (n·s^{-1}cm^{-2})	$n_{thermal}$	$n_{epithermal}$	n_{fast}	Dose rate, mSv/h
C	5.9×10^4	68	9	23	41.9 ±0.5
V1	1.6×10^4	55	14	31	5.7±0.7
V2	6.1×10^5	62	12	26	1.8±0.6

The Properly modeled neutron flux at the sample irradiation position allows a reliable estimation of the neutron radiation dose rate to the sample (see Table 3). D is calculated with MCNP6 using D(E) ICRP74 standard [7]. The dose rate for the sample in of the central channel is of order of ~42mSv/h, V1 channel ~6mSv/h, V2 channel ~2mSv/h.

7. Conclusions

External neutron dose rates using BF_3-NP neutron detector (see Fig.5) was measured at different positions (on the top and side walls) of PuBe neutron sources storage device. BF3-NP (Centronic BF_3-15EB20/25-SHV) is BF_3 - cylindrical proportional counter, which neutron measurement energy range: from 0.025 eV to 20 MeV, dose rate measurement range: from 10 nSv/h to 100 mSv/h with underestimation ≤ 10%: 2 μSv.
In table 4 the experimental values of measured neutron dose rate at different shielding conditions around PuBe neutron sources storage device and on the top of it is presented. The maximal values are obtained on the top of storage device with extracted plug – the dose rate is of order of 140.6 μSv/h. Also, the dose rate measurement with Cd plate for thermal neutron absorption estimation was performed, the epithermal and fast neutron dose is of order of 120μSv/h. The MCNP modeling of neutron transport and shielding will be performed in future work.

Table 4. External neutron dose rates using BF3-NP neutron detector (RSC).

Measurement No.	Concrete shielding, cm	Dose rate, μSv/h
1	24	2.19
2	20	2.28
3	18	1.89
4	20	1.74
5	24.5	1.14
6	27.5	0.81
7	30.5	0.78
8	26.5	1.32
9	with inserted plug	0.06
11	without plug	140.6
12	without plug with Cd shielding	118.2

Fig. 5. BF_3-NP neutron detector (RSC)

6. Conclusions

The absolute neutron intensity at dedicated irradiation points as well as neutron dose rates inside the irradiation cahnnels and outside PuBe neutron sources storage device are obtained. Experimentally measured neutron fluxes are in 2σ agreement for Al neutron activation sample with modelling (MCNP6) calculaetd neutron fluxes, but less agrrement obtained with Fe powder sample (most probably due to powder density underestimation). More neutron activation analysis experiment with other samples could help establishing corrected neutron intensity and energy distribution at sample irradition postions of the reconstructed central experimental channel with new design organic glass container for the 4 individual neutron sources and new design sample holder. According to Al sample NAA estimations, the dose rate for the sample in the dedicated irradiation position of the central channel is of order of 41.9±0.5 mSv/h, V1 channel – 5.7±0.7 mSv/h, V2 channel – 1.8±0.6 mSv/h. The external dose rate measured with BF3-NP neutron detector above neutron sources device without plug is order of 140.6 μSv/h, if only epithermaand fast neutrons are taken into account dose rate is of order of 120 μSv/h, on the floor around neutron sources storage device the dose rate is in the 0.8-2.3 μSv/h range.

7. References

1. Hamidatou L., Slamene H., Akhal T. and Zouranen B. Imaging and Radioanalytical Techniques in Interdisciplinary Research - Fundamentals and Cutting Edge Applications, Concepts, Instrumentation and Techniques of Neutron Activation Analysis, 2013, Ch. 6, 142, p. 155.
2. Pelowitz D.B., *MCNP6 User's Manual*, Version 1.0, Report LA-CP-13-00634, Los Alamos National Laboratory, New Mexico, 2013.
3. Chadwick M. et.al. ENDF/B-VII.0 : Next Generation Evaluated Nuclear Data Library for Nuclear Science and Technology, Nuclear Sciecne and Technology, 2006, 107, 12, p. 2931-3060.
4. IAEA-TECDOC-564 (1990) Practical aspects of operating a neutron activation analysis laboratory, IAEA, Vienna, ISSN 1011-4289
5. Park S.-T. and Jang N. H. Estimation and Calibration of Thermal Neutron Flux for Neutron Activation Analysis, Bull. Korean Chem. 2006, Soc., 27, no. 12, pp. 2061-2063
6. Gudelis A., Remeikis V., Plukis A., Lukauskas D. Efficiency calibration of HPGe detectors for measuring environmental samples. Envir. and Chem. Phys., 2000, 22, no. 3-4,pp. 117-125 .
7. Clement C. Independent but not isolated. Annals of the ICRP. 2012;41(3-4), pp. 1-3

MEDICAL PHYSICS IN THE BALTIC STATES 17 (2025)

Proceedings of International Conference "Medical Physics 2025"
06-08 November 2025, Kaunas, Lithuania

BLOCKING STRATEGIES FOR OPTIMAL THYROID PROTECTION FOR RADIOIODINE

Martin ANDERSSON[1], Eva FORSSELL-ARONSSON[1,2,3], Rich LEGGETT[4], Sören MATTSSON[5]
[1]Department of Medical Radiation Sciences, Institute of Clinical Sciences, Sahlgrenska Academy at University of Gothenburg, Gothenburg, Sweden, [2]Sahlgrenska Center for Cancer Research, Sahlgrenska Academy at University of Gothenburg, Gothenburg, Sweden, [3]Medical Physics and Biomedical Engineering, Sahlgrenska University Hospital, Gothenburg, Sweden, [4]Center for Radiation Protection Knowledge, Oak Ridge National Laboratory, Oak Ridge, TN, USA, [5]Medical Radiation Physics, Department of Translational Medicine, Malmö, Lund University, Malmö, Sweden
martin.andersson.2@gu.se; eva.forssell_aronsson@radfys.gu.se; leggettrw@ornl.gov; soren.mattsson@med.lu.se

***Abstract*:** After exposure to radioiodine, the absorbed dose to the thyroid can be much reduced by blocking its uptake by stable iodide. This is done when using radioiodine labelled pharmaceuticals, and also after nuclear accidents with release of radioiodine. The recent ICRP biokinetic iodine model was used for radioiodine as well as for stable iodide to illustrate the importance of amount of stable iodide and timing of blocking in relation to the radioiodine intake. Current guidelines for radiation protection for radioiodine are summarized.

Keywords: iodine, ICRP, biokinetic model, dosimetry

1. Introduction

Radioiodine intake, either orally or by inhalation or injection, is rapidly distributed in the blood. From the circulation, radioiodine is to a high extent, 10-40% in euthyroid humans, taken up by the thyroid gland [1].
Radioiodine is frequently used clinically for diagnosis (^{123}I, ^{124}I, ^{125}I and ^{131}I) and treatment (^{131}I) of various diseases. Radioiodide (I^-) is mainly used for thyroid diseases [2], while radioiodine labelled pharmaceuticals are developed for a number if other diseases [3]. These radiopharmaceuticals are to some extent catabolised in the body, and radioiodine is often released as iodide. The radiopharmaceuticals may also contain radioiodide as a radiochemical impurity.
Radioiodine, primarily ^{131}I, but also ^{132}I, ^{133}I, ^{135}I and other isotopes, are also released during nuclear accidents involving nuclear fission, e.g. at nuclear power plant accidents [4,5] and also at detonation of nuclear weapons [6,7]. To reduce unwanted thyroid uptake of radioiodide, iodine thyroid blocking (ITB) can be utilised, usually by stable iodide, but also by iodate (IO_2^-) or perchlorate (ClO_4^-) [8,9].
Previous measurements and computer models have demonstrated the importance of timing between thyroid blocking and radioiodine intake and the amount of stable iodide [10-12].
An improved biokinetic compartment model for iodine was recently developed by the International Commission on Radiological Protection (ICRP) [13,14]. The model includes 30 compartments and 48 transfer coefficients governing the kinetics of iodine in the adult human body. It has been used for internal dosimetry in patients undergoing nuclear medicine investigations using iodine labelled radiopharma-ceuticals and in case of thyroid blocking [15, 16].
The aim of this work was to use the ICRP model both for iodine intake and for stable iodide administration to illustrate the importance of amount of blocking iodide and timing in relation to the radioiodine exposure and to investigate the radiation absorbed dose reduction possibilities for blocking the uptake of ^{124}I, ^{125}I and ^{131}I.

2. Material and methods

To model the effect of stable iodide administration, the ICRP iodine model was extended to two parallel systemic models: one for stable iodine and one for radioactive iodine. Intake of stable iodine was modelled as a daily baseline amount of 160 µg [13], with additional amounts introduced to simulate blocking. The thyroid's uptake rate constant for iodide was described as a function of the total iodine content within the thyroid gland and reaching a point when uptake is saturated and suppressed. It was assumed that 8.35 mg of stable iodine in the thyroid completely blocks further iodine uptake [8,9]. To incorporate dynamic blocking, the ICRP thyroid transfer rate from iodide to organic iodine (95 d^{-1} under steady-state conditions) [11,12] was adjusted linearly over time so that at 8.31 mg of iodine in the thyroid, Tr=95 d^{-1} and at 8.35 mg of iodine in the thyroid, it is completely blocked, which means Tr=0 d^{-1}. Organ specific time-integrated activity coefficients were determined for

different blocking times relative to an administration of radioiodine. Organ absorbed doses and the effective dose were calculated using IDAC-Dose2.1 [17]. Calculations were performed for ^{124}I, ^{125}I and ^{131}I. ITB was simulated for amounts up to 128 mg of stable I, given up to 2 hours before and after radioiodine intake, respectively.

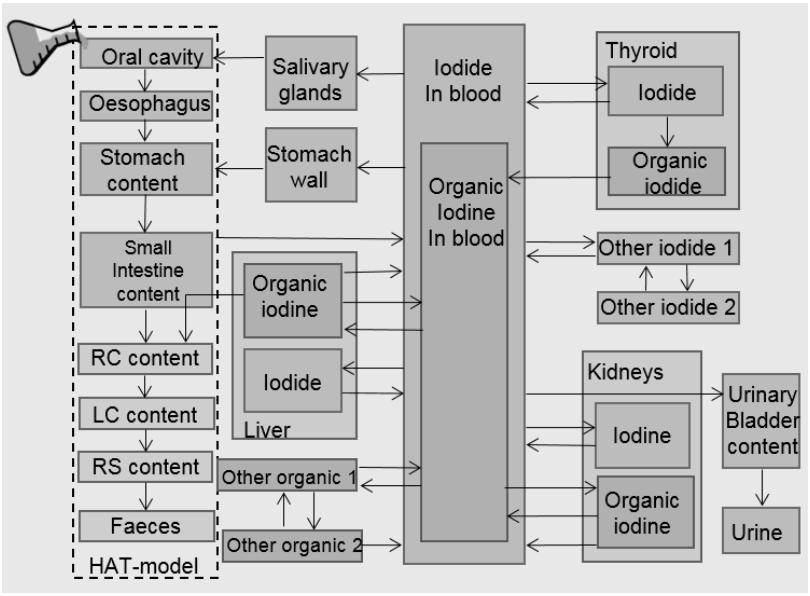

Fig. 1. The ICRP generic biokinetic model for iodine. It models both inorganic iodide and organic iodine and is based on a daily intake of 160 µg of iodine [13,14].

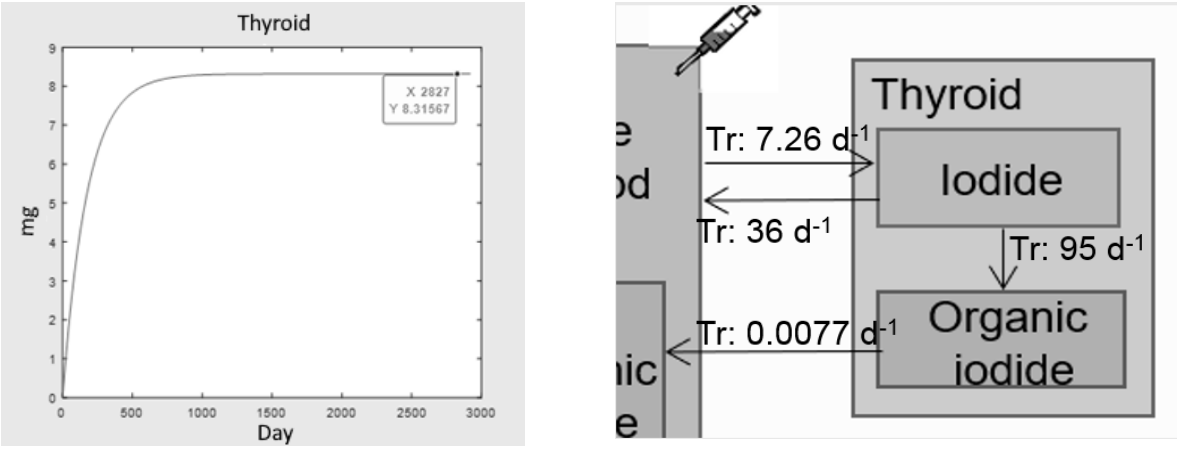

Fig. 2. Biokinetics for stable iodine. A daily intake of 160 µg iodine was assumed to give a steady state level of 8.31 mg of iodine in the thyroid.

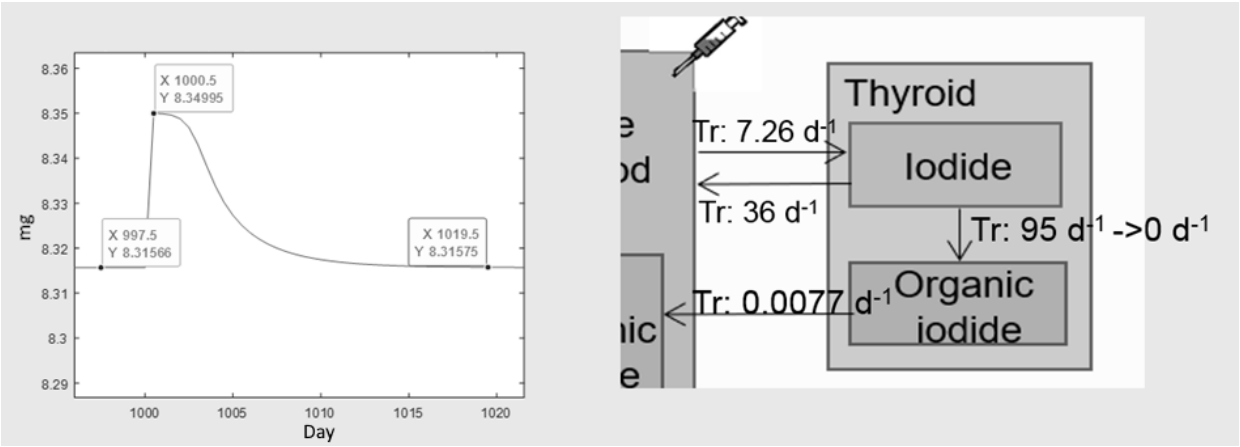

Fig. 3. Adding a dynamic blocking model for stable iodide. At 8.31 mg of iodide in thyroid, Tr= 95 d^{-1}**.** At 8.35 mg of iodine, the thyroid is completely blocked; Tr = 0 d^{-1}

3. Results and discussion

3.1 Effect of amount of stable I for ITB

The effect of ITB with 32 mg of stable I given at different time points relative to radioiodine (^{124}I, ^{125}I and ^{131}I) is shown in Figure 4. Figure 5 shows the corresponding effective dose coefficients (mSv/MBq).

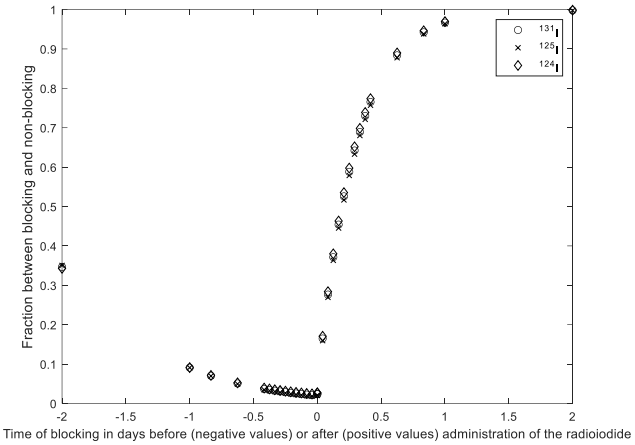

Fig. 4. The effect of ITB with 32 mg stable I given at different time points relative to radioiodine (^{124}I and ^{131}I) intake, presented as fraction of dose reduction to the thyroid (1 = no absorbed dose reduction to the thyroid).

Table 1. Effective dose coefficient, mSv/MBq for various amount of blocking substance given 1 hour before exposure.

Iodine isotope	No blocking	32 mg I	128 mg I
^{124}I	8.6	0.34	0.25
^{125}I	12.5	0.24	0.09
^{131}I	16.4	0.42	0.24

3.2. Effect of timing between radioiodine and ITB

The timing of ITB administration is very important. The lowest effective dose per ingested activity after 32 mg stable iodine administration 1 hour before radioiodine ingestion was 0.34, 0.24 and 0.42 mSv/MBq for ^{124}I, ^{125}I and ^{131}I, respectively (Table 1 and Figure 5). Corresponding data for 128 mg stable iodine was 0.25, 0.09 and 0.24 mSv/MBq for ^{124}I, ^{125}I and ^{131}I, respectively.

The optimal time window for taking iodine tablets is between 24 hours before and up to two hours after expected intake. Up to eight hours after exposure, it may still be justified to take iodine tablets. After that, the benefit is limited.

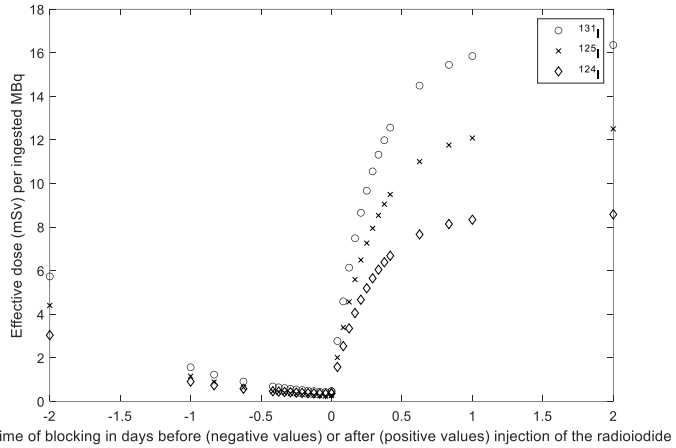

Fig. 5. Effective dose after ingestion of 1 MBq ^{124}I, ^{125}I and ^{131}I and ITB with 32 mg of stable I at different time points relative time of radioiodine ingestion.

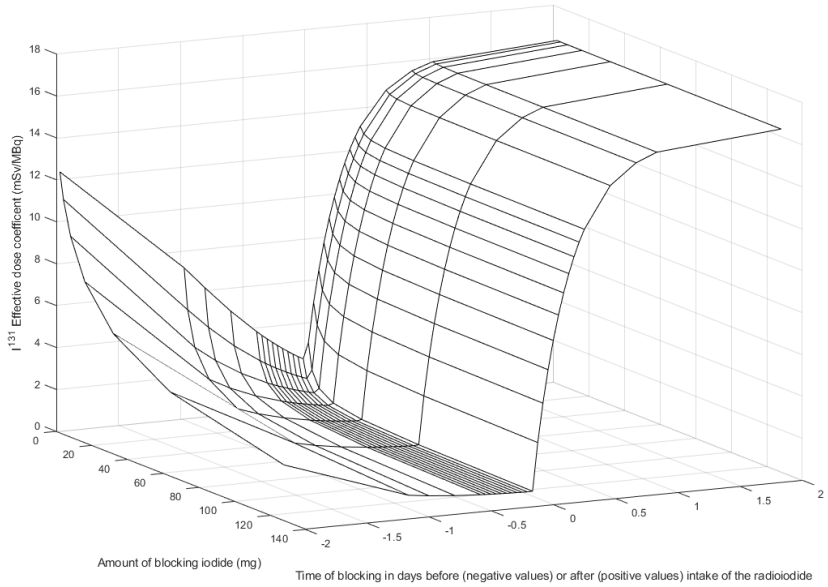

Fig. 6. Effective dose (mSv) as a function of blocking amount of I (mg) and time (day) before (t<0) or after (t>0) intake of 1 MBq ^{131}I.

3.3. Comparison with results of earlier studies

The ICRP biokinetic model separates the uptake of inorganic iodide from its incorporation into organic molecules. The thyroid‘s uptake rate has been described as a function of its total iodine content and reaching a point when uptake uptake is saurated and suppressed. The work by Kwon et al. [16] uses a matemathical relationship between serum iodide concentration and the degree of radioiodine uptake suppression. Similar results regarding timing and required amount of KI have previously been reported by Ramsden et al. [11], Wotton and Hammond [10], and Kwon et al. [16].

3.4. Priorities for future work

There is a need to extend the modelling to younger ages and other groups with significant differences in their biokinetics [18]. Radioiodine biokinetics should therefore be further studied in thyroid patients diagnosed or treated with ^{131}I or ^{123}I. Furthermore, the model should cover continuous exposures as in the clinic or during long-term environmental exposures, such as after the Chernobyl accident. More data are needed on the optimal amount and timing for multiple administrations of stable iodine in case of repeated or protracted releases of radioactive iodine, and the potential adverse health effects of stable iodine administration. Research on feasibility, acceptability and overall effect of use of ITB on psychosocial outcomes of radiation emergencies should also be performed.

4. Conclusions

The effectiveness of the thyroid blocking is dependent on both the amount and timing of supplementary stable iodide relative to radioiodide administration, and both parameters can be optimised with the model. The extended models and supporting computational tools were implemented, and simulations were performed for the iodine isotopes ^{124}I, ^{125}I and ^{131}I. This method enables more detailed dosimetric assessments and improved radiation protection strategies in nuclear medicine applications as well as for radiation and nuclear emergencies.

5. Appendix

Current recommendations for iodine thyroid blocking

A1. Recommendations in connection with nuclear medicine diagnostics and therapy

When ^{123}I, ^{124}I, ^{125}I or ^{131}I is administered as iodinated compounds, with or without iodide as a radiochemical impurity, a significant portion of the effective dose is derived from irradiation of the thyroid gland. Thyroid blocking is therefore recommended for all iodinated compounds not intended for imaging or treatment of the thyroid gland itself [15,19]. Blocking reduces the absorbed dose to the thyroid gland when radioiodine is administered as mIBG, albumin, fibrinogen or other labeled compounds. Before administering a radioiodine compound that is metabolised to iodide or that contains radioiodine impurities, consideration should be given to blocking the thyroid gland. Various formulations of iodide and iodate are available for oral and intravenous administration. The iodine content of commonly used blocking agents is: 65 mg of potassium iodide contains 50 mg of iodine; 1 ml of aqueous iodine (Lugol's iodine) contains 130 mg of iodine.

It should be noted that adverse effects might occur after high amounts of KI, such as hyper- or hypothyroidism and allergic and anaphylactic reactions. The incidence is, however, low and in many cases reversible [20]. If iodine is contraindicated, thyroid blocking can be performed with potassium perchlorate (200 mg for adults). Sodium perchlorate (2 ml vials containing 200 mg for intravenous use) can also be used [19].

A2. Recommendations in connection with nuclear emergencies in peacetime

The since long time discussed importance of iodine tablet intake in connection with releases associated with accidents at nuclear power plants gained significant attention after the Chernobyl disaster after which there was a notable increase in thyroid cancer, especially among childred exposed to ^{131}I [20-24].

International guidelines

WHO [25] has developed guidelines for iodine thyroid blocking in connection woth radiological and nuclear emergencies. Staying indoors is the primary protective measure in a radiation hazard situation. Taking iodine tablets is a supportive measure.

If there is a risk of exposure, iodine tablets are recommended for people under 40 years of age and for pregnant and breastfeeding women (Table 2). Children and pregnant women (fetuses) are particularly sensitive, which means that these groups should be prioritised if there is a shortage of iodine tablets. Iodine tablets should only be taken at the request of the competent authorities. Iodine prophylaxis is obligatory when the predicted thyroid dose levels are above 500 mSv for adults and above 50 mSv for children and pregnant women. These doses refer to the initial stage of the accident or to a one-week period after the accident.

Since KI provides protection for approximately 24 hours, it should be administered daily until the risk is no longer present. If primary public health protection measures (evacuation, protection, and control of the food supply) cannot be implemented immediately, multiple doses of KI may be required, sometimes up to 7–14 days. Unless other protective measures are available, repeated administration to pregnant women and neonates is not recommended. KI tablets can be stored and are effective for up to 12 years if stored in a dry place and at a temperature between 15 and 30 degrees C.

Nordic guidelines

The Nordic guidelines [26] apply for off-site preparedness and response for a nuclear or radiological emergency in peacetime, irrespective of the cause. They represent a common Nordic view on how the internationally accepted radiation protection principles apply in the Nordic countries, within the framework of

national regulations. The Nordic guidelines apply for the preparedness stage and emergency response, up until the transition from, and termination of, a nuclear or radiological emergency. The guidelines focus on such protective actions and other response actions where there is a need for cross-border alignment within the Nordic region. This includes actions relevant to implement:

1. at larger distances from a facility (e.g. nuclear power plant), i.e. beyond the emergency planning zones; and
2. in the event of an emergency arising from activities and acts where the location is not known beforehand, such as nuclear powered vessels at sea.

Dose criteria for intake of pre-distributed ITB are: 50 mSv equivalent dose to the thyroid gland for adults, and 10 mSv equivalent dose to the thyroid gland for infants and children (< 18 y).

Table 2. Recommended amount of stable iodine for various age groups [25].

Age	Mass of I (mg)	Mass of KI (mg)	Mass of KIO_3 mg	Fraction of tablet with 100 mg I	How often?
Neonates 0-1 month	12.5	16.3	21	1/8	Single intake only
1-36 months	25	32.5	42	1/4	Daily, crushed in food/fluids
3-12 years	50	65	85	1/2	Daily
Over 12 years. adults	100	130	170	1	Daily

National guidelines

National recommendations for iodine tablets differ from country to country [27], but are all primarily focused on their use during radiological emergencies such as nuclear power plant accidents. They emphasise the importance of taking the tablets only after instructions from the national authorities and focus on various amounts for differnt age groups.

A3. Nuclear weapon detonation

In the event of the worst nuclear and radiological disaster, a nuclear attack on the own country or a neighboring country in the event of war, the public in the risk area for radioactive fallout is urged to seek protection in a shelter. Taking iodine tablets is not normally a justified protective measure in the event of a nuclear weapon detonation [26]. The reason is that the fallout contains only a small amount of radioactive iodine compared to other radioactive materials that will harm people via external exposure.

6. References

1. Riggs D.S. Quantitative aspects of iodine metabolism in man. Pharmacol Rev 4, 284-370, 1952.
2. Mattsson, S., Johansson, L., Jönsson, H., and Nosslin, B. Radioactive iodine in thyroid medicine - How it started in Sweden and some of today's challenges, Acta Oncologica 45, 1031-1036, 2006.
3. Zhang, S., Wang, X., Gao, X., Chen, X., Li, L., Li, G., Liu, C., Miao, Ywang R., and Hu., K. Radiopharmaceuticals and their applications in medicine. Sig Transduct Target Ther 10, 1, 2025.
4. ICRP. Radiological protection of people and the environment in the event of a large nuclear accident: update of ICRP Publications 109 and 111. ICRP Publication 146.Ann. ICRP 49(4), 2020..
5. Drozdovitch V. Radiation Exposure to the Thyroid After the Chernobyl Accident. Front. Endocrinol. 11:569041, 2021.
6 .Bouville, A. Fallout from nuclear weapons tests: Environmental, health, political, and sociological considerations. Health Phys 118(4), 360–381, 2020.
7. Axelsson, A., Kock, P., Johansson, J., Lindgren, J., Blixt Buhr, A.M., Boson, J., Bäverstam, U., and Karlsson, S.. Radiological consequences of fallout from nuclear explosions. Report number: 2023:05e. ISSN: 2000-0456. Available at www.ssm.se.
8. Verger, P., Aurengo, A., Geoffroy, B., and Le Guen, B. Iodine kinetics and effectiveness of stable iodine prophylaxis after intake of radioactive iodine: A review. Thyroid 11(4), 353-360, 2001.
9. Paladino, M.E., Belingheri, M., Mazzagatti, R., and Riva, M.A. Iodine thyroid blocking. A lesson from the worst nuclear accidents in history. Intern Emerg Med **17**, 2449–2450, 2022.
10. Wootton, R. and Hammond, B.J.A. Computer simulation study of optimal thyroid protection during investigations involving the administration of radioiodine labelled pharmaceuticals. Br J Radiol 51, 265-272, 1978.
11. Ramsden, D.S., Passant, F.H., Peabody, C.O., and Speight, R.G. Radioiodine uptakes in the thyroid. Studies of the blocking and subsequent recovery of the gland following the administration of stable iodine. Health Phys 13(6), 633-646, 1967.
12. Rump, A., Eder, S., Hermann, C., Lamkowski, A., Kinoshita, M., Yamamoto, T., Take, J., Abend, M., Shinomiya, N., and Port, M. Modeling principles of protective thyroid blocking, Int J Radiat Biol, 98(5), 831-842, 2022.
13. Leggett, R.W. A physiological systems model for iodine for use in radiation protection. Radiat Res 174(4), 496-516, 2010.
14. ICRP. Occupational intakes of radionuclides: Part 3. ICRP Publication 137. Oxford: Pergamon Press. Ann. ICRP 46(3/4), 2017.
15. ICRP, International Commission on Radiological Protection. Radiation dose to patients from radiopharmaceuticals: a compendium of current information related to frequently used substances. ICRP Publication 128. Ann. ICRP 44, 7–321, 2015.
16. Kwon, T.-E., Chung, Y., Ha, W.-H., and Jin, Y.W. Application of the new ICRP iodine biokinetic model for internal dosimetry in case of thyroid blocking. Nuclear Engineering and Technology 52(8), 1826-1833, 2020.
17. Andersson, M., Johansson, L., Eckerman, K and Mattsson, S. IDAC-Dose 2.1, an internal dosimetry program for diagnostic nuclear medicine based on the ICRP adult reference voxel phantoms. EJNMMI Research 7, Article 88, 2017.
18. Kwon T-E, Chung Y and Jin YW. Korean-specific biokinetic model for iodine in radiological protection J. Radiol. Prot. 41 162–78, 2021.
19. ARSAC, Administration of Radioactive Substances Advisory Committee, UK. Notes for guidance on the clinical administration of radiopharmaceuticals and use of sealed radioactive sources. Updated 31 March 2025. https://www.gov.uk/government/publications/arsac-notes-for-guidance
20. Nauman, J., and Wolff, J. Iodide prophylaxis in Poland after the Chernobyl reactor accident: Benefits and risks. Am J Med 94, 524–432, 1993.
21. UNSCEAR. Evaluation of data on thyroid cancer in regions affected by the Chernobyl accident. A white paper to guide the Scientific Committee's future programme of work. United Nations, New York, 2018.
22. Kazakov, V., Demidchik, E., and Astakhova, L. Thyroid cancer after Chernobyl. Nature 359, 21, 1992.
23. Likhtarev, I., Sobolev, B., Kairo, I., Tronko, N., Bogdanova, T., Oleinic, V., Epshtein, E.V. and Beral, V. Thyroid cancer in the Ukraine. Nature. 375, 365, 1995.
24. Cardis, E., Kesminiene, A., Ivanov, V., Malakhova, I., Shibata, Y., Khrouch, V., et al. Risk of thyroid cancer after exposure to ^{131}I in childhood. Journal of the National Cancer Institute 97(10), 724–732, 1995.
25. WHO. Iodine thyroid blocking. Guidelines for use in planning for and responding to radiological and nuclear emergencies. ISBN 978 92 4 155018 5 © World Health Organization, 2017.
26. Kock, P., Johansson, J., Thørring, H., Kuusi, A., Israelson, C., Jónsson, G., and Breddam, K. Protective actions in a nuclear or radiological emergency. Nordic Guidelines, Nordic Emergency Preparedness Group (NEP). Nordic Radiation and Nuclear Safety Series, Number 02:2024. ISBN number: 978-91-990057-3-7..
27. Willems, P., Carr, Z., Dreger, S., Zeeb, H., Tchilian-Teng, N., Amith, V., and Van Bladel, L. Survey on national practices regarding iodine thyroid blocking in 2016-2017. Environmental Advances 8, 100252, 2022.

Level automatically in seconds, and with confidence

Achieve sub-millimeter accuracy in a single setup

Use preset machine-specific profiles

Your Trusted Partner for Clinical Workflow Solutions

Machine QA & Commissioning

myQA Blue Phantom³

Meet and test the most advanced 30 water phantom for reliable beam scanning on the market and test the new quick levelling function at site.

Learn more

Patient Specific QA in Motion-Guided RT

myQA SRS with QUASAR™ HD-Platform

Ensure precise QA in motion-guided Radiation Therapy. Are you hitting your target?

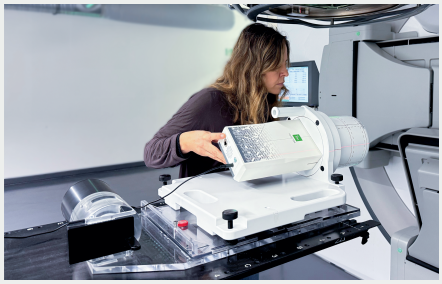

Learn more

Machine and Imaging QA

Radcal T3 QA Meter with NEW Accu-Gold 3 Sofware

Discover the industry-exclusive Smart Profile Technology in one single setup and multitask with ease. Now with extended Wi-Fi connectivity.

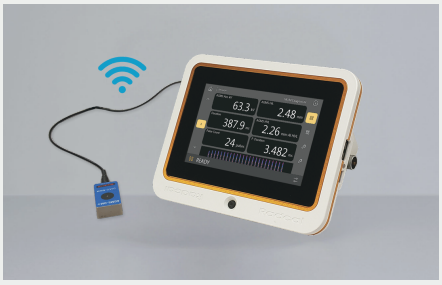

Learn more

Motion Management & SGRT

QUASAR™ Respiratory Motion Phantom 2.0

Simulate patient breathing, verify SGRT workflows, and avoid gated treatment errors.

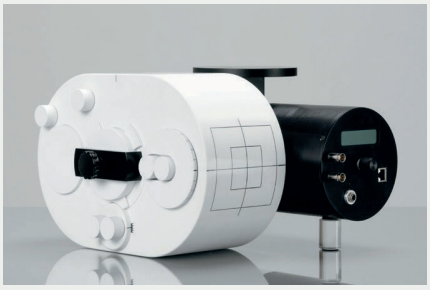

Learn more

For our latest updates, make sure to follow us on @ibadosimetry

MEDICAL PHYSICS IN THE BALTIC STATES 17 (2025)

Proceedings of International Conference "Medical Physics 2025"
06-08 November 2025, Kaunas, Lithuania

EVALUATION OF CT ACQUISITION PARAMETERS AND SIZE DISTORTIONS IN HYBRID SPECT/CT LUNG NODULES IMAGING USING ^{99M}TC: A PHANTOM-BASED STUDY

Kristina REPŠĖ[1], Vilius MILAŠIUS[2], Aurimas KRAULEIDIS[3], Vytenis PUNYS[4]
[1]Klaipeda University Hospital; [2]Klaipeda University Hospital; [3]Klaipeda University Hospital; [4]University of Klaipeda
[1]kristinarepse@gmail.com; [2]mvmilasius@gmail.com; [3]aurimas.krauleidis@gmail.com; [4]vytenis.punys@ku.lt

***Abstract*:** Hybrid SPECT/CT combines functional and anatomical information, enhancing diagnostic accuracy in nuclear medicine. Optimising CT acquisition parameters is essential for reliable attenuation correction and quantitative assessment. This study aimed to evaluate the impact of CT acquisition parameters on attenuation correction and image quality in SPECT imaging using a ^{99m}Tc source. CT acquisition parameters, injected dose, and attenuation mapping strongly influence SPECT/CT image quality. Minor inaccuracies were linked to attenuation coefficients, underscoring the need for further studies on reconstruction algorithms.

Keywords: SPECT; SPECT/CT; attenuation correction; size distortion.

1. Introduction

In diagnostic imaging, maintaining high image quality is essential for accurate clinical assessment. Hybrid single-photon emission computed tomography/computed tomography (SPECT/CT) has become an integral tool in quantitative nuclear medicine, particularly in patient-specific dosimetry. Its primary role is to enable precise attenuation correction of SPECT data through the CT component, thereby improving quantitative reliability while adhering to the ALARA (As Low As Reasonably Achievable) principle to minimize ionizing radiation exposure. During CT acquisition, it is therefore important to optimize imaging parameters in order to reduce radiation dose without compromising the anatomical fidelity required for attenuation correction, lesion localization, or volumetric assessment. Striking an appropriate balance between image quality and patient safety thus remains a key challenge in the development of SPECT/CT imaging protocols, especially in applications involving lung imaging with ^{99m}Tc tracers [1–4].

In nuclear medicine, functional imaging techniques provide information on physiological activity and underlying biological processes. By integrating anatomical data, it becomes possible to determine the exact location of radiotracer uptake observed on scans. This localization is critical for distinguishing normal physiological uptake from pathological findings. Once an abnormality is detected, accurate anatomical correlation greatly enhances diagnostic confidence and facilitates optimal treatment planning [5,6].

From a clinical perspective, precise measurement of lung nodule size is particularly important. Small differences in diameter or volume can determine whether a lesion is classified as benign, malignant, or indeterminate, directly influencing patient management. Furthermore, accurate anatomical correlation in hybrid imaging supports radiation therapy planning, assessment of treatment response, and early detection of recurrence. Consequently, understanding how imaging parameters affect the reliability of nodule size quantification is of significant clinical relevance [7,8].

A further methodological challenge in nuclear medicine research is the evaluation of image acquisition time and data quality. Systematic investigation of shortened acquisition protocols cannot be performed through repeated scans of the same human subject due to ethical considerations, the additional imaging burden, and the effects of radiotracer decay. Similarly, phantom studies are subject to the constraints of radioactive decay and scanner availability. For these reasons, methodological approaches that allow the resampling or re-binning of acquisition data into variable time frames are required to simulate shorter scan durations and assess their impact on image quality and quantitative accuracy [9,10].

Phantom-based studies provide a controlled and reproducible environment to evaluate these factors. By using anthropomorphic phantoms containing nodules of known size and composition, it is possible to systematically investigate the influence of CT acquisition parameters on size measurement bias and volumetric distortions in hybrid SPECT/CT imaging. This approach avoids the ethical and biological limitations associated

with patient studies, while enabling detailed analysis of scanner performance and protocol optimization. Therefore, the aim of this study is to evaluate the impact of CT acquisition parameters on size distortions in hybrid SPECT/CT imaging of lung nodules using ^{99m}Tc, based on a phantom experimental model.

2. Methods and Methodology

2.1. Study design

This experimental, phantom-based study was designed to evaluate the effect of different CT acquisition parameters on attenuation correction and image quality in hybrid SPECT/CT imaging of lung nodules. The use of a phantom allowed precise control over nodule size, radiopharmaceutical activity, and imaging conditions without the variability associated with human subjects.

2.2. Phantom specification and preparation

An anthropomorphic phantom (LUNGMAN; Kyoto Kagaku, Kyoto, Japan) was used to simulate the adult chest (Fig. 1). The phantom provides lung-equivalent regions and anatomically realistic thoracic structures, enabling reproducible placement of lesions within the lung fields.

Fig. 1. An anthropomorphic phantom "Lungman"

Artificial lung nodules were created using Eppendorf tubes of three volumes (0.2 ml, 1.0 ml, and 1.5 ml) (Fig.2.). Each tube was filled with ^{99m}Tc activity 10, 20, and 30 MBq, respectively, to model different tracer accumulation. Prepared nodules were positioned in predefined locations within the left and right lung compartments to simulate variable lesion sizes and activities.

Fig. 2. Eppendorf tubes of three different volumes

2.3. Imaging protocol

CT acquisition: Four CT protocols were tested, consisting of 100 kV and 120 kV tube voltages combined with 20 mA and 40 mA tube currents. Slice thickness, matrix size, and reconstruction kernel were kept constant to isolate the influence of kV and mA.

SPECT acquisition: SPECT imaging was performed using AnyScan SC hybrid SPECT/CT (Mediso, 2020) system equipped with a low-energy high-resolution (LEHR) collimator. The spatial resolution of the SPECT/CT system used in this study was 7,4 mm FWHM. An energy window of 140 keV ± 10% was applied for ^{99m}Tc. Data were acquired with a 128×128 matrix over 60 projections, with an acquisition time of 30 seconds per projection. SPECT images were reconstructed using iterative OSEM algorithms with 6 iterations and 10 subsets, including attenuation and scatter correction. Acquisition parameters were kept constant across all experiments to ensure comparability.

2.4. Image reconstruction and processing

CT data were reconstructed using standard filtered back-projection, and attenuation correction was applied to the corresponding SPECT datasets. SPECT images were reconstructed with attenuation, scatter, and resolution recovery corrections.

2.5. Image analysis

All images were processed using open-source software:

- **ImageJ** for two-dimensional measurements, signal intensity, and signal-to-noise ratio (SNR) calculations.
- **3D Slicer** for volumetric visualization and quantitative assessment of lesion size, volume distortions, and contrast recovery.

Signal-to-noise ratio (SNR) was calculated as:

$$SNR = \frac{S_{lesion}}{\sigma_{background}} \quad (1)$$

where S_{lesion} is the mean signal intensity within the lesion, and $\sigma_{background}$ is the standard deviation of background counts.

Size distortion (%) was assessed using:

$$Size\ distortion(\%) = \frac{V_{measured} - V_{true}}{V_{true}} \times 100 \quad (2)$$

where $V_{measured}$ is the nodule volume measured on SPECT/CT, and V_{true} is the known physical volume of the Eppendorf tube.

2.6. Statistical analysis

Quantitative parameters and image quality metric (SNR, noise levels, size distortions) were compared across different CT acquisition settings. Statistical analysis was performed using Microsoft Excel (Microsoft Corporation, USA). Descriptive statistics, including mean values, standard deviation, and percentage differences, were calculated to summarize the results obtained from ImageJ and 3D Slicer measurements.

3. Results

3.1. Dependence of SNR on CT acquisition parameters

Analysis demonstrated that SNR was strongly influenced by CT tube voltage and tube current settings (Table 1).

Table 1. Dependence of SNR on CT parameters

CT protocol	Nodule size 0.2 ml	Nodule size 1.0 ml	Nodule size 1.5 ml
100 kV/20 mA	5,4	9,3	13,0
100 kV/40 mA	6,0	10,5	14,7
120 kV/20 mA	7,9	11,5	15,7
120 kV/40 mA	10,3	15,5	17,2

Lower-dose protocols (100 kV / 20 mA) produced the lowest SNR values, particularly for the smallest nodules (0.2 ml), where the signal was highly affected by noise. Increasing either tube voltage (to 120 kV) or tube current (to 40 mA) improved SNR by up to 90 % compared with the lowest-dose protocol. The effect of CT acquisition parameters was most pronounced in small nodules, while larger nodules (1.5 ml) exhibited relatively stable SNR values across different CT settings (Fig.3).

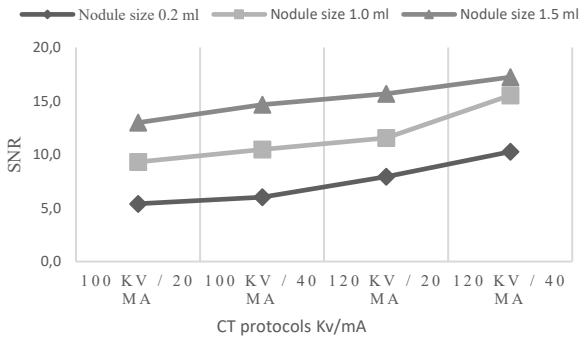

Fig. 3. Dependence of SNR on CT parameters

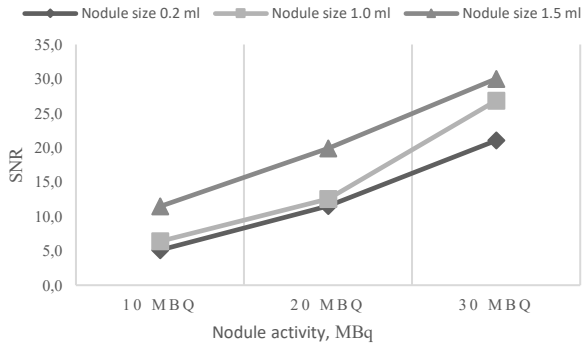

Fig.4. Dependence of SNR on the activity of the node

3.2. Dependence of SNR on nodule activity

SNR also depended on the injected activity of the nodules. At 10 MBq, SNR was lowest for all nodule sizes, with the greatest variability seen in the smallest nodules. Increasing the activity to 20 and 30 MBq significantly improved SNR, with average increases of 125% and 311% compared to 10 MBq. Larger nodules demonstrated higher baseline SNR values, but the relative improvement with increasing activity was more evident in the smaller nodules, confirming that activity amount plays a critical role in image quality (Fig.4).

3.3. Nodule size distortion in CT imaging

Assessment of measured versus true nodule volumes revealed systematic size distortions, particularly for the smallest nodules (Table 2).

The 0.2 ml nodules were consistently overestimated, with relative errors reaching up to 60% depending on the CT protocol. For 1.0 ml nodules, the distortion was smaller (on the order of 11%), while 1.5 ml nodules showed minimal differences (<7%). These findings indicate that partial volume effects and noise contribute substantially to the overestimation of small nodule volumes, while larger nodules are less affected by CT acquisition parameters (Fig.5).

Table 2. Distortion of Nodule Size in CT Imaging

Nodule true volume (ml)	CT protocol (kV/mA)	Measured volume (ml)	Absolute error (ml)	Relative error (%)
0,2	100 kV / 20 mA	0,32	0,12	60%
0,2	120 kV / 40 mA	0,21	0,01	5%
1	100 kV / 20 mA	1,11	0,11	11%
1	120 kV / 40 mA	1,03	0,03	3%
1,5	100 kV / 20 mA	1,6	0,1	7%
1,5	120 kV / 40 mA	1,53	0,03	2%

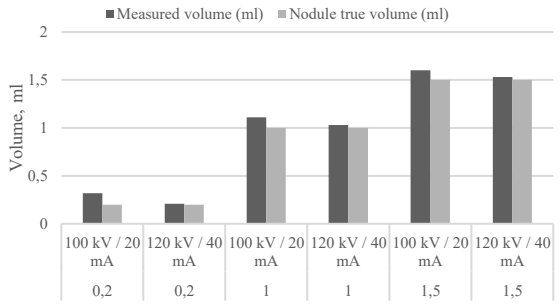

Fig. 5. Nodule size distortion in CT imaging

4. Discussion

This study demonstrated that CT acquisition parameters and nodule activity significantly affect SNR and size accuracy in SPECT/CT imaging. Higher tube voltage and current improved SNR, particularly in small nodules, while lower-dose protocols resulted in substantial noise contribution. These findings suggest that CT settings must be carefully optimized to balance image quality and radiation exposure.

The observed dependence of SNR on nodule activity highlights the importance of sufficient radiotracer concentration, especially for nodules below 1 ml, where partial volume effects and image noise have the greatest impact. Similar trends were reported by phantom studies demonstrating that reconstruction parameters—including

the number of iterations and scatter correction weight—significantly influence both quantitative accuracy and SNR in SPECT imaging using ^{99m}Tc [11].

Volume distortion was most pronounced in the smallest nodules (0.2 ml), consistent with partial volume effects and resolution limitations. Studies using IEC phantoms have shown substantial underestimation of regional uptake in small volumes (<10 cm), underscoring similar size-dependent distortions observed in our data [12;13]. The underlying mechanism—signal blurring for structures smaller than approximately twice the FWHM—has been well characterized in both SPECT and PET systems [12;13].

Additionally, recent research employing the LUNGMAN anthropomorphic phantom confirmed that CT acquisition settings (e.g., kV and mA) significantly affect size and density measurements of pulmonary nodules, offering a valuable parallel to our findings [14].

The main limitation of this study is the use of a lung phantom, which cannot fully replicate patient-specific anatomical variations and motion artifacts. Moreover, only one reconstruction method was evaluated. Future work should include patient datasets and advanced reconstruction algorithms to better assess clinical applicability.

Overall, the results indicate that optimizing CT protocols and ensuring adequate radiotracer activity are crucial for accurate attenuation correction and reliable nodule quantification in hybrid SPECT/CT imaging.

4. Conclusions

This phantom-based study demonstrated that CT acquisition parameters and nodule activity significantly influence image quality and quantitative accuracy in hybrid SPECT/CT imaging. Higher tube voltage and current settings improved the signal-to-noise ratio, particularly for small nodules, while low-dose protocols were associated with greater image noise and increased size distortion. Adequate radiotracer activity was also essential for reliable quantification, with insufficient activity leading to substantial SNR degradation.

Size distortions were most pronounced in nodules ≤0.2 ml, reflecting partial volume effects and resolution limitations, whereas nodules ≥1.5 ml showed minimal deviations from their true size. These findings highlight the importance of carefully optimizing CT protocols and ensuring sufficient radiotracer activity to achieve accurate attenuation correction and volumetric assessment in SPECT/CT imaging.

Future studies should focus on patient datasets and advanced reconstruction techniques to validate these results in clinical practice and further reduce inaccuracies in hybrid imaging.

5. References

1. Lassmann M, Eberlein U, Kamp F, et al. EANM guideline for quantitative SPECT in nuclear medicine. Eur J Nucl Med Mol Imaging. 2022;49(2):389-427.

2. International Atomic Energy Agency. SPECT/CT Atlas of Quality Control and Image Artefacts. IAEA Human Health Series No. 41. Vienna: IAEA; 2019. Available at: https://www-pub.iaea.org /MTCD/ Publications/PDF/PUB1971_web.pdf

3. Bailey DL, Willowson KP. Quantitative SPECT/CT: SPECT joins PET as a quantitative imaging modality. Eur J Nucl Med Mol Imaging. 2014;41(Suppl 1): S17-25.

4. Einstein AJ, Moser KW, Thompson RC, Cerqueira MD, Henzlova MJ. Radiation dose to patients from cardiac diagnostic imaging. Circulation. 2007;116(11):1290-1305.

5. Hutton BF, Buvat I, Beekman FJ. Review and current status of SPECT instrumentation. J Nucl Med. 2011;52(1):10-23.

6. Černá M, Ljungberg M, Söderberg M, et al. Hybrid SPECT/CT imaging in clinical practice: basic principles, applications and future directions. Phys Med. 2020; 76:199-209.

7. Zhao B, Tan Y, Tsai WY, Schwartz LH, Lu L. Exploring variability in CT characterization of tumors: a preliminary phantom study. Transl Oncol. 2014;7(1):88-93.

8. Gavrielides MA, Kinnard LM, Myers KJ, Petrick N. Noncalcified lung nodules: volumetric assessment with thoracic CT. Radiology. 2009;251(1):26-37.

9. Ljungberg M, Pretorius PH. SPECT data acquisition, modeling and reconstruction for quantitative SPECT. Phys Med Biol. 2018;63(1):01TR01.

10. Sanders JC, Kuwert T, Hornegger J, Ritt P. Quantitative SPECT/CT imaging of radionuclide distribution in the body. Phys Med Biol. 2015;60(22):R239-R276.

11. Enqvist O, Oddstig J, Tragardh E, Garpered S, Lubberink M, Oddstig J, et al. Performance characteristics of quantitative ^{99m}Tc SPECT/CT: a phantom study. EJNMMI Phys. 2021;8(1):61.

12. Tran-Gia J, Lassmann M. Partial volume effects in SPECT and PET and their impact on radionuclide dosimetry estimates. EJNMMI Phys. 2023;10(1):10.

13. Soret M, Bacharach SL, Buvat I. Partial-volume effect in PET tumor imaging. J Nucl Med. 2007;48(6):932–45.

14. Cheng S, Lee J, Kim Y, Goo JM. Quantitative CT evaluation of artificial pulmonary nodules with the LUNGMAN phantom: impact of tube voltage and current. BMC Med Imaging. 2023; 23:190.

MEDICAL PHYSICS IN THE BALTIC STATES 17 (2025)

Proceedings of International Conference "Medical Physics 2025"
06-08 November 2025, Kaunas, Lithuania

TRENDS IN OCCUPATIONAL RADIATION EXPOSURE RELATED TO FACILITY-SYNTHESISED PET RADIOPHARMECEUTICALS AT A UNIVERSITY HEALTH CENTER IN KAUNAS, LITHUANIA

Mantvydas MERKIS[1], Gabija NEMEIKŠĖ[2], Agnė LISAUSKAITĖ[3], Eglė BALČIŪNAITYTĖ[4], Deivydas GIEDRIMAS[5], Ieva JOGAITĖ[6]
[1-4, 6]The Hospital of Lithuanian University of Health Sciences Kauno klinikos; [2-5]Lithuanian University of Health Sciences
[1]mantvydas.merkis@kaunoklinikos.lt; [2]gabija.nemeikse@kaunoklinikos.lt; [3]agne.lisauskaite@kaunoklinikos.lt; [4]egle.balciunaityte@kaunoklinikos.lt; [5]deivydas.giedrimas@stud.lsmu.lt; [6]ieva.jogaite@kaunoklinikos.lt;

***Abstract*:** The demand for more radiological diagnostic procedures in nuclear medicine departments is rapidly increasing alongside the expanding indications for positron emission tomography (PET). During 2024, about 2000 PET exams were performed at the Hospital of the Lithuanian University of Health Sciences - Kauno Klinikos. PET imaging requires short half-life positron emitters bound to specific molecules, which may either indicate the level of glucose metabolism within tumor cells (^{18}F-FDG) or bind to tumor-specific receptors, located in prostate (^{68}Ga-PSMA) or neuroendocrine (^{68}Ga-DOTATATE) organs and tissues. In Q3 2024, studies using ^{68}Ga-PSMA and -DOTATATE were introduced, also at the end of Q1 2025 in-house production of ^{18}F-FDG was launched in the country's first cyclotron. This highlighted the need to access the potential increase in occupational exposure, particularly among radiochemists, who work in the ^{18}F-FDG synthesis laboratory or perform elution and radiolabeling of ^{68}Ga. The aim of this study was to evaluate the equivalent dose for lens of the eye Hp(3) and hands Hp(0.07), as well as the effective whole body dose Hp(10), measured by thermoluminescent, optically-stimulated luminescence (OSL) and electronic dosimeters. The acquired exposure data were compared with data from the previous quarter in order to determine the effect of these new procedures on occupational exposure of the personnel working in the department.

Keywords: nuclear medicine, occupational exposure, PET, dosimetry, radiochemistry.

1. Introduction

The use of radiopharmaceuticals in clinical practice is rapidly increasing due to their ability to precisely determine the spread of disease [1].

Radiopharmaceuticals generally consist of a radionuclide and a vector that enables targeted delivery. Positron emitters are particularly useful for diagnostic purposes. During positron-electron annihilation in tissues, two parallel photons are produced which enables precise localization of lesions and offers superior sensitivity compared to the widely used ^{99m}Tc-based compounds [2]. Common positron emitters are ^{18}F, ^{68}Ga, ^{13}N, and ^{11}C. Among these, ^{18}F is the most widely used for clinical purposes. When labeled with the glucose analogue FDG, the tracking of higher metabolic activity in cancerous tissue becomes possible [3]. There is also a high demand for ^{68}Ga-labeled radiopharmaceuticals such as ^{68}Ga-PSMA for prostate cancer imaging [4] or ^{68}Ga-DOTATATE for staging neuroendocrine tumors and deciding on treatment strategies [5]. ^{68}Ga-PSMA can be successfully used in a theragnostic approach alongside ^{177}Lu-PSMA to assess the response to therapy [6].
Despite the significant advantages of positron-emitting radiopharmaceuticals such as ^{18}F-FDG, their production is considerably more complex than that of radiopharmaceuticals used in Single Photon Emission Tomography (SPECT) for example ^{99m}Tc based compounds. The synthesis of ^{18}F-FDG in the Hospital of the Lithuanian University of Health Sciences - Kauno Klinikos is carried out in fully automated synthesis module housed in shielded hot cells. The radiochemical transformations – fluoride trapping, nucleophilic substitution, hydrolysis, purification, and formulation – are performed automatically using ABX cassettes, and reagent kits. Manual intervention is limited to preparatory steps such as loading reagent vials, positioning cassettes, or attaching prepared cartridge prior to synthesis. Most of the occupational exposure occurs not during synthesis itself, but rather at subsequent stages: when the final product vials are removed from the hot cell after dispensing, when containers are transported for clinical use, and during

mandatory quality control procedures. When performing QC tests – radiochemical purity, residual solvents, pH, sterility – outside the synthesis modules, radiochemists are most exposed to the radiation due to the high activity concentration of ^{18}F-FDG radiopharmaceutical [7].

In contrast, the preparation of ^{68}Ga-based radiopharmaceuticals using ^{68}Ge/^{68}Ga generators in combination with pre-prepared commercial kits is operationally simpler. Nevertheless, the method requires a higher degree of manual handling. Generator elution to the reaction vial, addition of buffer solutions, measure of the final radiopharmaceutical vial with dose calibrator, and sampling for quality control – all require direct intervention by the radiochemist. The manual manipulations with the kit are typically performed in shielded cabinets but still bring the operator's hands near radioactive material. In addition, radiochemists get radiation exposure during quality control test (radiochemical and radionuclidic purity along with pH). As a result, despite the relative simplicity of kit-based synthesis, manual operations remain the principal source of occupational radiation exposure during ^{68}Ga radiopharmaceutical preparation.

In Q3 2024, the first studies using ^{68}Ga-PSMA and ^{68}Ga-DOTATATE were fully introduced at the Hospital of the Lithuanian University of Health Sciences – Kauno Klinikos. This introduction increased the number of manual operations performed by radiochemists synthesizing these radiopharmaceuticals. Furthermore, in Q1 2025, in-house production of ^{18}F-FDG was launched at the country's first cyclotron, expanding the scope of procedures for radiochemists even further. This raises the question how the occupational exposure of radiochemists was affected after the introduction of new procedures for the synthesis of PET radionuclides. To answer this question, the equivalent dose for the lens of the eye, Hp (3), and hands, Hp(0.07), as well as the effective whole-body dose, Hp(10), were measured using thermoluminescent, optically-stimulated luminescence and electronic dosimeters. The acquired exposure data was compared to data from the previous quarter to determine the effect of these new procedures on the occupational exposure of personnel working in the department.

2. Materials and Methods

Doses of radiochemists working in the nuclear medicine department were monitored using thermoluminescent ring dosimeters (AWST-TL-TD70), optically-stimulated luminescence personal dosimeters (Landauer InLight), and electronic dosimeters (Polimaster PM1610B). Equivalent dose for the lens of the eye Hp(3) and hands Hp(0.07), as well as the effective whole body dose Hp(10) were monitored quarterly for one year, from Q2 2024 to Q2 2025. Dose and dose rate evaluations during single synthesis using electronic dosimeters were performed from Q4 2024 to Q2 2025.

The number of working radiopharmacists varied from 4 in Q2 2024 to 6 in Q2 2025. Therefore, a collective dose evaluation was performed to account for the varying workload.

Initially, the department only used ^{18}F-FDG for PET examinations, which was produced at another facility. The synthesis of ^{68}Ga-based radiopharmaceuticals (PSMA, DOTATOC) was fully introduced in Q3 2024 using a ^{68}Ge/^{68}Ga generator (1.91 GBq on April 11, 2024). At the end Q1 2025, two new ^{68}Ge/^{68}Ga generators (1.85 GBq on March 5, 2025) were introduced, increasing the number of ^{68}Ga examinations two-fold (two syntheses per day), while the number of ^{18}F-FDG investigations remained relatively the same. Also, at the end of Q1 2025, in-house synthesis of ^{18}F-FDG was introduced into the radiochemists' routine using ^{18}F produced at the facility's cyclotron (10-12 patients per day, 11 Gbq of ^{18}F-FDG ready for infusion on average).

3. Results and discussion

3.1. Collective doses

Quarterly collective ring doses (Hp(0.07)) and collective effective doses (Hp(10)) for radiopharmacists working in the facility are depicted in Fig. 1 and Fig. 2, respectively. Collective dose, instead of personal doses, was selected because the number of radiochemists working in the department changed during the time of this study. This could significantly influence the acquired doses because of the workload share among the radiochemists. The use of collective dose helps to account for this workload-sharing factor.

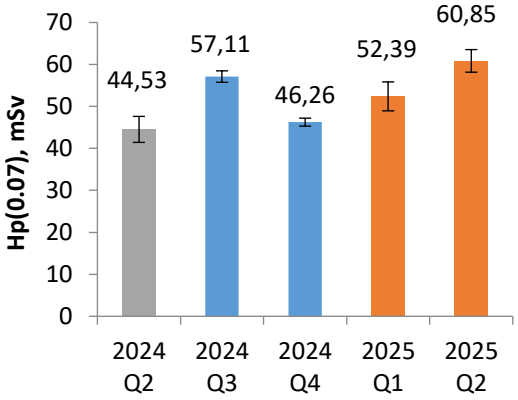

Fig.1. Collective ring doses (Hp(0.07)) of radiochemists working in the facility.

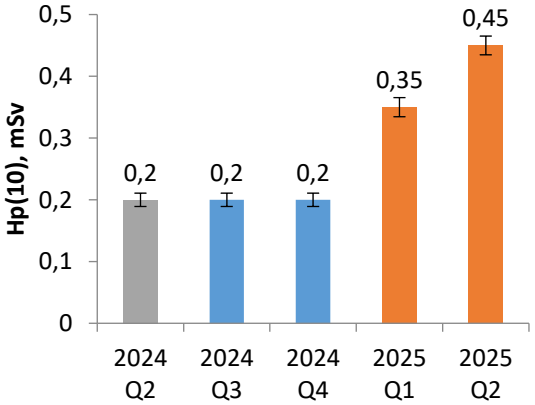

Fig. 2. Collective effective doses (Hp(10)) of radiopharmacists working in the facility.

The lowest collective ring dose of 44.53 mSv and effective dose of 0.2 mSv were recorded during Q2 2024,

a period when radiopharmacists were not involved in the preparation of PET radiopharmaceuticals. In Q3 2024, the production of ^{68}Ga-based radiopharmaceuticals (PSMA, DOTATOC) was fully introduced. This significantly affected the registered collective doses. The ring dose increased by 28% to 57.11 mSv, while the effective dose remained stable at 0.2 mSv, despite the workload being relatively the same (Fig. 3). This indicates that the main factor in the increase in collective ring dose is the introduction of ^{68}Ga-based radiopharmaceuticals into the radiochemists' work routine.

During Q4 2024, the registered collective ring dose was 23% lower (46.26 mSv) compared to Q3 2024, likely due to better mastery of ^{68}Ga-based radiopharmaceutical synthesis. Once again, the number of performed radiologic examinations remained relatively the same.

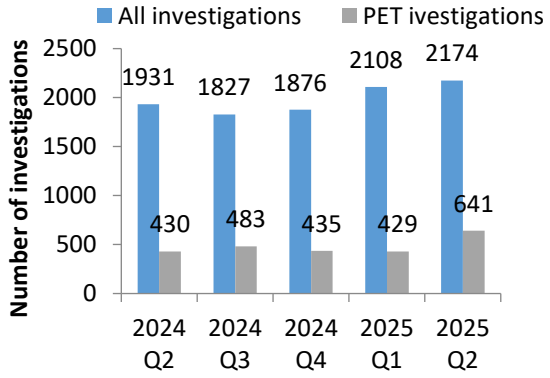

Fig. 3. Number of examinations in the nuclear medicine department

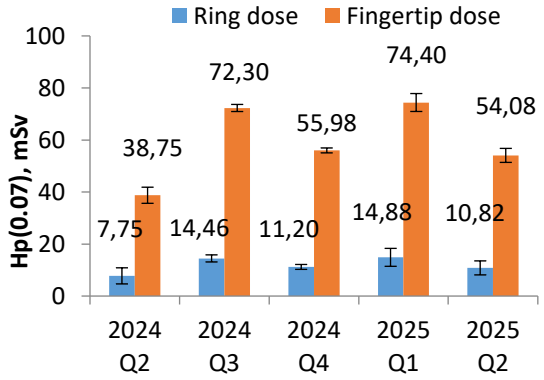

Fig. 4. Median ring and fingertip doses collected by a single radiochemist

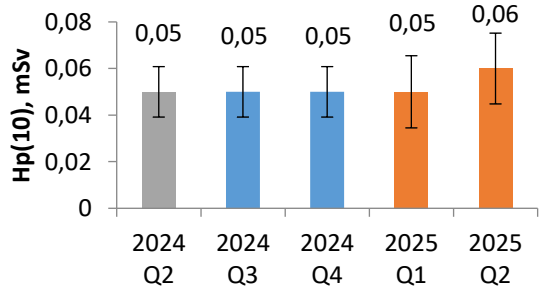

Fig. 5. Median effective doses collected by a single radiochemist

However, the collective ring dose was still slightly higher than in Q2 2024, when radiochemists were not involved with PET radionuclides. This indicates that improved handling of ^{68}Ga synthesis techniques does not entirely eliminate the additional doses collected by radiopharmacists. Regarding the collective effective dose, the introduction of ^{68}Ga radionuclides did not have a significant impact, as the effective dose remained low, close to the minimal detection limit.

Collective ring and effective doses significantly increased after introducing ^{18}F-FDG synthesis into the radiopharmacists' routine at the end of Q1 2025. Compared to the previous quarter (Q4 2024), the ring dose increased by 13%, and the effective dose increased by 75%. However, the registered effective dose was still very low (0.35 mSv), well below the annual limit (20 mSv).

Contrary to the case with introduction of ^{68}Ga-based radionuclides (2024 Q4), the registered ring and effective doses did not decrease in the next quarter after introduction of ^{18}F-FDG synthesis. Compared to Q1 2025, the collective ring dose at Q2 2025 increased by 16%, and the effective dose increased by 29%. This could be attributed to the radiochemists' higher workload, as two new ^{68}Ge/^{68}Ga generators were put into use in the department at the end of Q1 2025, and number of PET scans increased by 49%.

Table 1. Dose rate and effective dose during synthesis of ^{68}Ga radiopharmaceuticals

	Eluation		QC		Hp(10), µSv
	Average dose rate, µSv/h	Maximum dose rate, µSv/h	Average dose rate, µSv/h	Maximum dose rate, µSv/h	
2024Q4	1.02	1.77	16.92	312.78	0.78
2025Q1	1.39	3.58	7.41	336.62	0.77
2025Q2	7.66	53.83	22.59	211.33	2.72

3.2. Personal doses

The dynamics of doses collected by a single radiochemist (Fig. 4-5) generally resemble the dynamics of collective doses, except for Q2 2025, where a reduction in both ring and effective doses was noted. This could be attributed to a higher workload share among radiochemists because an additional radiochemist was hired during this quarter.

The absolute collective ring doses were well below the yearly limit for workers (500 mSv), and effective doses did not reach even 1 mSv. However, the acquired results may not accurately represent the maximum dose the hands could have received [8]. For a better estimation of fingertip doses, a multiplication factor of 6 was applied, based on research on dose assessment strategies for the tips of fingers in nuclear medicine [9]. During the one-year tracking period, the calculated median fingertip dose was 296 mSv, which is still below the yearly limit.

Starting in Q1 2025, eye doses were also monitored - the registered doses were near the minimal detectable limit of the dosimeter (0.25 mSv) for all radiochemists.

3.3. Single procedure doses

Additionally, dose rate and effective dose monitoring of radiochemists were performed at a single-procedure level. The synthesis procedures for ^{68}Ga-based radiopharmaceuticals were chosen over ^{18}F-FDG because they involve more manual operations.

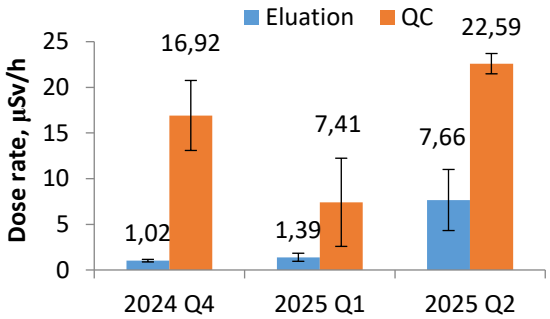

Fig. 6. Average dose rates during elution and QC steps of synthesis of ^{68}Ga-based radiopharmaceuticals

With electronic dosimeters, registered doses and average dose rates varied significantly during the investigation period (Table 1, Fig. 6). This can be attributed to the fact that two new ^{68}Ge/^{68}Ga generators were put into use in the department at the end of Q1 2025, which approximately doubled workload involving ^{68}Ga radiopharmaceutical production. Dose rate and dose analysis with the two new generators started in Q2 2025. In Q2 2025, doses collected during a single synthesis increased substantially comparing to previous quarters from 0.77-0.78 µSv to 2.72 µSv. The measured average dose rates during elution and quality control (QC) also increased and reached 7.66 µSv/h and 22.59 µSv/h, respectively. The registered maximum dose rates during the QC procedure remained similar, but the maximum dose rate during the elution phase increased substantially, from 1-3 µSv/h to 53.83 µSv/h.

4. Conclusions

The addition of PET radionuclide synthesis procedures to radiochemists' routines has a significant impact on their radiation exposure, even with varying workloads that affect individual doses and limited amount of data. This is supported by the increase in collective and personal doses observed after these new procedures were introduced. Despite the increase of dose, the acquired data shows that both extremity and effective doses remain within regulatory limits.

5. References

1. Zhang, S., Wang, X., Gao, X., Chen, X., Li, L., Li, G., ... & Hu, K.. Radiopharmaceuticals and their applications in medicine. Signal transduction and targeted therapy, 2025, 10(1), 1.
2. Lameka, K., Farwell, M. D., & Ichise, M. Positron emission tomography. Handbook of clinical neurology, 2016, 135, 209-227.
3. Conti, M., & Eriksson, L. Physics of pure and non-pure positron emitters for PET: a review and a discussion. EJNMMI physics, 2016, 3(1), 8.
4. Kwan, T. N., Spremo, S., Teh, A. Y., McHarg, D., Thangasamy, I., & Woo, H. H. Performance of Ga-68 PSMA PET/CT for diagnosis and grading of local prostate cancer. Prostate international, 2021, 9(2), 107-112.
5. Graham, M. M., Gu, X., Ginader, T., Breheny, P., & Sunderland, J. J. 68Ga-DOTATOC imaging of neuroendocrine tumors: a systematic review and metaanalysis. Journal of Nuclear Medicine, 2017, 58(9), 1452-1458.
6. Maffey-Steffan, J., Scarpa, L., Svirydenka, A., Nilica, B., Mair, C., Buxbaum, S., ... & Virgolini, I. (2020). The 68Ga/177Lu-theragnostic concept in PSMA-targeting of metastatic castration–resistant prostate cancer: impact of post-therapeutic whole-body scintigraphy in the follow-up. European journal of nuclear medicine and molecular imaging, 2020, 47(3), 695-712.
7. Rong, J., Haider, A., Jeppesen, T. E., Josephson, L., & Liang, S. H. Radiochemistry for positron emission tomography. Nature communications, 2023, 14(1), 3257. https://www.nature.com/articles/s41467-023-36377-4.pdf
8. McCann, A., Cherbuin, N., Covens, P., Dabin, J., Haruz-Waschitz, S., Gallo, L., ... & Kollaard, R. Finger doses due to 68Ga-labelled pharmaceuticals in PET departments—results of a multi-centre pilot study. Journal of Radiological Protection, 2023, 43(1), 011509.
9. Martin, C. J. Strategies for assessment of doses to the tips of the fingers in nuclear medicine. Journal of Radiological Protection, 2016, 36(3), 405.

MEDICAL PHYSICS IN THE BALTIC STATES 17 (2025)

Proceedings of International Conference "Medical Physics 2025"
06-08 November 2025, Kaunas, Lithuania

IMPACT OF Q.CLEAR RECONSTRUCTION ALGORITHM PARAMETERS ON SPECT/CT IMAGE QUALITY

Klāvs KASPARS[1], Vineta VANAGA[2], Laura Antra GRIKKE[3]
[1]Riga East University Hospital; [2]Riga East University Hospital; [3]Riga East University Hospital
[1]klavs.kaspars@aslimnica.lv; [2]vineta.vanaga@aslimnica.lv; [3]laura.grikke@aslimnica.lv

***Abstract*:** The study investigates the influence of Q.Clear reconstruction algorithm parameters on SPECT/CT image quality. Using "Jaszczak" and NEMA IEC body phantoms, the study evaluates the impact of β and γ regularization coefficients on image quality parameters such as uniformity, noise, contrast, resolution, contrast recovery coefficient, and background variability. Results show that there is no universal parameter; rather, optimal values depend on the task. The findings emphasize the importance of adapting reconstruction parameters to specific goals to enhance SPECT/CT image quality.

Keywords: SPECT/CT, Q.Clear, image reconstruction, β parameter, γ parameter.

1. Introduction

Single photon emission computed tomography/computed tomography (SPECT/CT) has become an essential tool in modern nuclear medicine, providing both functional and anatomical information for diagnosis and therapy planning. Since its clinical introduction more than 20 years ago, advances in hardware and software have significantly improved image quality and quantitative accuracy. In particular, the emergence of digital SPECT cameras with cadmium-zinc-telluride (CZT) detectors has led to better sensitivity and spatial resolution compared with conventional NaI(Tl)-based systems [1].
Reconstruction algorithms play a central role in image quality. Early methods such as filtered back projection (FBP) have been gradually replaced by iterative techniques, most notably ordered subsets expectation maximization (OSEM) [2]. Iterative methods allow incorporation of physical models such as attenuation, scatter, and collimator response, improving image quality compared to analytic techniques [3]. However, OSEM reconstructions are limited by noise amplification at higher iterations, requiring a trade-off between quantitative accuracy and image appearance [4].
To address these limitations, regularized iterative algorithms have been developed. One such is Q.Clear, originally introduced for PET imaging and later adapted to SPECT/CT systems such as the GE StarGuide. According to its inventors from GE Healthcare Q.Clear employs a penalized likelihood approach with two tunable parameters: β, which controls the degree of noise suppression, and γ, which regulates edge preservation [4]. By balancing these parameters, Q.Clear allows flexible adjustment of image properties, potentially leading to improved diagnostic performance.
While Q.Clear has been extensively studied in positron emission tomography (PET), its application in SPECT/CT is recent, and systematic evaluation of its parameters is limited. SPECT images are more susceptible to noise and scatter than PET, meaning that parameter optimization cannot be directly transferred [5]. Therefore, the aim of this study was to investigate the influence of Q.Clear reconstruction parameters β and γ on SPECT/CT image quality.

2. Materials and methods

2.1. Phantoms and Preparations

Two quality control phantoms were employed: the "Jaszczak" Flangeless Deluxe phantom that simulates uniform and cold region imaging to assess uniformity, noise, contrast, and spatial resolution; NEMA IEC body phantom that simulates uniform and hot region imaging with hot spheres for CRC and BV evaluation. Both filled with Tc-99m activity concentrations following standard protocols: ~400 MBq activity in the "Jaszczak" phantom and 8:1 sphere-to-background ratio in the NEMA IEC body phantom (200 MBq in the background and 170 MBq mixed in 1 L of water and filled into the spheres) [6-7]. Activities were measured using a calibrated activity meter with uncertainty assessments performed.

2.2. Acquisition and Reconstruction

SPECT/CT image acquisitions were performed with a 12-detector GE Healthcare StarGuide CZT system, using 386 projections per detector with energy windows centered at 140.51 keV ±10%. The matrix and pixel size were 256x256 and 2.46 mm, respectively. Acquisition length was 30 min for the "Jaszczak" phantom and 15

minutes for the NEMA IEC body phantom. Helical CT parameters were 120 kV, 80 mA, 3.75 mm slice thickness. Images were reconstructed with the Q.Clear algorithm varying β (0–12.8) and γ (0–64) parameters independently, using 150 iterations and 2 subsets without additional filtering, including attenuation and sensitivity (BySens) corrections.

2.3. Image Quality Assessment

"Jaszczak" phantom image analysis was done according to international guidelines using ImageJ Fiji with a dedicated IAEA NMQC plugin combined with a custom macro: [8]

Uniformity (Equation 1): differential and integral uniformity calculated in the useful and central field of view (UFOV, CFOV) [8].

$$Uniformity = \frac{counts_{max} - counts_{min}}{counts_{max} + counts_{min}} \quad (1)$$

Noise (Equation 2): root mean square (RMS) noise from uniform phantom regions [9].

$$RMS\ noise = \frac{\sigma}{\mu} \times 100, \quad (2)$$

where σ – standard deviation of the signal;
μ – mean of the signal.

Contrast (Equation 3): signal ratio between cold spheres and hot background in the "Jaszczak" phantom [8].

$$Contrast = \frac{\mu_s}{\mu_b} \times 100, \quad (3)$$

where μ_s – mean of the signal of the ROI;
μ_b – mean of the signal of the background.

Spatial Resolution: visually determined smallest resolvable rods in the "Jaszczak" phantom cold rods section.

The regions of interest (ROI) positions were determined using the CT information of the phantom images.

NEMA IEC phantom image analysis was done according to international guidelines using ImageJ Fiji with a custom macro [7].

Contrast recovery coefficient (CRC) and background variability (BV) (Equation 4 and Equation 2): computed from NEMA IEC phantom hot sphere and background ROIs. BV is calculated by the same equation as RMS noise.

$$CRC = \frac{\frac{\mu_s}{\mu_b} - 1}{\frac{a_s}{a_b} - 1} \times 100, \quad (4)$$

where μ_s – mean of the signal of the ROI;
μ_b – mean of the signal of the background;
a_s – activity concentration of the hot spheres;
a_b – activity concentration of the background.

3. Results

3.1 Jaszczak phantom

Results showed a clear dependence of image quality on the β parameter.

CFOV uniformity improved with higher β values (Fig. 1). Noise was significantly higher at the start of the β range, but it decreased as β was increased. However, the decrease plateaued after β value 3.2 (Fig. 2). The contrast and resolution were highest at lower β values (Fig. 3), the resolution completely deteriorating after β value 1.6 (Fig. 4).

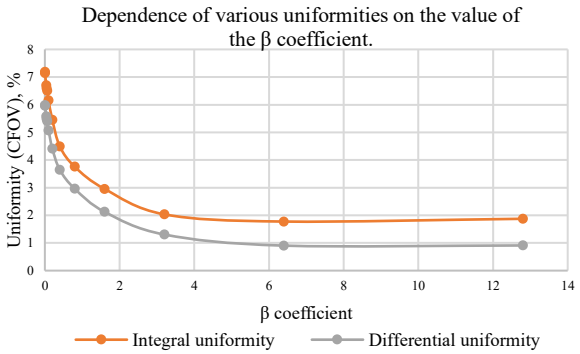

Fig. 1. Dependence of various uniformities on the value of the β coefficient.

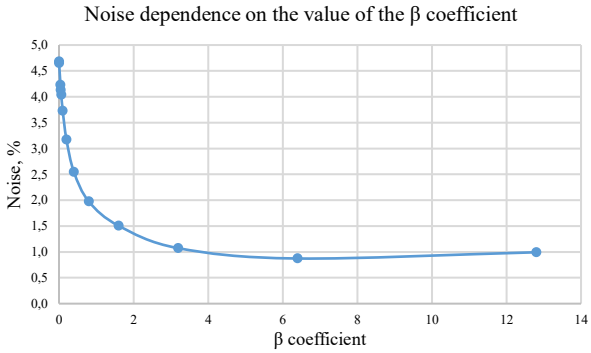

Fig. 2. Noise dependence on the value of the β coefficient.

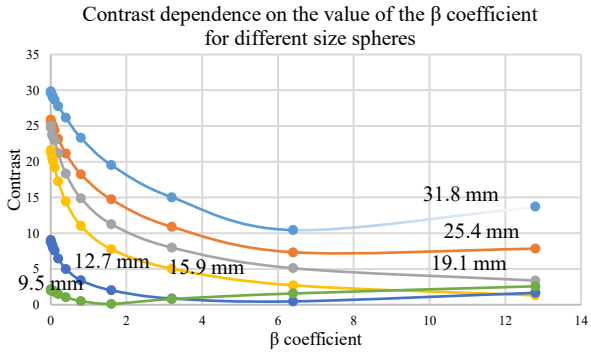

Fig. 3. Contrast dependence on the value of the β coefficient for different size spheres.

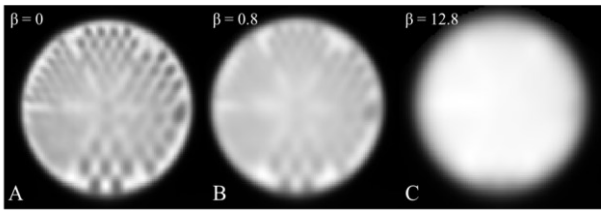

Fig. 4. Jaszczak phantom cold rods section with different β coefficient values.

The γ coefficient influenced edge sharpness: higher γ values slightly decreased contrast (Fig. 5) while

increasing noise (Fig. 6) and worsening uniformity (Fig. 7). However, image resolution was slightly improved (Fig. 8). The overall impact of γ coefficient on the image quality parameters was weaker than that of the β coefficient.

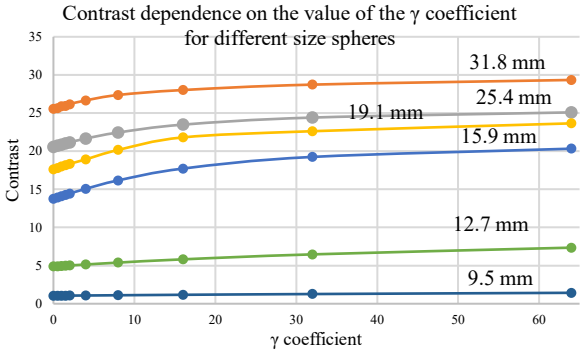

Fig. 5. Contrast dependence on the value of the γ coefficient for different size spheres.

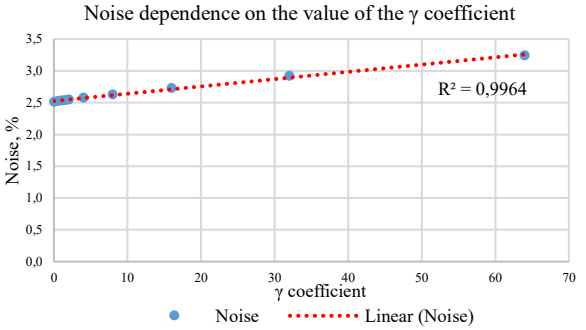

Fig. 6. Noise dependence on the value of the γ coefficient.

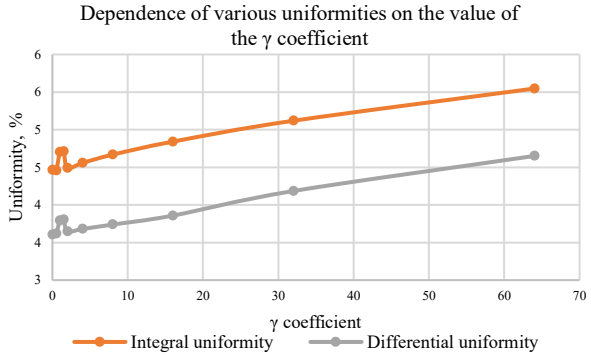

Fig. 7. Dependence of various uniformities on the value of the γ coefficient.

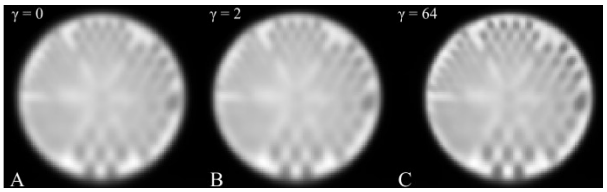

Fig. 8. Jaszczak phantom cold rods section with different γ coefficient values.

Overall, optimal balance in the "Jaszczak" phantom was achieved at intermediate β values combined with moderate γ.

3.2 NEMA IEC body phantom

For hot spheres, CRC decreased with increasing β, indicating worse recovery of true activity concentrations (Fig. 9). Similarly, BV also decreased, leading to less noisy background regions (Fig. 10).

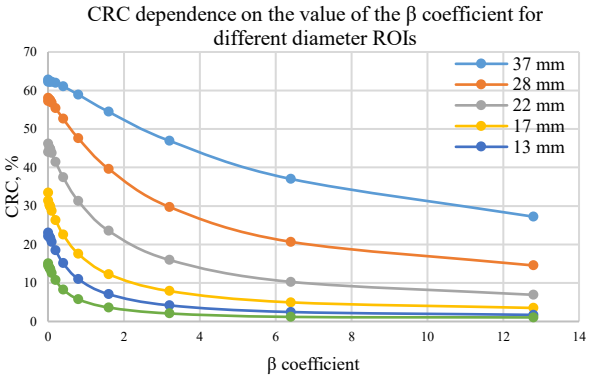

Fig. 9. CRC dependence on the value of the β coefficient for different diameter ROIs.

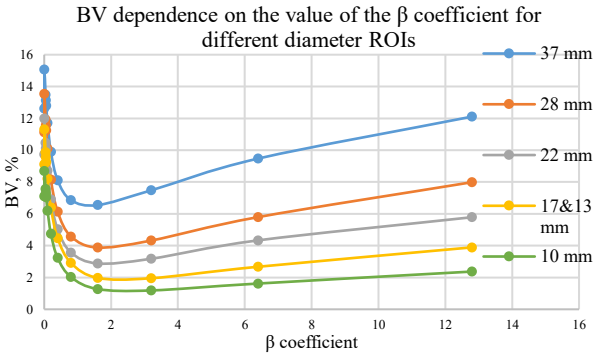

Fig. 10. BV dependence on the value of the β coefficient for different diameter ROIs

At low β, small hot spheres were better visualized, but the background appeared noisy. At high β, background was smoother, but CRC was reduced, underestimating activity in small spheres.
Increasing γ coefficient led to increases in CRC and BV, although they were quite small when compared to β coefficient case.

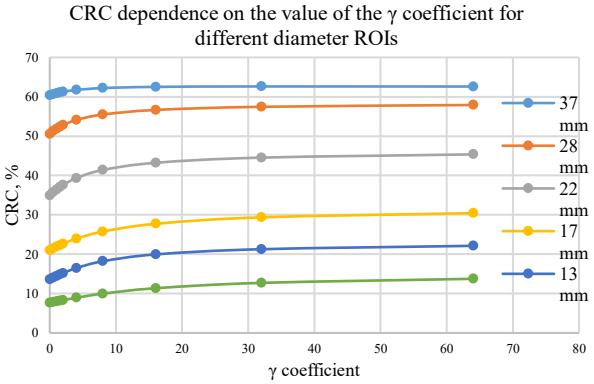

Fig. 11. CRC dependence on the value of the γ coefficient for different diameter ROIs.

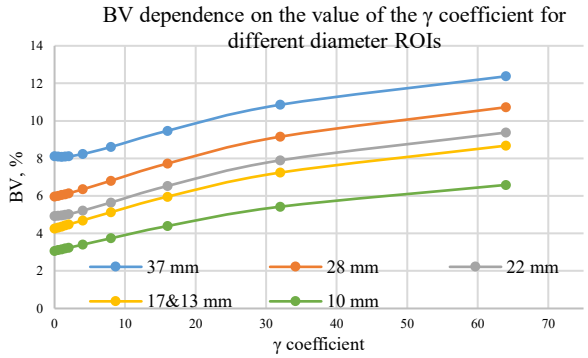

Fig. 12. BV dependence on the value of the γ coefficient for different diameter ROIs.

The γ parameter improved delineation of sphere boundaries, particularly for bigger size spheres.

3.3 Summary of findings

Low β (0 – 0.4): high resolution and contrast, but noisy images. Intermediate β (0.4 - 3.2): best compromise between noise and resolution for most diagnostic tasks. High β (3.2 - 12): smooth images at the cost of detail and contrast loss.

No significant impact on SPECT/CT image quality across the whole γ coefficient range was detected, however, increasing γ coefficient led to slight increase both in contrast and background noise.

These results confirmed the trade-off between noise suppression and boundary preservation in Q.Clear SPECT/CT reconstruction algorithm.

4. Conclusions

This study provides the first systematic evaluation of Q.Clear parameters for SPECT/CT. The results confirm that the β parameter primarily controls the noise–resolution trade-off, while γ governs contour preservation.

The findings are consistent with prior PET studies [10 - 12], where higher β improves noise but reduces CRC and contrast, and γ enhances edge detail. However, the optimal parameter ranges for SPECT differ due to higher scatter and lower sensitivity compared with PET.

Clinically, parameter selection should depend on diagnostic purpose:

- For tasks requiring detection of small lesions or high contrast (e.g., bone metastases), lower β values with moderate γ may be preferred.
- For tasks requiring uniformity and smooth appearance (e.g., myocardial perfusion imaging), higher β values may be advantageous.

Importantly, no single combination of parameters was universally optimal. Reconstruction settings should therefore be tailored to each clinical protocol.

5. References

1. M. F. Santarelli et al., “CZT Detectors-Based SPECT Imaging: How Detector and Collimator Arrangement Can Determine the Overall Performance of the Tomograph,” Electronics (Basel), vol. 10. lpp 2230, Sep. 2021, doi: 10.3390/electronics10182230.
2. V. Vukomanovic, V. Ignjatovic, M. Stevic, N. Mijatovic, and M. Jeremic, “HYBRID IMAGING IN CONVENTIONAL NUCLEAR MEDICINE,” 2020, p. 65.
3. G. Zeng, “Image reconstruction - A tutorial,” Comput Med Imaging Graph, vol. 25. lpp. 97–103, Mar. 2001, doi: 10.1016/S0895-6111(00)00059-8.
4. S. Ross, “Q.Clear.”. Available: https://www.gehealthcare.co.kr/-/jssmedia/739d885 baa59485aaef5ac0e0eeb44a4.pdf
5. “SPECT-CT versus PET-CT: The ‘little sister’?”. Available: https://healthcare-in-europe.com/en/news /SPECT-CT-versus-pet-CT-the-little-sister.html
6. IAEA, “IAEA Human Health Series no. 6 Quality Assurance for SPECT Systems,” 2009. Available: http://www.iaea.org/Publications/index.html
7. “NEMA NU 1-2023 Performance Measurements of Gamma Cameras,” 2023.
8. A. V. Gil, L. T. Aroche, and G. L. Poli, “Medicine IAEA-NMQC Toolkit For Fiji Application Version 1.00 User´s Manual,” OCT. 2017. . Available: http://bitly.com/IAEA-NMQC
9. “Acceptance Testing and Annual Physics Survey Recommendations for Gamma Camera, SPECT, and SPECT Systems The Report of AAPM Task Group 177,” 2019.
10. E. K. Lysvik, L. T. G. Mikalsen, M. E. Rootwelt-Revheim, K. E. Emblem, and T. Hjørnevik, “Optimization of Q.Clear reconstruction for dynamic 18F PET imaging,” EJNMMI Phys, vol. 10, no. 1, Dec. 2023, doi: 10.1186/s40658-023-00584-1.
11. T. Andersen and P. F. Hoilund-Carlsen, “The Q.Clear PET reconstruCTion algorithm: Evaluation using the NEMA IQ phantom,” Journal of Nuclear Medicine, vol. 57, no. supplement 2 lpp 1973, 2016, : https://jnm.snmjournals.org/content/57/supplement_2/1973
12. K. Miwa et al., “Impact of γ factor in the penalty function of Bayesian penalized likelihood reconstruction (Q.Clear) to achieve high-resolution PET images,” EJNMMI Phys, vol. 10, Nov. 2023, doi: 10.1186/s40658-023-00527-w.

POLIMASTER®

RadFlash DOSIMETER

ISO 17025 calibration is available

RadFlash EPD combines all the advantages of an active dosimeter with advanced real-time monitoring capabilities, empowering users to stay aware of their radiation exposure as it happens. Designed for professionals working with X-ray and gamma radiation, it measures personal dose equivalent and dose rate, triggers alarms when thresholds are exceeded, and transfers data wirelessly via Bluetooth®. Lightweight, rugged, and IP67-rated, RadFlash features a clear LCD display, wireless charging, and intuitive one-button operation — delivering reliable, immediate protection in demanding environments.

RadFlash is compatible with **RadSight™ Dosimetry System.**

RadSight™ is a modular software and hardware ecosystem developed for real-time radiation monitoring and dose management using RadFlash® electronic personal dosimeters (EPDs). The system supports flexible EPD assignment, access control, session-based tracking, dose reporting, and customizable graphical displays — all designed for the fast-paced clinical environment.

www.polimaster.com

www.radsight.com

MEDICAL PHYSICS IN THE BALTIC STATES 17 (2025)

Proceedings of International Conference "Medical Physics 2025"
06 – 08 November 2025, Kaunas, Lithuania

RESPIRATORY MOTION-INTEGRATED DOSE VERIFICATION IN VMAT: A STUDY OF THE ARCCHECK-3DVH SYSTEM

Aurimas KRAULEIDIS[1,2], Dainius BURDULIS[2], Kristina REPŠĖ[2], Romas VILKAS[2],
Lina GERDAUSKIENĖ[2], Diana ADLIENĖ[1]
[1]Kaunas university of technology; [2]Klaipėda university hospital
aurimas.krauleidis@gmail.com; dainius.burdulis@gmail.com; kristinarepse@gmail.com; romasvilkas@yahoo.com; linavesp@gmail.com; diana.adliene@ktu.lt;

***Abstract*:** Modern dynamic radiotherapy techniques, such as volumetric modulated arc therapy (VMAT), face significant challenges due to tumor motion primarily caused by patient respiration which can compromise accurate dose delivery and optimal sparing of organs at risk (OARs). These challenges necessitate complex and precise dosimetric verification methods. This study evaluated the impact of respiratory-induced tumour motion on dose delivery accuracy in VMAT radiotherapy for 30 lung cancer cases using a 3D diode array system under static and dynamic conditions. The mean gamma pass rates were 99.4% under static conditions (3%/3 mm) and 55.6% under motion-simulated conditions (2%/2 mm). Significant dose variations were observed in the PTV mean dose, maximum dose, D2%, D95%, D98% under motion, with corresponding differences in organs at risk (OARs) further confirming the impact of motion.

***Keywords*:** Lung cancer, VMAT, Respiratory motion, Dosimetric verification, ArcCheck.

1. Introduction

Accurate dose delivery is critical in advanced radiation therapy techniques such as intensity-modulated radiation therapy (IMRT), volumetric modulated arc therapy (VMAT), and stereotactic body radiotherapy (SBRT), which achieve highly conformal dose distributions with steep gradients. However, in thoracic and abdominal treatments, respiratory motion remains a major source of uncertainty, causing potential underdosage of the target and unintended irradiation of surrounding organs at risk (OARs) [1-4]. Intra-fractional anatomical changes due to breathing can lead to significant geometric and dosimetric deviations, particularly in the lung, which is both a critical OAR and a site prone to large motion amplitudes [5,6].

Traditional quality assurance (QA) approaches, such as static phantom measurements and gamma analysis, do not adequately capture these motion-induced dose discrepancies [7]. Although internal target volume (ITV)-based planning attempts to encompass the full range of respiratory motion, it cannot fully account for patient-specific variability between fractions [8]. Moreover, planned dose distributions are inherently static and do not represent the time-integrated dose actually received by a moving target [9,10].

Recent advances in patient-specific QA have introduced motion-inclusive strategies to better evaluate the interplay between respiratory motion and dose delivery [11,12]. Systems like ArcCHECK-3DVH (Sun Nuclear Corporation, Melbourne, FL, USA) software enable three-dimensional dose reconstruction using measurement-guided data, providing a more clinically relevant verification of the delivered dose [13,14]. When combined with moving phantoms simulating respiratory motion, ArcCheck can capture the dosimetric impact of dynamic anatomical changes [15,16]. This approach allows comparison between planned and motion-inclusive reconstructed doses, highlighting the potential blurring and dose uncertainties that respiratory motion introduces.

Several studies have demonstrated that respiratory motion increases dose heterogeneity within the planning target volume (PTV) and adjacent healthy tissue [17,18]. By capturing the true dynamic nature of dose delivery, this methodology enhances the confidence in complex treatment techniques and supports the development of safer, more effective motion management strategies in radiotherapy [19,20].

This study aimed to evaluate the impact of respiratory motion on dosimetric accuracy using ArcCheck dosimetry in a motion-inclusive setup. By simulating realistic breathing patterns with a moving phantom and performing three-dimensional dose reconstruction, the discrepancies between planned and delivered doses were quantified in lung and thoracic treatments. This analysis will provide valuable insights into the dosimetric consequences of respiratory motion and inform strategies for improving motion management QA in clinical practice.

2. Methods and materials

2.1 Preparation of VMAT plans

In this section, a total of 30 VMAT treatment plans for lung cancer patients were created using the Eclipse 15.6 Treatment Planning System (Varian Medical Systems, Palo Alto, USA). Treatment planning was performed using 6 MV photon beams delivered by a Varian TrueBeam linear accelerator with HD120 MLC (high-definition multi-leaf collimator. The VMAT plans were optimized for full and partial arcs, including 1–2 full arcs or up to 2 half arcs per plan, with arc rotations ranging from 179° to 181° in both clockwise (CW) and counterclockwise (CCW) directions. The Photon Optimizer algorithm was used to simultaneously optimize MLC (maximum leaf speed 5 mm/deg and 2.5 cm/s), dose rate (up to 600 MU/min), and gantry speed (maximum 72 s/turn, ≈5°/s) to achieve the desired degree of modulation. Dose calculations were performed using the Anisotropic Analytical Algorithm (AAA) with a 2.5 mm grid resolution. The treatment plans achieved the clinical requirement of delivering at least 95% of the prescribed dose to 95% of the PTV, with maximum target dose (Dmax) kept below 110% of the prescription dose. Organs-at-risk (OARs), including the right and left lungs, PRV spinal cord, spinal cord, esophagus and heart were contoured, and dose constraints were applied based on QUANTEC guidelines.

2.2 ArcCHECK-3DVH system

The dose distributions were verified using the ArcCHECK-3DVH system. The ArcCheck phantom is a cylindrical 3D diode array consisting of 1,386 diodes, each with a detector size of 0.8 × 0.8 mm², arranged helically at 10 mm intervals around a 21 cm diameter cylinder. To derive a patient-specific 3D dose distribution from ArcCheck measurements, the 3DVH software version was used, which incorporates an internal computation algorithm known as ArcCheck Planned Dose Perturbation (ACPDP) [17]. This process requires a set of inputs: the reference DICOM RT plan, CT images, structure set, DICOM RT dose data (representing the TPS-calculated dose for both the patient and the ArcCheck phantom), and the ArcCheck measurement file. The ACPDP algorithm executes several steps: (a) aligning the planned data with the ArcCheck's virtual inclinometer data, (b) generating a relative 3D dose distribution on a uniform cylindrical phantom for each sub-beam, (c) adjusting the relative dose using the ArcCheck measurements to create a 3D absolute dose within the phantom, (d) calculating the voxel-by-voxel ratio of reconstructed to TPS-calculated dose within the phantom, and (e) applying these ratios to perturb the patient's original TPS dose distribution [16]. The resulting reconstructed dose grid maintains the same resolution as the original TPS dose. A key benefit of 3DVH is its ability to compute gamma passing rates across the full irradiated volume and individually for each region of interest (ROI). By comparing measured and planned planar doses, 3DVH determines discrepancies, which are then back-projected into the treatment plan to generate an adjusted 3D dose distribution that accounts for per-field QA errors.

Additionally, because the ArcCheck diode spacing is less dense than the grid resolution of the TPS dose, a proprietary interpolation method called "Smarterpolation" is applied. This enables 3DVH to compute 3D gamma index maps for the entire plan, evaluate DVH differences for individual structures, and compare gamma indices between the planned and perturbed dose matrices.

Gamma analysis was performed using dose difference (DD) and distance-to-agreement (DTA) criteria set at 3%/3 mm, 3%/2 mm, and 2%/2 mm, with a threshold level of 10%. The analysis utilized absolute dose values in combination with the gamma method to determine the γ passing rates between measured and calculated dose distributions. Using the 3DVH software, the percentage dose difference (DD, %) was calculated for both the planning target volume (PTV) and surrounding normal organs. For each PTV, the predicted values from the ArcCheck Planned Dose Perturbation (ACPDP) algorithm—mean dose (Dmean), maximum dose (Dmax), and doses received by 2%, 95%, and 98% of the volume (D2%, D95%, and D98%) were compared with the corresponding values from the treatment planning system (TPS). For normal tissues, evaluation was based on their Dmean and Dmax values. The dose difference percentage (DD, %) was defined as follows:

$$DD, \% = (D_{3DVH}-D_{TPS})/D_{DTPS} \times 100 \quad (1)$$

D_{3DVH} represents the dose by 3DVH, whereas D_{TPS} represents the dose calculated by Eclipse TPS.

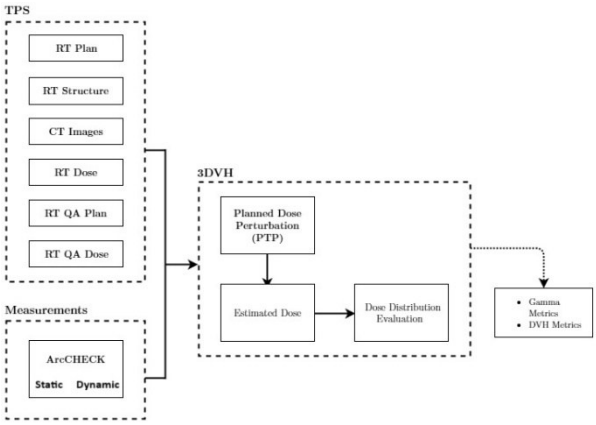

Fig. 1. Overview of the workflow, illustrating the key files, equipment, and processes involved in 3DVH analysis

2.3 Phantom Setup and Respiratory Motion Simulation

To evaluate the dosimetric effects of respiratory motion, initial dose measurements were performed using a static setup of the ArcCheck phantom. Subsequent measurements were conducted under motion conditions simulating respiratory movement along a single axis. The ArcCheck phantom was connected to a respiratory gating robot (Anzai Medical) and mounted on four wheels to allow movement (fig. 2). It was subjected to sinusoidal motion in the craniocaudal (CC) direction, which is most affected by respiration (fig. 3) [20]. A peak-to-peak

motion amplitude of 20 mm was tested at a frequency of 15 rpm to simulate realistic respiratory cycles.

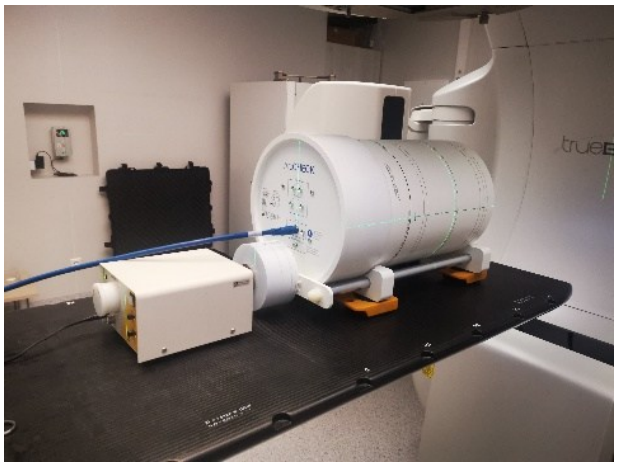

Fig. 2. ArcCheck array setup before performing dose measurements.

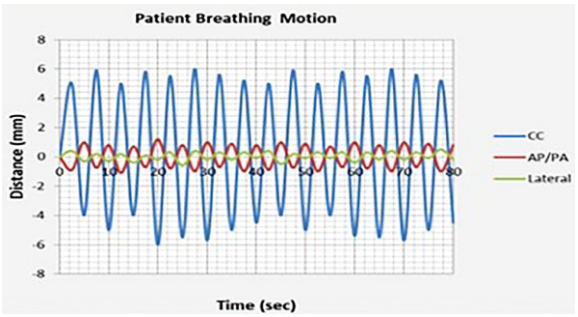

Fig. 3. The respiratory motion simulation. Cranio-caudal (CC); anteroposterior (AP); and lateral (LAT) directions.

3. Results and discussion

3.1 Dosimetric analysis

Before 3D reconstructed dose analysis, the 2D planar dose measured by ArcCheck for all patients' treatments plans was evaluated using SNC Patient software ver. 8.4 (Sun Nuclear Corporation, Melbourne, FL, USA). Two kinds of comparisons were made, the first was a dose mapping with 2D/3D gamma evaluation and the second was a DVHs comparison.

Treatment delivery dose map comparison obtained with and without motion using ArcCheck for a representative patient is shown in Figure 4. As seen in the figure, the peripheral planar dose distribution is the integration of the entrance and the exit dose distributions. The ArcCheck measurement with motion shows a distorted dose distribution comparing with the one without motion. This implies that the intra-fractional motion should be included in the delivered dose for a moving target. Under the static condition (fig. 4b), the dose distribution is more compact and sharply defined. High-dose regions (90% and above) are concentrated in the target area with minimal blurring, indicating accurate and consistent dose delivery without the influence of motion. In the dynamic condition (fig. 4a), the dose distribution shows visible blurring and smearing of the high-dose regions. The darkest regions are less focused, and there is a noticeable expansion of low-to-mid dose regions (10–60%). This effect indicates motion-induced dose averaging which can reduce the precision of dose delivery.

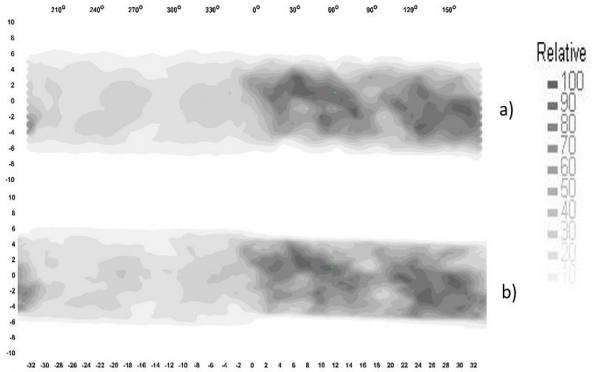

Fig. 4. Treatment delivery QA comparison for a patient with (a) 20 mm CC motion and (b) no motion (gamma index criteria of 3%/3 mm).

Figure 5 compares the measured dose differences beyond the ±3% dose agreement level for detectors depending motion conditions. The gray scales represent the dose distributions and the red/blue points represent gamma evaluation results, likely where gamma failing points are.

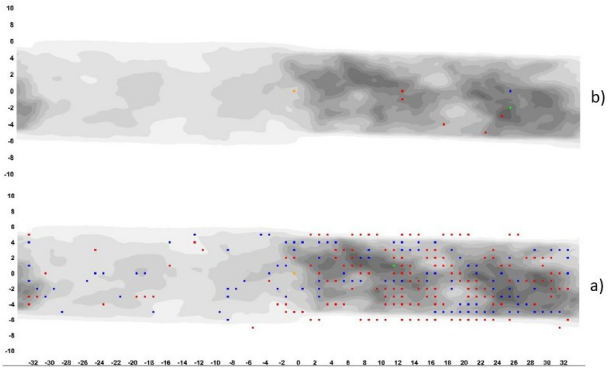

Fig. 5. Percent difference in measured dose with (a) and without (b) motion. Blue and red dots represent the detectors that fail the 3%/3 mm gamma index passing criteria.

The static dose map (fig. 5b) shows a compact, well-defined high-dose region with minimal gamma points, indicating a high gamma pass rate and accurate, consistent dose delivery in the absence of motion. In contrast, the dynamic dose map (fig. 5a) exhibits smeared high-dose regions and numerous gamma points, reflecting a lower pass rate and motion-induced dose inconsistencies, including broader low-dose spread and reduced precision in target coverage.

Differences in dose distribution are also evident because the beam delivery was not synchronized with the detected respiratory motion, and the phase doses were combined without considering temporal dynamics. During treatment, individual fields or segments may begin in one respiratory phase and end in another, leading to dose contributions from incomplete breathing cycles. This results in spatial dose variations, commonly referred to as the interplay effect, which is characteristic of dynamic delivery techniques such as VMAT. This effect can manifest anywhere within the treatment field where multiple points failed to meet the criteria.

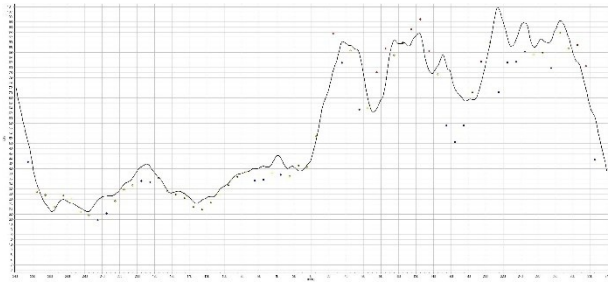

Fig. 6. Central dose profile measured by ArcCheck.

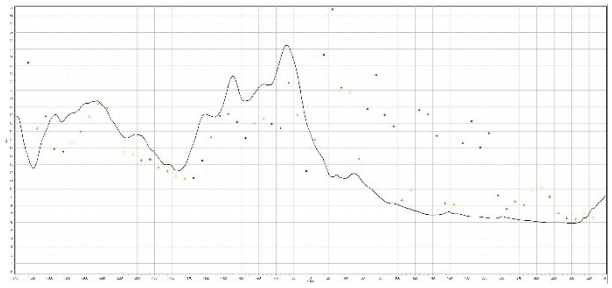

Fig. 7. Peripheral dose profile measured by ArcCheck.

In the profile comparisons (fig. 6), the solid lines and the dots indicate measured doses without and with motion, respectively. Comparing profile data, the dynamic profile generally follows the static profile, but some fluctuations are visible. In the central high-dose regions, the agreement is good, although small deviations appear in the slope and shoulder areas. The low-dose valleys in the dynamic profile are slightly more scattered, indicating motion-induced dose blurring. Overall, motion has a minimal effect on the central axis, and the target dose remains mostly stable. In the peripheral profile (fig. 7), the dynamic measurement deviates significantly from the static curve, especially in the high-dose fall-off and low-dose tail regions. Motion introduces blurring, underdosage in peak regions, and spreading of low-dose areas. Many measured points appear scattered and do not follow the smooth static profile, confirming motion-induced dose perturbations. Peripheral regions are more sensitive to motion due to beam penumbra and dose averaging effects.

Figure 8 shows detectors dose points deviations in three different intervals under 3%/3 mm criteria. This indicates that respiratory motion caused an additional 10.8± 3.9% of the detectors to measure a dose difference greater than 3% and 9.2± 3.1% detectors lower that 3%. That means 78± 6.1% of dose points stayed within ±3%, indicating notable dose inaccuracy. Without motion, 95.7 ± 1.9% of doses were within ±3%, with almost no large deviations beyond ±3% of irradiated dose.

Additionally, the averaged maximum dose deviations due to motion factor were 26.9% ± 5.9% with motion and without motion – 7.7% ± 2.1% respectively. Comparing with several VMAT SBRT plans calculated with Flattening Filter Free (FFF) 6 MV energy, maximum dose differences increased to 44% with motion versus 14 % without motion.

Figure 9 shows the averaged gamma passing rates at the diode level (2D) and the 3D gamma passing rates calculated by using the 3DVH software for static and dynamic conditions. Under static conditions, both ArcCheck (2D) and 3DVH (3D) systems exhibited high gamma pass rates (>92% for 2%/2 mm) with minimal standard deviations (<2.1), indicating that planned and delivered doses are highly consistent in the absence of motion.

However, dynamic conditions, which simulate the effect of target motion due the respiration, resulted in clinically unacceptable gamma pass rates. ArcCheck (2D) pass rates dropped from 99.4±0.6% (static, 3%/3 mm) to 75.1±8.6% (dynamic, 3%/3 mm), and from 96.3±1.7% to 57.6±8.9% for the stricter 2%/2 mm criterion. 3DVH (3D) showed a similar pattern, with reductions from 97.8±1.1% to 71.6±9.6% (3%/3 mm) and 92.6±2.1% to 53.1±10.1% (2%/2 mm). These decreases of approximately 20–40% demonstrate that motion introduces significant deviations between planned and delivered dose distributions. As it was mentioned this indicates that intrafraction motion can lead to inconsistent dose delivery, likely due to interplay effects between moving targets and multileaf collimator (MLC) modulation in dynamic treatments.

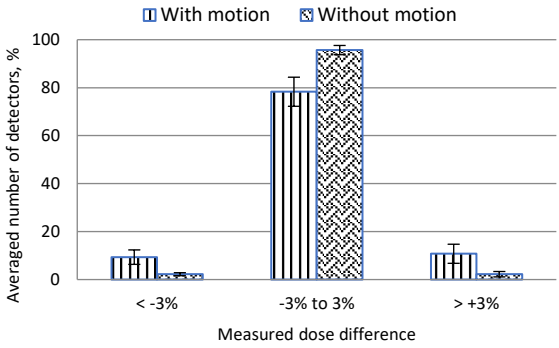

Fig. 8. Averaged detector response to dose difference.

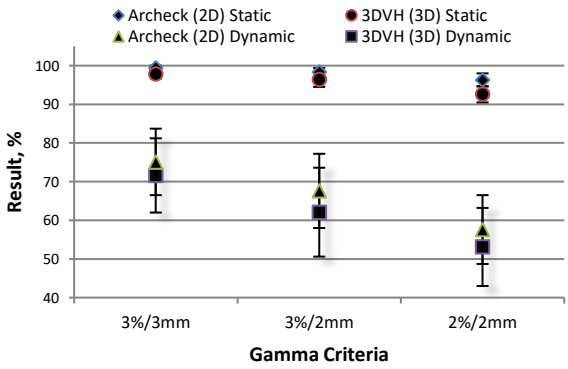

Fig. 9. Averaged gamma passing rate under different condition.

In summary, the data show that motion strongly degrades dose agreement, both by lowering average gamma pass rates and by increasing variability. These results underscore the critical importance of motion management strategies, such as gating or tracking, to maintain dose accuracy during dynamic radiotherapy delivery.

3.2 DVH analysis

Figure 10 illustrates the dose–volume histogram (DVH) comparison between static and motion-affected dose distributions for a lung cancer case. Solid lines represent the dose calculated in the treatment planning system

(TPS), while dotted lines correspond to the measured dose using a moving ArcCheck with the ACPDP algorithm applied to patient CT structures. It shows that variable dose differences can occur in the real volumes of the target and OARs under the moving organ condition. Overall, the dynamic DVHs (dotted) demonstrate reduced PTV coverage, increased dose heterogeneity, and higher OAR exposure, consistent with the quantitative dose difference data. These findings underscore the detrimental effect of respiratory motion on dose conformity and organ sparing, emphasizing the need for motion mitigation strategies such as gating or tumor tracking in lung radiotherapy.

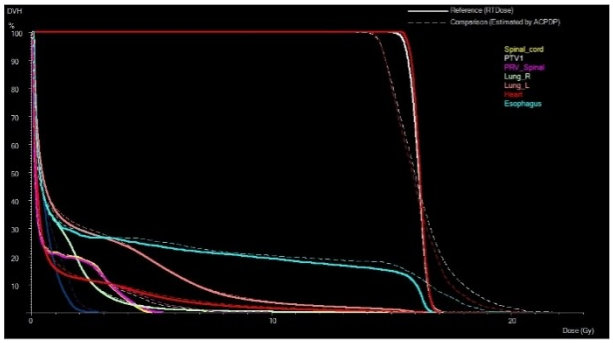

Fig. 10. Calculated DVH data of lung cancer patient by TPS (solid) and 3DVH with motion effect (dashed).

The figure 11 compares sagittal (A, B) and axial (C, D) dose distributions calculated by 3DVH ACPDP algorithm for a lung cancer patient with and without respiratory motion simulation.

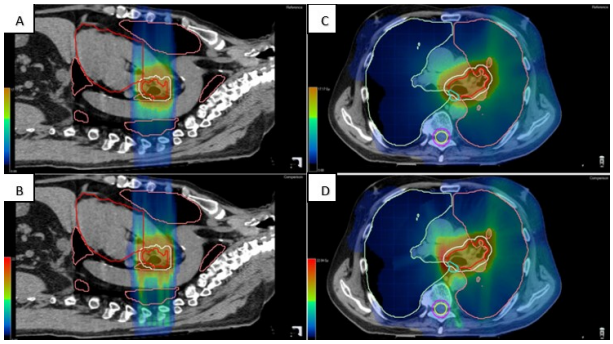

Fig. 11. Dose distribution comparison of lung cancer patient without motion (A,C) and with motion (B,D).

Table 1 shows averaged percentage dose difference for lung cancer patient the for target and normal organs under dynamic and static conditions calculated by 3DVH ACPDP algorithm.

The evaluation of dose delivery under static and motion conditions highlights the significant impact of respiratory motion on radiotherapy accuracy for lung cancer patients. Quantitative analysis from ArcCheck measurements revealed that respiratory motion caused a clear increase in dose discrepancies for both the planning target volume (PTV) and organs at risk (OARs). Under static conditions, dose differences were minimal, with PTV mean deviations below 2% and low variability (SD < 1%), reflecting highly consistent dose delivery. In contrast, under dynamic conditions simulating respiration, the PTV exhibited substantial deviations, with Dmean rising to 4.45% and Dmax to 9.86%, accompanied by much higher standard deviations. This indicates both underdosage at the tumor periphery (D95% and D98%) and localized hotspots caused by the interplay between tumor motion and beam modulation.

Table 1. Averaged percentage dose difference for target and normal organs under dynamic and static conditions.

		Dynamic (Respiration simulation)		Static	
Structure	Parameter	DD,%	SD	DD,%	SD
PTV	Dmean	4.45	2.65	1.61	0.62
	Dmax	9.86	7.52	2.64	2.21
	D2%	5.88	4.31	2.32	0.74
	D95%	7.91	3.44	3.36	0.85
	D98%	8.02	3.58	2.49	0.66
Right Lung	Dmean	2.35	1.21	0.65	0.25
	Dmax	9.76	7.86	2.32	1.24
Left Lung	Dmean	2.62	1.46	2.41	0.54
	Dmax	8.33	5.06	4.24	1.84
PRV_spinal cord	Dmean	6.32	4.43	1.25	0.98
	Dmax	11.84	8.81	2.10	0.75
Spinal cord	Dmean	6.35	4.38	1.28	1.12
	Dmax	11.86	8.94	1.34	1.14
Esophagus	Dmean	5.28	3.77	2.65	0.23
	Dmax	8.13	7.17	4.12	0.34
Heart	Dmean	5.58	4.67	2.24	1.95
	Dmax	6.43	4.83	3.14	1.66

Organs at risk were also adversely affected by motion. The spinal cord and its PRV experienced the largest increases in Dmax, reaching nearly 12% under motion compared to approximately 2% in static conditions. The lungs, esophagus, and heart showed elevated low-to-intermediate dose exposure and greater dose variability, consistent with an increased risk of radiation-induced toxicity. These findings are visualized in the DVH comparison (fig. 10), where dynamic (dotted) curves shift leftward for the PTV, indicating reduced target coverage, and upward for OARs, indicating increased exposure.

The dose distribution maps further confirm these observations. In the static condition, the high-dose regions conform tightly to the PTV with a steep fall-off, minimizing dose to surrounding tissues. Under motion, dose blurring and smearing are evident, resulting in poorer target conformity and the extension of low-to-intermediate dose regions into surrounding lung tissue and mediastinal structures. Hotspots in the spinal cord and esophagus become more pronounced, aligning with the quantitative dose differences and DVH deviations.

4. Conclusions

This study demonstrates that respiratory motion has a substantial and clinically significant effect on dose delivery accuracy in VMAT for lung cancer. Under static conditions, both ArcCheck and 3DVH systems achieved high gamma pass rates (>95% for 3%/3 mm) with minimal variability, confirming excellent agreement between planned and delivered doses. In contrast, the

introduction of simulated respiratory motion led to a marked reduction in gamma pass rates (decreasing by 20–40%), pronounced dose blurring, and increased variability in both PTV and surrounding OARs. 3DVH reconstructions revealed that motion-induced interplay effects reduced target coverage (D95% and D98%), increased hotspots within the PTV, and elevated Dmax values for critical OARs such as the spinal cord and esophagus. These findings underscore the need for robust motion management strategies including respiratory gating, tumor tracking, or motion-inclusive planning, and highlight limitations of conventional VMAT QA, which assesses only machine accuracy. The proposed dynamic QA process, integrating ArcCheck-3DVH with motion-simulated phantom measurements, enabled clinically relevant evaluation of dosimetric effects in moving anatomy. This approach provides a valuable tool for detecting motion-induced uncertainties and for developing safer, more accurate thoracic radiotherapy protocols.

5. References

1. Otto K. Volumetric modulated arc therapy: IMRT in a single gantry arc. Med Phys. 2008;35(1):310–317.
2. Timmerman R, Paulus R, Galvin J, et al. Stereotactic body radiation therapy for inoperable early-stage lung cancer. JAMA. 2010;303(11):1070–1076.
3. Wong JY, Liu A, Schultheiss T. Total marrow and total lymphoid irradiation. Semin Radiat Oncol. 2014;24(4):273–282.
4. Keall PJ, Mageras GS, Balter JM, et al. The management of respiratory motion in radiation oncology: report of AAPM Task Group 76. Med Phys. 2006;33(10):3874–3900.
5. Shirato H, Shimizu S, Kitamura K, et al. Four-dimensional treatment planning and real-time tumor tracking radiotherapy. Int J Radiat Oncol Biol Phys. 2000;48(2):435–442.
6. Seppenwoolde Y, Shirato H, Kitamura K, et al. Precise and real-time measurement of 3D tumor motion in lung due to breathing and heartbeat. Int J Radiat Oncol Biol Phys. 2002;53(4):822–834.
7. Tang D, et al. Evaluation of Delta4DVH Anatomy in 3D patient-specific IMRT quality assurance. Technol Cancer Res Treat. 2020; 19:1–12. doi:10.1177/1533033820945816.
8. Burton A, et al. Design and validation of a novel dosimetry phantom for motion management audits. J Appl Clin Med Phys. 2025;26: e70091. doi:10.1002/acm2.70091.
9. Keall PJ. 4-dimensional computed tomography imaging and treatment planning. Semin Radiat Oncol. 2004;14(1):81–90.
10. Song JY. Evaluation of Dynamic Delivery Quality Assurance Process for Internal Target Volume Based RapidArc. Prog Med Phys. 2017;28(4):181–188. doi:10.14316/pmp.2017.28.4.181.
11. Court LE, Wagar M, Ionascu D, et al. Management of respiratory motion in radiation oncology. Med Dosim. 2011;36(2):123–129.
12. Liu HH, Balter P, Tutt T, et al. Assessing respiration-induced tumor motion and internal target volume using 4DCT for radiotherapy of lung cancer. Int J Radiat Oncol Biol Phys. 2007;68(2):531–540.
13. Sawant A, Venkat RB, Srivastava V, et al. Management of 3D intrafraction motion through real-time DMLC tracking. Med Phys. 2008;35(5):2050–2061.
14. Nelms BE, Opp D, Robinson J, et al. VMAT QA: measurement-guided 4D dose reconstruction on a patient. Med Phys. 2012;39(7):4228–4238.
15. Feygelman V, Zhang G, Stevens C, et al. Evaluation of a new VMAT QA device, ArcCHECK. Med Dosim. 2011;36(3):295–300.
16. Saito M, et al. Comparison of DVH-based plan verification methods for VMAT: ArcCHECK-3DVH system and dynalog-based dose reconstruction. J Appl Clin Med Phys. 2017;18(4):206–214. doi:10.1002/acm2.12123
17. Song JH, et al. Dosimetric Verification by Using the ArcCHECK System and 3DVH Software for Various Target Sizes. PLoS ONE. 2015;10(3):e0119937.
18. Park JH, et al. Comparison of 3DVH Software with Two-dimensional Array Systems on Pretreatment Verification for VMAT. J Nucl Med Radiat Ther. 2016; 7:284. doi:10.4172/2155-9619.1000284
19. Jacob P. Comparison of Arccheck and Portal Dosimetry in Dose Verification for IMRT and RapidArc Plans. J Oncol Res Rev Rep. 2024;5(5):1–5.
20. Kavak AG, et al. Impact of respiratory motion on lung dose during total marrow irradiation. Front Oncol. 2022; 12:924961. doi:10.3389/fonc.2022.92496

MEDICAL PHYSICS IN THE BALTIC STATES 17 (2025)

Proceedings of International Conference "Medical Physics 2025"
06-08 November 2025, Kaunas, Lithuania

THE IMPACT OF RAPIDPLAN™ MODEL CONFIGURATION PARAMETERS ON THE CLINICAL ACCEPTABILITY OF THE PROSTATE SIB TREATMENT PLAN

Elina STENCELE[1,2], Sandra STEPINA[2]
[1]Riga Technical University; [2]Liepaja Regional Hospital
elinastencele@gmail.com; stepinna.sandra@gmail.com

***Abstract*:** The aim of this study is to systematically evaluate how different *RapidPlan*™ model configuration parameters affect the quality and clinical acceptability of prostate simultaneous integrated boost (SIB) treatment plans. A total of 28 *RapidPlan*™ models were generated, each model tested on 3 different CT datasets. Plans were assessed based on target volume (PTV) coverage, organ-at-risk (OAR) volume compliance with dose-volume criteria, and dosimetric verification. As a result, the most effective *RapidPlan* model configuration was identified.

Keywords: RapidPlan, model configuration, prostate, SIB, clinical plan acceptability.

1. Introduction

Prostate cancer is the fourth most common cancer worldwide, and radiotherapy is one of its main treatment methods [1]. Volumetric modulated arc therapy (VMAT) with simultaneous integrated boost (SIB) is increasingly used for prostate irradiation, offering reduced exposure of organs at risk (OARs), shorter treatment times, and improved biological effectiveness [2].

If radiotherapy is prescribed, the initial step involves topometric imaging to localize the tumor. Subsequently, organs at risk (OARs) are delineated, the target volume is defined, the prescription dose is determined, a treatment plan is generated, and dosimetric verification is performed. In 1.2% of cases, repeated topometric imaging and re-planning are required prior to treatment initiation. The most frequent causes of repeated topometric imaging include patient positioning errors (11.73%), anatomical changes (9.86%), and rectal filling variations (8.45%) [3]. Anatomical variations and organ filling differences are influenced by the interval between topometric imaging and treatment commencement [4].

The use of *RapidPlan*™ has been shown to reduce planning time by approximately 50% compared to manual optimization [5], thereby shortening also the interval between topometric imaging, treatment initiation and minimizing the likelihood of anatomical changes. *RapidPlan*™ has demonstrated the ability to generate clinically acceptable plans for single-target treatments such as lung [6] and prostate [5] cancers, as well as for simultaneous integrated boost (SIB) plans [7]. While several studies have investigated the application of *RapidPlan*™ [7], the influence of model configuration parameters – including the number of training plans, selected plan structures, applied dose constraints, and optimization objectives – on the clinical quality and dosimetric validity of prostate SIB plans has not yet been systematically evaluated.

2. Methods

To configurate *RapidPlan*™ model parameters, an initial selection of plans should be performed. When selecting plans to configure the *RapidPlan*™ model, a number of conditions need to be met: 1) the plans define several target volumes with different prescribed doses, 2) the prescribed dose is the same for all plans, 3) dose is delivered to all target volumes at the same time - planning is done using the SIB technique, 4) the plans are clinically appropriate (dose to target areas meets V(100%) ≥ 95%, all organ dose constraints are met), 5) Plan dosimetric verification results meet the Gamma criterion of 2%/2mm for more than 97% evaluated points.

All plans were based on CT images acquired using a *Discovery RT* CT scanner. Treatment planning was performed in *Eclipse 17.0*, configured for a *Varian TrueBeam 2.7* linear accelerator.

For model training, 45 clinically acceptable SIB treatment plans with prescribed doses of 2.4/2.85/3 Gy × 20 fractions = 48/57/60 Gy were selected. Treatment plans were optimized to meet the following dose constraints: rectum V20 Gy < 85%, V30 Gy < 57%, V40 Gy < 38%, V50 Gy < 22%, bladder V40.8 Gy < 50%, V48.6 Gy < 25%, V60 Gy < 5% and femoral heads V40.8 Gy < 50% [8].

For optimization, additional structures were created, including PTV and OAR overlap regions, OAR

substructures outside the PTV, and a ring structure surrounding the target with lowest prescribed dose.

To evaluate the impact of *RapidPlan*™ configuration parameters on plan quality, 28 models were created and grouped into four categories:

1. **Training set size** – models were built with different numbers of training plans while keeping other parameters constant. Starting with the minimum requirement of 20 plans (model M1.0), additional models used 30 (M2.0) and 40 (M3.0) plans.
2. **Structures included in optimization** – variants of the 20-plan models (M1.0, M1.1, M1.2) were created with progressively added structures: OAR and PTV overlap volumes (M1_OVL), OAR structures excluding PTV (M1_OAR), additional auxiliary structures (ring, small intestine) (M1_RING).
3. **Dose restrictions** – based on the best-performing baseline models, additional variants were generated by including: dose constraints for OAR–PTV overlap regions (M1_RES-1), dose constraints for OAR part outside PTV (M1_RES-2), additional PTV dose limits (M1_RES-3).
4. **Optimization criteria** – using the best structural and restriction configurations, model M4.0 was built and further modified: manual prioritization based on observed correlations (M4.1), manual prioritization according to clinical practice (M4.2), normal tissue objective (NTO) set automatically (M4.3), NTO defined manually (M4.4).

For model validation, three sets of 3D CT images from patients without prior radiotherapy plans were selected. All test plans were generated using two arcs in opposing directions, 6 MV photon energy, and a non-rotated table position. For each plan only one optimization cycle was performed.

To assess clinical acceptability, each model validation plan was normalized that 95% of the prescribed dose (57Gy for PTV_3/60) covered 100% of the PTV_3/60 volume. Dose – volume histograms (DVHs) were evaluated for organs at risk (OARs) using the corresponding clinical dose-volume criteria. For the PTVs: 95 % of the prescribed dose had to cover 100 % of each PTV (D100% ≥ 95 %), and the maximum dose had to remain below 107 % of the prescription and be located within PTV_3/60.

The minimum and maximum PTV dose values represent point-specific information. As part of the study, it was also decided to analyze the PTV_2.85/57 and PTV_2.4/48 sub-volumes receiving <95 % of the prescribed dose. For this purpose, the 95 % isodose structure $V_{95\%}$ was generated and intersected with each PTV V_{PTV}. The underdosed volume $V_{<95\%}$ was defined as the difference and expressed as a percentage $V_{\%}$ of the PTV volume (1).

$$V_{\%} = \frac{V_{PTV} - V_{95\%}}{V_{PTV}} \cdot 100 \qquad (1)$$

Volumes $V_{\%}$ below 1 % were considered clinically insignificant, as the under-covered regions are most often located between the 3D CT image slices — above the superior PTV boundary or below the inferior PTV boundary. The same approach was used to compute the PTV volume receiving >107 % of the prescribed dose.

Although the ALARA principle is applied in clinical practice to minimize the dose to organs at risk (OARs), the aim of this study was to determine whether the respective dose-volume criteria were fulfilled at all. Therefore, only criteria that were not met were included in the assessment of OARs. For each non-compliant criterion, the absolute deviation between the calculated volume receiving the specified dose V_{plan} and the reference volume defined by the criterion $V_{criterion}$ was determined. Based on these deviations, the root-mean-square error (RMSE) was calculated (2) in order to quantify overall deviation of OAR dose–volume parameters from the clinical acceptance criteria.

$$\mathrm{RMSE} = \sqrt{\frac{\sum(V_{criterion} - V_{plan})^2}{n}}, \qquad (2)$$

where n - the number of dose-volume criteria not met for the OARs.

Dosimetric verification of the treatment plans was performed using *Varian EPID* (Electronic Portal Imaging Device) portal dosimetry. The plans generated with the *RapidPlan*™ model were recalculated with the *Varian PDIP* (Portal Dose Image Prediction) algorithm to obtain a verification dose distribution, which was subsequently measured using the EPID detector integrated in the linear accelerator. The measured and calculated dose distributions were compared using gamma analysis. A gamma criterion of 2 mm/2 % with a minimum of 97 % of points meeting the criterion was applied, and it was additionally verified that the maximum gamma index did not exceed 3,5.

As part of the *RapidPlan*™ model evaluation, the repeatability of selected models was assessed by testing their ability to produce consistent results. Using the same 3D CT dataset and the respective *RapidPlan*™ model, six separate plans were generated. The DVH points corresponding to the dose–volume constraints were then compared. To quantitatively evaluate repeatability, the relative standard deviation (RSD) was calculated according to equation (3), expressing the standard deviation (SD) of the dose or volume values at the evaluated DVH points relative to their mean value V_{mean}.

$$\mathrm{RSD} = \frac{SD}{V_{mean}} \cdot 100 \qquad (3)$$

3. Results

In the first group, three *RapidPlan*™ models (M1.0, M2.0, and M3.0) were generated **using 20, 30, and 40 plans for model training**. All models used identical configuration parameters. In the optimization the original OAR structures and automated priority assignment for optimization were used. For OAR optimization, dose-volume constraints were set as DVH objectives restrictions. Dose–volume restrictions for the target volumes were consistently applied, ensuring D100% ≥ 95% and D_{max} ≤ 105%. The normal tissue objective (NTO) parameters were set according to values most commonly used clinically for prostate SIB plan

optimization: distance from target border 0,3 cm, start dose 95%, end dose 30%, and a fall-off coefficient of 0,05.

The **PTV results** for the plans generated during model testing are shown in Figure 1. The bar graphs represent the mean value of minimum dose D_{min} for each of the three target volumes across the models, while the green line indicates the corresponding dose–volume constraint. As shown in Figure 1, the D_{min} for PTV_3/60 meets the criterion in all models, as the plans were normalized to this value. For PTV_2.4/48, the minimum dose falls short of the criterion by an average of 1,46 Gy, and for PTV_2.85/57, it is on average 3,47 Gy below the required value.

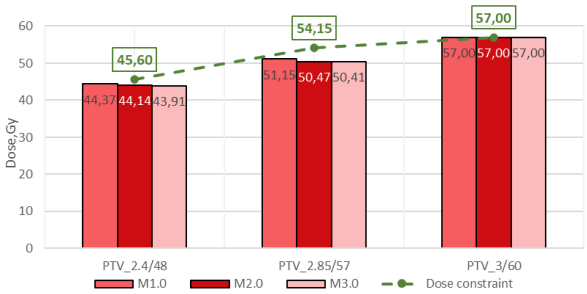

Fig. 1. PTV dose in models with different training set size

The calculated PTV volumes receiving less than 95% of the prescribed dose or more than 107% range from 0,012% to 0,915%, and can therefore be considered negligible. Within the model plans, areas receiving less than the prescribed dose are primarily located in PTV regions overlapping the bladder and rectum. Increasing the number of training plans results in a larger underdosed volume in PTV_2.85/57, whereas the underdosed volume in PTV_2.4/48 remains unaffected.

All dose–volume criteria for the **bladder** were achieved. The bladder volumes in the plans were, on average, 20,78% lower than the limit for V40.8Gy < 50%, 2,43% lower for V48.6Gy < 25%, and 3,78% lower for V60Gy < 5%. In contrast, the only rectum dose–volume criterion met by all models was V20Gy < 85%.

The **rectum** dose–volume criteria V30Gy < 57%, V40Gy < 38%, and V50Gy < 22% were not met in any plan. Specifically, V30Gy < 57% was exceeded on average by 2,97%, V40Gy < 38% by 3,66%, and V50Gy < 22% by 4,51%.

The volume deviation of OARs from the dose–volume constraints for the first group of models is shown in Figure 2. As illustrated, increasing the number of plans used for model training reduces the OAR volume deviations from the constraints.

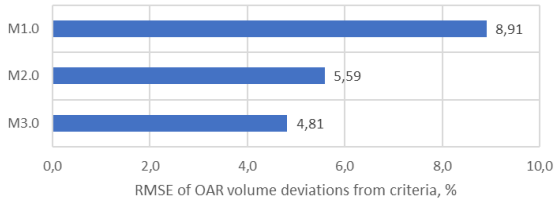

Fig. 2. First model group: RMSE of OAR volume deviations

Second model group are models with **different structures included in optimization.** This group is based on three models trained with 20 plans: M1.0, M1.1, and M1.2, using the same structures as the first group (M1). Derived models were created by progressively adding structures, but other model configuration parameters (training set size, dose–volume restrictions, priority asignment type, NTO parameters) remaining the same:

- **M1_OVL** included PTV and OAR overlap regions (PTV_bladder and PTV_rectum) with restriction Dmax < 60 Gy to reduce hot spots.
- **M1_OAR** included only OAR parts outside the PTV (Bladder-PTV, Rectum-PTV) with mean dose restrictions (17 Gy for bladder, 21.5 Gy for rectum) to improve dose–volume compliance.
- **M1_RING** added structures near but outside the target (Ring, Small_intestinum) with mean dose limits (3,5 Gy and 1 Gy) to reduce high-dose regions.

The **PTV results** for the second model group's plans are shown in Figure 3. On average, an additional 1,52 Gy is required to meet the PTV_2.4/48 criterion, whereas 4,23 Gy is needed for PTV_2.85/57. The figure shows that in the M1_RING model, the minimum dose received by PTV_2.85/57 is substantially lower (on average by 3,40 Gy) compared to the other models. The minimum dose for PTV_2.4/48 is comparable across all models (SD=0,56 Gy), although it is slightly lower in the M1_RING model.

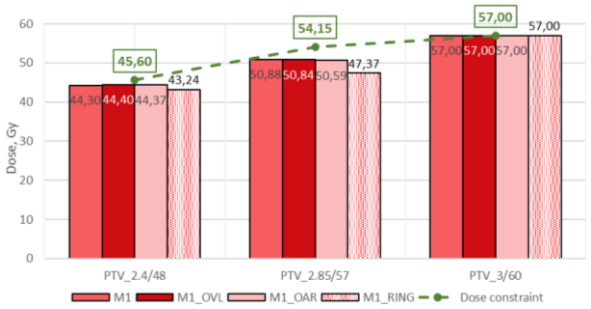

Fig. 3. PTV dose in models with different structures included in optimization

In models M1, M1_OVL, and M1_OAR, the PTV volume receiving doses below the prescribed level is <1%, ranging from 0,004% to 0,869%. For the M1_RING model, this underdosed volume increases to over 1% ($V\%_{(PTV\_2.85/57)}$ = 1.664%). Adding OAR structures with dose constraints, while keeping PTV limits unchanged, can reduce OAR doses but may also slightly compromise PTV coverage. Therefore, for this subgroup, the impact on OAR doses will be further evaluated.

All **bladder** dose–volume criteria were met. On average, bladder volumes were 21,98% below the limit for V40.8Gy < 50%, 4,26% below for V48.6Gy < 25%, and 4,10% below for V60Gy < 5%. For V48.6Gy < 25%, bladder volumes decreased with the addition of more optimization structures. The lowest V60Gy < 5% volume occurred in M1_OVL, where fewer additional structures allowed the plan to better reduce high doses in the PTV and overlap regions.

For the **rectum**, only V20Gy < 85% was met in all models, with volumes on average 7,21% below the limit. The criteria V30Gy < 57%, V40Gy < 38%, and V50Gy < 22% were not achieved in any plan, exceeding the limits by 2,48%, 3,95%, and 4,83%, respectively.
Overall, analysis of the OAR results (Figure 4) shows that the addition of supplementary optimization structures reduces the volume deviations from the dose–volume constraints.

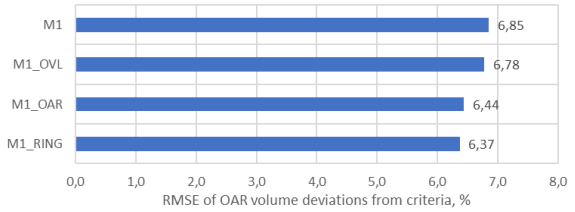

Fig. 4. Second model group: RMSE of OAR volume deviations

The third model group includes models with **different dose restrictions.** These models are based on the M1_RING models. In model **M1_RES-1**, additional gEUD limits (g = 38, D = 58 Gy) were applied to the PTV and OAR overlap regions, but this resulted in increased OAR deviations. In **M1_RES-2**, stricter mean dose limits were selected for OAR regions outside the PTV (from 17 Gy to 15 Gy for Bladder–PTV and from 21,5 Gy to 20 Gy for Rectum–PTV) and applied together with *Line* type restriction to further reduce OAR doses. In **M1_RES-3**, the upper PTV_3/60 dose limit was reduced from 105 % to 103 %, while the lower limits for PTV_2.4/48 and PTV_2.85/57 were increased from 95 % to 100 %, and the mean dose limits for Bladder–PTV and Rectum–PTV were returned to 17 Gy and 21.5 Gy to support improved PTV coverage.
The **PTV results** for the models with different dose restrictions are shown in Figure 5. On average, the PTV_2.4/48 criterion falls short by 2,10 Gy and the PTV_2.85/57 criterion by 6,47 Gy. In the models prioritising OAR sparing (M1_RING, M1_RES-1 and M1_RES-2), the minimum dose for all targets is similar (SD = 0,25% for PTV_2.4/48 and SD = 0,08% for PTV_2.85/57). As illustrated in the figure 5, model M1_RES-3 provides improved target coverage: the minimum dose for PTV_2.85/57 is on average 1,5 Gy higher and for PTV_2.4/48 on average 2,0 Gy higher compared with the other models.

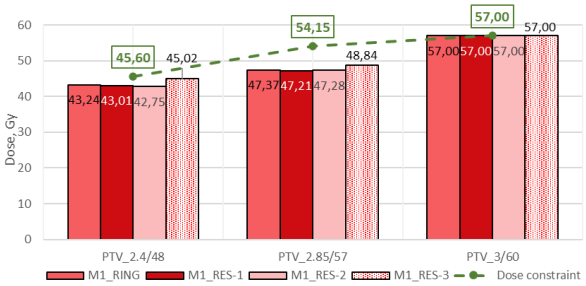

Fig. 5. PTV dose in models with different dose restrictions

In models M1_OAR, M1_RES-1 and M1_RES-2, underdosed regions were observed in both PTV_2.4/48 and PTV_2.85/57 (0,000% – 1,664%), and in PTV_2.85/57 the volume exceeded 1% of the target. This is due to strict OAR dose limits forcing a reduction of dose to the target during optimisation. When stricter PTV dose constraints were introduced (M1_RES-3), the underdosed volume in PTV_2.4/48 decreased to <0,1 cm³ (0,000%) and in PTV_2.85/57 to 0,275%, which is clinically negligible.
As in the previous model groups, all **bladder** dose–volume criteria were fulfilled. The bladder volumes were, on average, 23,51% below the limit for V40.8Gy < 50%, 5,28% below for V48.6Gy < 25%, and 3,26% below for V60Gy < 5%. The highest bladder volumes were obtained in model M1_RES-3, with the most pronounced difference (≈ 2,5%) observed for the V60Gy < 5% criterion.
For the **rectum**, only the V20Gy < 85% criterion was achieved in all models (on average 13,11% below the limit). The V30Gy < 57% criterion was met in models M1_RES-2 and M1_RES-3 (~4,6% below the limit), but exceeded by ~1,9% in M1_RING and M1_RES-1. The higher-dose criteria V40Gy < 38% and V50Gy < 22% were exceeded on average by 2,72% and 4,84%, respectively. Although V20Gy < 85% was achieved in all models, the rectal volume was notably lower in M1_RES-2 (68,68%) and M1_RES-3 (68,06%) compared with M1_RING (75,55%) and M1_RES-1 (75,26%). A similar pattern was observed for V30Gy < 57%, with values of 58,90% and 58,93% for M1_RING and M1_RES-1, and 52,46% for M1_RES-2 and 52,29% for M1_RES-3.
As shown in Figure 6, applying stricter dose constraints to OARs promotes closer adherence of organ volumes to the dose–volume constraints without substantially affecting PTV coverage. Conversely, implementing more stringent dose restrictions on the PTV increases OAR volumes at the dose–volume thresholds while significantly improving PTV coverage.

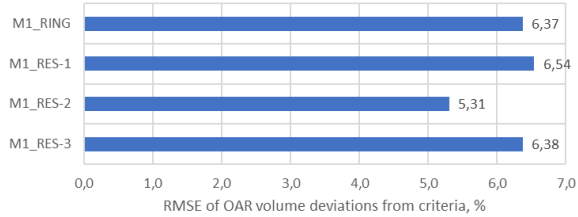

Fig. 6. Third model group: RMSE of OAR volume deviations

The fourth group included models with **different optimization criteria. M4.0** combined M3.0 training plans with the structures and dose constraints of M1_RES-3. Two variants were created per criterion type (dose constraint priorities and NTO parameters). In **M4.1**, priorities were manually assigned based on plans achieving the highest adherence to clinical dose–volume criteria, with average values across six top plans: PTV – 120, bladder and femoral heads – 115, rectum – 102, PTV_bladder – 95, PTV_rectum – 111, Bladder-PTV – 41, Rectum-PTV – 37, Ring – 109, small bowel – 51. NTO settings: 0,3 cm margin from the target, start dose 95%, end dose 30%, fall-off coefficient 0,05. **M4.2** applied clinical practice–based priorities, allowing different values for multiple constraints of the same structure, yielding: PTV_3/60 upper/lower – 140/150,

PTV_2.8/48 and PTV_2.85/57 upper/lower – 240/250, bladder – 100, femoral heads/ring – 65, rectum – 105, PTV_bladder/PTV_rectum – 100, Bladder-PTV – 105, Rectum-PTV – 110, small bowel – 60. The NTO parameter values are the same as in model M4.1. Testing showed that manually assigned priorities outperformed other methods, making M4.1 the reference model. **M4.3** used automatic NTO assignment without user-accessible parameter values, whereas **M4.4** applied theoretically optimal NTO settings: 0,2 cm margin from the target, start dose 103%, end dose 60%, fall-off coefficient 0,13. [9]

The **PTV results** for the models with different optimization criteria are shown in Figure 7. The minimum dose for PTV_2.4/48 across all models is close to the criterion, with an average shortfall of 0,6 Gy. For PTV_2.85/57, the average shortfall is 5 Gy. The best result was achieved with model M4.2, where the minimum dose shortfall to meet the PTV_2.85/57 criterion was 4,26 Gy, and for PTV_2.4/48, only 0,08 Gy.

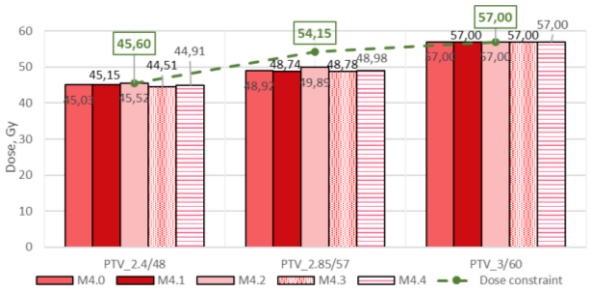

Fig. 7. PTV dose in models with different optimization criteria

In all developed plans, the volume of the target receiving insufficient dose is below 1% (0,000% –0,277%), which is considered negligible within the study. Moreover, these values are substantially lower than those observed in plans generated using models from other groups.

The only dose–volume compliance criterion not met for the **bladder** is V60Gy < 5% in model M4.2, where the bladder volume exceeds the limit by 2.19%. In other models, V60Gy < 5% values are also higher compared to previous model groups.

All models meet the **rectum** V20Gy < 85% and V30Gy < 57% criteria. The volume values achieved in the plans are on average 13,87% below the V20Gy < 85% limit and 3,63% below the V30Gy < 57% limit. For V40Gy < 38%, the volume exceeds the limit by an average of 1,48%, and for V50Gy < 22%, by 5,14%.

Figure 8 shows that model M4.2 produced the least favorable outcomes, indicating that clinically assigned priorities are suboptimal for *RapidPlan*™. Models M4.0 and M4.1 yielded similar results (SD = 0.12%), with slightly lower OAR doses when priorities were manually assigned. The lowest OAR doses are achieved using model M4.3, suggesting that automatic NTO parameter assignment is preferable.

Dosimetric verification confirmed that all model-generated plans **for all model groups** met the Gamma analysis criteria of 2 mm/2% with passing rates > 97% (range: 99,0–100%), and the maximum Gamma index did not exceed 3,5 (range: 1,11–2,81).

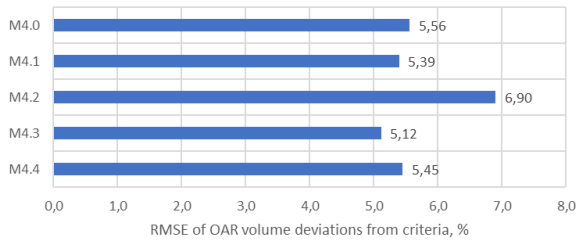

Fig. 8. Fourth model group: RMSE of OAR volume deviations

Table 1 summarizes the **repeatability** results of the model-generated plans, with reference values obtained from models M1.0, M2.0, and M3.0 (mean values reported) and compared with the study's optimal model, M4.1.

Table 1. Repeatability assessment of M4.1 plans compared with previously established RSD values

Structure	Constraint	RDS, %	
		Mean (M1.0, M2.0, M3.0)	M4.1
PTV_3/60	Dmax ≤ 107%	0,21	0,17
	Dmin ≥ 95%	0,00	0,00
PTV_2.85/57	Dmin ≥ 54.15Gy	0,53	0,29
PTV_2.4/48	Dmin ≥ 45.6Gy	0,22	0,13
Bladder	V 60Gy < 5%	37,92	5,18
	V 48.6y < 25%	0,28	0,15
	V 40.8Gy < 50%	0,23	0,22
Right femoral head	V 40.8Gy < 50%	0,00	0,00
Left femoral head	V 40.8Gy < 50%	0,00	0,00
Rectum	V 50Gy < 22%	0,35	0,30
	V 40Gy < 38%	0,20	0,23
	V 30Gy < 57%	0,15	0,17
	V 20Gy < 85%	0,11	0,26

The data show that plans generated with M4.1 exhibit high stability. Although the bladder dose–volume criterion V60Gy < 5% shows a relatively wide range in M4.1, its reproducibility is markedly improved (from 37,92% to 5,18%). The results for the other dose–volume criteria demonstrate high repeatability, with relative standard deviations below 1%. The deviation in reproducibility of M4.1 from the initial models is also below 1%, and reproducibility has improved for all structures except the rectum.

4. Discussion

Previous studies suggest that *RapidPlan*™ model performance is strongly influenced by the selection and quality of training plans. Higher-quality plans, assessed by metrics such as APQM% (Adjusted Plan Quality Metric), improve model accuracy, whereas low-quality or anatomically challenging plans can reduce it. [10] In this study no clear relationship was observed between training plan quality and model test plan results. Comparing models M1.0 and M1.1, both with similar PTV coverage, for M1.0 training 4 plans that did not meet all OAR constraints were used, resulting in a higher OAR deviation (8,91%) than M1.1 (5,96%), which included 8 such plans in training.

Increasing the number of training plans does not always guarantee better clinical plan generation; after a certain threshold, plan quality becomes more critical than

quantity. [11] In this study, it was not possible to determine whether adding more training plans beyond a certain number would yield diminishing returns, making plan quality more important than quantity. However, within the available dataset, a trend was observed that increasing the number of training plans improved the quality of model-generated plans.

The inclusion of additional structures, such as rings or modified PTVs excluding OARs, can reduce dose to organs at risk and prevent hotspots outside the target. [12, 13] The results from this study confirm previous findings: including additional structures in optimization reduced OAR doses and prevented high-dose regions outside the PTV. However, this approach negatively affected overall plan quality due to a significant reduction in PTV coverage.

Manually assigned priorities can have a greater impact on dose distribution than automatically generated ones. [13] The results of this study partially support the notion that manually assigned priorities may influence dose distribution more than automatically assigned ones. The best outcomes were observed in model M4.3, where priorities were set manually. However, these values were determined based on previous models in which priorities had been assigned automatically.

5. Conclusions

With the *RapidPlan*™ configurations used in this study, clinically acceptable prostate SIB plans could not be achieved. In the optimal model (M4.1), PTV_2.85/57 coverage was insufficient and rectal dose–volume criteria were exceeded. Although the underdosed PTV volume was only 0,28%, clinical requirements demand D100% ≥ 95%. Rectal V40Gy and V50Gy were exceeded by 2,07% and 4,81%, respectively.

Increasing the training plan number from 20 to 40 slightly raised the underdosed PTV volume (from 0,755% to 0,915%) but reduced OAR deviations (8,91% → 4,81%). Including overlapping and additional structures (Ring, small bowel) improved OAR compliance (6,85% → 6,37%) but increased underdosed PTV (0,895% → 1,711%). Stricter OAR constraints improved compliance without affecting coverage, while stricter PTV constraints increased coverage (PTV_2.4/48: 42,75 Gy → 45,02 Gy; PTV_2.85/57: 47,28 Gy → 48,84 Gy) with slight OAR dose increase.

Manual assignment of dose restriction priorities based on study-identified optimal values reduced OAR deviations, whereas automatic NTO parameters provided the best OAR compliance (5,12% deviation) with a minimal increase in underdosed PTV (0,04%).

Dosimetric verification using an EPID portal detector confirmed that all *RapidPlan*™ generated plans meet clinical requirements (Gamma 2%/2 mm, 97% threshold).

RapidPlan™ ensures high DVH stability, with relative standard deviation <1% for all DVH metrics except bladder V60Gy <5%, which shows 5.18% in the optimal model.

6. References

1. The International Agency for Research on Cancer. *Global cancer burden growing, amidst mounting need for services.* [online]. World Health Organization, 2024 [viewed on 18th of February, 2025]. Available from: https://www.who.int/news/ item/01-02-2024-global-cancer-burden-growing--amidst-mounting-need-for-services
2. Li, X. A., Wang, J. Z., Jursinic, P. A., et al. Dosimetric advantages of IMRT simultaneous integrated boost for high-risk prostate cancer. *Internatinal Journal of Radiatin Oncology, Biology, Physics.* 2005, 61 (4), 1251 – 1257 p. PMID: 15752907. Available from: doi: 10.1016/j.ijrobp.2004.11.034
3. Metzger, A., Renz, P., Hasan, S., et al. Unforeseen Computed Tomography Resimulation for Initial Radiation Planning: Associated Factors and Clinical Impact. *Advances in Radiation Oncology.* 2019, 4 (4), 716 – 721 p. PMID: 31673665. Available from: doi: 10.1016/j.adro.2019.06.002
4. Sonke, J. J., Aznar, M., Rasch, C. Adaptive Radiotherapy for Anatomical Changes. *Seminars in Radiation Oncology.* 2019, 29 (3), 245 – 257 p. Available from: doi: 10.1016/j.semradonc.2019.02.007
5. Ayuthaya, I. I. N., Sanghangthum, T., Oonsiri, P., et al. Multi-planner validation of RapidPlan knowledge-based model for volumetric modulated arc therapy in prostate cancer. *Journal of Applied Clinical Medical Physics.* 2023, 25 (1). PMID: 38009569. Available from: doi: 10.1002/acm2.14223
6. Harms, J., Zhang, J., Kayode, O., et al. Implementation of a Knowledge-Based Treatment Planning Model for Cardiac-Sparing Lung Radiation Therapy. *Advances in Radiation Oncology.* 2021, 6 (6). PMID: 34604606. Available from: doi: 10.1016/j.adro.2021.100745
7. Cilla, S., Ianiro, A., Romano, C., et al. Template-based automation of treatment planning in advanced radiotherapy: a comprehensive dosimetric and clinical evaluation. *Scientific Reports* 2020, 10 (1): 423. Available from: doi: 10.1038/s41598-019-56966-y
8. NSW Government. Prostate adenocarcinoma definitive EBRT high-risk. [online]. [viewed on 9th of February, 2025]. Available from: https://www. eviq.org.au/radiation-oncology/%20urogenital/prostate/235-prostate-adenocarcinoma-definitive-ebrt-high-r#dose-prescription
9. Jolly, D., Alahakone, D., Meyer, J. A RapidArc planning strategy for prostate with simultaneous integrated boost. *Journal of Applied Clinical Medical Physics.* 2010, 12 (1), 35 – 49 p. PMID: 21330979. Available from: doi: 10.1120/jacmp.v12i1.3320
10. Fusella, M., Scaggion, A., Pivato, N., et al. Efficiently train and validate a RapidPlan model through APQM scoring. Medical Physics. 2018, 45 (6), 2611 – 2619p. PMID: 29611213. Available from: doi: 10.1002/mp.12896
11. Van Gysen, K., O'Toole, J., Le, A., et al. Rolling out RapidPlan: What we've learnt. Journal of Medical Radiation Sciences. 2020, 67 (4), 310 – 317 p. PMID: 32881407. Available from: doi: 10.1002/jmrs.420
12. Vaassen, F., Hazelaar, C., Canters, R., et al. The impact of organ-at-risk contour variations on automatically generated treatment plans for NSCLC. Radiotherapy and Oncology. 2021, 163, 136 – 142p. PMID: 34461185. Available from: doi: 10.1016/j.radonc.2021.08.014
13. Ueda, Y., Fukunaga, J., Kamima, T., et al. Evaluation of multiple institutions' models for knowledge-based planning of volumetric modulated arc therapy (VMAT) for prostate cancer. Radiation Oncology. 2018, 13 (1): 46. PMID: 29558940. Available from: doi: 10.1186/s13014-018-0994-1

MEDICAL PHYSICS IN THE BALTIC STATES 17 (2025)

Proceedings of International Conference "Medical Physics 2025"
06-08 November 2025, Kaunas, Lithuania

ASSESSMENT OF FLASH-INDUCED ROS SUPPRESSION ACROSS MULTIPLE DOSE AND DOSE RATE REGIMES

Akvilė ŠLĖKTAITĖ-KIŠONĖ[1,2], Vytautas VELIČKA[2], Marius BURKANAS[1], Aleksandras CICINAS[1], Mindaugas DŽIUGELIS[1,2], Benas DIRGĖLAS[3], Jonas VENIUS[1,2]
[1]National Cancer Center, Medical Physics Department, Vilnius, Lithuania, [2]National Cancer Institute, Biomedical physics laboratory, Vilnius, Lithuania; [3]Faculty of Physics, Vilnius University, Vilnius, Lithuania;
akvile.slektaite@nvc.santa.lt, velic.vytautas@gmail.com, marius.burkanas@nvc.santa.lt, aleksandas.cicinas@nvc.santa.lt, mindaugas.dziugelis@nvc.santa.lt, dirbenas@gmail.com, jonas.venius@nvc.santa.lt

***Abstract*:** The FLASH effect, characterized by reduced a normal tissue toxicity without the compromising tumor control during ultra-high dose rate (UHDR) irradiation. However, the underlying mechanisms of the effect remain unclear. Current hypotheses suggest that physicochemical factors, such as ROS generation and transient oxygen depletion, along with cellular responses, may contribute to the effect.
In this study, we investigated differences between reactive oxygen species (ROS) formation using conventional (CONV) and FLASH irradiation. UHDR pulses of 2 or 4 Gy, with total doses up to 32 Gy were used. ROS generation was measured using a fluorescent probe DHR123. Results showed that higher dose rates and larger doses per pulse consistently suppressed ROS yield. The highest dose rate (96 Gy/s) produced the lowest radical levels. Slope analysis confirmed a slower rate of ROS formation at higher dose rates. These findings support the role of enhanced radical-radical recombination in the FLASH effect and reinforce the potential of UHDR radiotherapy.

Funding: Research Council of Lithuania (LMTLT), agreement No. S-MIP-24-134.

Keywords: FLASH effect, ultra-high dose rate (UHDR), reactive oxygen species (ROS)

1. Introduction

A radiation therapy (RT) remains one of the most effective modalities for cancer treatment. However, its efficacy is limited by the risk of damage to surrounding healthy tissues. Ultra-high dose rate (UHDR) irradiation, known as FLASH-RT, has recently emerged as a novel irradiation technique, showing great potential in maintaining tumour control while reducing normal tissue toxicity [1]. Preclinical studies in animal and cell models have confirmed the FLASH effect, and early clinical trials are now in progress [2]. Despite these advances, the mechanisms underlying the FLASH effect remain incompletely understood. Leading theories explain this phenomenon through radiolytic oxygen depletion, radical-radical recombination, Fenton reactions, ferroptosis, metabolic differences between healthy and cancerous cells and the role of the immune system [3,4]. It is likely that multiple mechanisms contribute to the reduced toxicity in normal tissue.
Studying mechanisms in biological systems can be complicated due to their complexity, where numerous interacting variables can obscure causal relationships. Simplified model systems are therefore essential for clarifying the underlying mechanisms. Experiments in chemical solutions make it possible to isolate radiation-induced physicochemical reactions from subsequent biological responses.
The interaction of ionizing radiation with water produces reactive oxygen species (ROS) such as hydroxyl radicals, hydrogen peroxide, and superoxide, which are primary mediators of radiation damage to DNA and other biomolecules [5]. Additionally, pH affects water radiolysis pathways and radical chemistry. This raises the possibility that differences in acidity between cancerous and healthy tissues can add to the FLASH response. The most normal tissues maintain a stable extracellular pH around 7.4 under well-perfused conditions. In contrast, tumors typically exhibit more acidic extracellular environment (pH ~6.7 or less) due to an aerobic glycolysis (the Warburg effect) and the poor vascularization, that together promote lactate accumulation and lower pH [6].
Since ROS mediate much of the cellular damage induced by ionizing radiation, studying its production is critical for the understanding the diverse effects of FLASH versus conventional (CONV) dose rate irradiation. However, direct measurement of ROS is technically challenging. Fluorescent probes such as dihydrorhodamine 123 (DHR123) provide a sensitive

approach of detecting oxidants, though its fluorescence response is influenced by complex photophysical and chemical processes [7]. In the pure water, oxidation cannot proceed through the peroxidase activity and the probe is not efficiently oxidized by H_2O_2 alone [8]. The measured signal must therefore arise from the secondary chemistry initiated by radiolytic products.

In this work, we investigated ROS yields in water following 6 MeV electron beam irradiation with a modified clinical VARIAN TrueBeam particle accelerator. Using DHR123 fluorescence as a readout, we systematically varied dose rate, total dose, dose per impulse and pH of the solution. Our findings provide further insight into how FLASH irradiation modifies ROS generation compared to CONV exposure.

2. Materials and Methods

2.1. Irradiation setup

All irradiations were performed on a Varian TrueBeam particle accelerator operated in 6 MV photon mode. The target and the flattening filter were removed and an electron scattering foil inserted to generate a pulsed 6 MeV electron beam, following the previously reported approach [9]. For FLASH exposures, samples were positioned in a custom holder on a 2 mm acrylic plate (Fig.1). A dose control relied on photodiode detection of Cherenkov light from each beam pulse.

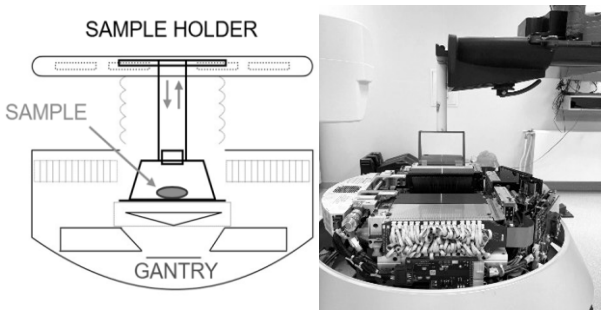

a b

Fig. 1. Left: Schematic diagram of the custom 3D-printed sample holder, designed to attach to the linac table and be positioned within the gantry. Right: Photograph of the holder and setup used for sample irradiation.

FLASH irradiations were delivered at dose rates of 12, 48, and 96 Gy/s with a pulse width of ~3.6 µs. Total doses of 8, 16, 24, and 32 Gy were achieved using either 2 or 4 Gy per pulse. Conventional irradiations were performed at 0.15 Gy/s with samples irradiated through a 10 mm acrylic plate placed at the isocenter.

2.2. Dosimetry

A dosimetry was verified using Gafchromic EBT-4 films calibrated under conventional dose rates. A reproducible irradiation geometry was maintained using custom 3D-printed holders. A film readout was performed 24 hours post-irradiation, after full film contrast stabilization, using a high-pass optics-capable Epson Perfection V850 Pro scanner.

2.3. Sample preparation

Dihydrorhodamine 123 (Sigma-Aldrich) was used as the fluorescent probe for ROS detection. For each irradiation parameter combination, identical water samples were prepared. DHR123 was added prior to the irradiation at a final concentration of 5 µmol/l, following the manufacturers' instructions. The probe was thoroughly mixed by pipetting, and all preparations were performed under a low-light conditions. Care was taken during experiments to ensure equal environmental exposure across samples.

For pH experiments, phosphate-buttered saline (PBS; Sigma-Aldrich) was prepared and adjusted to pH 6, 7, and 8 by stepwise addition of NaOH (Sigma-Aldrich) to a master solution.

2.4. Fluorescence signal processing

Fluorescence was measured 30 min post-irradiation using a Varian Cary Eclipse spectrophotometer. Fluorescence spectra were baseline-corrected using non-irradiated controls, and peak intensities were extracted in the 520–540 nm range of the DHR123 emission spectrum. Triplicate measurements were assessed for consistency with outliers excluded.

3. Results and Discussion

3.1. Dose rate dependence

A total ROS production increased linearly with the radiation dose under both FLASH and CONV irradiation (Fig. 2. a). However, the magnitude of ROS generation was consistently about 4 times higher with the CONV irradiation compared to FLASH across all dose levels.

These findings indicate that while ROS production increases with a dose in both irradiation methods, FLASH consistently suppresses ROS generation relative to CONV, supporting the notion of an altered radical chemistry under UHDR irradiation. This agrees with other studies in water that reported reduced hydrogen peroxide yields under UHDR compared with the conventional irradiation [5]. This phenomenon can be attributed to enhanced probability of radical-radical recombination at the elevated instantaneous concentrations [10].

Although the measured ROS generation differences between various FLASH parameters are smaller than those between FLASH and CONV, some clear tendencies can still be observed in Fig.2 b). ROS production under different FLASH beam parameters shows that both an average dose rate and a dose-per-pulse influence the final outcome, but with differing magnitudes. In all conditions, ROS levels increased approximately linearly with the radiation dose. At a fixed average dose rate, increasing the dose-per-pulse from 2 Gy to 4 Gy consistently reduced ROS yields by about 30% across the examined dose range. By contrast, varying the average dose rate from 12 Gy/s to 96 Gy/s produced a smaller reduction of ~10–20% within each dose-per-pulse group. These findings indicate that although both parameters modulate ROS production, a dose-per-pulse exerts a stronger influence than average dose rate.

This shows that the temporal structure of delivery alters chemical yields, in agreement with radiation-chemical perspectives that identify pulse size as a key factor in spur kinetics and recombination balance [10]. The result is also consistent with Monte Carlo simulations of water radiolysis, which reported that higher dose-per-pulse accelerates radical recombination and reduces the yield and lifetime of oxidant species [11].

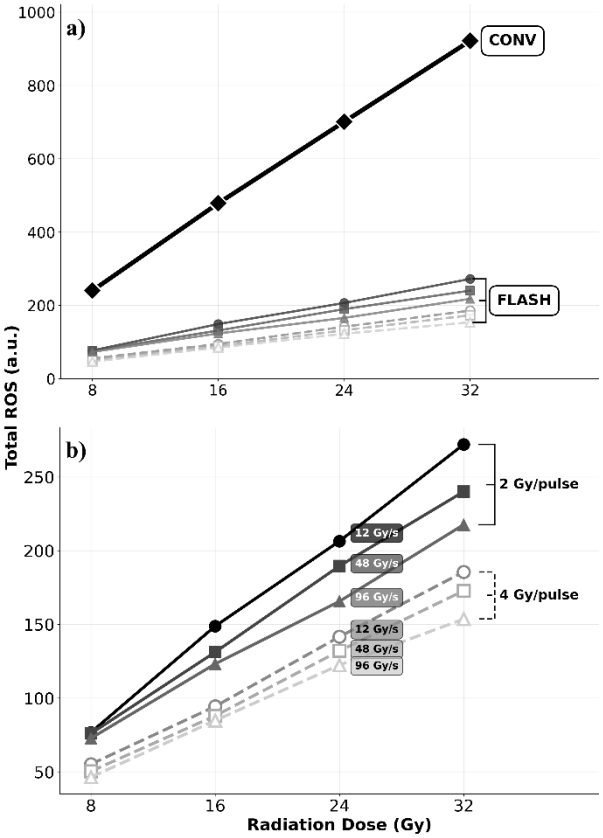

Fig. 2. Total ROS measured by DHR123 fluorescence as a function of radiation dose. a) Comparison of FLASH and CONV irradiation. b) Magnified view of FLASH irradiation groups (dose-per-pulse of 2 and 4 Gy and mean dose rates of 12, 48 and 96 Gy/s). Data are presented as group averages.

These findings indicate that maximizing the FLASH effect is more effective with higher dose-per-pulse settings. However, in our setup, and likely in others using similar modifications, higher doses per pulse lead to the smaller field sizes and a reduced homogeneity.

3.3. The pH dependence under FLASH Irradiation

Fluorescence measurements in buffered solutions across pH conditions revealed pronounced differences between the FLASH and CONV irradiation (Fig.3) not only in overall signal intensity, but also dependance on solution properties. Under FLASH conditions, the fluorescence signal decreased systematically with increasing pH with highest emission at pH 6 and the lowest values at pH 8 (Fig. 3a). In contrast, a CONV irradiation showed no measurable pH dependence (Fig. 3b), consistent with prior reports that hydrogen peroxide yields in the aerated water remain stable across this range [12].

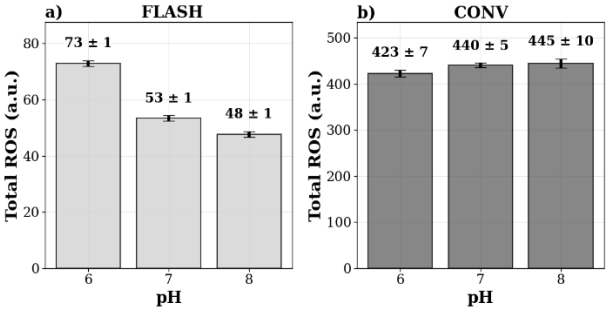

Fig. 3. Fluorescence spectra of DHR123 at pH 6, 7 and 8 following irradiations with a total dose of 16 Gy using a) FLASH irradiation at 96 Gy/s and 2 Gy per pulse, b) CONV irradiation with 0.15 Gy/s dose rate.

Since acidic conditions are a recognized feature of tumour microenvironment [6], the reduced oxidant yield observed under FLASH at the lower pH suggests that ROS suppression could be less pronounced in tumours than in the surrounding normal tissue. This differential response may represent one of the underlying mechanisms contributing to the FLASH effect, where healthy tissues are protected while effective tumor control is maintained. However, this interpretation should be treated cautiously, as the present results were obtained in aqueous solution and do not reflect the complexity of cellular environment.

To our knowledge this is the first study of pH-dependent effects under FLASH irradiation and it highlights the need for further work in the biologically relevant models.

4. Conclusions

At all tested doses, FLASH irradiation produced ~ 4 times fewer ROS than CONV irradiation, consistent with the enhanced radical-radical recombination theory.

During FLASH irradiation both an average dose rate and a dose-per-pulse affected ROS production, but a dose-per-pulse had the stronger effect. Doubling the dose-per-pulse reduced ROS yields by ~30%.

ROS yields decreased systematically with the increasing pH (the highest at pH 6, the lowest at pH 8), whereas CONV irradiation showed no pH dependence. Since tumors often exhibit acidic microenvironments, this suggests FLASH may differentially affect normal versus tumor tissues.

These findings support the hypothesis that FLASH modifies radical chemistry in ways that could reduce a toxicity in normal tissues while preserving the tumor control.

5. References

1. Favaudon V., Caplier L., Monceau V., Pouzoulet F., Sayarath M., Fouillade C., Poupon M. F., Brito I., Hupé P., Bourhis J., Hall J., Fontaine J. J., and Vozenin M. C. Ultrahigh dose-rate FLASH irradiation increases the differential response between normal and tumor tissue in mice. Science Translational Medicine, 2014, 6(245).
2. Limoli C. L. and Vozenin M. C. Reinventing radiobiology in the light of FLASH radiotherapy. Annual Reviews, 2023, 7:1–21.
3. Chow J. C. L. and Ruda H. E. Flash radiotherapy: innovative cancer treatment. Encyclopedia, 2023, 3(3):808–23.
4. Esplen N., Mendonca M. S. and Bazalova-Carter M. Physics and biology of ultrahigh dose-rate (FLASH) radiotherapy: a topical review. Physics in Medicine and Biology, 2020, 65(23).

5. Zhang T., Stengl C., Derksen L., Palskis K., Koritsidis K., Zink K., Adeberg S., Major G., Weishaar D., Theiß U., Jin J., Spadea M. F., Theodoridou E., Hesser J., Baumann K.-S., and Seco J. Analysis of hydrogen peroxide production in pure water: ultrahigh versus conventional dose-rate irradiation and mechanistic insights. Medical Physics, 2024, 51(12):7439–52. doi:10.1002/mp.17335.
6. Oraiqat I., Al-Snayyan E., Calcaterra A., Clarke R., Rehemtulla A., and El Naqa I. Measuring tumor microenvironment pH during radiotherapy using a novel Cerenkov emission multispectral optical probe based on silicon photomultipliers. Frontiers in Physics, 2021, 9:636001. doi:10.3389/fphy.2021.636001.
7. Djiadeu P., Kotra L. P., Sweezey N., and Palaniyar N. Biophysical basis of fluorescence emission induced by oxidized DHR123. PLoS One, 2017, 12(2):e0172613. doi:10.1371/journal.pone.0172613.
8. Jávega B., Herrera G., Martínez-Romero A., and O'Connor J.-E. Flow cytometry of oxygen and oxygen-related cellular stress. Oxygen, 2023, 3(2):222–55. doi:10.3390/oxygen3020016.
9. Šlėktaitė-Kišonė A., Burkanas M., Cicinas A., Čeponis T., Džiugelis M., Merkys M., Adlienė D., and Venius J. First experience on Varian TrueBeam generated ultra-high dose rate electron beam dosimetry using conventional dosimetry methods. In: Medical Physics in the Baltic States 16; 2023 Nov 9–11; Kaunas, Lithuania. p. 92–95.
10. Wardman P. Radiotherapy using high-intensity pulsed radiation beams (FLASH): a radiation-chemical perspective. Radiation Research, 2020, 194(6):607–17. doi:10.1667/RADE-19-00016.
11. Chappuis F., Tran H. N., Jorge P. G., Zein S. A., Kyriako I., Emfietzoglou D., Bailat C., Bochud F., Incerti S., and Desorgher L. Investigating ultra-high dose rate water radiolysis using the Geant4-DNA toolkit and a Geant4 model of the Oriatron eRT6 electron linac. Scientific Reports, 2024, 14:26707. doi:10.1038/s41598-024-76769-0.
12. Roth O. and LaVerne J. A. Effect of pH on H_2O_2 production in the radiolysis of water. Journal of Physical Chemistry A, 2011, 115(5):700–8. doi:10.1021/jp1099927

MEDICAL PHYSICS IN THE BALTIC STATES 17 (2025)

Proceedings of International Conference "Medical Physics 2025"
06-08 November 2025, Kaunas, Lithuania

THE IMPORTANCE OF PRECISE PATIENT POSITIONING IN IMAGE-GUIDED RADIOTHERAPY: RETROSPECTIVE EVALUATION OF ESTIMATED IRRADIATION BY REGISTERED DAILY CONE-BEAM COMPUTED TOMOGRAPHY IMAGES

Renata PAUKŠTAITIENĖ[1], Robertas PETROLIS[1], Reda ČERAPAITĖ-TRUŠINSKIENĖ[1,2], Algimantas KRIŠČIUKAITIS[1], Diana MEILUTYTĖ-LUKAUSKIENĖ[1,3], Vita ŠPEČKAUSKIENĖ[1], Greta KARPAVIČIENĖ[1,2]
[1]Lithuanian University of Health Sciences; [2]Hospital of Lithuanian University of Health Sciences Kaunas Clinics, Oncology Hospital; [3]Lithuanian Energy Institute
[1]renata.paukstaitiene@lsmu.lt; [2]robertas.petrolis@lsmu.lt; [3]reda.cerapaite-trusinskiene@lsmu.lt; [4]algimantas.kriksciukaitis@lsmu.lt; [5]diana.meilutyte-lukauskiene@lsmu.lt; [6]vita.speckauskiene@lsmu.lt; [7]greta.karpaviciene@lsmu.lt

***Abstract*:** Maximisation of irradiation accuracy of malignant tissues is a key challenge on the way to optimal radiotherapy. Strategies to improve irradiation accuracy should balance the expected clinical benefit against the feasibility and procedural demands of the method used. This pilot study marks an initial step toward retrospectively evaluating patient positioning accuracy, analysing CBCT images in relation to clinical outcomes, and estimating actual irradiation of target and surrounding tissues.
The CBCT images were acquired from head and neck patients treated with the Halcyon V3.1 linear accelerator. The algorithms for precise alignment of images, which made it possible to estimate the detailed changes in tumour tissue density during treatment sessions were developed in the MATLAB. The recalculation of the actual dose showed that even small positioning errors can lead to significant changes in the delivered dose, especially in areas where critical organs are affected.

Keywords: Image-guided radiotherapy, Positioning, Irradiation dose, Image analysis, Deviations.

1. Introduction

Head and neck cancer (HNC) is responsible for more than 500,000 new cases per year worldwide, with squamous cell carcinoma (SCC) accounting for approximately 90% of cases [1]. Due to the complex anatomy of this region and the proximity of tumour to critical organs at risk (OARs), a high-precision radiotherapy is essential to ensure the local tumour control while minimising toxicity [2]. Modern techniques such as an intensity modulated radiotherapy (IMRT) and volumetric modulated arc therapy (VMAT) provide a highly conformal dose distribution, but their effectiveness depends not only on the accuracy of treatment planning, but also on the consistent reproduction of the patient anatomy and the positioning throughout the treatment course [3].
Even small deviations in the patient positioning or anatomical changes such as a tumour shrinkage, an inflammation or an oedema, can lead to significant discrepancies between the planned and delivered dose [4, 5]. This is particularly relevant in HNC, where critical structures such as the spinal cord, optic nerves, and salivary glands are highly sensitive to radiation [6]. Positioning errors as small as 2–3 mm can lead to clinically significant dose variations, emphasizing the need for an adaptive radiotherapy strategy in selected patients [5].
An image-guided radiotherapy (IGRT), particularly using a daily cone beam computed tomography (CBCT), has become an indispensable tool for monitoring and correcting positioning errors during the treatment [3]. Mechanical immobilisation systems are commonly used to minimise inter-fraction variability. However, they cannot compensate for internal anatomical changes such as tumour regression, an oedema or an organ displacement during the fractionated radiotherapy [7, 8]. CBCT enables three-dimensional visualisation of the patient's anatomy at the time of treatment and forms the basis for anatomy-adaptative (A-ART) and response-adaptive (R-ART) approaches [9]. However, the routine use of daily CBCT remains limited due to the additional workflow complexity, a time requirement, and image quality limitations [10]. Furthermore, accurate registration of CBCT with planning CT is complicated by varying acquisition conditions, such as slice mismatches, rotations, and geometric distortions, which can lead to systematic errors in patient positioning and dose

calculation. Although volumetric and density-based imaging criteria have been used in other cancers, such as hepatocellular carcinoma [11], their role in predicting treatment outcomes in HNC has not been sufficiently explored. This knowledge gap is particularly important in patients with rapid tumour regression, where discrepancies between planned and administered doses may affect tumour control and increase the risk of OARs toxicity [6].

The present pilot study retrospectively investigates positioning deviations and dose discrepancies in HNC patients who showed significant tumour shrinkage during radiotherapy. By analysing daily CBCT datasets with a volumetric image registration algorithm, we recalculated the administered doses and quantified tumour density and volume changes. The aim of this study is to quantify the clinical significance of anatomical changes during the treatment and to support the integration of an adaptive radiotherapy into the clinical workflow. As a pilot analysis, it aims to confirm the feasibility of CBCT-based volumetric registration for accurate dose recalculation and help guide future large-scale studies.

2. Methods

A retrospective study was conducted in patients with head and neck cancer treated in the Lithuanian University of Health Sciences Kaunas Clinics, Affiliated Hospital of Oncology, Department of Radiotherapy. Ethical approval was granted by the Kaunas Regional Biomedical Research Ethics Committee for Biomedical Research (approval number BE-2-90). Eligible patients had a locally advanced disease, were prescribed a radical radiotherapy, and demonstrated a clear anatomical response to the treatment.

Patients positioning was verified daily using a kilovoltage cone beam computed tomography (kV-CBCT) integrated into the Halcyon V3.1 linear accelerator (Varian Medical Systems, Polo Alto, CA, USA). For this analysis, the kV-CBCT data sets of the first 25 treatment fractions were collected retrospectively. Patients with a significant tumour regression during the treatment were included to assess the dosimetric impact of anatomical changes.

An actual patient position displacement of current radiotherapy session regarding to the first (reference) fraction was estimated by spatial transform needed to achieve optimal volumetric alignment of the same ROI in the patient body registered during the two sessions. Only the bone structures of the patient body remain unchanged during the radiotherapy, while soft tissues undergo significant changes in a density and a geometrical shape. Therefore, we utilized the segmented bone structures as a spatial reference fiducial body to estimate needed a rigid transformation. The bone structures segmentation consisted of a simple selection of voxels with the density values above empirically estimated threshold and a three-dimensional mathematical morphology operation erosion for filtering. The closest point finding algorithm was used to find translation and rotation needed to apply to the compared registered volume to get the optimal alignment with the volume registered during the first radiotherapy fraction.

The deviations in patient positioning in the current radiotherapy session along the X, Y, and Z axes were quantified and used to calculate actual dose differences for the planning target volume (PTV) and selected organs at risk, including the spinal cord, parotid glands, oesophagus and larynx. An actual soft tissue density changes were estimated as difference in voxel values in ROIs of already aligned whole volumes using determined rigid spatial transform as described above.

All imaging and volumetric calculations were performed in MATLAB (MathWorks, USA) computational environment using custom made applications.

Statistical data analysis was performed using IBM SPSS Statistics (version 30.0, IBM Corp., Armonk, NY, USA). Descriptive statistics was used to summarise positional deviations and dose variations. Associations between positional shifts and dose variations were assessed using Kendall-Tau correlation coefficients with 95% confidence intervals (CI). Associations were considered statistically significant at $p < 0.05$.

3. Results

The pilot study has shown that even minimal anatomical changes during the treatment can affect the dose administered to patients with head and neck cancer, especially those with rapidly regressing tumours. Such anatomical changes may render the original treatment plan suboptimal and increase the risk of deviations in dose delivery discrepancies to planning tumour volume and organs at risk.

Fig. 1 illustrates the malignant tumour shrinkage observed during radical radiotherapy treatment. A significant reduction in tumour volume was observed between the planning CT and the kV-CBCT scans taken at the 25th and final fractions. The temporal changes in tumour density also reflect dynamic shifts in the tissue composition during treatment were at $p < 0.05$.

Patients' positioning errors were estimated by applying spatial transformations to align volumetric regions of interest across treatment fractions. Fig. 2 shows representative examples of unaligned kV-CBCT images compared to the first session, highlighting the spatial discrepancies. The results show that each fraction deviates from baseline, emphasizing the importance of daily monitoring of adjustment and providing insight into the potential impact of radiation exposure to nearby OARs.

A soft tissue density changes were assessed by comparing voxel values throughout the investigation. Fig. 3 shows representative kV-CBCT comparisons with planning CT images: where local density changes were observed within the tumour at fractions 5 and 6. A subsequent shrinkage of the entire tumour volume was observed at fraction 14.

The mean positional shifts for all patients are summarised in Table 1. Across the cohort, the mean (SD) value of displacements was 0.216 (0.111) cm along the lateral (X-axis), 0.230 (0.055) cm along the vertical (Y-axis), and 0.213 (0.080) cm along the longitudinal (Z-axis), indicating overall consistent positioning throughout the treatment with minor deviations. The similar displacement magnitudes across all axes indicate that

patient setup accuracy was consistent in all directions, without systematic shifts favouring any particular axis.

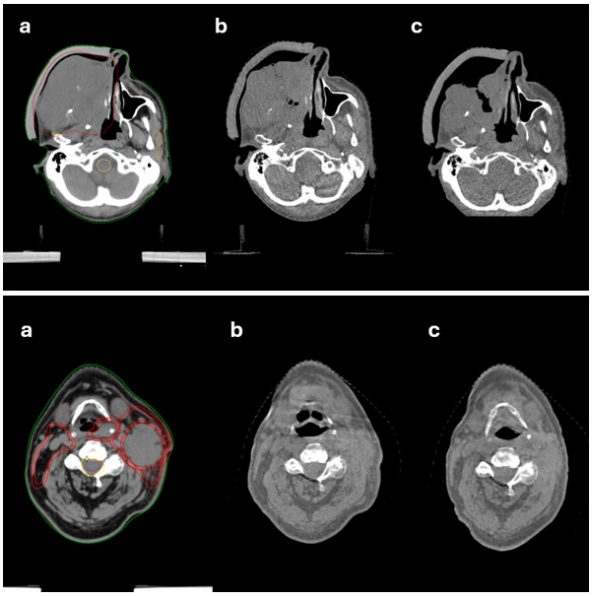

Fig. 1. Visible changes in tumour volume and density during radiotherapy. a – planning CT, b – CBCT at the 25th fraction, c – CBCT at the last fraction.

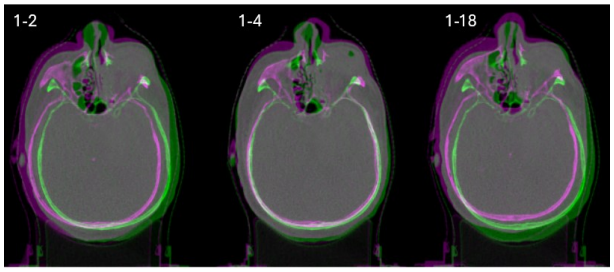

Fig. 2 Spatial differences in patient position during selected sessions of radiotherapy regarding to the first session position. The figures indicate the numbers of the fractions compared.

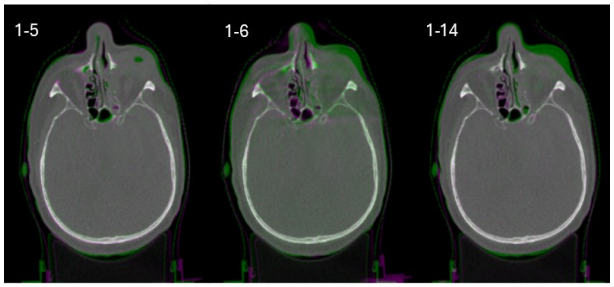

Fig. 3 Differences in soft tissue density during the different radiotherapy sessions regarding to the first one. The green colour indicates decreased density. The figures indicate the numbers of the compared sessions.

The slightly higher mean displacement along the vertical axis may reflect variations in couch height adjustment or breathing-related motion.

Based on these positional deviations for all patients, the actual dose distributions were recalculated (Table 2). The dose distribution data presented in the table includes the maximum dose to the spinal cord and the mean doses to other critical organs. These values are evaluated in accordance with established clinical treatment planning assessment protocols. The planning target volume generally received slightly lower doses than planned, while the OARs, particularly the spinal cord and parotid glands, showed measurable deviations.

Table 1. Mean coordinate deviations (cm) with standard deviations (SD) for all patients.

Patient	Coordinate deviation Mean value (SD)		
	X	Y	Z
1	0.132 (0.103)	0.152 (0.123)	0.136 (0.155)
2	0.100 (0.071)	0.232 (0.163)	0.152 (0.166)
3	0.352 (0.187)	0.228 (0.184)	0.316 (0.180)
4	0.308 (0.216)	0.176 (0.179)	0.196 (0.167)
5	0.320 (0.212)	0.256 (0.238)	0.332 (0.281)
6	0.092 (0.09)	0.316 (0.227)	0.164 (0.150)
7	0.214 (0.151)	0.236 (0.151)	0.191 (0.133)

Table 2. Mean dose deviations (Gy/fraction) with standard deviations (SD).

Patient	Dose deviation, Gy/fraction Mean value (SD)				
	PTV	Spinal Cord	Parotids	Oesophagus	Larynx
1	-0.016 (0.008)	0.026 (0.062)	0.013 (0.070)	0.005 (0.014)	0.005 (0.020)
2	-0.022 (0.071)	-0.024 (0.056)	0.004 (0.057)	0.001 (0.018)	0.004 (0.046)
3	-0.050 (0.148)	0.010 (0.201)	0.042 (0.179)	0.029 (0.095)	
4	-0.043 (0.019)	0.033 (0.073)	0.012 (0.085)	0.002 (0.017)	0.011 (0.021)
5	-0.057 (0.043)	-0.014 (0.091)	0.001 (0.182)	0.001 (0.035)	0.000 (0.010)
6	-0.025 (0.022)	0.076 (0.159)	0.011 (0.066)	-0.015 (0.088)	-0.011 (0.017)
7	-0.038 (0.024)	0.015 (0.083)	0.021 (0.045)	-0.001 (0.032)	-0.005 (0.093)

Although, the overall dose variations between patients were minor, analysis of individual fractions showed that certain positional alterations may be repeated, and therefore dose discrepancies may be larger in certain cases. This is illustrated in Fig. 4, where boxplots show dose deviations per fraction for the spinal cord and parotid glands.

Our previous study (Vainiūtė et al., 2023) demonstrated that patient positioning deviations did not follow a consistent pattern but varied randomly between fractions instead [12]. In the present study, we extended this analysis to assess whether deviations along specific axes were associated with PTV and OARs dose discrepancies. Statistical data analysis revealed significant correlations between patient positioning errors and dose deviations to both target volumes and organs at risk. Notably, CTV dose coverage showed a strong negative correlation with both X-axis and Z-axis displacements (for both $\tau = -0.714$, $p = 0.024$; 95% CI: –0.928 to –0.147) indicating

that even small lateral and longitudinal shifts resulted in reduced dose delivery to the clinical target volume. These findings imply that small misalignments directly compromise target coverage, potentially lowering treatment effectiveness.

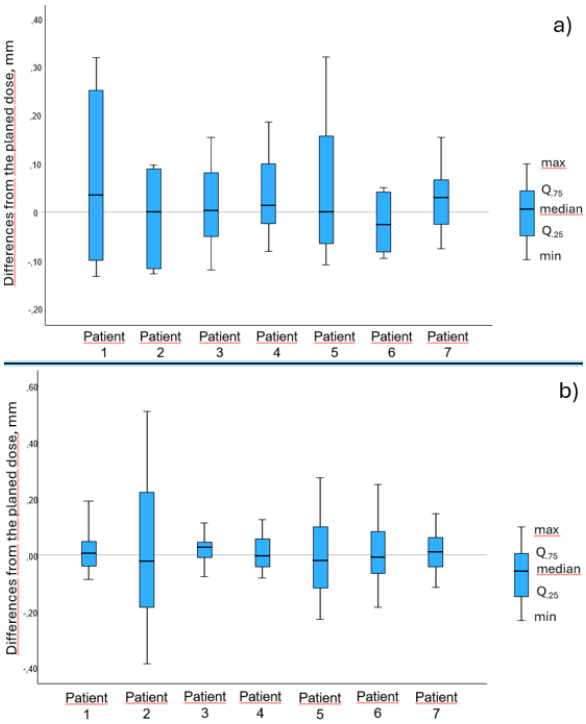

Fig. 4. Dose deviations per fraction for the studied patients: a – spinal cord; b – parotids.

In the conducted analysis, only oesophageal dose deviations were associated with vertical axis displacements ($\tau = -0.683$, $p = 0.031$; 95% CI: –0.991 to –0.095). This relationship highlights sensitivity of oesophagus on vertical setup variations, where even subtle shifts may expose the organ to higher doses than planned, thus increasing the risk of treatment-related toxicity.

Taken together, these findings demonstrate that positioning errors along all three axes are not random or negligible but systematically linked to clinically relevant dosimetric consequences. The strength of the correlations, combined with their statistical significance, emphasizes the necessity for continuous verification during treatment delivery. Even sub-centimetre deviations, often considered minor in routine clinical practice, may translate into underdosage of the target or overexposure of OARs.

Although the observed deviations were generally small, their clinical significance is supported by previous studies. Yadav et al (2022) reported set-up errors of up to 4.4 mm, suggesting that a 5 mm margin is required to ensure adequate planning target volume coverage in image modulated radiotherapy [13]. Similarly, Li et al (2022) showed that in nasopharyngeal carcinomas, dose variations of up to 9.7% for the spinal cord were due to setup errors, while anatomical contour changes explained only 1.7% [14]. These findings are consistent with our results and emphasise the critical importance for daily review and the potential benefit of adaptive replanning in patients with significant anatomical changes.

Adaptive replanning strategies have been shown to mitigate such effects. For example, You et al (2012) have demonstrated that adaptive planning reduces xerostomia for patients with a significant reduction in neck diameter (>10%) or substantial weight loss (>5%) [15]. Our results are consistent with these observations and highlight the value of adaptive approaches for patients in whom the tumour regresses rapidly during treatment.

4. Conclusions

This study has shown that even minimal positioning errors can lead to clinically significant changes in the delivered radiation dose in patients with head and neck cancer. Although the average deviations appeared small, their fraction-specific effects were considerable, especially in regions close to organs at risk such as the spinal cord and parotid glands. A kilovoltage cone beam computed tomography is based on image analysis provided quantitative insights into both anatomical changes and the positional accuracy, confirming its value for the treatment verification and the adaptive radiotherapy.

The results emphasise the importance of rigorous daily review protocols and support the integration of adaptive strategies to maintain planning target volume coverage while reducing organs at risk toxicity.

Overall, these results emphasise the clinical relevance of precise patient positioning and adaptive planning. The integration of advanced imaging and dose monitoring into routine workflow could significantly improve both the safety and efficacy of radiotherapy in patients with rapidly changing anatomy. Moreover, this work highlights the necessity for further investigation into the quantitative assessment of temporal changes in the tumour volume and the density, that may enhance treatment response evaluation with underlying biological processes.

Acknowledgment

This project has received funding from the Research Council of Lithuania (LMTLT), agreement No. P-ITP-25-1.

5. References

1. Alfouzan, A. F.. Radiation therapy in head and neck cancer. Saudi medical journal, 42(3), 2021. 247 p.
2. Grégoire V., Ang K., Budach W., Grau C., Hamoir M., Langendijk J. A., ... & Lengele B.. Delineation of the neck node levels for head and neck tumors: a 2013 update. DAHANCA, EORTC, HKNPCSG, NCIC CTG, NCRI, RTOG, TROG consensus guidelines. Radiotherapy and Oncology, 110(1), 2014. p.172-181.
3. Bujold A., Craig T., Jaffray D. and Dawson L. A.. Image-guided radiotherapy: has it influenced patient outcomes? In Seminars in radiation oncology, 22(1), 2012. p. 50-61.
4. McCulloch M. M., Lee C., Rosen B. S., Kamp J. D., Lockhart C. M., Lee J. Y., ... and Brock K. K.. Predictive models to determine clinically relevant deviations in delivered dose for head and neck cancer. Practical radiation oncology, 9(4), 2019. p. e422-e431
5. Gan Y., Langendijk J. A., Oldehinkel E., Lin Z., Both S. and Brouwer C. L.. Optimal timing of re-planning for head and neck adaptive radiotherapy. Radiotherapy and Oncology, 194, 2024. 110145.
6. Castadot P., Lee J. A., Geets X. and Grégoire V.. Adaptive radiotherapy of head and neck cancer. Seminars in radiation oncology, 20(2), p. 84-93.

7. Morgan H. E. and Sher D. J.. Adaptive radiotherapy for head and neck cancer. Cancers of the head & neck, 5(1), 2020. p.1.
8. Chung C. and Brock K.. Image-guided radiation therapy: looking beyond what we currently see. Future Oncology, 13(26), 2017. p. 2317-2319.
9. Mc Parland N. A.. kV-cone beam CT as an IGRT tool in the treatment of early stage prostate cancer: a literature review. Journal of Medical Imaging and Radiation Sciences, 40(1), 2009. p.9-14.
10. Lavrova E., Garrett M. D., Wang Y. F., Chin C., Elliston C., Savacool M., ... and Horowitz D. P.. Adaptive radiation therapy: a review of CT-based techniques. Radiology: Imaging Cancer, 5(4), 2023. p. e230011
11. Yamamichi J., Kawaguchi Y., Otsuka T., Nakashita S., Mizobe H., Eguchi Y. and Kimura S.. Assessment of tumor volume and density as a measure of the response of advanced hepatocellular carcinoma to sorafenib: application of automated measurements on computed tomography scans. JGH Open, 4(2), 2020. p. 145-152.
12. Vainiūtė G., Jonušaitė M., Čerapaitė-Trušinskienė R., Šutienė K., Laurikaitienė J., Laurikaitis M.. Investigation of positioning deviations and irradiation Dose for daily head and neck patients image-guided Radiotherapy. Medical Physics in the Baltic States 16, 2023. p. 46-49
13. Yadav R., Chauhan A. K., Kumar P., Nigam J. and Silambarasan N. S.. Setup Errors in Interfraction Radiotherapy in Patients of Head and Neck Cancer. SRMS JOURNAL OF MEDICAL SCIENCE, 7(02), 2022. p. 46-55.
14. Li Y., Wei Z., Liu Z., Teng J., Chang Y., Xie Q., ... and Chen, L.. Quantifying the dosimetric effects of neck contour changes and setup errors on the spinal cord in patients with nasopharyngeal carcinoma: establishing a rapid estimation method. Journal of radiation research, 63(3), 2022. p. 443-451.
15. You S.H., Kim S.Y., Lee C.G. et al. Is there a clinical benefit to adaptive planning during tomotherapy in patients with head and neck cancer at risk for xerostomia? American journal of clinical oncology, *35*(3), 2012. p. 261–266

MEDICAL PHYSICS IN THE BALTIC STATES 17 (2025)

Proceedings of International Conference "Medical Physics 2025"
06-08 November 2025, Kaunas, Lithuania

ARTIFICIAL INTELLIGENCE DRIVEN PATIENT POSITIONING PLATFORM FOR RADIOTHERAPY TREATMENT

Martins PIKSIS[1], Janath Navod Ranaweera KANKANAMALAGE[2]
[1] Radiation Safety Department, Liepaja Regional Hospital, Latvia, [2] Faculty of Civil and Mechanical Engineering, Riga Technical University, Latvia
[1]martins.piksis@liepajasslimnica.lv, [2]Janath-Navod-Ranaweera.Kankanamalage@edu.rtu.lv

***Abstract*:** Current radiotherapy patient positioning relies on manual positioning followed by kilovoltage (kV) imaging verification. This approach is time-consuming and susceptible to human error during the initial positioning phase. While kV imaging remains essential for final verification, improvements to the manual positioning component could significantly enhance workflow efficiency. The AI-driven positioning system demonstrates potential for improving manual positioning components in radiotherapy setup using standard clinical hardware.

Keywords: radiotherapy, patient positioning, artificial intelligence, computer vision, Python programming

1. Introduction

Radiotherapy treatment effectiveness depends critically on accurate patient positioning to ensure precise dose delivery to target volumes while minimizing exposure to healthy tissues [1]. Current clinical workflows typically involve manual patient positioning by radiation therapists followed by kilovoltage (kV) imaging verification using cone-beam computed tomography (CBCT) or planar imaging systems [2]. While imaging-based verification provides the gold standard for positioning accuracy, the initial manual positioning phase remains time-consuming and prone to inter-operator variability [3]. Recent advances in computer vision and machine learning have opened new possibilities for automated positioning assistance [4,5]. MediaPipe, developed by Google, offers robust real-time pose estimation and facial landmark detection capabilities that could potentially enhance the manual positioning workflow [6]. However, the clinical application of such technologies requires careful validation of accuracy, reliability, and integration with existing radiotherapy protocols [7].

This study presents the development and initial validation of an AI-driven patient positioning platform designed to supplement, rather than replace, existing kV imaging verification protocols.

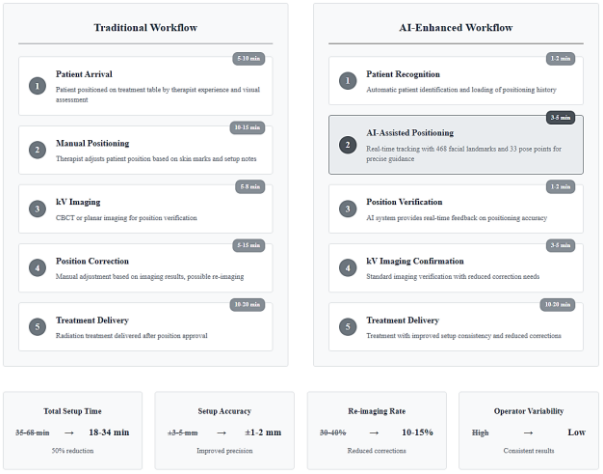

Fig. 1. Example of clinical workflow integration.

The system (Fig. 1.) aims to improve the efficiency and consistency of the initial manual positioning phase while maintaining the established safety protocols that rely on imaging-based verification.

2. Materials and methods

The positioning platform was developed in Python using the following key components:

a.) Google MediaPipe was employed for real-time pose estimation and facial landmark detection [6]. The system tracks 468 facial landmarks using the Face Mesh solution and 33 body pose key points using the Pose solution.

b.) Standard HD webcams (1920×1080 resolution) were used for image acquisition, making the system compatible with commonly available clinical hardware.

c.) A custom calibration protocol was developed using grid-based phantoms to establish pixel-to-millimeter conversion ratios and correct for camera distortion [8].

d.) Facial recognition capabilities were integrated to enable patient-specific positioning protocols and tracking history.

Three distinct tracking modes were implemented:

1. Facial Landmark Tracking utilizes 468 facial landmarks to track head position and orientation with high precision for head and neck treatments.
2. Body Pose Tracking employs 33 key points to monitor overall body positioning, particularly useful for thorax and abdomen treatments.
3. Combined Tracking integrates both facial and pose tracking for comprehensive positioning monitoring suitable for various treatment sites.

The calibration system employs a grid-based phantom with known geometric dimensions placed at standardized distances (50-150 cm) from the camera, where two calibration modes were implemented:

a.) automatic computer vision-based detection of calibration markers,
b.) manual, user-assisted marker identification for challenging lighting conditions.

Calibration parameters including camera intrinsic matrix, distortion coefficients, and pixel-to-millimeter conversion ratios are stored and validated through repeated measurements [9]. Position accuracy was evaluated through 100 measurements across different tracking modes and various positioning scenarios (center, offset positions). Deviations were calculated in three dimensions (X, Y, Z) with total deviation computed as the Euclidean distance from reference positions. Facial recognition performance was assessed through 60 test cases under controlled lighting conditions - normal (80-100 lx), dim (<50 lx), bright (>120 lx), and different viewing angles (front, side, angled). System calibration stability was evaluated through repeated calibration procedures under various environmental conditions to assess reproducibility and reliability.

2.1. Computational Methods

The system employs MediaPipe's machine learning models for anatomical feature detection [6]. The mathematical foundation relies on convolutional neural networks that output normalized landmark coordinates [10].

or each detected face, the system extracts 468 three-dimensional landmark points.

$$L_{face} = \{(x_i, y_i, z_i) \mid i = 1, 2, \ldots, 468\} \quad (1)$$

where coordinates are normalized to the range [0, 1] relative to the input image dimensions.

The pose estimation model outputs 33 key points representing major anatomical landmarks.

$$L_{pose} = \{(x_j, y_j, z_j, v_j) \mid j = 1, 2, \ldots, 33\} \quad (2)$$

where v_j represents the visibility confidence score for each key point.

The transformation from pixel coordinates to real-world measurements employs a calibrated scaling factor [11].

$$\begin{aligned} X_{world} &= (x_{pixel} - c_x) \times s_x \times d / f_x \\ Y_{world} &= (y_{pixel} - c_y) \times s_y \times d / f_y \\ Z_{world} &= z_{normalized} \times d \times scale\_factor \end{aligned} \quad (3)$$

where:

(c_x, c_y) = camera optical center
(s_x, s_y) = pixel-to-millimeter scaling factors
d = calibrated distance from camera
(f_x, f_y) = camera focal lengths
scale_factor = depth calibration constant

The camera calibration establishes the intrinsic parameter matrix [8]:

$$K = \begin{bmatrix} f_x & 0 & c_x \\ 0 & f_y & c_y \\ 0 & 0 & 1 \end{bmatrix} \quad (4)$$

Radial and tangential distortion corrections follow the Brown-Conrady model [12]:

$$x_{corrected} = x(1 + k_1 r^2 + k_2 r^4 + k_3 r^6) + 2 p_1 xy + p_2(r^2 + 2x^2) \quad (5)$$

$$y_{corrected} = y(1 + k_1 r^2 + k_2 r^4 + k_3 r^6) + p_1(r^2 + 2y^2) + 2 p_2 xy \quad (6)$$

where $r^2 = x^2 + y^2$ and (k_1, k_2, k_3, p_1, p_2) are distortion coefficients.

The system establishes a reference configuration R_{ref} from initial positioning:

$$R_{ref} = \{P_{ref,i} \mid i \in selected\_landmarks\} \quad (7)$$

where $P_{ref,i} = (x_{ref,i}, y_{ref,i}, z_{ref,i})$ represents the reference position of landmark i.

For each real-time frame, the system calculates positional deviations.

$$\delta_i = \|P_{current,i} - P_{ref,i}\|_2 = \sqrt{[(x_{c,i} - x_{r,i})^2 + (y_{c,i} - y_{r,i})^2 + (z_{c,i} - z_{r,i})^2]} \quad (8)$$

The system computes a weighted average deviation based on landmark reliability:

$$\delta_{total} = (\Sigma_i w_i \times \delta_i) / (\Sigma_i w_i) \quad (9)$$

where w_i represents the confidence weight for landmark i.

The system employs standard statistical measures for accuracy evaluation [13]:

Mean Absolute Deviation:

$$MAD = (1/n) \times \Sigma_i |\delta_i - \delta| \quad (10)$$

Root Mean Square Error:

$$RMSE = \sqrt{[(1/n) \times \Sigma_i (\delta_i - \delta_{true,i})^2]} \quad (11)$$

Standard Deviation of Measurements:

$$\sigma = \sqrt{[(1/(n-1)) \times \Sigma_i (\delta_i - \delta)^2]} \quad (12)$$

To reduce measurement noise and improve tracking stability, the system implements a discrete Kalman filter [14].

$$x_k = [position_x, position_y, position_z, velocity_x, velocity_y, velocity_z]^T \quad (13)$$

Prediction Equations:

$$\hat{x}\_k|k\text{-}1 = F\_k \times \hat{x}\_k\text{-}1|k\text{-}1 \quad (14)$$

$$P\_k|k\text{-}1 = F\_k \times P\_k\text{-}1|k\text{-}1 \times F\_k^T + Q\_k \quad (15)$$

Update Equations:

$$K_k = P_k|k\text{-}1 \times H_k^T \times (H_k \times P_k|k\text{-}1 \times H_k^T + R_k)^{-1} \quad (16)$$

$$\hat{x}_k|k = \hat{x}_k|k\text{-}1 + K_k \times (z_k - H_k \times \hat{x}_k|k\text{-}1) \quad (17)$$

$$P_k|k = (I - K_k \times H_k) \times P_k|k\text{-}1 \quad (18)$$

where F_k is the state transition model, H_k is the observation model, Q_k is the process noise covariance, and R_k is the observation noise covariance [14].

For different patient-to-camera distances, the system applies proportional scaling:

$$scale\_factor = d_{current} / d_{calibration} \quad (19)$$

$$measurement_{adjusted} = measurement_{raw} \times scale\_factor \quad (20)$$

Based on modified Z-Score Method [15] the system identifies outliers using the modified Z-score:

$$M_i = 0.6745 \times (x_i - median_{(X)}) / MAD_{(X)} \quad (21)$$

Points with $|M_i| > 3.5$ were classified as outliers and filtered from calculations. For time-series data, the system applies a temporal filter.

$$validity\_check = |x_t - x_t\text{-}1| < threshold \times \sigma_{temporal} \quad (22)$$

The overall position confidence combines individual landmark confidences:

$$C_{total} = (\Sigma_i c_i \times w_i) / (\Sigma_i w_i) \quad (23)$$

where c_i is the individual landmark confidence and w_i is its importance weight.

Confidence decreases over time without fresh measurements:

$$C_{(t)} = C_0 \times e\text{^}(-\lambda t) \quad (24)$$

where λ is the decay constant and t is the time since last reliable measurement.

For derived quantities, uncertainty propagates according to [16]:

$$\sigma\_f^2 = \Sigma_i (\partial f/\partial x_i)^2 \times \sigma_i^2 \quad (25)$$

where f is the derived quantity and σ_i represents individual measurement uncertainties.

The system accounts for calibration uncertainties in final measurements:

$$\sigma_{total}^2 = \sigma_{measurement}^2 + \sigma_{calibration}^2 + \sigma_{systematic}^2 \quad (26)$$

This mathematical framework ensured robust, accurate position tracking while maintaining computational efficiency suitable for real-time clinical applications. The multi-layered approach to uncertainty quantification and error correction provided the desired precision.

3. Results

The accuracy testing revealed distinct performance characteristics for different tracking modes. The significant difference between facial and pose tracking accuracy suggests different coordinate systems or calibration factors, with pose tracking demonstrating millimeter-level precision suitable for clinical applications [17]. Recognition testing across 60 trials revealed significant dependence on environmental conditions. The results indicate that facial recognition performance is critically dependent on optimal lighting conditions, with complete failure under suboptimal lighting scenarios. The calibration system demonstrated 100% marker detection accuracy across multiple distance settings (50-150 cm) and stable calibration parameters across repeated procedures. The platform successfully integrated multiple tracking modalities with the following capabilities:

- real-time processing at HD resolution (1920×1080)
- simultaneous facial and pose tracking
- patient-specific positioning history logging
- customizable distance settings for different clinical scenarios.

Fig. 2. Position Accuracy Distribution Comparison.

Box plots (Fig. 2.) display the five-number summary (minimum, Q1, median, Q3, maximum) with boxes representing the interquartile range (IQR) containing 50% of the data. Whiskers extend to 1.5×IQR from quartile boundaries, with outliers plotted as individual points beyond this range. The red line within each box represents the median value. The box plot analysis reveals distinct performance characteristics across the

three measured parameters. Pose tracking (Fig. 2.a.) demonstrates exceptional consistency with a narrow distribution (IQR = 0.5mm) and minimal variance (σ = 0.30mm), indicating robust precision suitable for radiotherapy applications.

Face tracking (Fig. 2.b.) exhibits significantly higher variability (σ = 30.11 pixels) with a broader interquartile range (41.8 pixels), suggesting potential calibration inconsistencies that require optimization. The larger spread indicates less predictable performance compared to pose tracking.

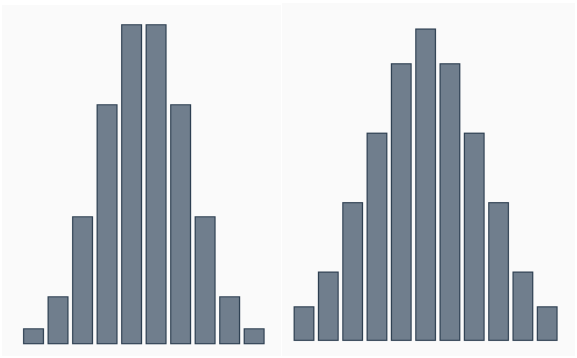

a) **b)**

Fig. 2. Tracking distributions: a) Pose; b) Face

Recognition performance shows extreme bimodal distribution characteristics, with success rates varying from 0% to 42.3% based on environmental lighting conditions. The high standard deviation (21.2%) compared to the mean (11.4%) reflects the binary nature of performance under different conditions.

The statistical distributions confirm that pose tracking meets clinical precision requirements, while face tracking and recognition modules require further development for reliable clinical deployment. The analysis indicates system robustness under controlled conditions but sensitivity to environmental variations.

4. Discussions

The developed AI positioning platform demonstrates significant potential for improving the manual positioning component of radiotherapy workflows [19]. The millimeter precision achieved in pose tracking approaches the accuracy requirements for many radiotherapy applications, particularly when used as a positioning aid rather than a replacement for imaging verification [1]. The contrasting performance between facial landmark tracking and pose tracking warrants further investigation. The large deviations observed in facial tracking suggest potential issues with coordinate system calibration or the need for specialized calibration procedures for facial landmarks. In contrast, the excellent precision of pose tracking indicates robust performance for body positioning applications. The facial recognition results highlight a critical limitation of the current system. The complete failure under dim lighting conditions (0% success rate) severely limits clinical applicability, as clinical environments often have variable lighting conditions. The 42.3% success rate under optimal lighting, while promising, requires significant improvement for routine clinical use. The use of standard HD webcams and open-source software frameworks makes the system cost-effective and accessible for clinical implementation [20]. However, several factors must be addressed:

a.) clinical implementation would require standardized lighting protocols to ensure reliable recognition performance,

b.) the system must be integrated with existing radiotherapy workflows without disrupting established safety protocols [2],

c.) clinical staff require training in system operation and interpretation of positioning feedback [21].

5. Limitations

This study has several limitations that must be acknowledged:

a.) testing was performed on a limited number of subjects, requiring expansion for comprehensive validation,

b.) testing was conducted under controlled conditions that may not fully represent clinical environments.

c.) the facial recognition component requires significant optimization for clinical viability.

d.) different tracking modes appear to require different calibration approaches.

6. Conclusions

This study presents the successful development of an AI-driven patient positioning platform that demonstrates certain potential for improving manual positioning procedures in radiotherapy. The system utilizes standard hardware (HD webcam) and open-source software, making it cost-effective and widely implementable. The platform successfully integrates multiple tracking modalities with patient-specific logging and customizable clinical protocols. Facial recognition performance requires significant optimization, particularly under variable lighting conditions. The platform represents a remarkable step toward AI-assisted radiotherapy positioning, though further development is required to address recognition limitations and expand clinical validation [22]. Future work will focus on expanding patient testing, optimizing recognition algorithms, and conducting comprehensive clinical integration studies to fully validate the system's potential for improving radiotherapy positioning workflows.

7. Acknowledgements

The authors acknowledge the support of Liepaja Regional Hospital's Radiation Safety Department and expresses special thanks to the volunteers (department staff) who participated in the testing procedures.

8. References

1. Bissonnette, J.P., et al. "Quality assurance for image-guided radiation therapy utilizing CT-based technologies: a report of the AAPM TG-179." Medical Physics 39.4 (2012): 1946-1963.

2. Jaffray, D.A. "Image-guided radiotherapy: from current concept to future perspectives." Nature Reviews Clinical Oncology 9.12 (2012): 688-699.

3. Korreman, S., et al. "The European Society for Radiotherapy and Oncology-European Institute of Radiotherapy (ESTRO-EIR) report on 3D CT-based in-room image guidance systems: a practical and technical review and guide." Radiotherapy and Oncology 94.2 (2010): 129-144.
4. Litjens, G., et al. "A survey on deep learning in medical image analysis." Medical Image Analysis 42 (2017): 60-88.
5. Sahiner, B., et al. "Deep learning in medical imaging and radiation therapy." Medical Physics 46.1 (2019): e1-e36.
6. Zhang, F., et al. "MediaPipe: A Framework for Building Perception Pipelines." arXiv preprint arXiv:1906.08172 (2019).
7. Thompson, S., et al. "Artificial intelligence in radiation oncology: a specialty-wide disruptive transformation?" Radiotherapy and Oncology 129.3 (2018): 421-426.
8. Zhang, Z. "A flexible new technique for camera calibration." IEEE Transactions on Pattern Analysis and Machine Intelligence 22.11 (2000): 1330-1334.
9. Bradski, G. "The OpenCV Library." Dr. Dobb's Journal of Software Tools (2000).
10. LeCun, Y., et al. "Deep learning." Nature 521.7553 (2015): 436-444.
11. Hartley, R., & Zisserman, A. "Multiple view geometry in computer vision." Cambridge University Press (2003).
12. Brown, D.C. "Decentering distortion of lenses." Photogrammetric Engineering 32.3 (1966): 444-462.
13. Taylor, J.R. "An introduction to error analysis: the study of uncertainties in physical measurements." University Science Books (1997).
14. Kalman, R.E. "A new approach to linear filtering and prediction problems." Journal of Basic Engineering 82.1 (1960): 35-45.
15. Iglewicz, B., & Hoaglin, D.C. "How to detect and handle outliers." ASQC Quality Press (1993).
16. Bevington, P.R., & Robinson, D.K. "Data reduction and error analysis for the physical sciences." McGraw-Hill (2003).
17. Kalet, I.J. "The use of medical images in planning and delivery of radiation therapy." Journal of the American Medical Informatics Association 4.5 (1997): 327-339.
18. Keall, P.J., et al. "The management of respiratory motion in radiation oncology report of AAPM Task Group 76." Medical Physics 33.10 (2006): 3874-3900.
19. Van Herk, M. "Errors and margins in radiotherapy." Seminars in Radiation Oncology 14.1 (2004): 52-64.
20. OpenCV Development Team. "OpenCV: Open Source Computer Vision Library." Available at: https://opencv.org/
21. Dawson, L.A., & Jaffray, D.A. "Advances in image-guided radiation therapy." Journal of Clinical Oncology 25.8 (2007): 938-946.
22. Hosny, A., et al. "Artificial intelligence in radiology." Nature Reviews Cancer 18.8 (2018): 500-510.

MEDICAL PHYSICS IN THE BALTIC STATES 17 (2025)

Proceedings of International Conference "Medical Physics 2025"
06-08 November 2025, Kaunas, Lithuania

LAP LUNA 3D – THE NEW MORE IN SGRT

Ramune Ulrich
LAP GmbH Laser Applikationen, Sales Support Manager
r.ulrich@lap-laser.com

LUNA 3D - Makes precision effortless

At LAP, our legacy of an innovation the for laser-based patient positioning has set the standard for precision in radiotherapy for decades. Building on this foundation, we developed LUNA 3D, a cutting-edge SGRT system designed to revolutionize patient positioning and the motion monitoring in the radiation therapy.
LUNA 3D leverages high-resolution stereoscopic cameras and an advanced blue speckle light projection to deliver a submillimetre accuracy for patient setup and continuous real-time monitoring. This allows for precise patient positioning for each treatment fraction, enabling focused patient care.
LUNA 3D simplifies workflows with its user-friendly interface and support of ergonomic setup positions, allowing focused patient care. The real-time monitoring capabilities provide peace of mind by instantly detecting and correcting patient movement. Its seamless integration and browser-based architecture offer easy access to critical data, supporting informed decision-making and continuous improvement of treatment protocols. LUNA 3D embodies LAP's commitment to precision and safety in radiation therapy. Embrace the future with LUNA 3D for superior patient positioning and motion monitoring.

RadCalc - Precision where it matters most

Simplify and accelerate radiation therapy quality assurance with RadCalc. Powered by Fast Monte Carlo technology that's 6 times faster, RadCalc ensures precise dose calculations in significantly less time.
The RadCalc portal, designed for simplicity, offers an intuitive interface streamlining workflows. With in-vivo and logfile-based dose verification and phantom-free patient QA workflows, RadCalc combines accuracy and efficiency, allowing clinicians to focus more on delivering exceptional patient care.

Empowering smarter decisions before treatment with LUNA 3D and RadCalc TrueDose

RadCalc TrueDose brings dose-guided analytics directly to the treatment console, empowering teams to catch dosimetric errors before the beam is delivered. Leveraging daily surface data to reflect patient positioning variations enables pre-treatment dose validation with clarity and confidence. Simple pass/fail alerts guide therapists in making precise, dose-informed shifts without adding complexity to the workflow. Precision you can see and confidence you can act on.

www.lap-laser.com, www.radcalc.com

LAP

LUNA 3D

The New More in SGRT

Get more information on www.lap-laser.com

RadCalc

End-to-end patient QA solution

- 3D volumetric Collapsed Cone and Monte Carlo plan validation
- Phantom-free 3D EPID solution for pre-treatment and in-vivo fractional delivered dose QA
- Now with Fast Monte Carlo Dose Calculations in under 30 Seconds

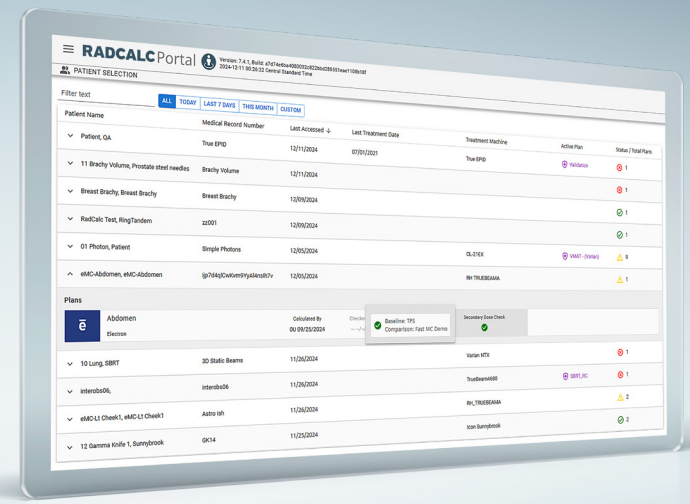

RADCALC

Contact us on www.radcalc.com

www.lap-laser.com

Simply Precise

MEDICAL PHYSICS IN THE BALTIC STATES 17 (2025)

Proceedings of International Conference "Medical Physics 2025"
06-08 November 2025, Kaunas, Lithuania

REVIEW OF TWO INSTITUTION IAEA QUAADRIL BASED INTERNAL CLINICAL AUDIT RESULTS

Sandra STEPINA
Liepaja Regional Hospital
stepinna.sandra@gmail.com

***Abstract*:** Internal clinical audit is a powerful quality improvement tool for radiation therapy, interventional radiology and radiodiagnostic departments, as it includes review of wide range of topics connected to patient radiation safety, overall clinical experience, technical opportunities and gives detailed guidelines for further process development.
The aim of this study is to make systematic review of two Latvian radiodiagnostic institution internal clinical audits which are based on IAEA QUAADRILL methodology and worksheets. The audit result review gives an insight into practical methods and tools for internal audit performance, paying attention to possible positive findings as well as parts of clinical practice where improvements are needed.

Keywords: Radiology, clinical audit, audit

1. Introduction

To introduce clinical audit approach into quality control (QC) procedures of institution, it is useful to look at different definitions of this concept.
Clinical audit as defined within the BSSD (*Basic Safety Standards Directive)* is "a systematic examination or review of medical radiological procedures that seeks to improve the quality and outcome of patient care through structured review, whereby medical radiological practices, procedures and results are examined against agreed standards for good medical radiological procedures, with modification of practices, where appropriate, and the application of new standards if necessary." [1]

The ESR (*European Society of Radiology)* defines clinical audit defines as: "a tool designed to improve the quality of patient care, experience and outcome through formal review of systems, pathways and outcome of care against defined standards, and the implementation of change based on the results" [2].

The IAEA comes with definition of clinical audit as a tool which „involves evaluation of data, documents, and resources to check performance against standards. It is essentially a process of fact finding and interpretation and, as such, provides an efficient tool for improvement of quality". [3]
To compile all definitions, clinical audit can be understood as a review of clinical approach of radiology practice for further clinical process improvement.
Clinical audits are often internal, i.e., carried out within a certain health care institution. Internal audits should be routine activities within a good quality system. External audits, on the other hand, are performed by auditors that are external to the institution and thus totally independent. [3]
There are different audit guidelines, guiding through different parts of radiology practice thus helping auditors to get full spectrum review of clinical practice in department. The most popular are ESR Guide *Esperanto* 4th edition [4] and IAEA QUADRILL [3] guidelines. They include basic explanation of audit importance in QC program and give templates for practical use in internal audits.
In Latvia, there is a Regulations Regarding Protection Against Ionizing Radiation in Medical Exposure which defines clinical audit periodicity once per five years including all imaging modalities used in institution.[5] This regulation does not include any of audit methodology, main points of interest or definition of involved personnel. Radiation Safety Centre as a Regulator in Latvia gives brief guidelines on clinical audit performance. [6]
The implementation of clinical audits into quality control (QC) programs within Latvian radiology departments faces several challenges. These include a lack of specialized training and education, as well as limited personnel resources. The process is further hindered by a prevailing "blame culture," which prevents institutions from fully leveraging the benefits of an audit. Additionally, the availability of outsourced clinical audit services may discourage the development of internal audits as an integral component of an institution's QC system.

The methodology for clinical audit, adapted from the IAEA, and the practical findings from two internal audits reviewed here provide a framework for implementing audits in a radiology department. This approach is particularly useful for institutions with limited workforce capacity.

2. Methods

Internal clinical audits were performed in two radiology departments in Latvia between January 2024 and May 2025.
Both institutions have full technological support which gives a wide spectrum of diagnostic examinations possible (see Table 1.).

Table 1. Technological support

Method	Institution 1	Institution 2
Mammography	1	1
CT	1	2
Conventional X-Ray	2	2
Fluoroscopy X-Ray	1	1
Mobile X Ray	1	3
C-Arm	4	2
Angiography	1	0

The audit was planned and conducted within the daily routine without dedicated time slots. The clinical audit methodology was based on the IAEA QUADRILL worksheet templates, which were translated into Latvian for use by all involved personnel. The worksheets were created in MS Excel and organized by topic, including general questions, department structure, education and research, patient referral, examination procedures, optimization, infrastructure, radiation protection and safety, equipment, quality assurance (QA) procedures, and measuring devices.
An audit team consisted of local personnel, including a medical physicist, a Radiological Technologist (RTT), and a radiologist (or a traumatologist for C-arm machines). A medical physicist also delivered an introductory presentation outlining the audit's aims and objectives.
The internal clinical audit methods included:

- Interviews with involved personnel and the institution's board.
- Review of documentation and technology.
- On-site visits and process observations.
- A review of clinical practices from the patient's perspective, including an evaluation of documentation flow, communication, and patient education.
- An analysis of imaging quality and radiation safety, including dose analysis.

All findings were compiled in a comprehensive audit review, which highlighted both positive outcomes and areas requiring improvement. The results were then presented to the involved personnel and institution board members. The entire audit process—from supervision to the final review and presentation—was conducted by the medical physicist.

3. Results

Both institutions have clear visions of becoming the leading multi-profile medical centers in the region, which provides high-quality healthcare, and education centers for medical professionals. The annual number of examinations is defined in table 2.

Table 2. Number of examinations per year (statistics from 2024)

Method	Institution 1	Institution 2
Mammography	3084	441
CT	14082	20346
Conventional X-Ray	11004	29343
Fluoroscopy X-Ray		
Mobile X Ray		
C-Arm	1000	236
Angiography	1400	na

To facilitate a more qualitative analysis of department workload in the future, it is essential to develop a robust methodology for data collection. This should include collecting demographic data on patients (e.g., adults and children) and defining the workload on the equipment used for specific procedures.
Institution number 2 has two main branches that serve the northern part of the Latvian West Coast region.
While both institutions are involved in training new professionals, they have limited research activities due to a scarcity of research resources and staff. This same limitation significantly impacts the development of quality documentation, which is crucial for ensuring a standardized approach to work and for reducing the number of errors and unnecessary radiation exposures.
The departments are well-equipped with new machinery (less than 10 years old), capable of performing a full range of patient examinations and procedures. The oldest equipment is scheduled for replacement after 10 years of use.
Both institutions also provide emergency services. The examination rooms are clean, well-conditioned, and arranged with restricted access for personnel only. Radiation control areas are clearly marked, and emergency equipment and air panels are available in all rooms.
Staff members regularly attend continuing education events and effectively implement their new skills and knowledge in their daily work. Both departments have a dedicated Radiation Safety department, which is equipped with all the necessary instrumentation to perform quality assurance (QA) procedures. All radiation protection activities are performed regularly and thoroughly.

3.1. Documentation review

There is a high importance of clinical and quality control activity process reflection in documentation. In both institutions the largest part of documentation is in a paper form. The documentation include:

- patient specific documents: patient examination registration journals, patient referral, patient health/pregnancy status questionnaires, volunteer

questionnaires, patient examination procedure guidelines;
- radiation safety specific documents: incident registration journals, journal of rejected examinations; radiation survey protocols, patient dose analysis reports;
- instrumentation/ machine specific documentation: medical equipment journal, user manuals;
- quality control specific documentation: QA procedure description, dosimetry equipment list, list of acceptability criteria, instructions, QA procedure templates etc.

The medical physicist conducted the documentation review during the on-site visits.
Patient examination data is entered into a registration journal in compliance with the Cabinet of Ministry regulations for manipulation traceability. Additionally, patient dose and weight are recorded for subsequent dose analysis, especially in the absence of an automatic dose management system. It was frequently observed that these data inputs lacked precision and completeness, often with missing dose or weight values.
Before CT examinations with contrast media, patient health status questionnaires are utilized. The content and quality of these forms were deemed acceptable. However, it was noted that forms related to patient pregnancy status and volunteer questionnaires were not implemented correctly, as the reproductive age was not defined, leading to a lack of clear instructions for personnel. Furthermore, the volunteer form did not include information about the person being examined.
No clinical guidelines for examination procedures were in place. All manipulations were based on individual experience and "well-known truths," which creates room for misunderstandings and varying clinical approaches.
A clear procedure for accepting new equipment into operation is necessary. This procedure should involve verifying compliance with all parameters specified in the technical documentation. The acceptance report should be signed by both the medical physicist and the supplier and then stored in the equipment's log. It is crucial that the medical physicist participates in the acceptance testing.
Regarding medical technology documentation, it was found that regular entries were not being made in the journals. This was due to the journals' frequent changes in their storage location, which led to service institutions skipping the input.
Quality Assurance (QA) procedure protocols, radiation survey acceptability criteria, and instructions were stored electronically. While some protocols were in the process of being developed according to international guidelines, their compliance with national regulations was confirmed.

3.2. Involved personnel and institution board interview

The medical physicist conducted interviews with the institution's board to understand their vision for the radiology department's development, their future technological needs, and their awareness of current limitations and resource shortages. The interviews revealed that the number of staff is insufficient to maintain a level of work quality consistent with good clinical practice. Possible solutions and the need for greater staff involvement were identified during these discussions.
Interviews regarding workflow, procedures, and radiation safety were conducted with the corresponding department heads. The answers were compiled in an MS Excel worksheet, and the main findings are summarized in Chapter 3.3.

3.3. Onsite visits and process review

The medical physicist conducted unscheduled on-site visits to all types of imaging modalities as part of the daily routine, ensuring that all radiation safety procedures were followed.
Conventional X-Ray machines. Radiographic examinations are performed according to the projection recommendations learned by assistants during their training. In Institution 2, an inappropriate imaging machine is used for traumatological examinations, as it lacks the necessary equipment (e.g., handles, mobile detectors). Following the audit, a recommendation for process improvement was made.
CT machines. Institution 1 has an insufficient number of staff to ensure a quality of work consistent with good clinical practice. For instance, there should be two Radiological Technologists (RTTs) per CT machine. Currently, a single radiologist assistant performs all manipulations, including patient positioning, explaining the procedure, connecting the contrast medium administration system, and completing the manipulation journal. By contrast, Institution 2 provides a positive example of effective workload management between RTTs and nurses. In both departments, built-in scanning protocols are used, but it was found that correctly implemented scanning protocols for children are lacking.
Mammography machines. Mammography procedures were found to be consistent with good clinical practice and adhered to patient healthcare guidelines. The number of mammography screening procedures is intentionally increased each year. However, it was noted that there is no system for registering unreasonable exposures, even though examinations are sometimes repeated.
Fluoroscopy and C-Arm machines. On-site visits were highly valuable for observing the real-time positions of personnel during exposure, as well as the "worst-case" positions of X-ray machines (e.g., rotation angles, collimation) in combination with staff locations. This information is crucial for conducting future radiation surveys under conditions that closely simulate reality to predict high-exposure regions.
Additionally, the audit examined the radiation safety culture, including the correct use of protective aprons and glasses, as well as adherence to the principles of distance, time, and shielding. The on-site visit revealed a lack of protective aprons for all personnel to meet hygiene standards for personal use. Furthermore, the fixations on the existing aprons were of poor quality, making them uncomfortable. The purchase of new aprons was organized following the audit.

Images from C-arm machines were not being transferred to the PACS system for two main reasons: patients were not correctly identified, with empty tags and missing information; and the machine was not configured to send images to the PACS. Following the audit, personnel were trained on complete patient data entry, and the connection to the PACS was established for machines with this technical capability.

Individual Dosimetry and Radiation Safety Culture. It was necessary to re-instruct personnel in all imaging rooms on the correct use of individual dosimeters. These devices are essential for analyzing the dose of ionizing radiation received by staff and for assessing the effectiveness of room protective barriers. Based on the doses recorded, personnel are categorized as A or B employees, which determines the maximum permissible dose. All employees in a controlled zone are obligated to wear their issued individual dosimeters. Regularly conducting on-site audits is essential to improve the culture of wearing individual protective equipment.

On-site visits also provided a valuable opportunity for staff to ask questions about radiation safety, technology use, and examination quality. Small issues and minor information gaps were resolved immediately, as well as serious inaccuracies in radiation safety procedure.

3.4. Review of clinical practice

This review of clinical practice combines insights from interviews and on-site process observations, with a particular focus on the patient's perspective. It includes an analysis of documentation flow, communication, and patient education.

Patient Referrals. Patients are referred for radiological examinations by a family doctor, a specialist, or through a mammography screening invitation (sent to women aged 50 and over every two years). No patient is examined without a doctor's referral, even if the e-health system is down and electronic referrals are unavailable. Referrals are always provided in paper format, even if they were originally issued electronically.

Radiological Technologists (RTTs) are trained to evaluate referral indications to determine the necessity of an examination. They check if a similar examination has been performed previously or if required laboratory analyses have been completed. If a patient does not have sufficient indications or if the examination cannot be performed due to laboratory results, the RTT declines the examination. The patient is informed of the reason for the refusal and provided with recommendations for further action. Such cases are documented in the "Journal of Refused Examinations," noting the reason for refusal and retaining the referral.

It was found that referrals from local department specialists are often incomplete, lacking essential clinical indications and information about the referring physician. In these cases, the RTT must contact the specialist for clarification. If the specialist is unavailable, the on-site radiologist makes the final decision regarding the necessity of the examination.

Examination Procedures and Patient Care. Mammography examinations are conducted in accordance with local screening guidelines. In Institution 1 an ultrasound (US) device is available in the mammography room for further clarification. Before any examination, the procedure is explained to the patient in a way and language they can easily understand.

To ensure patient confidentiality, most examination rooms use a queueing system where patients are called by the number they received at the reception desk. Before an examination, the patient is positively identified by repeatedly confirming their last name. Personnel are aware of potential breaches of confidentiality, such as copying DICOM files, sending patient data screenshots via messaging platforms (e.g., WhatsApp), or using unauthorized access. Patients do not have access to other patients' examination data, outpatient charts, or other documentation.

For special patient groups, such as pregnant women, the need for an examination is carefully assessed, and alternative methods that do not use ionizing radiation are offered. Women sign a questionnaire regarding their pregnancy status. When examining children, optimization principles are followed, including beam collimation and the selection of an appropriate imaging protocol. If a child requires an accompanying person, that individual signs a consent form to be a volunteer assistant.

Infection control procedures are strictly followed during patient care. These include wearing protective gloves, disinfecting surfaces, or covering them with a napkin, and proper management of sharp medical waste.

Training and Documentation. In the case of new staff, work instructions and training are conducted by a designated trainer. However, no formal documentation has been developed to describe the instructions for performing specific manipulations. As part of the quality program, it is essential to develop detailed manipulation instructions for each imaging technique and anatomical localization.

Examination Description. A radiologist conducted an analysis of examination descriptions, verifying their acceptability against good clinical practice. When creating an examination description, the referral is attached, and the clinical indications are clearly stated. The specific examination performed and the patient's position are noted. If a contrast agent is used, its name and volume are recorded. All other necessary fields in the description meet the required standards.

3.5. Image quality, radiation safety, dose analysis

Image quality. During on-site visits and interviews with radiologists, image quality was found to be at a good and acceptable level. However, no internal clinical guidelines existed for classifying image quality into the Commission of European Communities (CEC) defined PGMI ranges (Perfect, Good, Moderate, Inadequate). Image quality is regularly tested using a test pattern and phantoms. Equipment tests are conducted twice a year for each device, in accordance with Latvian regulations on protection against ionizing radiation in medical irradiation. Test procedures and forms have been developed to ensure a uniform methodology, facilitate the comparison of results, and monitor trends. High-quality testing equipment is also available at the hospital.

A key challenge is that some equipment criteria specified in legislation are not applicable to modern technology. Additionally, the required compliance criteria are often significantly higher than the equipment's actual accuracy.

Radiation safety. Both institutions have a Radiation Safety Department with two medical physicists and medical physics experts. Radiation safety instructions are available for each department.

Each employee is provided with appropriate individual dosimeters based on the type of manipulation they perform. Personal chest dosimeters are used in radiation diagnostics, eye dosimeters are worn in the angiography department, and electronic dosimeters can be issued to pregnant employees, as well as to guests or students.

Annually, the medical physics expert submits a report to the Regulator on all activities involving ionizing radiation sources. This report includes information on equipment inspections, personnel compliance, and the dose indicators received by both personnel and patients. The Radiation Safety Center also conducts periodic inspections, providing a report with recommendations for improvements in the departments' work with X-ray-generating machines.

While the responsibilities of radiographers and radiologist assistants regarding quality assurance, radiation protection, and patient dose recording have been explained, their understanding appears incomplete. This highlights a need to improve the practical knowledge of Radiological Technologists (RTTs) and radiologists concerning radiation safety.

It is necessary to re-explain the importance of new guidelines for the use (or non-use) of lead-equivalent aprons for patients. The audit found that aprons are still used on infants, but only when the machine is in manual mode (without automatic exposure control). The possibility of potential errors and negative effects on patients from apron use must be addressed. To improve patient awareness, informative posters should be placed in waiting rooms to educate them on modern radiation safety requirements.

Dose analysis. A dose analysis was conducted on last year's examinations. In Institution 1, two methodologies for dose recording are used: a paper-based form with RTT inputs and Radiation Dose Structured Reports generated and exported from the device. In Institution 2, all radiological devices except the mammography unit are from a single vendor and are connected to an automatic dose monitoring system. However, no dose records from C-arm machines were analyzed due to incomplete patient data in both institutions, such as missing IDs and patient weight.

Patient data records include patient identification, patient weight (or breast compression thickness for mammography), and dose readings (DLP for CT, DAP for X-ray machines, and dose meter for mammography and angiography units). The median dose value for each projection was calculated for five different weight ranges. For the reference patient weight range of 60 to 80 kilograms, the median value was compared to Dose Reference Levels (DRLs) (Table 3). For mammography, four breast compression thickness regions were defined, and the median dose value was calculated accordingly. Only the dose value for a breast thickness of 40 to 50 mm was compared to the defined DRL (Table 4).

The majority of the calculated median dose values fell within the DRLs. Examination regions that exceeded the DRLs were further investigated. For example, it was found that the CT examination for paranasal sinuses used a head protocol, resulting in a higher dose for patients. In response, a separate protocol was created. For cervical vertebrae X-ray examinations, the median dose exceeded the DRL by 2%, which was attributed to the collimation used and the specific clinical approach to the examination.

The median dose for mobile X-ray examinations exceeded the DRLs in both institutions. As these units lack automatic exposure control, the manually used parameter presets were found to be unoptimized. While image quality was generally acceptable, some overexposed images were noted, leading to a recommendation for exposure optimization.

Table 3. Dose analysis for lung x ray examination

Weight, kg	AP/PA, μGy·m²	LL, μGy·m²	DRL, μGy·m²	
			AP	LL
≤50	4.53	7.85	-	-
(50-60]	4.93	12.43	-	-
(60-80]	6.19	21.10	13	35
(80-90)	7.61	31.86	-	-
≥90	10.14	50.34	-	-

Table 4. Dose analysis for mammography examination

Compression thickness, mm	RCC, mGy	LCC, mGy	RMLO, mGy	LMLO, mGy	DRL, mGy
≤40	0.84	0.84	0.86	0.87	-
(40-50]	0.91	0.985	0.96	1.06	2
(50-60)	1.06	1.115	0.95	1.2	-
≥60	1.38	1.26	1.39	1.32	-

A significant finding was the lack of specific CT examination protocols for children aged 4–18 years. Consequently, adult scanning protocols are being used, which results in a higher radiation dose for pediatric patients. To address this, there is a clear necessity to develop and implement dedicated pediatric CT protocols. Furthermore, there is a need to optimize CT imaging protocols for combined examinations, for example: head and cervical vertebrae, where the head requires both hard tissue and soft tissue contrast, the neck requires only hard tissue contrast; neck soft tissue and lungs (for oncology patients); lungs and abdomen and pelvis.

4. Discussion

An internal clinical audit is a powerful tool for reviewing clinical practices. It can reveal technical limitations and identify gaps in personnel knowledge regarding radiation safety procedures. The audit also provides a structured way to review documentation and connect it directly to the clinical workflow.

Despite its benefits, clinical audits are often viewed as a means of finding errors and assigning blame, rather than as a tool for improvement. To address this perception, regular personnel training is crucial.

Both audits were led by a medical physicist. As such, the review of processes and documentation, except for

examination descriptions, was conducted from the medical physicist's perspective. While the full involvement of RTTs (radiological technologists) and radiologists was requested, it was not as comprehensive as needed. Consequently, not all aspects of the clinical process may have been fully evaluated.

The audit process, including the preparation of the final report, is extremely time-consuming. Because these audits were conducted alongside the medical physicist's daily responsibilities, the entire process was extended over several months.

After the audit, it is essential to present the results to all involved personnel and board members, providing insight into the actions needed. The list of findings and potential solutions must be discussed and then implemented promptly. Follow-up audits are also essential to ensure that changes, new implementations, and improvements in personnel radiation safety culture are maintained.

5. Conclusion

Regular clinical audits are effective tools for significantly improving clinical practice and enhancing radiation safety. These audits serve as a systematic review of the entire procedure chain. On-site visits are particularly valuable as they provide a realistic view of how imaging devices are used, revealing insights into personnel radiation safety culture and education. The data collected from these visits helps to identify specific areas that need improvement.

Establishing clinical guidelines based on an institution's specific practices is crucial for ensuring both high-quality images and patient radiation safety. Before an external audit is performed, it is essential to conduct an internal clinical audit. This step helps to identify and correct most inaccuracies or errors in clinical practice, making the process more efficient and effective.

6. References

1. Council Directive 2013/59/Euratom on basic safety standards for protection against the dangers arising from exposure to ionizing radiation and repealing Directives 89/618/Euratom, 90/641/Euratom, 96/29/Euratom, 97/43/Euratom, and 2003/122/Euratom. (2014). Official Journal of the European Union, 57, L13, 1–73. https://doi.org/10.2833/552398

2. European Society of Radiology, ESR Subcommittee on Audit and Standards. (2010). Clinical audit—ESR perspective. Insights into Imaging, 1(1), 21–26. https://doi.org/10.1007/s13244-009-0002-2

3. International Atomic Energy Agency. (2007). Comprehensive audits of radiotherapy practices: A tool for quality improvement. IAEA.

4. European Society of Radiology. (n.d.). ESR Guide to Clinical Audit in Radiology (4th ed.). Retrieved from https://www.myesr.org/app/uploads/2025/03/2025_Esperanto-ESR-Guide-to-Clinical-Audit-in-Radiology-4th-_20-02.pdf

5. Republic of Latvia, Cabinet Regulation No. 482. (2014, August 19). Regulations Regarding Protection Against Ionising Radiation in Medical Exposure.

6. Latvian Association of Radiology. (2017). Clinical audit guidelines for medical exposure in radiodiagnostics and radiotherapy. Latvian Association of Radiology.

MEDICAL PHYSICS IN THE BALTIC STATES 17 (2025)

Proceedings of International Conference "Medical Physics 2025"
06-08 November 2025, Kaunas, Lithuania

DATA ACQUISITION SYSTEM FOR SCINTILLATION DETECTORS USING SIGNAL SHAPING AND POST-PROCESSING ALGORITHMS

Vilius ŽALĖNAS, Jevgenij GARANKIN, Deividas RŪŠKYS, Artūras PLUKIS
Center for Physical Sciences and Technology, Savanorių pr. 231, LT-02300 Vilnius, Lithuania
vilius.zalenas@ftmc.lt

***Abstract*:** Spectroscopy is a substantial tool and one of the key enablers in nuclear research and its applications. As the demand for available and promising healthcare grows worldwide, equipment and medical measurement tools have to match the increasing expectations. The topic of this work focuses on developing a low-cost and user-friendly digitization tool that captures and analyzes scintillator detector pulses by generating the particle dependent energy spectrum at the end of the measurement.

Keywords: spectroscopy, particle energy analysis, signal processing.

1. Introduction

Radiology has long been one of the foundation branches of modern medicine. X-ray, PET, mammogram and other procedures greatly expand the healthcare capabilities and knowledge of the human body and its behavior to various factors. Although mentioned technologies are not new, their complexity still challenges the accessibility and benefit even today. There is an obvious demand for reducing cost and intricacy, hence enhancing the availability of nuclear technology-based medical equipment worldwide. While developing a standalone medical diagnostic system might require significant time period, securing different compliance certificates that have extremely strict regulation due to the industry's specifics and extensive funding, there are still alternative ways to improve nuclear technology-based medical procedures. One of the possible approaches is to develop a real-time pulse registering and digitizing system that is also kept low-cost and relatively simple to use. Functionality could vary from simple examples like crude equivalent dose approximation that is received during medical procedures to complex nuclide absorption/emission imaging of PET scan using detector arrays. Exactly such a device is described in great detail throughout this article.

2. Device architecture and working principle

Following system has several assumptions for its ideal use case:

- Physical method for registering ionizing radiation is light-based (scintillator is used as a primary pulse capturing device.) Longer excitation and decay time materials are preferred, for example, sodium iodide.
- Electrical pulse has shaping/preconditioning before direct digitization.
- Maximum system data load that is continuously processed is couple hundred pulses per second. Extreme measurement object activity overwhelms the system.
- Personal computer or other Ethernet capability supporting device is required for final data processing and statistical depiction. System only incorporates analog front end, digitization and data transfer.

These prerequisites allow to reduce complexity and cost of the system. The analog front end and chosen analog to digital converter determine that 3-6 μs duration pulses are processed and interpreted with the highest accuracy offered by the system. It implies the need of signal shaping (most often cascaded integration or Gaussian form) that expands fast scintillator pulses preserving the amplitude to duration and form relation. Goal of this step is to yield enough signal duration for digitization process without implementing complex and costly signal processing hardware. While the design of analog scintillator signal shaping amplifier is not a topic of this article, it is sufficient to mention that the exact amplifier used for system testing consisted of two cascaded Sallen-Key active filters.
Following challenge of the data acquisition system is triggering, storage and transfer algorithm, since pulses are not deterministic. Not a single sample of every pulse can be missed, while simultaneously checking for pulse-threshold compliance with the established setup. Simple rising edge trigger based digitization would result in

loss of crucial signal part - initial rising stage that is still below the threshold. Solving this issue requires more sophisticated data management algorithm. Circular constant sampling buffer is implemented in conjunction with delayed square signal falling edge trigger. Considering constant 10 MSPS sample rate, 32 element buffer size was experimentally picked as the best compromise. Mentioned parameters result in maximum theoretically registerable pulse of 6.4 µs. These numbers are important to understand the trigger mechanism and its relation with circular buffer. Every pulse from the amplifier is lead through a comparator with adjustable threshold. Upon threshold reaching pulse comparator generates a short square signal, which is then deliberately prolonged to some adjustable value. Falling edge of the prolonged signal triggers a current state circular buffer copy that is later written into digital memory and sent via Ethernet to host processing device. No matter, how long the actual pulse is (as long as it is in the specified interval), it's beginning in time domain will always be almost perfectly aligned with the first element of circular buffer. That is achieved by fine-tuning the delay time of square pulse. The main benefit of this seemingly complex algorithm is the ability to digitize complete pulse even when part of it has already passed during threshold comparison. Figure 1 provides associative signal, time domain, trigger and circular buffer relation depiction.

Another noteworthy aspect of this system is running parallel processes. Apart from pulse registering this system runs another very important task – *TCP/IP* client that is regularly transferring data to the personal computer. Handling full (1500 byte) frame packets frequently also requires substantial processing power, which is likely unachievable on one core processing system without significant pauses in pulse registering routine. ESP32-S3 microcontroller was chosen to fulfill 2 core processor requirements, it was also preferred over its rivals for convenient software development framework *ESP-IDF* and large online community.

Device also incorporates software procedures for dynamic IP address acquisition and a custom handshake mechanism with its host device that enables secure and reliable usage even in large and complex networks as long as DHCP server is present. Device control is implemented through a Python script, that is also run by the host device. This approach reduces the overall overhead for the digitization device, since all the measurement parameters, such as counting mode, measurement time / count target, etc. are entered by the user in the Python script and send to the hardware device in one packet. Final results are written to a text file in a form of a numerical oscillogram of a pulse: each pulse has its own time attribute and 32 values representing amplitude of it. Data can also be written to a binary file, as well as depicted in a form of energy spectrum with adjustable histogram class widths. There are several more options including every pulse graphical depiction in time domain, or time domain analysis similar to spectrum analysis, but only expressed in classes of time difference between neighboring pulses captured.

Figure 2 depicts a simplified device block diagram consisting of a hardware device itself and its separate blocks, as well as all the additional system components. Double-ended arrow between ADC and ESP32 means that microcontroller not only reads the data, but also generates a clock for ADC. Clock is simply generated by constantly toggling one of the general purpose pins between high and low states. This mechanism ensures, that converter will ever work just as fast as the microcontroller, data congestion is avoided. It is also important to mention that Cremat shaping amplifier is noted in the diagram for versatility and clarity. Any shaping amplifier can be used instead. Lastly, block diagram also shows, that system supports power over Ethernet technology, so cable count and general setup can be reduced.

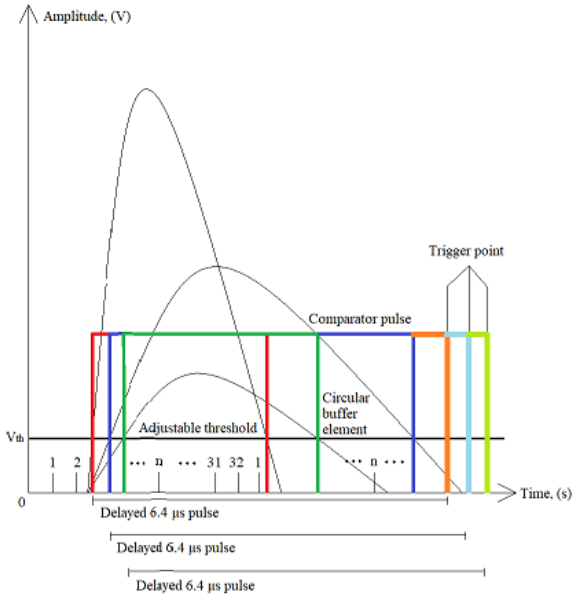

Fig. 1. Signal digitization and trigger algorithm

Taking a step backwards, it is important to explain the circular buffer sample sequence reconstruction algorithm and its inherent flaw that might lead to some small data discrepancies and uncertainties. Trigger event almost never happens right after circular buffer turns over to the first element again and starts overwriting itself. Most often trigger is met with a buffer of some latest iteration values and part of it still holds previous iteration values, but its inherent nature and already described algorithm assure us, that all the current values hold signal in it. The actual problem that arises is not knowing exactly which sample was the first and which one was the last. Of course, having a general understanding in signal form that is expected offers a simple solution–dividing the buffer into 2 parts according to the highest value holding array index and swapping it. While this approach works perfectly in most cases, some anomalies might arise analyzing very low amplitude pulses. Unfortunately, this is the inherent flaw of such data acquisition algorithm that cannot be eliminated without fundamental system design revision. Figure 1 provides a graphical awareness of this aspect again.

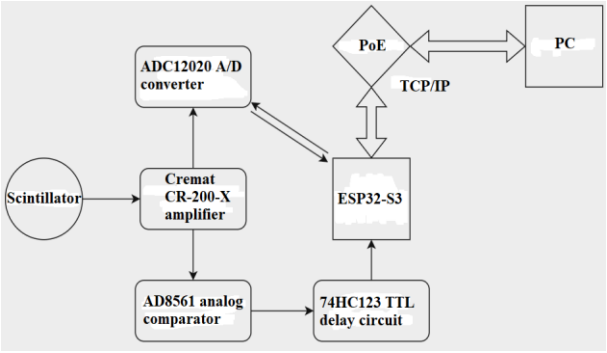

Fig 2. System block diagram

3. Test results

This section focuses on actual results and the observed performance of the system. Testing such a device immediately in medical equipment use cases might be difficult and somewhat misleading since it would stress the device in a very specific way. A better practice is to make more various condition tests, so as many flaws or imperfections would be encountered as possible. Siglent SDG2042X function generator is used to expose the device response to different measurement scenarios.

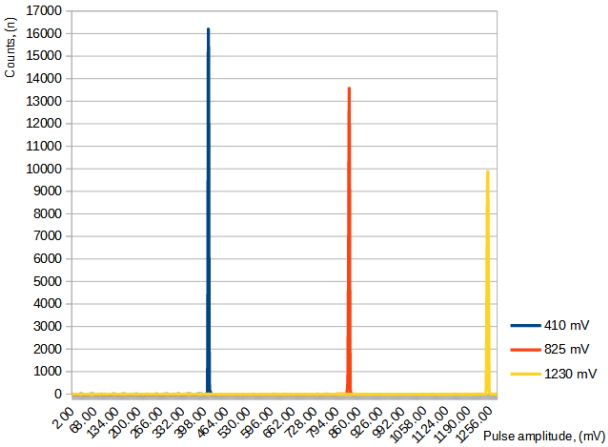

Fig. 3. Measurement result histogram

Three independent measurements of 500 seconds each were taken. Trapezoid shape signal with 1.5 µs both rising and falling edges time, 1.2 µs high level time of 100 Hz was used during all three measurements. All other possible measurement conditions were identical. The only parameter that differed throughout the measurements was the amplitude of the trapezoid signal. Mentioned signal form was chosen to eliminate any possible discrepancies that could have been introduced by shaping amplifier. Ideally the device should register exactly 50000 counts only in one histogram bin (even a negligible width one) based on described measurement conditions. Figure 3 illustrates the test result histogram. As we can see from the legend, 410 mV, 825 mV and 1230 mV amplitude signals were used, peak bins match these numbers almost perfectly. Peak lines do not reach 50000 because bin width of only 1 is used, so same amplitude pulses spread over 2-4 main bins (zooming on X axis would clarify that). Error spread across further neighboring bins is practically unobservable, but function generator jitter also has to be taken into account of measurement result offset from the ideal case. Observed results in Figure 3 assure that device is indeed fully functional and fulfills all its requirements. Its performance can be directly implied to use cases with scintillators, signal shaping amplifiers and other medical equipment.

4. Conclusions

An innovative system that has the potential to improve medical equipment was presented in this article. A low cost and complexity scintillation detector pulse-registering device was characterized in great detail including its advantageous trigger and circular buffer digitizing algorithm, some other hardware solutions (such as main microcontroller and data transfer bus) and their justification. Provided test results substantiated the expectations and proved high accuracy of measurement under different conditions. Minor further improvements and additional feature adaptation to this system would result in copious operation in X-ray, PET scans, mammograms, isotope imaging and other nuclear technology related medical procedures.

5. References

1. Knoll G. F. Radiation Detection and Measurement. Third edition, John Wiley & Sons, 2000. 816 p.
2. Krane K. S. Introductory Nuclear Physics. John Wiley & Sons, 1988. 845 p.
3. Hyde E. K. The Nuclear Properties of the Heavy Elements. Vol. III. Fission Phenomena. Prentice-Hall, 1964. 752 p.
4. Lutz G. Semiconductor Radiation Detectors. Springer, 1999. 356 p.
5. Griffiths D. Introduction to Elementary Particles. John Wiley & Sons, 1987. 392 p.

BRACHYDOSE

Personalized radiation sensor for accurate dose measurement in HDR brachytherapy

HOW THE BRACHYDOSE WORKS

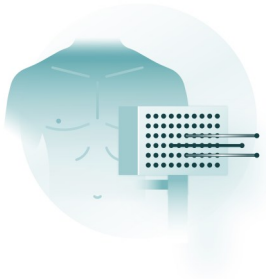

Doctor places a sensor into an organ that must be saved from radiation

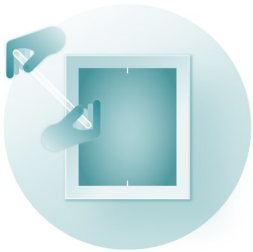

Sensor measures the radiation dose during treatment

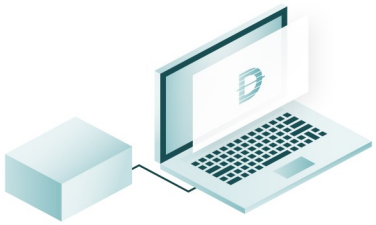

Collected data used to improve patient's treatment and avoid side effects

VALUE FOR A HOSPITAL

Saves 50% of medical personnel's time

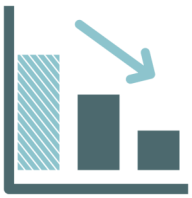

Reduces 25% of overall cost per patient

Patient leaves hospital 3-5 days earlier

Prevents up to 100% of treatment-caused injuries

www.brachydose.net

info@brachydose.com

K. Baršausko g. 59-B507, Kaunas, Lithuania

MEDICAL PHYSICS IN THE BALTIC STATES 17 (2025)

Proceedings of International Conference "Medical Physics 2025"
06-08 November 2025, Kaunas, Lithuania

A NOVEL DIFFERENTIAL REFRACTOMETER FOR HIGH-PRECISION ANALYSIS OF BINARY LIQUID MIXTURES

Vladimirs KOZLOVS[1], Mikhail BARYSHEV[1], Dmitrijs MERKULOVS[2], Shimons SVIRSKIS[1]
[1]Institutite of Microbiology and Virology, Riga Stradin University; [2]ELMI Ltd., Riga
[1] Vladimirs.Kozlovs@rsu.lv; [2]dmitrijs_merkulovs@yahoo.co.uk

***Abstract*:** We present the design and operating principles of a novel differential refractometer optimized for high-resolution analysis of binary liquid mixtures. Experimental evaluation demonstrated a refractive index resolution of $5 \cdot 10^{-7}$ nD. Notably, the method shows low sensitivity to minor temperature fluctuations, making it especially suitable for the analysis of low-concentration aqueous dispersions of polymer nanoparticles, where ultra-high resolution (better than $1 \cdot 10^{-5}$ nD) and stable temperature control are essential.

Keywords: refractometry, high resolution, polymer nanoparticles, concentration

1. Introduction

Microplastics (MPs) are pollutants consisting of plastic particles smaller than 5 mm. These particles can adversely affect humans, aquatic organisms, and entire ecosystems. A fraction of MPs, known as nanoplastics (NPLs), has particle sizes in the range of 1–100 nm. Environmental plastic waste may degrade into NPLs under the influence of external factors such as ultraviolet radiation [1]. NPLs often exhibit properties distinct from bulk plastics and may be more hazardous. Although research in nanotoxicology has advanced significantly in recent years, knowledge of the biological effects of MPs remains limited [2]. Progress in toxicity studies is hampered by the difficulty of detecting MPs, particularly their nanoscale fraction [3]. Specialized analytical methods are therefore required. In our previous work [4], we demonstrated that refractometric methods can detect very low concentrations (down to 1 mg/L) of NPLs in aqueous media. However, this approach required strict temperature stabilization of the sample, which complicates practical use. A differential refractometer, as proposed in [5], overcomes this limitation. The present study investigates the potential of such a refractometer for the quantitative determination of nanosized polymer particles in aqueous media (mineral freshwater OECD201) using commercial carboxylated polystyrene spheres of 26, 40, and 100 nm as model NPLs.

2. Measurement principle

A differential refractometer is a specialized instrument used to measure the difference in the refractive index (RI) between two substances - a sample and a reference material with known RI. Differential refractometer [5] consists of two identical measuring cells one of which is shown in Fig. 1.

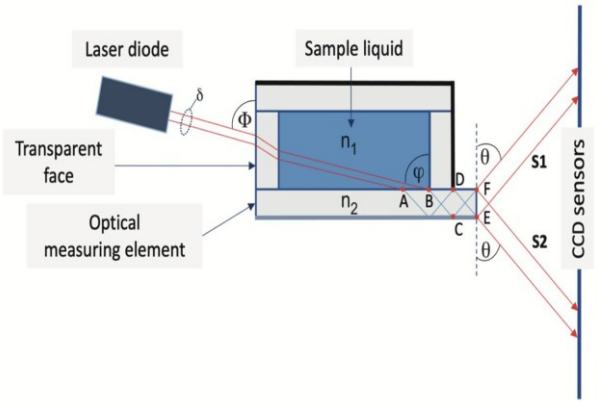

Fig. 1. Measuring cell with a plane–parallel plate as the measuring element. S1 and S2 — refracted beams; δ — laser beam width; Φ — angle of incident laser beam; φ — incidence angle on the measuring element; θ — outgoing angle; A–F — reference points; n_1 — RI of the sample liquid; n_2 — RI of the optical element.

The position of the beams S1 and S2 on the CCD-sensor it is uniquely determined by RI n_1 of sample liquid. In turn, n_1 is uniquely determined by the concentration of in the sample. By examining the path of light rays in a measuring cell, it can be shown that the refractive index n_1 is related to the angle θ as follows:

$$n_1 = \sqrt[2]{n_2^2 + cos^2\Phi - sin^2\theta} \qquad (1)$$

Thus, the accuracy of determining the angle θ is determined by the accuracy of measuring the position of the signals S1, S2 on the sensors. This is achieved due to two experimentally observed factors [5]. Firstly, with a

change in the refractive index, a parallel shift of the signal occurs along the sensor without changing its shape. Secondly, there are sections of linear decrease in the signal amplitude. To confirm these observations, we conducted a computer simulation of the signals, the results of which are shown in Fig. 2. The measurement results are also shown there.

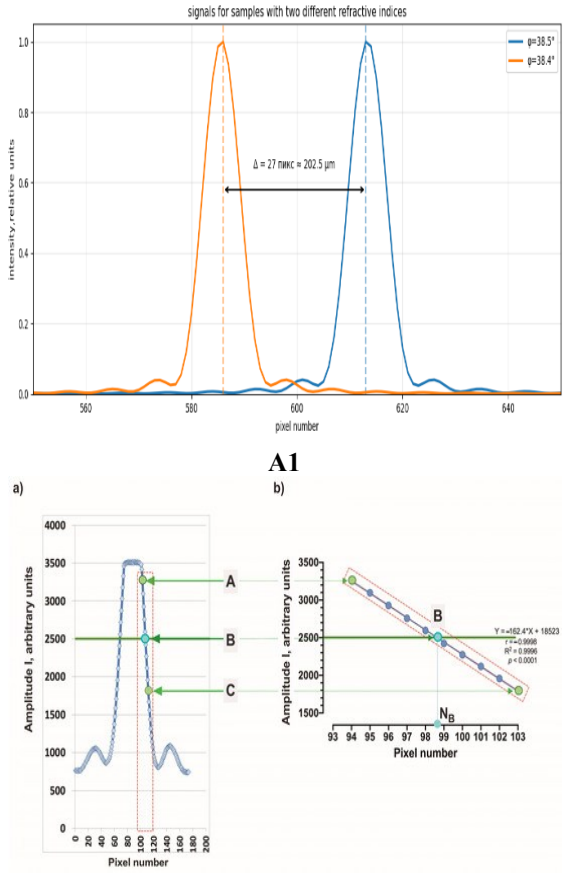

Fig. 2. A1 - the result of numerical modeling of CCD- sensor signals for two values of the refractive index of the sample; **A2** a) - measured signal of the CCD-sensor, b) - linear approximation of the front of the signal of the CCD-sensor

To determine the position of the signal image on the sensor, it is generally sufficient, to indicate the of any selected point B, which we select as follows. Let us consider the section AC of the right edge of the signal (see Fig.2. A2 b)), which includes signals from pixels whose readings lie in the interval (0.8 – 0.5) from the maximum value of the signal amplitude. Now, we can determine the "coordinates" N_B of point B from the condition that the value of signal amplitude takes on a certain given value Ig. In the calculations, we assumed that Ig = 2500. The diagram of the differential refractometer is shown in Fig.3.

The differential refractometer consisted of two measuring cells. The first cuvette contains a solvent with a refractive index of n3. Another cuvette contains a solution with a refractive index of n4. The light beam from the laser diode was divided into two parts using a splitter, one of which was directed directly at the input window of the first cuvette. The second part is directed using a mirror to the entrance window of the second cell, and the mirror is positioned such that the angles Φ of incidence of both beams are equal to each other. The light beams emerging from the measuring elements were recorded using a CCD sensor. In this case, when n3 = n4 and θ = θ1, the rays emerging from the measuring elements are parallel. The images of the signals from the sensor are shown in Fig.4. The position of the signals on the sensor is determined by points B0 and B1, the coordinates of which, N(n3) and N1(n4), are determined in the manner described above.

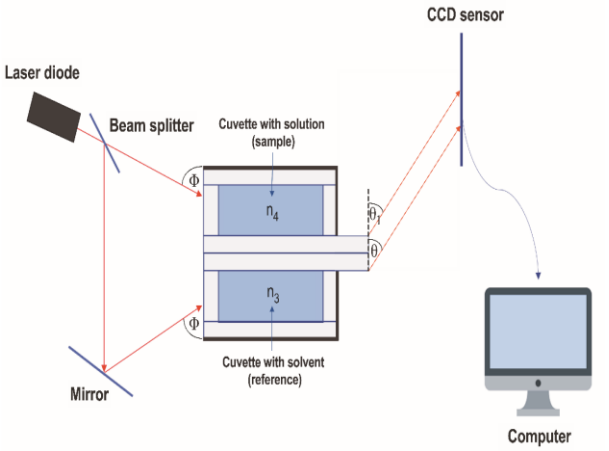

Fig. 3. Diagram of a differential refractometer. φ – angle of incoming laser beam; θ – angle of outgoing light rays; n3 – solvent; n4 – solute; red arrows – light rays.

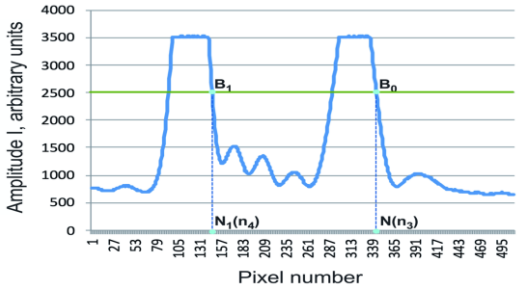

Fig. 4. Sensor signals from a cuvette with a solvent (right signal) and a cuvette with a solution (left signal). B0, B1— position of signals on the sensor; N(n3) and N1(n4)—pixel number coordinates for the position of signals B0 and B1, respectively.

The distance Δ(n3,n4) = N(n3) − N1(n4) changes only with a change in the concentration the solution, and is practically independent of temperature [5].

3. Results and discussion

The model particles used in this study were carboxylated polystyrene (PS-COOH) spheres with diameters of 26, 40, and 102 nm. These particles were dispersed in OECD202 artificial freshwater at a concentration of 100 mg/L. To register the signals, a Hamamatsu monochromatic linear 1024-pixel image sensor S9226 with a pixel pitch of Δp = 0.0078 mm was employed. The measured displacements of the CCD signals were 7.8, 7.7, and 7.9 pixels for particles with diameters of 26, 40, and 102 nm, respectively. The minimum reliably detectable displacement is 0.1 pixel [5]. Therefore, the proposed method allows the detection of polymer nanoparticles at concentrations below 1 mg/L. A detailed description of light propagation in liquids containing

nanoparticles should be based on Mie theory [6], which allows calculation of the phase shifts (and corresponding refractivity changes) caused by nanoparticle scattering. However, for suspensions with very low particle concentrations, light propagation can be adequately described within the framework of effective medium theory (EMT), for example, the Maxwell–Garnett approximation [7].

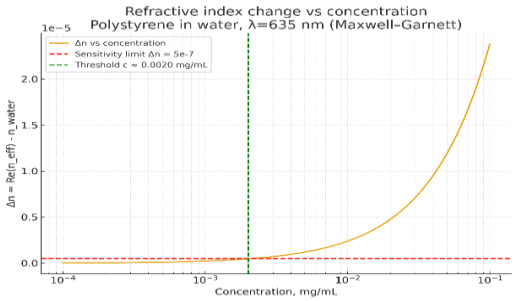

Fig. 5. Dependence of the refractive index on the concentration of polymer nanoparticles in water.

Figure 5 shows the calculated dependence of the refractive index on nanoparticle concentration using the Maxwell–Garnett model. The calculations are in reasonable agreement with the obtained experimental data. Importantly, unlike in our previous work [4], where nanoparticle signatures could not be clearly observed, the differential refractometer allowed robust detection and quantification of polymer nanoparticles at very low concentrations. This confirms that the proposed instrument combines the strengths of classical refractometry with the robustness of differential measurements. Compared to conventional techniques such as dynamic light scattering or turbidity analysis, the refractometric approach provides direct access to the refractive index increment with significantly higher resolution and lower sensitivity to temperature fluctuations. This makes the method especially promising for environmental monitoring of nanoplastics, where precise detection at trace concentrations is required. In addition to polymer nanoparticles, the proposed method can be extended to other nanoscale particles of biological origin, such as bacteriophages. Since phages are nanometer-sized entities with dimensions comparable to synthetic nanoparticles, their presence and concentration also induce measurable changes in the refractive index of aqueous suspensions. This opens the possibility of applying differential refractometry for rapid and precise phage concentration measurements, eliminating the need for labor-intensive plaque assays or costly qPCR analysis.

4. Conclusions

A novel differential refractometer was designed and experimentally validated for the analysis of nanosized polymer particles in aqueous dispersions. The device achieves a refractive index resolution of $5 \cdot 10^{-7}$ nD and allows detection of nanoparticle concentrations below 1 mg/L. The experimental measurements performed with carboxylated polystyrene spheres of 26, 40, and 102 nm confirmed the linear dependence of the refractive index change on particle concentration, in agreement with theoretical predictions based on effective medium theory. The results demonstrate that the method is largely insensitive to temperature fluctuations, which often limit the accuracy of conventional refractometry. In comparison with other analytical approaches, such as light scattering or turbidity measurements, the proposed refractometer provides superior resolution, robustness, and quantitative accuracy. This makes it a valuable tool for studying nanoplastics and polymer nanoparticle dispersions in environmental and biomedical contexts. Future work will focus on extending the technique to more complex multicomponent systems and evaluating its performance in real environmental water samples. Beyond nanoparticle analysis, the proposed differential refractometer has strong potential for biomedical applications, including rapid determination of bacteriophage concentrations. Phages are increasingly used in antimicrobial materials, biosensing, nanomedicine, and therapeutic applications. The ability to quantify phages in early-stage experiments within minutes, without resorting to plaque assays (≥18 h) or qPCR (≈4 h), represents a radical improvement in both speed and cost-effectiveness. Thus, the developed method provides not only a powerful tool for nanoplastics research but also a versatile platform for emerging applications in biotechnology and medicine. However, it should be noted that at very high nanoparticle concentrations, multiple scattering and inter-particle interactions can significantly complicate the interpretation of refractive index changes. In such cases, more advanced theoretical models, beyond the simple effective medium approximation, may be required.

5. References

1. Lu T., Hong,W., Hu J., Penuelas J, Qian H. Global Distribution of Marine Microplastics and Potential for Biodegradation. J. Hazard. Mater. 2023, 451, 131198
2. Yan X. et.al. Nanoplastics toxicity is a subset of nanotoxicology not a separate field. Environ. Health 2025, 3, 920-930
3. Silva A.B., Bastos A.S., Justino C.I.L., da Costa J.P., Duarte A.C., Rocha-Santos T.A.P. Microplastics in the environment: Challenges in analytical chemistry - A review. Analytica Chimica Acta 2018,1017, 1-19.
4. Kozlov V., Heinlaan M., Merkulov D. Measurement of the concentration of functionalized polymer nanoparticles using light refraction. In Proceedings of the 14th International Conference "Medical physics in the Baltic States", Kaunas, Lituania, 7–9 November 2019; pp. 134–136
5. Svirskis S. , Merkulovs D. , Kozlovs V. Proposal for a New Differential High-Sensitivity Refractometer for the Simultaneous Measurement of Two Refractive Indices and Their Differences. Sensors 2024, 24, 3340.
6. Bohren G.F., Huffman D.R. Absorption and scattering of light by small particles. J.Wiley@ Sons,1983, 521 p.
7. Markel V.A. Introduction to the Maxwell Garnett approximation:tutorial. J.Opt.Soc. Am. A 2016, 33, 1244-125

WHY idose

Flexibility

Customize the system to your needs so that you can focus on what's important to you.

Exceeding alerts

Monitor in real-time the safety of your patients with dose exceeding alerts

Drag&Drop reports

Maximize productivity by placing all the necessary information where it matters most.

Process automation

Save up to 90% of time preparing reports

Simple integration

Compliance with:
HL7, DICOM, IHE

Multilingual

Work efficiently in your language

Versitile

Access data from every kind of x-ray device or PACS system in real-time.

All in one place

Seamlessly connect to industry-leading devices and store all the radiation dose data in one, neatly organized place.

Cloud or local

You can choose SAAS model (cloud) or a permament license (on premise)

Dose calculator

Internal dose calculator in compliance with:
IEAE TRS 450, AAPM, EFOMP, ICRP

idose.eu

info@idose.eu

Solution partner UAB MedUS Medical

MEDICAL PHYSICS IN THE BALTIC STATES 17 (2025)

Proceedings of International Conference "Medical Physics 2025"
06-08 November 2025, Kaunas, Lithuania

POTENTIAL FOR CITIZEN SCIENCE WITH AFFORDABLE HAND-HELD RADIATION DETECTORS

Christian BERNHARDSSON[1], Erik EWALD[2]
[1]Medical Radiation Physics, Department of Translational Medicine, Lund University
[2]Medical Radiation Physics, Institution of Clinical Sciences in Lund, Lund University
[1]christian.bernhardsson@med.lu.se; [2]er4416be-s@student.lu.se

***Abstract*:** This study investigated the fundamental dosimetric properties of commonly available hand-held radiation detectors that are aimed for public use. As a reference, measurements were also conducted with a "professional" GM-based detector. Two of the detectors were also investigated for their intra detector model variability by studying seven and five individual units, respectively. The overall aim was to understand if these detectors are reliable and if they potentially fit for citizen science projects.

Keywords: Citizen science, detectors, GM-tube, CsI(Tl), radiation protection

1. Introduction

After the Fukushima Daiichi nuclear power plant accident in 2011 the "Safecast" detector [1] became popular among the public for measuring and mapping radiation levels, jointly contributing with data to a public database [2]. The database currently consists of more than 150 million readings, and is continuously growing. This is an example of a *citizen (radiation) science* project, where the participants engage in data collection, data processing, curriculum-based and community science [3]. In connection with citizen science projects related to radiation mapping, several online databases have appeared [2, 4, 5, 6]. Works in other initiatives have studied various aspects of citizen sciences related to radiation assessments *e.g.* using mobile telephone applications [7, 8], radon [9], collection of mushrooms [10], and more generally, for potentially increasing public understanding of science [3]. In summary, this indicates a great public interest in measuring radiation, to take part in one's own radiation protection and to learn more about radiation science.

During recent years the amount of affordable radiation detectors, aimed for public use, has increased. These detectors are mainly based on Geiger Müller (GM) tubes or scintillation crystals but also, as mentioned, mobile telephone applications [11]. However, the questions arise: how accurate are these detectors, what are their limitations, how do they compare to similar professional radiation protection instruments. In this project, we have surveyed a limited amount of publicly available and affordable hand-held radiation protection instruments and compared them to a professional version of such detectors. The dosimetric properties investigated included: dose and dose rate response, energy and angular response, as well as the intra detector variability. Measurements were conducted in laboratory condition at Skåne University Hospital in Malmö and in the city centre of Malmö. Preliminary results from these benchmarking will be presented together with observations that should be considered when using the detectors in an unknown exposure situation.

2. Material and methods

The selection of detectors was based on a quick survey on internet forums and shops; what is currently used and easily available in Sweden. Four different detectors were finally selected:

Safecast – an old version of the common Safecast detector (bGeigie Nano kit) was available in the lab, previously bought on the Safecast homepage. It is based on a pancake GM tube, show the instant dose rate on a display and can log data on a memory card and/or send the data to the Safecast database. It is intended for mobile mapping *e.g.* mounted in a car. On the Safecast homepage [1] there are manuals and detailed information about the device. Today's Safecast detector can be bought assembled ($750) or in parts for self-assembling the device ($475).

FNIRSi – the detector (model: GC-01) was bough online at *Elgiganten* homepage, that has physical and web-based shops in the Nordic countries. The detector is also available in several other internet shops. The device is based on a GM tube and show current, average and maximum dose rate since start-up, as well as

accumulated dose. It has a search mode displaying a graphical time trend of the dose rate and several alarm modes. It is delivered with a quick guide on how to operate it and some technical specifications, also provided on the manufacturer homepage [12]. The FNIRSi (GC-01) can be bought for €30-40, our version was purchased for €70.

UNI-T – the detector (model: UT334A) was bought online at *Clas Ohlson* webpage, that has physical and web-based shops in Sweden, Norway and Finland. The device is based on a GM tube and shows current and average dose rate as well as accumulated dose, since start-up. It has an internal storage for ten scheduled measurements and alarm functions for dose rate and dose. It is delivered with a quick guide on how to operate it and some technical specifications, also provided on the manufacturer homepage [13]. The detector was purchased for €90.

Radiacode – the detector (model: 103) was bought on the Radiacode homepage [14] at a price of €320. It is a dosemeter-spectrometer based on a 1 cm^3 CsI(Tl) scintillation crystal, have support to be operated from a mobile telephone application (or computer software) for dose rate mapping (using the mobile telephones GPS) or spectrometry acquisition. On the Radiacode homepage [14] there are detailed manuals, specifications and help-pages with useful examples on its various operations.

These four detectors were exposed to a range of laboratory conditions to benchmark some key dosimetric properties (sections 2.1 to 2.6), using various types of radiation point sources. For each exposure situation, a reference "professional" detector was used – **Automess** (model: 6150AD) with a GM-probe (model: 6150AD-18/E) [15]. To minimise the exposure of the operator, the detectors were exposed in bulk and the displayed dose information was recorded by a web-camera. These recordings were analysed by an in-house made tool that converted the readings to an excel data file.

Apart from the inter variability in the detector response between the four detectors, the intra detector response of the FNIRSi and the UNI-T was also investigated. For that purpose, seven FNIRSi detectors and five UNI-T detectors were exposed under the same conditions and the intra detector response was compared for the various dosimetric properties investigated.

All detectors were imaged with an X-ray C-arm to compare the configuration and positioning of the respective detector volumes.

2.1. Dose rate

The ambient dose equivalent rate response of the detectors was tested for a ^{137}Cs point source (760 MBq) at three different source-detector distances (0.5 m, 1.0 m, 2.0 m). For each distance the radiation source was shielded in a lead jar in a lead cave. At each distance, the lead was removed, during ~4 minutes, after which the source was shielded again. The time from background to the measured dose rate, as well as the time from measured dose rate back to background levels were recorded as τ_r and τ_f, respectively. Here τ_r and τ_f are defined as the operator-observed response times. The variation in the registered dose rate during the exposure was noted.

2.2. Dose

The accumulated ambient dose equivalent was studied for the FNIRSi and UNI-T detectors at three dose levels: 11 µSv, 42 µSv and 56 µSv, as calculated with Rad Pro Calculator [16] for ^{137}Cs sources at different distances and exposure times of 11 min (±15 s).

2.3. Angular dependence

The angular sensitivity of the detectors was studied for both the azimuthal (0° correspond to the radiation field incident perpendicular to the detector casing backside) and polar (0° correspond to the radiation field incident perpendicular to the top-front side of the detector casing) rotations. This was done by positioning the detector in the centre of a circular angle disc made from plywood while registering the dose rate for a ^{137}Cs point source (250 MBq) with 10° or 30° increments. For each position of the source an average dose rate of five measurements was calculated.

2.4. Energy dependence

The detectors energy dependence was studied in the limited energy range from 140 keV to 1.25 MeV, using point radiation sources of ^{99m}Tc, ^{133}Ba, ^{137}Cs and ^{60}Co.

2.5. Background variation

The variation of the detector responses was studied in a well-shielded iron room, normally used for whole body counting. The detectors were positioned in the centre of the room with the iron door closed. The dose rate of each detector was noted continuously during 30 min and the variation in relation to the average dose rate was determined.

2.6. Activity determination

Using the conversion coefficients for point sources in Radionuclide and Radiation Protection Data Handbook 2002, [17] the activity of a ^{137}Cs source was estimated, using the same setup as in Section 2.1. (*i.e.,* for three different dose rates (distances)).

3. Results

All results presented are as measured, *i.e.* with no background correction applied.

3.1. Dose rate

The average dose rates and corresponding average variation (C_v), response (τ_r) and recovery (τ_f) times are provided in Table 1, for the various detectors and for three different dose rates.

For all dose rates, the investigated detectors underestimate the dose rate measured with the reference Automess detector. The under estimation is proportionally larger for higher dose rates. It is observed that the UNI-T has the fastest response, but the larges variation in the measured value. The variation in dose

rate between the tested detector types is rather low, but the UNI-T varies the most both between the same type of detectors as well as within individual units. However, the UNI-T has a slightly better response and recovery times than the FNIRSi detectors. For the Safecast detector, which reports 60-second averaged dose rates (with displayed values updated every 5 seconds), τr and τf were excluded from the comparison.

Table 1. Average dose rates of the FNIRSi (#7), UNI-T (#5), and Safecast detectors as compared to the Automess detector for three different dose rates using a Cs-137 source. Provided are also the coefficient of variation (C_v), signal rise (τ_r) and fall (τ_f) times (as averaged for the seven and five detectors of each model).

	Avg. dose rate [μSv/h]	**C_v [%]**	**τ_r [s]**	**τ_f [s]**
Automess	**234**			
FNIRSi	128	1	32	33
UNI-T	154	3	21	20
Safecast	169	1	-	-
Automess	**60**			
FNIRSi	40	2	36	15
UNI-T	49	6	31	15
Safecast	48	1	-	-
Automess	**17**			
FNIRSi	13	3	32	39
UNI-T	14	10	19	17
Safecast	13	1	-	-

3.2. Dose

The accumulated doses after about 10 min of exposure are shown in Table 2.

Table 2. Average accumulated doses with the FNIRSi (#7) and UNI-T (#5) detectors and the range of registered doses in parenthesis for three different Cs-137 exposures.

Calculated abs. dose [μSv]	**FNIRSi [μSv]**	**UNI-T [μSv]**
11	7 (5-8)	5 (4-5)
42	19 (15-21)	14 (12-16)
56	25 (20-28)	18 (16-21)

Both detectors underestimate the actual dose for the three exposures. More important is that all five of the UNI-T detectors drastically and incorrectly changes the registered value of the accumulated dose when the exposure stops. This is observed on the detector display, that correctly accumulate the dose during the exposure but when the exposure stops, the accumulated dose drops abruptly by precisely 42% within 10 s. The reason for this severe error is unclear, but it is important to be aware of and need further investigations, especially by monitor the accumulated dose for longer time after the exposure stops.

3.3. Angular dependence

The angular dependence for the investigated detectors is illustrated in Fig. 1.
As can be observed in Fig. 1, the detectors perform well with rather small deviations, expect when oriented with the electronics and battery between the radiation source and the detector volume. The Safecast detector, with its pancake GM tube (and configuration of the electronics), varies in its response for the azimuthal rotation which should be considered when positioning it.

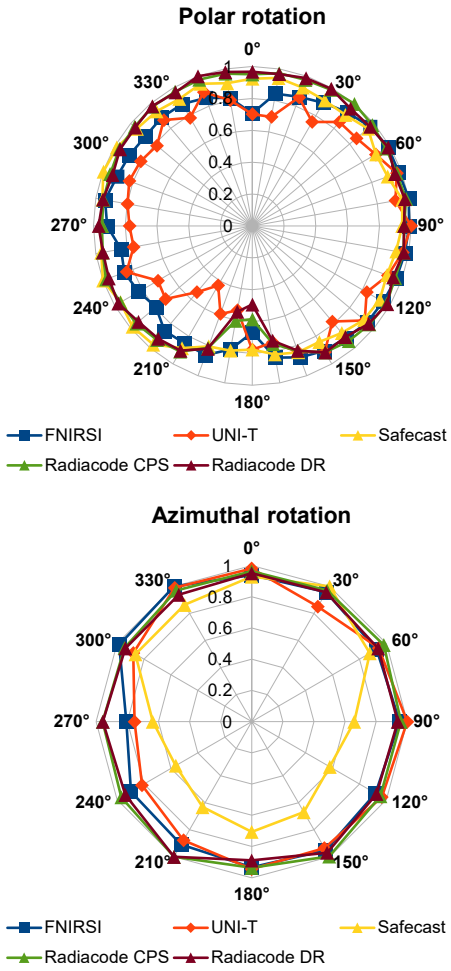

Fig. 1. Relative angular response, polar (θ) and azimuthal rotations (α), for the different detectors. The registered measurements are normalised to the maximum value for the respective detectors.

3.4. Energy dependence

The energy dependence follows what is expected from an uncompensated GM tube in the investigated energy range, rather flat between ~0.3 – 1.2 MeV (within a factor 0.5). However, the UNI-T has a relative response of 2 for the lowest energy and almost linearly drop down to 0.5 for the highest energy. The Radiacode (scintillation detector) has a flat energy response in the energy interval investigated.

3.5. Background variation

The seven FNIRSi detectors showed an average dose rate in the range from 0.040 to 0.068 µSv/h with an individual detector variability, in terms of standard deviation of the mean for the measuring period, of about 44% (range: 38%–45%). The same numbers for the five UNI-T detectors were 0.083 to 0.097 µSv/h with an individual variability of about 12% (range: 7%–18%). The Safecast detector register the dose rate based on CPM and 5 s measurements, that showed 0.059±18% µSv/h and 0.057±78% µSv/h, respectively. The Radiacode detector showed approx. 60 counts for a 600 s measurement.

3.6. Activity determination

Based on the dose rate measurements with the FNIRSi, UNI-T, and Safecast detectors, the estimated activity of a 760 MBq ^{137}Cs was determined (Table 3).

Table 3. Calculated activity, *A*, for a Cs-137 source with an activity of 760 MBq at three different source-to-detector distances. Provided in the parenthesis are the ranges of the estimated activities for the seven FNIRSi and five UNI-T detectors.

Distance [m]	FNIRSi, *A* [MBq]	UNI-T, *A* [MBq]	Safecast, *A* [MBq]
0.5	332 (291-365)	399 (373-457)	438
1.0	415 (366-451)	504 (463-607)	497
2.0	546 (465-616)	590 (544-700)	550

Although these activity determinations are associated with several uncertainties, they provide useful insight into how thedetector responses reflect on the activity determinations. The distance to the source is an important factor due to the inverse square law and the configuration of the GM tube inside the detector (in relation to the radiation field). It is therefore recommended to conduct the measurement at more than one appropriate distance from the source, with only air between the source and detector, taking potential under-response into account, as well as possible background corrections if necessary.

4. General considerations

For constancy control of these detectors, without access to radiation sources, it is possible to find locations with elevated natural background**.** Monuments or constructions with large blocks of granite is one such example. A quick survey in the city of Malmö revealed one such monument, with a dose rate of ~0.5 µSv/h, that could serve as a point for constancy control. For personal use, it is important to get acquainted with the detector, be aware of potential shortcomings, perform repeated measurements at the same positions/locations, understand background variations and corrections when needed, make constancy checks, and to view several sources for information when in doubt.

5. Conclusions

The tested detectors perform rather well in the investigated situations and for their price. However, it is important to be aware of some of their shortcomings. Further studies are needed to identify and better described these shortcomings.

5. References

1. Safecast homepage, current available detectors. https://safecast.org/devices/ (18 August 2025, Date accessed)
2. Safecast, drive map data. https://map.safecast.org/?y=29&x=71&z=2&l=0&m=0 (18 August 2025, Date accessed).
3. Philips T.B., Bonney R., Ballard H.L., Enck J.W. Can citizen science enhance public understanding of science? Public understanding of science 2016;25(1):2-16.
4. Openradiation, homepage. https://www.openradiation.org/ (4 September 2025, date accessed).
5. Radiaverse portal, homepage. https://www.radiaverse.com/ (4 September 2025, date accessed).
6. Saveecobot, homepage. https://www.saveecobot.com/ (4 September 2025, date accessed).
7. Odenwald S. Smartphone sensors for citizen science applications: radioactivity and magnetism. Citizen science: theory and practice 2019;4(1):18, pp. 1-15.
8. Liutsko L., Oughton D., Tomkiv Y., et al. Resilience after a nuclear accident: readiness in using mobile phone applications to measure radiation and health indicators in various groups (SHAMISEN SINGS project). Journal of radiological protection 2023;43:041511.
9. Martell M., Perko T., Tomkiv Y., Long S., Dowdall A. Evaluation of citizen science contributions to radon research. Journal of environmental radioactivity 2021;237:106685.
10. Gustavsson C., Andersson-Sundén E., Barker A., Hjalmarsson A., Lantz M., Lundén K., Pomp S. Citizen science in radiation research. EPJ web of conferences 2020;239:25001.
11. Van Hoey O., Salavrakos A., Marques A., Nagao A., Willems R., Vanhavere F., Cauwels V., Nascimento L.F. Radiation dosimetry properties of smartphone CMOS sensors. Radiation protection dosimetry 2016;168(3):314-321.
12. FNIRSi detector homepage. https://www.fnirsi.com/ (4 September 2025, date accessed).
13. UNI-T detector homepage. https://meters.uni-trend.com/ (4 September 2025, date accessed).
14. Radiacode detector homepage. https://www.radiacode.com/ (4 September 2025, date accessed).
15. Automess detector homepage. https://www.automess.de/ (4 September 2025, date accessed).
16. Radpro calculator homepage. http://www.radprocalculator.com/ (4 September 2025, date accessed).
17. Delacroix D., Guerre J.P., Leblanc P., Hickman C. Radionuclide and radiation protection data handbook 2002. Radiation protection dosimetry 2002;98(1);9-1.

Content

AUTHOR INDEX

ISSN 1822–5721